Scuola Universitaria Superiore IUSS Pavia

An innovative timber retrofit for unreinforced masonry structures: impacts on seismic performance and preliminary considerations on environmental sustainability

A Thesis Submitted in Partial Fulfilment of the Requirements
for the Degree of Doctor of Philosophy in

EARTHQUAKE ENGINEERING AND ENGINEERING SEISMOLOGY

Obtained in the framework of the Doctoral Programme in
Understanding and Managing Extremes

by

Marco Miglietta

May, 2022

Scuola Universitaria Superiore IUSS Pavia

An innovative timber retrofit for unreinforced masonry structures: impacts on seismic performance and preliminary considerations on environmental sustainability

A Thesis Submitted in Partial Fulfilment of the Requirements
for the Degree of Doctor of Philosophy in

EARTHQUAKE ENGINEERING AND ENGINEERING SEISMOLOGY

Obtained in the framework of the Doctoral Programme in
Understanding and Managing Extremes

by

Marco Miglietta
Supervisors: Prof. Guido Magenes (Scuola Universitaria Superiore IUSS Pavia)
Prof. Francesco Graziotti (Scuola Universitaria Superiore IUSS Pavia)

May, 2022

ABSTRACT

The present thesis is a scientific study on a newly proposed timber system for the structural upgrade of light masonry buildings exposed to induced seismicity. It fits within the framework of a comprehensive project aiming at characterising the seismic response of masonry buildings typical of the Groningen region (The Netherlands), interested by earthquake events induced by gas-extraction activities.

The mechanical interaction between masonry and retrofit system was initially investigated through in-plane quasi-static shear-compression tests on two identical full-scale masonry piers, one in bare and one in retrofitted configuration. Experimental results allowed to evaluate the effectiveness of the solution in improving the lateral performance of masonry elements and to derive analytical prediction equations. These activities were followed by the dynamic incremental shake-table tests up to near collapse conditions performed on two nominally identical full-scale unreinforced masonry cavity-wall buildings, the former in un-strengthened conditions and the latter in retrofitted configuration. Experimental results were used to assess the impact of the retrofit system from an overall building point of view, considering its beneficial effects also in improving the connections masonry-to-floor systems. Damage limit thresholds were experimentally defined and correlated to an engineering demand parameter for both configurations.

A numerical study was carried out to assess the impact of the timber retrofit system on the variability of the lateral response of a case-study building characterized by the most common features that can be found in the Groningen region, considering simultaneously global and local failure mechanisms. The related multi-degrees-of-freedom models were derived from the ones calibrated on the incremental dynamic tests, and reduced to single-degree-of-freedom oscillators to perform cloud non-linear time-history analysis using the latest ground motion database representative of the area. Numerical results were post-processed to produce damage state global fragility functions conditioned to the seismic intensity for bare and retrofitted conditions. The local out-of-plane assessment of masonry piers was carried out as well through cloud non-linear time-history analysis. The latest ground motion database was employed for element at the ground floor level while filtered accelerations from global analysis were employed for elements at the first-floor level. The outcomes were used to fit collapse fragility functions conditioned to the seismic intensity for bare and retrofitted masonry piers. Finally, global and local vulnerability assessments

were unified into single damage states fragility functions that consider simultaneously global and local behaviours.

The concluding section of the thesis discusses qualitatively the main aspects of environmental sustainability within the proposal of a new structural upgrading intervention. The review of retrofit details under the light of "life cycle thinking" allows to reach more ambitious environmental and economical goals, especially with the view of large-scale applications.

ACKNOWLEDGEMENTS

Il dottorato è un lungo viaggio che non può essere portato a termine senza l'aiuto di colleghi competenti, ma altrettanto non può essere potato a termine senza l'aiuto della propria famiglia e delle persone più care. Con l'inizio della mia esperienza la durata del programma è stata estesa da regolamento da 3 a 4 anni, poi all'inizio del terzo anno la pandemia globale di COVID-19 si è fatta avanti. Il ministero dell'istruzione, che ringrazio, ha permesso un estensione dell'anno accademico. Mi ritrovo ora a scrivere i ringraziamenti a 5 anni abbondanti dall'inizio della mia esperienza, un tempo lunghissimo, caratterizzato da alti, altissimi e bassi, bassissimi, che uniti mi hanno dato un bagaglio di conoscenza per il quale ora sono molto fiero, e che mi ha fatto incontrare e collaborare con gente che sono molto felice di aver incontrato.

I primi ringraziamenti vanno a tutte le persone che hanno lavorato con me per lo svolgimento dei test sperimentali in EUCENTRE. I ragazzi della Damiani Costruzioni s.r.l, Adriano, Gaetano, Giorgio, Blendi, Astrit, e Francesco e Claudio (che arrivavano da Brescia in laboratorio prima di me), per avermi rispettato, e per avermi ascoltato fin dall'inizio della nostra collaborazione, nonostante la mia esperienza in cantiere fosse nulla al tempo. E come dimenticare Luca Grottoli, senza di lui non avrei elaborato i dati di un bel niente. E grazie ai laureandi, Luca Mazzella (n°1), Laura Gandini (grandissima), Ilaria Nasso, Gian Carlo De Sanctis, indispensabili specialmente nei primi 2 anni del dottorato.

Un particolare ringraziamento va a tutto lo staff tecnico dell'EUCENTRE e del DICAr, con cui ho collaborato per tutto il mio dottorato. Albe, il Bone, Luca e Jerry, Roberto, Riccardo, Riccardone, Simo Girello e Claudio, è stato un piacere lavorare con ognuno di loro, non solo perché mi hanno permesso di imparare in maniera corretta, ma anche per avermi allietato tantissimi momenti tra chiacchiere e minchiate, o semplicemente salutandoci al mio passaggio in laboratorio (e per questo un merito particolare va a Luca Rotonda) o in vespa (e per questo un merito particolare va ad Alberto). Le chiacchiere di sport con Jerry…

Ringrazio anche tutte persone con cui ho avuto modo di avere a che fare dello staff EUCENTRE, Luisa Corona, Saverio, Monica, Ettore, Gabriele Ferro, e Gabriele dell' IT, Rustio e Andrea dell'IT, per la loro disponibilità e serietà. In particolare, ringrazio Paolo e Winna, che per gli ultimi 2 anni e mezzo mi hanno accolto in reception tutti i giorni, sempre

sorridenti, sempre gentili, un toccasana per l'inzio delle giornate lavorative (ci vorrebbero più Paoli e Winne al mondo).

E ovviamente un grazie gigante a tutti i ragazzi del team di muratura: Gabriele Guerrini, Annalisa Rosti, Stefano Bracchi, Ilaria Senaldi, Martina Mandirola persone estremamente competenti che sono sempre state disponibili ad aiutarmi a risolvere le più diverse questioni. E un gigantissimo grazie ai miei colleghi dottorandi, Stelios, Umbe e Satya, i primi che ho incontrato nel mio percorso, , l'aiuto di Stelios per la mia tesi è stato indispensabile, molte volte gli ho rotto veramente le palle, e c'è sempre stato. Con lui e Satyone (my old friend) è nata una forte amicizia, che porterò avanti per sempre. Per non parlare delle altri dottorandi fantastici con cui oltre ad avere un ottimo rapporto lavorativo ho condiviso gli ultimi tre anni e ho stretto un forte legame. Chiara Morandini, Nicolò Damiani, Christian Salvatori, Maithree, grazie di tutto, vi voglio bene.

Per concludere il lato ingegneristico dei ringraziamenti, ovviamente quelli più sentiti vanno ai miei supervisors, Guido Magenes e Francesco Graziotti, che mi hanno guidato nel lungo lavoro di ricerca che è culminato nella presente tesi. Grazie a loro ho imparato il metodo scientifico e ad applicarlo ad ogni aspetto del mio lavoro, e perché no, anche nella vita quotidiana. I loro commenti e consigli sono sempre stati illuminanti e mi hanno fatto crescere molto. E a proposito di ciò, un ringraziamento sentitissimo va a Gabriele Guerrini, la sua incredibile dedizione e il suo amore per l'ingegneria sismica (che a volte culmina in apici di precisione vagamente umani) sono stati un insegnamento non misurabile. Lo ringrazio per la sua grande generosità, per essere sempre stato disponibile al chiarimento di qualsiasi questione (dai tecnicismi più spinti alle cose più buratriche amministrative, passando per qualsiasi consiglio quotidiano).

Un perticolare ringraziamento va a Michele Palmieri, che senza che inizialmente me ne rendessi conto è tra i motivi principali per cui mi trovo a scrivere queste righe…mi ha ispirato lui ad intraprendere il percorso che sto ora concludendo, ed effettivamente è rimasto fonte di ispirazione sia professionale che umana.

Infine….i ringraziamenti a tutte le persone che mi sono state vicino in questi anni al di fuori della sfera lavorativa. Ognuna di loro è stata fondamentale, in tutti quei momenti in cui le motivazioni vengono a mancare, che in un lungo dottorato sono spesso dietro l'angolo. In primis, voglio ringraziare il sostegno della mia famiglia, che mi ha permesso di portare avanti i miei studi fino ad ora, che con le regole attuali non sono neanche autofinanziabili, se non a discapito dell'attività stessa. Ma tralasciando l'aspetto economico, posso dire di avere la fortuna di aver ricevuto ogni altro tipo di sostegno dalla mia famiglia, ringrazio i miei genitori e i loro compagni, i miei fratelli, i miei zii e i miei nonni, per tutto. Un grazie infinito và alla mia stupenda dolce metà, la Franci, con la quale sto crescendo dalla tenera età di 17 anni e amo ancora come all'inizio. I suoi sorrisi, la sua dolcezza, la sua disarmante

bellezza interiore ed esteriore sono la mia linfa vitale, che riesce anche a farmi arrivare alla fine di un dottorato in ingegneria, cosa che ai tempi del liceo, ma direi anche dell'università, sicuramente era ritenuta da tutte le persone che mi conoscevano (amici, parenti e professori compresi) tra le cose meno probabili che sarebbero potute accadere. Voglio infatti ringraziare anche me stesso, per non accontentarmi mai del livello raggiunto, per voler ostinatamente capire tutto, e per averci creduto fino alla fine, fino ad ora, che ci sono riuscito.

Questa tesi la voglio dedicare alla mia famiglia e alla mia Franci, ma soprattutto a due persone tra le più importanti della mia vita, che mi hanno visto iniziare questa esperienza credendoci fin da subito più di me, con cui inevitabilmente non potrò festeggiare il mio successo. Mi stanno aiutando e mi aiuterranno sempre in maniera diversa, illuminandomi la strada dall'alto.

To my family, to my beloved Francesca

&

to Pierì and Chiara, who illuminate my path from the sky, like the sun.

TABLE OF CONTENTS

ABSTRACT v
ACKNOWLEDGEMENTS vii
TABLE OF CONTENTS xiii
LIST OF FIGURES xvii
LIST OF TABLES xxv
LIST OF ACRONYMS xxvii
1. INTRODUCTION 1
1.1 BACKGROUND 1
1.2 RESEARCH OBJECTIVES 3
1.3 OUTLINE OF THE THESIS 6
1.4 REFERENCES 7
2. CYCLIC RESPONSE OF MASONRY PIERS RETROFITTED WITH TIMBER FRAMES AND BOARDS 11
ABSTRACT 11
2.1 INTRODUCTION 11
2.2 DESCRIPTION OF THE TEST SPECIMENS 13
2.2.1 Masonry piers 13
2.2.2 Retrofit system 13
2.2.3 Material mechanical properties 16
2.3 TESTING PROCEDURE 17
2.3.1 Tests setup 17
2.3.2 Instrumentation and data acquisition 18
2.3.3 Loading protocol 18
2.4 EXPERIMENTAL RESULTS 18
2.4.1 Unstrenghtened specimen 18
2.4.2 Retrofitted specimen 22

2.4.3 Comparison of the test results 26
2.5 ANALYTICAL PREDICTION OF EXPERIMENTAL RESULTS 30
2.5.1 Unretrofitted specimen 30
2.5.2 Retrofitted specimen 32
2.6 CONCLUSIONS 33
2.7 ACKNOWLEDGEMENTS 34
2.8 REFERENCES 35
3. FULL-SCALE SHAKE-TABLE TESTS ON TWO UNREINFORCED MASONRY CAVITY-WALL BUILDINGS: EFFECT OF AN INNOVATIVE TIMBER RETROFIT SYSTEM 43
ABSTRACT 43
3.1 INTRODUCTION 44
3.2 CHARACTERISTICS OF THE SPECIMENS 45
3.2.1 General Overview 45
3.2.2 Details of the bare structure 47
3.2.3 Details of the retrofit system 51
3.2.4 Masses 57
3.2.5 Material mechanical properties 57
3.3 TESTING PROTOCOL AND INSTRUMENTATION 59
3.3.1 Instrumentation 59
3.3.2 Testing protocols 61
3.4 TEST RESULTS 65
3.4.1 General overview 65
3.4.2 Bare specimen damage evolution 66
3.4.3 Retrofitted specimen damage evolution 69
3.4.4 Hysteretic responses 73
3.5 SUMMARY AND DISCUSSION OF THE TEST RESULTS 76
3.6 CONCLUSIONS 81
3.7 ACKNOWLEDGEMENTS 83
3.8 REFERENCES 83
4. SEISMIC VULNERABILITY OF IRREGULAR DUTCH URM TERRACED HOUSE UNITS EXPOSED TO INDUCED SEISMICITY CONSIDERING GLOBAL AND LOCAL

MECHANISMS – INFLUENCE OF THE NEW RETROFIT SYSTEM - A CASE-STUDY BUILDING 89

4.1 INTRODUCTION 89

4.2 MODELLING APPROACHES 92

4.2.1 SDOF oscillators 92

4.2.2 MDOF systems 95

4.3 SIMULATION OF THE INCREMENTAL SHAKE-TABLE TESTS 102

4.3.1 SDOF simulation 102

4.3.2 MDOF simulation 107

4.4 FRAGILITY CURVES DERIVATION 116

4.5 CASE STUDY BUILDING NUMERICAL MODELS (MDOF): EXPERIMENTAL VS REAL DIMENSIONS 118

4.6 CALIBRATED SDOF OSCILLATORS FOR CASE STUDY BUILDING IN BARE AND RETROFITTED CONFIGURATIONS 124

4.6.1 Bare conditions 124

4.6.2 Retrofitted conditions 132

4.7 DEFINITION OF LIMIT STATE THRESHOLDS 139

4.8 GROUND MOTION DATABASE 141

4.9 GLOBAL SEISMIC VULNERABILITY ASSESSMENT 143

4.10 LOCAL VULNERABILITY ASSESSMENT 148

4.10.1 Introduction 148

4.10.2 Methodology 149

4.10.3 Bare building 155

4.10.4 Retrofitted building 161

4.10.5 Results comparison 163

4.11 DISCUSSION 164

4.12 CONCLUSIONS 168

4.13 REFERENCES 170

5. PRELIMINARY CONSIDERATIONS ON THE SUSTAINABILITY OF THE RETROFIT INTERVENTION 179

5.1 INTRODUCTION 179

5.2 RE-ENGINEERING OF THE RETROFIT SYSTEM 184

5.2.1 Mechanical characterization of the improved connection 185
5.3 ENVIRONMENTAL IMPACT COMPARISON 187
5.4 CONCLUSIONS 190
5.5 REFERENCES 191
6. SUMMARY AND CONCLUSIONS 197
6.1 EXPERIMENTAL CAMPAIGN 197
6.2 NUMERICAL STUDY 200
6.2.1 Multiple-degrees-of-freedom models 201
6.2.2 Single-degree-of-freedom models 202
6.3 PRELIMINARY CONSIDERATIONS ON SUSTAINABILITY 202
6.4 TOPICS FOR FUTURE RESEARCH 203
APPENDIX A. DATASETS FROM FULL-SCALE SHAKE TABLE TESTS ON TWO UNREINFORCED MASONRY CAVITY-WALL BUILDINGS TO EVALUATE AN INNOVATIVE TIMBER RETROFIT 207
INTRODUCTION 207
VALUE OF DATA 207
A.1 DATA DESCRIPTION 208
A.1.1 Traditional data: accelerometers and potentiometer recordings 210
A.1.2 Optical data: three-dimensional optical motion-capture system recordings 212
A.2 EXPERIMENTAL DESIGN, MATERIALS AND METHODS 213
A.3 REFERENCES 237

LIST OF FIGURES

Figure 1.1 Camerino historical center (Sept. 2019) 3

Figure 2.1 Bare masonry pier geometry. Units of m. 13

Figure 2.2 Retrofitted specimen geometry. Units of m. 14

Figure 2.3 Retrofit system components. 15

Figure 2.4 In-plane shear-compression cyclic tests setup. Units of m. 17

Figure 2.5 Bare pier crack pattern corresponding to: a) first cracking; b) maximum recorded shear; c) ultimate conditions. 20

Figure 2.6 Bare pier hysteretic response. 20

Figure 2.7 Displacement contributions: a) sub-elements with reference nodes; b) flexural and shear deformation modes. 21

Figure 2.8 Bare pier displacement contributions. 22

Figure 2.9 Retrofitted pier crack pattern corresponding to: a) first cracking; b) maximum recorded shear on the bare pier; c) ultimate conditions of the bare pier and maximum recorded shear on the retrofitted pier; d) ultimate conditions. 23

Figure 2.10 Retrofitted pier: vertical displacement of the pier top at zero lateral force. 24

Figure 2.11 Retrofitted pier hysteretic response. 24

Figure 2.12 Retrofitted pier displacement contributions. 25

Figure 2.13 Retrofit system response: a) elongation of the tie-down connection at the bottom-North corner; b) OSB shear deformation. 26

Figure 2.14 Bare and retrofitted pier backbone curves and bilinear idealisations, positive loading direction. 27

Figure 2.15 Hysteretic response up to 0.25% drift ratio: a) bare pier; b) retrofitted pier. 28

Figure 2.16 Ultimate conditions: a) bare pier; b) retrofitted pier; c) buckled tie-down steel angle. 29

Figure 2.17 Bare and retrofitted pier hysteretic energy dissipation. 29

Figure 2.18 Bare and retrofitted pier equivalent viscous damping. 30

Figure 3.1 Typical terraced house of the Groningen area: (a) front façade; (b) lateral façade. 45

Figure 3.2 Overall photos of the specimens: (a) North and West façades; (b) South and East façades; (c) North façade; (d) South façade. Shaking direction indicated by yellow arrows. 47

Figure 3.3 Elevations of the load-bearing CS inner leaves from the outside: (a) West façade, (b) East façade, (c) North façade, (d) South façade. Units of cm. 48

Figure 3.4 Plan views of the bare structure: (a) ground floor; (b) first-floor RC slab; (c) second-floor timber framing. Units of cm. 49

Figure 3.5 Bare structure construction photos: (a) top view of the cavity-wall section; (b) first-storey inner-leaf lintel; (c) first-floor RC slab connection detail above longitudinal CS leaves; (d) L-shape steel anchors between second-floor joists and transverse; (e) second-floor framing at staircase hole; (f) roof finishes; (g) internal steel rigid frame. 50

Figure 3.6 Retrofit system details: (a) vertical section of the typical longitudinal wall retrofit, (b) timber frame applied to the longitudinal East wall, (c) OSB panels nailed to the longitudinal East wall frame, (d) completed retrofit of the transverse South wall... 52

Figure 3.7 Retrofit system construction photos: a) longitudinal-wall timber frame, b) nailing of a OSB for in-plane strengthening of longitudinal walls, c) completed transverse walls retrofit not including OSB panels. 53

Figure 3.8 Second-floor diaphragm retrofit details: (a) OSB layout; (b) joists and blocking beams layout; (c) installation of OSB; (d) view from below of the connection between inner- and outer-leaf spreader beams. 54

Figure 3.9 Retrofit system-to-floor connection details: (a, b) first-storey longitudinal-wall posts to RC slab; (c, d) transverse-wall sill plates to first-floor RC slab; (e, f) second-storey longitudinal-wall frame to inner-leaf spreader beam; (g, h) second-store 55

Figure 3.10 Input record EQ-NPR scaled at 100%: (a) acceleration time-series; (b, c) elastic pseudo-acceleration and displacement response spectra for 5% viscous damping ratio. 62

Figure 3.11 Bare masonry building damage pattern evolution on the load-bearing CS inner leaves, viewed from inside. New cracks in red, existing cracks in black. 67

Figure 3.12 Bare masonry building final conditions: a, b second-storey North-West corner of the CS leaf, c, d second-storey North-East corner of the CS leaf, e brick dislocation on the North CS wall, f second-storey South-East corner of the CS leaf. 68

Figure 3.13 Retrofitted building damage pattern evolution on the load-bearing CS inner leaves, viewed from inside. New cracks in red, existing cracks in black. 70

Figure 3.14 Retrofitted building final conditions: (a) first-storey North CS wall close to West corner; (b) brick dislocation on the North CS wall; (c) first-storey North CS wall close to East corner; (d) first-storey South CS wall close to the centre; (e, f, g) So 71

Figure 3.15 Hysteretic responses comparison: (a) with EQ-NPR signal scaled at 133% of its amplitude; (b) during the final test runs. 74

Figure 3.16 Experimental responses comparison: (a) backbone curves; (b) evolution of the equivalent viscous damping ratio. 75

Figure 3.17 Evolution of the bare specimen response. 77

Figure 3.18 Evolution of the retrofitted specimen response. 78

Figure 3.19 Relationship between experimental damage states and input PGA. 80

Figure 4.1 Reference SDOF models: (a) hysteretic AD response of system with ξ_{hyst} = 17.1% (50%SD); (b) elastoplastic idealisation of monotonic AD response, reproduced from Kallioras *et al.*, [2019]. 95

Figure 4.2 Nonlinear macroelement behaviour: nonlinear flexural degrading model; role of parameter β on the shear model; role of parameter G_{cl} on the shear model. 97

Figure 4.3 Bare building discretization and piers mapping (adapted from Damiani *et al.*, [2022]). 98

Figure 4.4 Retrofitted pier model scheme. 99

Figure 4.5 EUC-BUILD-6 incremental dynamic test simulation with $SDOF_b$: hysteresis overlap. 105

Figure 4.6 EUC-BUILD-6 incremental dynamic test simulation with $SDOF_{b,DS4}$: hysteresis overlap. 106

Figure 4.7 EUC-BUILD-7 incremental dynamic test simulation with $SDOF_r$: hysteresis overlap. 106

Figure 4.8 EUC-BUILD-7 incremental dynamic test simulation with $SDOF_{r,DS4}$: hysteresis overlap. 107

Figure 4.9 EUC-BUILD-6 incremental dynamic test simulation with EF system from run EQ-NPR-20% to EQ-NPR-66%: hysteresis overlap. 108

Figure 4.10 EUC-BUILD-6 incremental dynamic test simulation with EF system from run EQ-NPR-85% to EQ-NPR-133%-rev: hysteresis overlap. 109

Figure 4.11 EUC-BUILD-6 incremental dynamic test simulation with EF system: displacement time histories overlap. 109

Figure 4.12 EUC-BUILD-6 incremental dynamic test simulation with EF system: displacement time histories overlap. 110

Figure 4.13 EUC-BUILD-6 incremental dynamic test simulation with EF system: experimental vs numerical maximum values. 110

Figure 4.14 EUC-BUILD-7 incremental dynamic test simulation with EF system from EQ-NPR-66% to EQ-NPR-133%: hysteresis overlap. 112

Figure 4.15 EUC-BUILD-7 incremental dynamic test simulation with EF system: displacement time histories overlap. 113

Figure 4.16 EUC-BUILD-7 incremental dynamic test simulation with EF system: 1st floor acceleration time history overlap. 113

Figure 4.17 EUC-BUILD-7 incremental dynamic test simulation with EF system from EQ-NPR-133%-roof to EQ-NPR-266%-roof: hysteresis overlap. 114

Figure 4.18 EUC-BUILD-7 incremental dynamic test simulation with EF system from EQ-NPR-133%-roof to EQ-NPR-266%-roof: displacement time histories overlap. 114

Figure 4.19 EUC-BUILD-7 incremental dynamic test simulation with EF system from EQ-NPR-133%-roof to EQ-NPR-266%-roof: 1st floor acceleration time history overlap. ... 115

Figure 4.20 EUC-BUILD-7 incremental dynamic test simulation with EF system: experimental vs numerical maximum values (DS1, DS2, DS3). 115

Figure 4.21 EUC-BUILD-7 incremental dynamic test simulation with EF system: experimental vs numerical maximum values (DS4). 116

Figure 4.22 Plan view of the case-study building: Or_1, weak direction (left) and Or_2, strong direction (right). 118

Figure 4.23 Case-study building elevations: (a) West; (b) East; (c) North; (d) South. 119

Figure 4.24 Numerical simulation of test EUC-BUILD-6: global hysteresis overlaps of EF model of case-study building and of experimental prototype (Or_1, weak direction). 121

Figure 4.25 Numerical simulation of test EUC-BUILD-6: maximum values comparison of EF model of case-study building and of experimental prototype (Or_1, weak direction). 122

Figure 4.26 Numerical simulation of test EUC-BUILD-6: global hysteresis overlaps of EF model of case-study building and of experimental prototype (Or_2, strong direction). ... 122

Figure 4.27 Numerical simulation of test EUC-BUILD-6: maximum values comparison of EF model of case-study building and of experimental prototype (Or_2, strong direction). 122

Figure 4.28 Numerical simulation of test EUC-BUILD-7: global hysteresis overlaps of EF model of case-study building and of experimental prototype (Or_1). Runs up to EQ-NPR-133% (DL3). 123

Figure 4.29 Numerical simulation of test EUC-BUILD-7: global hysteresis overlaps of EF model of case-study building and of experimental prototype (Or_1). Runs from EQ-NPR-133%-roof to EQ-NPR-266%-roof (DS4). 123

Figure 4.30 Numerical simulation of test EUC-BUILD-7: equivalent frame MDOF models with experimental and real transversal dimensions: maximum values comparison (Or_1). 124

Figure 4.31 Simulation of the test on EUC-BUILD-6 with $SDOF_{b,1,2}$ and EF MDOF system in Or_1 from EQ-NPR-20% to EQ-NPR-66%: hysteresis overlaps. 126

Figure 4.32 Simulation with $SDOF_{b,1,2}$ and with EF MDOF system in Or_1 of the EUC-BUILD-6 test runs from EQ-NPR-20% to EQ-NPR-66% (DL2): displacement TH overlaps. 127

Figure 4.33 Simulation with $SDOF_{b,1,2}$ and with EF MDOF system in Or_1 of the EUC-BUILD-6 test runs from EQ-NPR-20% to EQ-NPR-66% (DL2): 1st floor acceleration TH overlaps. 127

Figure 4.34 Simulation with $SDOF_{b,1,2}$ and with EF MDOF system in Or_1 of the EUC-BUILD-6 test runs from EQ-NPR-20% to EQ-NPR-66% (DL2): maximum values comparison. 128

Figure 4.35 Simulation with $SDOF_{b,3,4}$ and with EF MDOF system in Or_1 of the EUC-BUILD-6 test runs from EQ-NPR-85% (DL3) to EQ-NPR-133%-rev (DS5): hysteresis overlap. 128

Figure 4.36 Simulation with $SDOF_{b,3,4}$ and with EF MDOF system in Or_1 of the EUC-BUILD-6 test runs from EQ-NPR-85% (DL3) to EQ-NPR-133%-rev (DS5): displacement TH overlap. 129

Figure 4.37 Simulation with $SDOF_{b,3,4}$ and with EF MDOF system in Or_1 of the EUC-BUILD-6 test runs from EQ-NPR-85% (DL3) to EQ-NPR-133%-rev (DS5): 1st floor accelerations TH overlaps. 129

Figure 4.38 Simulation with $SDOF_{b,3,4}$ and with EF MDOF system in Or_1 of the EUC-BUILD-6 test runs from EQ-NPR-85% (DL3) to EQ-NPR-133%-rev (DS5): 2nd floor accelerations TH overlaps. 130

Figure 4.39 Simulation with $SDOF_{b,3,4}$ and with EF MDOF system in Or_1 of the EUC-BUILD-6 test runs from EQ-NPR-85% (DL3) to EQ-NPR-133%-rev (DS5): maximum values comparison. 130

Figure 4.40 Simulation with $SDOF_{b,Or2}$ and with EF MDOF system in Or_2 of the EUC-BUILD-6 test runs from EQ-NPR-85% to EQ-NPR-133%-rev: hysteresis overlap. 131

Figure 4.41 Simulation with $SDOF_{b,Or2}$ and with EF MDOF system in Or_2 of the EUC-BUILD-6 test: maximum values comparison. 131

Figure 4.42 Simulation with $SDOF_{r,1,2,3}$ and with EF MDOF system in Or_1 of the of EUC-BUILD-7 test runs from EQ-NPR-66% (DL1) to EQ-NPR-133% (DL3): hysteresis overlaps. 133

Figure 4.43 Simulation with $SDOF_{r,1,2,3}$ and with EF MDOF system in Or_1 of the of EUC-BUILD-7 test runs from EQ-NPR-66% (DL1) to EQ-NPR-133% (DL3): displacement TH overlap. 134

Figure 4.44 Simulation with $SDOF_{r,1,2,3}$ and with EF MDOF system in Or_1 of the of EUC-BUILD-7 test runs from EQ-NPR-66% (DL1) to EQ-NPR-133% (DL3): 1st floor acceleration TH overlap. 134

Figure 4.45 Simulation with $SDOF_{r,1,2,3}$ and with EF MDOF system in Or_1 of the of EUC-BUILD-7 test runs from EQ-NPR-66% (DL1) to EQ-NPR-133% (DL3): 2nd floor acceleration TH overlap. 135

Figure 4.46 Simulation with $SDOF_{r,1,2,3}$ and with EF MDOF system in Or_1 of the of EUC-BUILD-7 test runs from EQ-NPR-66% (DL1) to EQ-NPR-133% (DL3): maximum values comparison. 135

Figure 4.47 Simulation with $SDOF_{n4}$ and with EF MDOF system in Or_1 of the of EUC-BUILD-7 test runs from EQ-NPR-133%-roof to EQ-NPR-266%-roof (DL4): hysteresis overlap. 136

Figure 4.48 Simulation with $SDOF_{n4}$ and with EF MDOF system in Or_1 of the of EUC-BUILD-7 test runs from EQ-NPR-133%-roof to EQ-NPR-266%-roof (DL4): displacement TH overlaps. 136

Figure 4.49 Simulation with $SDOF_{n4}$ and with EF MDOF system in Or_1 of the of EUC-BUILD-7 test runs from EQ-NPR-133%-roof to EQ-NPR-266%-roof (DL4): 1st floor accelerations TH overlaps. 137

Figure 4.50 Simulation with $SDOF_{n4}$ and with EF MDOF system in Or_1 of the of EUC-BUILD-7 test runs from EQ-NPR-133%-roof to EQ-NPR-266%-roof (DL4): 2nd floor accelerations TH overlaps. 137

Figure 4.51 Simulation with $SDOF_{n4}$ and with EF MDOF system in Or_1 of the of EUC-BUILD-7 test runs from EQ-NPR-133%-roof to EQ-NPR-266%-roof (DL4): maximum values comparison. 138

Figure 4.52 Simulation with $SDOF_{nOr2}$ and with EF MDOF system in Or_2 of the of EUC-BUILD-7 test runs from EQ-NPR-133%-roof to EQ-NPR-266%-roof (DL4): hysteresis overlap. 138

Figure 4.53 Simulation with $SDOF_{nOr2}$ and with EF MDOF system in Or_2 of the of EUC-BUILD-7 test runs from EQ-NPR-133%-roof to EQ-NPR-266%-roof (DL4): maximum values comparison. 139

Figure 4.54 GM database intensity measure distributions: *PGA* (left), $D_{s,5\text{-}75}$ (right) 142

Figure 4.55 GM database acceleration and displacement spectra. 142

Figure 4.56 NLTHA outcomes, bare conditions (Or_1): cloud results (left) and DS fragility curves conditioned to PGA (right). 144

Figure 4.57 NLTHA outcomes, bare conditions (Or_2): cloud results (left) and DS fragility curves conditioned to PGA (right). 145

Figure 4.58 Damage states global fragility functions for experimental and real dimensions, bare conditions: case-study building in Or_1 (left) and in Or_2 (right). 145

Figure 4.59 NLTHA outcomes, retrofitted conditions (Or_1): cloud results (left) and DS fragility curves conditioned to PGA (right). 146

Figure 4.60 NLTHA outcomes, retrofitted conditions (Or_2): cloud results (left) and DS fragility curves conditioned to PGA (right). 146

Figure 4.61 Damage states global fragility functions for experimental and real dimensions, retrofitted conditions: case-study building in Or_1 (left) and in Or_2 (right). 146

Figure 4.62 Damage states global fragility functions for bare and retrofitted conditions: case-study building in Or_1 (left) and in Or_2 (right). 147

Figure 4.63 Schematic representation of the OOP response of cavity walls and associated F-u relationship (reproduced from Tomassetti *et al.*, [2018]). 151

Figure 4.64 Tri-linear force displacement relationship for retrofitted masonry piers. 151

Figure 4.65 Preselected failure mechanisms and boundary conditions (reproduced from Vaculik, [2012]). 153

Figure 4.66 Masonry wall geometrical properties (reproduced from Sharma *et al.*, 2021) 154

Figure 4.67 Loss of horizontal top restrain mechanism, notation (reproduced from Sharma *et al.*, [2021]). 155

Figure 4.68 Charts for assessing restraint at the top edge of URM walls as a function of the geometry and stiffness of the floor system (plotted for $\theta = 1.25\%$) (reproduced from Sharma *et al.*, [2021]). 155

Figure 4.69 Vertical elevation of North and South sides. Notation for OOP seismic assessment. 157

Figure 4.70 Floor acceleration and displacement spectra for Orientation 1 OOP assessment, bare conditions. 157

Figure 4.71 OOP collapse fragility functions for bare conditions: derived through virtual work method (PCR, 2WB, left) and derived by NLTHA for one-way bending failure mechanism (right). 158

Figure 4.72 Vertical elevations of West and East walls. Notation for OOP seismic assessment. 159

Figure 4.73 Floor acceleration and displacement spectra for Orientation 2 OOP assessment, bare conditions. 160

Figure 4.74 Collapse fragility functions for squat walls, bare conditions: derived by virtual work method (PCR, left) and derived through NLTHA (right). 161

Figure 4.75 Collapse fragility functions, bare conditions: slender piers (left) and for all piers in 1WB for Or_2 161

Figure 4.76 Floor acceleration and displacement spectra for Orientation 1 OOP assessment, retrofitted conditions. 162

Figure 4.77 Floor acceleration and displacement spectra for Orientation 2 OOP assessment, retrofitted conditions. 162

Figure 4.78 OOP collapse fragilities for retrofitted configuration in Or_1 (left) and Or_2 (right). 163

Figure 4.79 OOP collapse fragility functions for bare and retrofitted configurations in Or_1 and Or_2. 164

Figure 4.80 Fragility curves comparison with and without consideration of OOP verifications, bare conditions: global results for Or_1 (left) and Or_2 (right). 167

Figure 4.81 Fragility curves comparison with and without consideration of OOP verifications, retrofitted conditions: global results for Or_1 (left) and Or_2 (right). 167

Figure 4.82 Combined damage states fragility functions for bare and retrofitted configurations considering global in-plane and local OOP vulnerabilities. 167

Figure 4.83 Global damage states fragility functions derived for EUC-BUILD-6 [Miglietta *et al.*, 2020] compared with results provided by Kallioras *et al.*, [2019] for regular buildings 168

Figure 5.1 Example of double entrance table for classification of buildings. Qualitative image reproduced from Caruso *et al.*, [2020]) 182

Figure 5.2 Python screw. 185

Figure 5.3 Test setup. 186

Figure 5.4 Experimental force-displacement curves 187

Figure 5.5 environmental impacts of the different retrofit components with original and improved connection timber-to-masonry 189

LIST OF TABLES

Table 2.1 Masonry mechanical properties. 16

Table 2.2 Nominal lateral loading protocol. 19

Table 2.3 Backbone curve parameters, positive loading direction. 27

Table 2.4 Bilinear idealisation parameters, positive loading direction. 27

Table 3.1 Prototype masses breakdown. 58

Table 3.2 Masonry mechanical properties of the bare and retrofitted prototype buildings. Comparison with estimates obtained from in-situ tests on buildings in the Groningen province [Tondelli *et al.*, 2015]. 60

Table 3.3 Bare building main testing sequence with intensity measures. 63

Table 3.4 Retrofitted building main testing sequence with intensity measures. 64

Table 3.5 Comparison of maximum longitudinal interstorey drift-ratios, corresponding to damage limits, with values proposed by Tomassetti *et al.* [2019a]. 80

Table 3.6 Comparison of maximum transverse interstorey drift ratios, at first cracking and ultimate conditions, with values found by Graziotti *et al.* [2016]. 81

Table 4.1 Properties of the reference hysteretic models (reproduced from Kallioras *et al.*, [2019]). 94

Table 4.2 Macroelements material properties, bare and retrofitted conditions. 98

Table 4.3 Retrofit system nonlinear beams equivalent parameters. 99

Table 4.4 Floor and roof diaphragms assigned properties. 100

Table 4.5 Bare building (EUC-BUILD-6) test runs numerical models 103

Table 4.6 Retrofitted building (EUC-BUILD-7) test runs numerical models 103

Table 4.7 SDOF system properties. 104

Table 4.8 Global damage limit thresholds for bare and retrofitted buildings in weak direction (Or_1). 141

Table 4.9 Global damage limit thresholds for bare and retrofitted buildings in strong direction (Or_2). 141

Table 4.10 Parameters of fitted lognormal distributions (for all considered DLs) of the case-study building. 147

Table 4.11 Coefficients to calculate PCR for two-way-spanning walls (reproduced from AS 3700 [2018]) 154

Table 4.12 Overall characteristics of North and South facade piers for OOP seismic assessment, bare conditions 158

Table 4.13 Overall characteristics of West and East façade piers for OOP seismic assessment, bare conditions. 160

Table 4.14 Parameters of fitted lognormal distributions (for all considered DLs) for bare and retrofitted conditions, with and without the consideration of local failure mechanisms. 166

Table 4.15 Parameters of fitted lognormal distributions (for all considered DLs) for the case-study building in bare and retrofitted conditions considering global and local mechanisms. 168

Table 5.1 Partial weights, costs, and embodied carbon for the original and the improved retrofit system 189

LIST OF ACRONYMS

1WB	= One-way bending
2WB	= Two-way bending
AD	= Acceleration-displacement
AMP	= Acceleration amplification factor
AWC	= American wood council
BSC	= Base shear coefficient
C.o.V.	= Coefficient of variation
CAV	= Cumulative absolute velocity
CDF	= Cumulative distribution function
CL	= Clay
CO2e	= Equivalent carbon-dioxide
CS	= Calcium-silicate
DB	= Database
DICAr	= Department of civil engineer and architecture of the University of Pavia
DL	= Damage limit
DS	= Damage state
ECF	= Embodied carbon factors
EDP	= Engineering demand parameter
EF	= Equivalent frame
EI	= Environmental impact
EIO	= Economic input-output

EPD	= Environmental product declaration
FD	= Flexure-dominated
GDR	= Global drift ratio
GHG	= Green house gasses
GM	= Ground motion
HI	= Housner intensity
IDR	= Interstorey drift-ratio
IM	= Intensity measure
LCA	= Life-cycle analysis
LCT	= Life-cycle thinking
LPCM	= Life-cycle performance metric
MDOF	= Multi-degrees of freedom system
mHI	= Modified Housner intensity
NLKM	= Non-linear kinematic method
NLTH	= Non-linear time history
NLTHA	= Non-linear time-history analysis
OOP	= Out-of-plane
Or_1	= Orientation 1
Or_2	= Orientation 2
OSB	= Oriented strand boards
PCR	= Peak cracking resistance
PGA	= Peak ground acceleration
PGV	= Peak ground velocity
PSA	= Pseudo-spectral acceleration
RC	= Reinforced concrete
SBR	= Sustainable building renovation

SBR-D	= Sustainable building renovation design framework
SD	= Shear-dominated
SDOF	= Single degree of freedom system
TH	= Time history
TMC	= Timber-masonry composite
UHS	= Uniform hazard spectrum
URM	= Unreinforced masonry
VSSW	= Vertical spanning strip wall

1.INTRODUCTION

1.1 BACKGROUND

Historically, timber has been widely used as construction material throughout the world. In the recent past, it is gaining increasing attention due to the manufacturing industry scientific progress and the availability of technologies that allow to produce new derived composites with mechanical properties far beyond typical values available in nature. The consolidation of existing structures is among its important applications, especially for fast strengthening interventions after the occurrence of earthquake events. Its natural very high strength over density ratio makes it particularly suitable to be transported in-situ and rapidly applied to existing structures to reduce their seismic vulnerability after being damaged. Even from the environmental point of view, timber is widely appreciated due to its high durability, high thermal resistance, and the possibility of being naturally produced and manufactured under a sustainable management. In literature, several examples can be found on the use of timber for fast strengthening interventions after an earthquake. Figure 1.1 shows some images of the city of Camerino in Central Italy, which was hit by an earthquake event with a moment magnitude M6.1, followed by two earthquakes (M5.9 and M6.5) on the 26th and 30th of October 2015 and on the 24th of August 2016. The historical centre of the town underwent severe damages since it is characterized by old adjacent masonry buildings often with different storey height and generally without seismic details. Many buildings and churches required temporary interventions for safety against further collapse while the area was closed by the national authorities. In the reported examples it can be clearly appreciate the importance of timber for such interventions as well as its ease implementation with other materials (i.e., steel rods, connectors, or profiles).

The need to structurally upgrade buildings is usually associated with tectonic seismic zones, where natural events can reach significant intensities. However, it is acknowledged that human activities can affect the natural non-seismic nature of a region. Nowadays, the seismicity induced by gas extraction is a well-known and never easy problem, due to the amount of money involved in such activities and their significant positive impacts on regional and national finances. In Europe it is contemporary the case of the Groningen region, in the North-East part of The Netherlands, bordering with the North Sea and Germany, where the underground gas-field has been operated since the 1960s. Around thirty years later ('90s), shallow earthquakes started to be recorded and increased in amount with the continuing extraction. Induced earthquakes are characterized by short significant duration and low intensity, by maximum Richter scale magnitudes of 3-3.5, and are

generally considered as light and unproblematic. However, it has to be considered that the building stock of zones historically not prone to seismic events is designed to achieve appropriate thermal insulation and vertical stability rather than safety against lateral loads, therefore it is highly vulnerable to ground movements. Despite the low intensity of induced seismic events, being the buildings already subjected to small settlements due the poor characteristics of the soil, numerous claims for structural light damage imputed to seismic activities are raised by the population and the issue is brought to national attention. Following these events, the government imposed to the extracting company to fund a comprehensive project to assess and mitigate the seismic risk of the region. The total absence of literature regarding the seismic behaviour of typical existing buildings, combined with the need to define the real impact of the extraction activities on the built environment, also motivated the launch of an extended experimental campaign aiming to characterize the lateral capacities of the involved structural typologies, since they have never been of interest in the seismic engineering field. With the increasing knowledge on the building typologies and their structural weaknesses, the interest moved also to possible light structural retrofit interventions. Within this context, a new timber strengthening system for irregular Dutch terraced house of late'70s – early '80s is proposed and tested at the EUCENTRE laboratories in 2018.

In the current historical period, the proposal of a new retrofit system should not be constrained to structural aspects and ignore the environmental impacts of the intervention. Nowadays, the global warming phenomenon had become a serious issue that need to be faced by the collaboration of all the nations worldwide through agreed policies. In Europe, it has been recognized that a large percentage of the total gas emission of the continent is produced by the construction sector in all its stages: construction, operating life, and demolition (recycle). Moreover, it has been demonstrated that an ideal substitution of the European building stock with a new one, safe and energy efficient, would not be environmentally sustainable. The use of unspoiled lands for new constructions increases the burden on the environment, as well as the demolition of existing buildings generate additional waste to be disposed, increasing even more the pressure on landfills. Consequently, the European Commission is working on policies to favourite the energetic upgrading of old buildings, and in case of seismic zones also the structural retrofit. This is motivated by the expected economic, social, and environmental losses connected to seismic events, which would also jeopardize any previous energetic intervention. It is well-known that the largest part of the economic losses caused by an earthquake are due to damage to non-structural elements, and they are anyhow required to be installed in seismically safe buildings and designed against seismic action. Within this framework, it is always important to consider possible integrations of energetic upgrades in a structural retrofit intervention and to consider the environmental impacts of the new system in construction, operating life, and demolition phases.

Figure 1.1 Camerino historical center (Sept. 2019)

1.2 RESEARCH OBJECTIVES

In order to assess a regional seismic risk, three main components are to be defined: the natural hazard of the interested area, the exposure of the building stock, and its associated vulnerability to earthquake events. Among them, the seismic engineering field is mainly focused on the development of the exposure model and the evaluation of the vulnerability of existing buildings. In the case of Groningen region, national databases, field surveys, and local engineering expertise were used to produce knowledge of the involved building stock. An earlier version of the exposure database [Arup, 2015] was used for the Hazard and Risk Assessment of November 2015. Since then, the database has been regularly updated up to the latest version of the exposure published in April 2020 [Arup, 2020]. One of the main objectives is to identify the most vulnerable structural typologies and the most contributing to the seismic risk of the region, to focus on them modelling effort for the development of a reliable fragility model [Crowley *et al.*, 2017a] and for the estimation of the local personal risk [Crowley *et al.*, 2017b]. With the development of the regional building inventory, it emerged that unreinforced masonry buildings constitute the largest portion of the considered portfolio (> 250.000 units) and therefore have a large impact on the overall regional seismic risk, especially considering the most of them as old constructions, with poor materials and without any seismic detail. In accordance with this early finding, and considering the lack of knowledge on the lateral capacity of Dutch unreinforced (URM) masonry buildings, significant effort was put in the investigation of these structural systems since the very first stages of the project.

It is well-known that masonry building performance under earthquake loading represent an issue in the seismic engineering field. The behaviour of these structures has always been recognized as a complex topic, due to the high variability of masonry mechanical properties and the difficulties inherent in the estimation of such parameters [Lourenço, 2002]. Moreover, unreinforced masonry structures are often old constructions that could have suffered aging and lack of maintenance. In literature, significant effort was devoted to the investigation on the lateral capacity of masonry assemblies and entire buildings. Among others, Tomaževič *et al.* [1991], Magenes *et al.* [2014], Senaldi *et al.* [2014; 2019], Vintzileou *et al.* [2015], and Guerrini *et al.* [2019]) performed experimental tests on stone-masonry buildings, with and without strengthening intervention, while Tomaževič and Weiss [1994], Bothara *et al.* [2010] and Candeias, [2017] explored the response of clay-brick URM buildings. Nevertheless, no scientific studies could be found in literature on masonry structures typical of the Northern part of Europe apart from the study carried out by Degée *et al.*, [2007].

In 2014 an extensive experimental campaign is launched aiming at characterizing the seismic behaviour of structural components, assemblies, and entire building systems, to assist in the development of models to predict damage and collapse of URM structures in Groningen [Graziotti *et al.*, 2018]. Former activities included the identification of masonry typologies of the area and their mechanical characterization through in-situ and laboratory tests [Tondelli *et al.*, 2015], followed by the investigation on the in-plane and out-of-plane capacity of masonry piers through quasi-static and dynamic tests [Graziotti *et al.*, 2016]. In 2015, the first full-scale URM building specimen was tested on the shake-table at the EUCENTRE laboratories in Pavia, Italy [Graziotti *et al.*, 2017], it was an end-unit of a regular Dutch URM terraced house of late '70-early '80s. One year later, a prototype of a typical Dutch URM detached house was tested as well on the shake-table [Kallioras *et al.*, 2018]. In 2017, the superior portion of the first building specimen (first storey and roof) was reproduced and tested on the shake-table at the LNEC laboratory in Lisbon, Portugal, aiming to reach collapse of the structure [Tomassetti *et al.*, 2019a]. The experiment was followed by dynamic tests also on a full-scale specimen of the gable-roof subsystem [Tomassetti *et al.*, 2019b], and another prototype of a typical Dutch URM detached house. At this stage, the produced knowledge of the URM systems mostly diffused in the area allowed to identify in the Dutch URM terraced houses of late '70-early '80s the building typology most vulnerable to lateral actions. Accordingly, in 2018 a new full-scale building prototype belonging to this category was tested on the shake-table at the EUCENTRE laboratories [Miglietta *et al.*, 2021]. The prototype was conceived to present the most unfavourable conditions in terms of plan and elevation irregularities, connection details and floor diaphragms. The basic idea was to test the most vulnerable configuration of the most vulnerable building typology, to determine a sort of lower bound for the lateral capacity of these particular buildings, and design a new light retrofit system tailored to overcome their structural weaknesses. The structural intervention was required to be as much rapid,

economical, and sustainable as possible. To this end, two cyclic shear-compression tests were performed on two identical single-whyte calcium silicate piers, one in bare conditions and one retrofitted with a new timber system [Guerrini *et al.*, 2021]. The study allowed firstly to look into the lateral behaviour resulting from the interaction between masonry and timber, and secondly to calibrate reliable analytical and numerical models in terms of force-displacement response. The same strengthening solution was then applied to a full-scale replica of the last full-scale building specimen and dynamically tested with the same loading protocol to investigate the effectiveness of the intervention in improving the seismic performance [Miglietta *et al.*, 2021]. Parallel to the activities carried out at the EUCENTRE laboratories, in 2014 an experimental campaign was also launched at the TU Delft University of Technology (Delft, The Netherlands) to assist in the characterization of connections, structural components, assemblies, and entire building systems of the Groningen area [e.g., Messali *et al.*, 2017, Esposito *et al.*, 2019, Arslan *et al.*, 2021, Sarhosis *et al.*, 2021].

URM terraced houses can be typically found in the Northern part of Europe. They are usually constituted by adjacent units and characterised by a cavity-wall structural system, constituted by an internal single-wythe loadbearing calcium silicate leaf and an external clay veneer with no structural function, each other connected by a net of steel ties. Units are structurally independent while they all share the external envelope of clay masonry. The use of two leaves separated by an air gap mainly responds to the need of keeping outside the houses water and humidity, and the need of having a good thermal insulation. The use of clay bricks for the external non-loadbearing leaf is due to their good durability and resistance to atmospheric agents, while calcium silicate bricks are often used for the internal loadbearing leaf because they are cheaper, with mechanical characteristics sufficient to sustain the vertical loads coming from design permanent and live loads. It is evident that this typology of buildings was conceived without considering the occurrence of any ground movement and accordingly they are not seismically detailed. The proposed timber retrofit system is conceived to overcome the structural deficiencies of cavity-wall masonry buildings with a light, economic and sustainable intervention.

The experimental tests discussed in the present work provide information on the full-scale in-plane response of single-whyte calcium silicate piers and on the lateral capacity of cavity-wall URM buildings, in bare conditions and retrofitted with the newly proposed timber system. It also constitutes a large experimental dataset on the interaction between masonry and timber elements. Experimental evidence is fundamental to produce analytical and numerical models [Andreotti *et al.*, 2018; Malomo *et al.*, 2018a, 2018b; Tomassetti *et al.*, 2018; Kallioras *et al.*, 2019] able to produce reliable building responses, to assist the estimation of parameters for the seismic performance-based assessment and the development of seismic vulnerability models.

1.3 OUTLINE OF THE THESIS

The present thesis is composed by six chapters: the introduction to the scientific issue is followed by the description of experimental activities, the numerical study, the considerations on the sustainability of the intervention, and the summary of conclusions and results. The first part, including Chapt. 2 and Chapt. 3, deals with the experimental tests performed at the EUCENTRE laboratories in 2018 to investigate the influence of the newly proposed timber retrofit system on cavity-wall URM structures typical of the Groningen region. They are two scientific papers published in the journals Proceedings of the Institution of Civil Engineers-Structures and Buildings and Bulletin of Earthquake Engineering, respectively. Chapt. 4 and Chapt. 5 constitute the second part of the thesis, which is never been published. Chapter 4 deals with the numerical study performed to assess the influence of the retrofit system on the seismic vulnerability of typical irregular Dutch terraced houses, while Chapt. 5 presents a qualitative discussion on the sustainability of the intervention. The last part of the thesis includes supporting information on shared experimental data of the tests presented in Chapt. 2 and Chapt. 3 (APPENDIX A). Below the synopsis of each chapter:

- Chapter 2 presents the mechanical and analytical interpretation of the cyclic in-plane shear-compression tests performed on two identical single-whyte calcium-silicate piers, one in bare and one in retrofitted configurations, named respectively EUC-COMP-1 and EUC-COMP-2. The specimens were tested up to the reaching of near collapse conditions.
- Chapter 3 discusses the incremental dynamic shake-table tests performed on two identical full-scale buildings belonging to the category of irregular Dutch URM cavity-wall terraced houses of late ’70-early ‘80s, one in bare conditions and one in retrofitted configuration. The prototypes were tested scaling the same ground motion up to near collapse conditions to allow the most effective comparison of results between the two. Experimental observations were used to define damage limit thresholds with a suitable engineering demand parameter.
- Chapter 4 contains the numerical study carried out to assess the seismic vulnerability of a case study building with geometrical and mechanical properties that can be typically found in-situ, taking into account global and local failure mechanisms. Multi-degrees of freedom system (MDOF) systems were derived from the ones calibrated on experimental tests and reduced to single degree of freedom system (SDOF) systems to perform NLTH cloud analysis using the latest ground motion database of the Groningen region. Results were post-

processed to produce damage states fragility functions using experimentally defined limit thresholds.

- Chapter 5 analyses the proposed retrofit solution from the sustainability point of view. Social, economic, and environmental aspects are qualitatively discussed, and the re-engineering of the connections retrofit-to-masonry is proposed. Embodied impacts are computed to estimate the environmental benefits of the connection upgrade.
- Chapter 6 concludes the thesis by summarising its main outcomes and providing thoughts and recommendations for future research.

1.4 REFERENCES

Andreotti, G., Graziotti, F., Magenes, G. [2018] "Detailed micro-modelling of the direct shear tests of brick masonry specimens: the role of dilatancy", *Engineering Structures*, Vol. 168, pp. 929-949. https://doi.org/10.1016/j.engstruct.2018.05.019.

Arslan, O., Messali, F., Smyrou, E., Bal, İ. E., Rots, J. G. [2021] "Mechanical modelling of the axial behaviour of traditional masonry wall metal tie connections in cavity walls". *Construction and Building Materials*, 310, 125205.

Arup [2015] "Groningen Earthquakes - Structural Upgrading, Exposure Database V2", ARUP, Amsterdam, The Netherlands.

Arup [2020] "Groningen Earthquakes - Structural Upgrading, Exposure Database V7", *229746_031.0_REP2015*, ARUP, Amsterdam, The Netherlands.

Bothara, J.K., Dhakal, R.P., Mander, J.B. [2010] "Seismic performance of an unreinforced masonry building: An experimental investigation", *Earthquake Engineering and Structural Dynamics*, Vol. 39, No. 1, pp. 45-68. https://doi.org/10.1002/eqe.932 .

Candeias, P. X., Campos Costa, A., Mendes, N., Costa, A. A., & Lourenço, P. B. [2017]. "Experimental assessment of the out-of-plane performance of masonry buildings through shaking table tests". *International Journal of Architectural Heritage*, 11(1), 31-58.

Crowley, H., Pinho, R., Polidoro, B., Van Elk, J. [2017a] "Developing fragility and consequence models for buildings in the Groningen field", *Netherlands Journal of Geosciences*, Vol. 96, No. 5, pp. 247-257. https://doi.org/10.1017/njg.2017.36.

Crowley, H., Polidoro, B., Pinho, R., Van Elk, J. [2017b] "Framework for developing fragility and consequence models for local personal risk", *Earthquake Spectra*, Vol. 33, No. 4, pp. 1325-1345. https://doi.org/10.1193/083116EQS140M.

Degée, H., Denoël, V., Candeias, P. A. U. L. O., Campos Costa, A., & Coelho, E. [2007] "Experimental investigation on the seismic behaviour of north European masonry houses". *In Proceedings of SISMICA 07*, Sismic Congress (p. 12).

Esposito, R., Messali, F., Ravenshorst, G. J., Schipper, H. R., Rots, J. G. [2019] "Seismic assessment of a lab-tested two-storey unreinforced masonry Dutch terraced house". *Bulletin of Earthquake Engineering*, 17(8), 4601-4623.

Graziotti F, Rossi A, Mandirola M, Penna A, Magenes G [2016] "Experimental characterization of calciumsilicate brick masonry for seismic assessment". *Proceedings of the 16th international brick and block masonry conference, IBMAC*. https://doi.org/10.1201/b21889

Graziotti F, Tomassetti U, Kallioras S, Penna A, Magenes G [2017] "Shaking table test on a full scale URM cavity wall building". *Bulletin of Earthquake Engineering*, 15:5329–5364. https://doi.org/10.1007/s1051 8-017-0185-8

Graziotti, F., Penna, A., Magenes, G. [2018] "A comprehensive in situ and laboratory testing programme supporting seismic risk analysis of URM buildings subjected to induced earthquakes", *Bulletin of Earthquake Engineering*. https://doi.org/10.1007/s10518-018-0478-6.

Guerrini, G., Senaldi, I., Graziotti, F., Magenes, G., Beyer, K., Penna, A. [2019]. "Shake-table test of a strengthened stone masonry building aggregate with flexible diaphragms". *International Journal of Architectural Heritage*, 13(7), 1078-1097.

Guerrini, G., Damiani, N., Miglietta, M., Graziotti, F. [2021]. "Cyclic response of masonry piers retrofitted with timber frames and boards". *Structures and Buildings*, 174(5), 372-388.

Kallioras, S., Guerrini, G., Tomassetti, U., Marchesi, B., Penna, A., Graziotti, F., Magenes, G. [2018]. "Experimental seismic performance of a full-scale unreinforced clay-masonry building with flexible timber diaphragms". *Engineering Structures*, 161, 231-249.

Kallioras, S., Graziotti, F., Penna, A. [2019]. "Numerical assessment of the dynamic response of a URM terraced house exposed to induced seismicity". *Bulletin of Earthquake Engineering*, 17(3), 1521-1552.

Lourenço, P. B. [2002]. "Computations on historic masonry structures". *Progress in Structural Engineering and Materials*, 4(3), 301-319.

Magenes, G., Penna, A., Senaldi, I.E., Rota, M., Galasco, A. [2014] "Shaking table test of a strengthened full-scale stone masonry building with flexible diaphragms", *International Journal of Architectural Heritage*, Vol. 8, No. 3, pp. 349-375. https://doi.org/10.1080/15583058.2013.826299.

Malomo, D., Pinho, R., Penna, A. [2018a] "Using the applied element method for modelling calcium silicate brick masonry subjected to in-plane cyclic loading", *Earthquake Engineering & Structural Dynamics*, Vol. 47, No. 7, pp. 1610-1630. https://doi.org/10.1002/eqe.3032

Malomo D., Pinho, R., Penna, A. [2018b] "Using the applied element method to simulate the dynamic response of full-scale URM houses tested to collapse or near-collapse conditions", *Proceedings of 16th European Conference on Earthquake Engineering (ECEE)*, Thessaloniki, Greece.

Messali, F., Skroumpelou, G., Esposito, R. [2017] "Tests on existing wall ties: shear and axial tests". *Report number C31B67WP6-2*. Delft University of Technology, The Netherlands.

Miglietta, M., Damiani, N., Guerrini, G., Graziotti, F. [2021]. "Full-scale shake-table tests on two unreinforced masonry cavity-wall buildings: effect of an innovative timber retrofit". *Bulletin of Earthquake Engineering*, 19(6), 2561-2596.

Sarhosis, V., Dais, D., Smyrou, E., Bal, I. E., Drougkas, A. [2021] "Quantification of damage evolution in masonry walls subjected to induced seismicity". *Engineering Structures*, 243, 112529.

Senaldi, I.E., Magenes, G., Penna, A., Galasco, A., Rota, M. [2014] "The effect of stiffened floor and roof diaphragms on the experimental seismic response of a full-scale unreinforced stone masonry building", *Journal of Earthquake Engineering*, Vol. 18, No. 3, pp. 407-443. https://doi.org/10.1080/13632469.2013.876946.

Senaldi, I. E., Guerrini, G., Comini, P., Graziotti, F., Penna, A., Beyer, K., Magenes, G. [2020]. "Experimental seismic performance of a half-scale stone masonry building aggregate". *Bulletin of Earthquake Engineering*, 18(2), 609-643.

Tomassetti, U., Graziotti, F., Penna, A., Magenes, G. [2018] "Modelling one-way out-of-plane response of single-leaf and cavity walls", *Engineering Structures*, Vol. 167, pp. 241–255. https://doi.org/10.1016/j.engstruct.2018.04.007.

Tomassetti, U., Correia, A. A., Candeias, P. X., Graziotti, F., Costa, A. C. [2019a]. "Two-way bending out-of-plane collapse of a full-scale URM building tested on a shake table". *Bulletin of Earthquake Engineering*, 17(4), 2165-2198.

Tomassetti, U., Correia, A. A., Graziotti, F., Penna, A. [2019b]. "Seismic vulnerability of roof systems combining URM gable walls and timber diaphragms". *Earthquake Engineering and Structural Dynamics*, 48(11), 1297-1318.

Tomaževič, M., Weiss, P., Velechovsky, T. [1991] "The influence of rigidity of floors on the seismic behaviour of old stone-masonry buildings", *European Earthquake Engineering*, Vol. 5, No. 3, pp. 28–41.

Tomaževič, M., Weiss, P. [1994] "Seismic behaviour of plain- and reinforced- masonry buildings", *Journal of Structural Engineering*, Vol. 120, No. 2, pp. 323-338. https://doi.org/10.1061/(ASCE)0733-9445(1994)120:2(323) .

Tondelli M, Graziotti F, Rossi A, Magenes G [2015] "Characterization of masonry materials in the Groningen area by means of in situ and laboratory testing". *Technical Report*, EUCENTRE Foundation, Pavia, Italy. Available online at www.eucentre.it/nam-project

Vintzileou, E., Mouzakis, C., Adami, C.E., Karapitta, L. [2015] "Seismic behaviour of three-leaf stone masonry buildings before and after interventions: Shaking table tests on a two-storey masonry model", *Bulletin of Earthquake Engineering*, Vol. 13, No. 10, pp. 3107-3133. https://doi.org/10.1007/s10518-015-9746-x.

2. CYCLIC RESPONSE OF MASONRY PIERS RETROFITTED WITH TIMBER FRAMES AND BOARDS

In *Proceedings of the Institution of Civil Engineers-Structures and Buildings* 2021, 174(5), 372-388.

ABSTRACT

The quasi-static in-plane cyclic response of two single-leaf calcium silicate unreinforced masonry piers was investigated to show the effectiveness of an innovative timber retrofit solution. The aim of the intervention is to increase the pier in-plane and out-of-plane strength and displacement capacity, thus reducing the seismic vulnerability of this typology of unreinforced masonry construction with a light, cost-effective, sustainable and reversible approach. The retrofit technique consists of a timber frame mechanically connected by means of steel fasteners to the masonry pier and building floors. Oriented strand timber boards are then nailed to the frame. In-plane quasi-static shear–compression cyclic tests were performed on two single-leaf calcium silicate brick piers with identical geometry and masonry mechanical properties: one was tested un-strengthened while the other was tested in the retrofitted configuration. The experimental results showed evident improvements in the lateral force–displacement response of the retrofitted specimen. More specifically, compared with the bare masonry pier, the retrofitted pier exhibited slightly higher stiffness, larger strength and significantly greater displacement capacity.

Keywords: Buildings, structures & design; Seismic engineering; Timber structures.

2.1 INTRODUCTION

Unreinforced masonry cavity wall construction is a common solution for residential buildings in several parts of the world. When this construction typology is adopted in regions associated with low seismic hazard, it is often characterised by insufficient seismic details. However, recent events have demonstrated that both natural (i.e. the slip of an unknown fault [Horton and Williams, 2012] and induced earthquakes (i.e. due to gas extraction [Bourne *et al.*, 2015; Crowley *et al.*, 2018; Graziotti *et al.*, 2018]) can result in ground motions with intensity higher than anticipated in low-seismicity sites.

These occurrences have prompted interest on possible retrofit solutions to reduce the vulnerability of existing buildings in these regions. Several retrofit techniques for unreinforced masonry have been investigated and implemented in the past. One of the most common interventions to improve the in-plane capacity of walls consists of applying

an additional material layer to the masonry. These additional layers include fibrereinforced composites [Alcaino and Santa-Maria, 2008; ElGawady *et al.*, 2007; Luccioni and Rougier, 2011; Marcari *et al.*, 2007; Mosallam and Banerjee, 2011; Tomaževič *et al.*, 2015], fibre-reinforced cementitious matrices [Babaeidarabad *et al.*, 2014; D'Ambrisi *et al.*, 2013; Mantegazza *et al.*, 2006] and externally bonded grids [Borri *et al.*, 2011; Facconi *et al.*, 2015; Giaretton *et al.*, 2018; Papanicolaou *et al.*, 2011; Prota *et al.*, 2006; Yardim and Lalaj, 2016]. Further possibilities for enhancement of the in-plane response include the application of steel elements mechanically connected to the masonry [Darbhanzi *et al.*, 2014; Farooq *et al.*, 2006; Taghdi *et al.*, 2000] and the introduction of post-tensioning systems [Laursen and Ingham, 2001; Ma *et al.*, 2012; Wight *et al.*, 2006]. Similarly, the out-of-plane capacity of walls can be increased by applying fibre-reinforced strips or bars [Derakhshan *et al.*, 2018; Galati *et al.*, 2006; Willis *et al.*, 2010], mortars reinforced with polymer textiles [Ismail and Ingham, 2016; Kadam *et al.*, 2015; Kariou *et al.*, 2018] or post-tensioning systems [Bailey *et al.*, 2014; Ismail and Ingham, 2012; Popehn *et al.*, 2007] to the masonry. Moreover, the improvement of connections between intersecting walls [Calderini *et al.*, 2015; Calderini *et al.*, 2019; Celik *et al.*, 2009; Podestà and Scandolo, 2019] and between floor diaphragms and masonry walls [Moreira *et al.*, 2014, 2016; Senaldi *et al.*, 2019; Valluzzi, 2007] has proved to be effective in terms of both in-plane and out-of-plane behaviour enhancement.

Essential requirements for the suitability of retrofit systems for residential buildings in low-seismicity areas may include light weight, low cost, sustainability and reversibility. In light of these principles, retrofit systems made of timber are particularly interesting. With recognition of the ability of timber to supply tensile strength to masonry, combinations of masonry and timber as load-bearing structural systems have been adopted for buildings in seismic-prone zones for centuries [Cardoso *et al.*, 2004; Gülkan and Langenbach, 2004; Tobriner, 1983]. The seismic performance of existing masonry buildings that originally included timber elements for structural enhancement has been studied both numerically and experimentally [Graziotti *et al.*, 2014; Kouris and Kappos, 2012; Meireles *et al.*, 2012; Vintzileou, 2008]. However, the application of timber as a retrofit solution to masonry elements has been proposed only recently. For example, Giaretton *et al.* [2016] and Dizhur *et al.* [2017] experimentally investigated the out-of-plane strengthening of slender masonry piers using timber strong-backs. Giongo *et al.* [2017] and Riccadonna *et al.* [2019] proposed and tested the use of crosslaminated timber panels connected to piers to enhance their in-plane capacity, while Sustersic and Dujic [2014] studied a similar technique for masonry infills. Building on previous findings, the fundamental idea of the retrofit system discussed in this paper is to increase both the in-plane and out-of-plane capacities of masonry piers using a timber frame and oriented strand board (OSB) panels mechanically connected to the masonry, to the foundation and to the floor diaphragms.

This paper presents and compares experimental results obtained from two in-plane quasi-static shear–compression cyclic tests on full-scale masonry piers with identical geometry

and masonry mechanical properties – one consisting of bare masonry and the other strengthened using the proposed solution. The experimental campaign was conducted at the Eucentre laboratories in Pavia, Italy and at the Department of Civil Engineering and Architecture (DICAr) of the University of Pavia, Italy. The geometry and loading conditions of the pier specimens reproduced the longest ground-floor pier of two Dutch terraced house full-scale prototypes. They were subjected to unidirectional dynamic shake-table tests [Damiani *et al.*, 2019; Miglietta *et al.*, 2018]. These identical building prototypes were also tested in bare and retrofitted configurations, with the specific pier excited in-plane. All the processed data and instrumentation schemes of the quasi-static component tests and shake-table experiments are available elsewhere (Eucentre, 2022).

2.2 DESCRIPTION OF THE TEST SPECIMENS

2.2.1 Masonry piers

The two single-wythe masonry piers consisted of 33 courses of calcium silicate (CS) bricks with average dimensions of 210 x 100 x 70 mm, and 10-mm-thick mortar joints. This resulted in height H = 2.70 m, length L = 2.00 m, and thickness t = 0.10 m (Figure 2.1). The two specimens were built simultaneously and matured under the same environmental conditions.

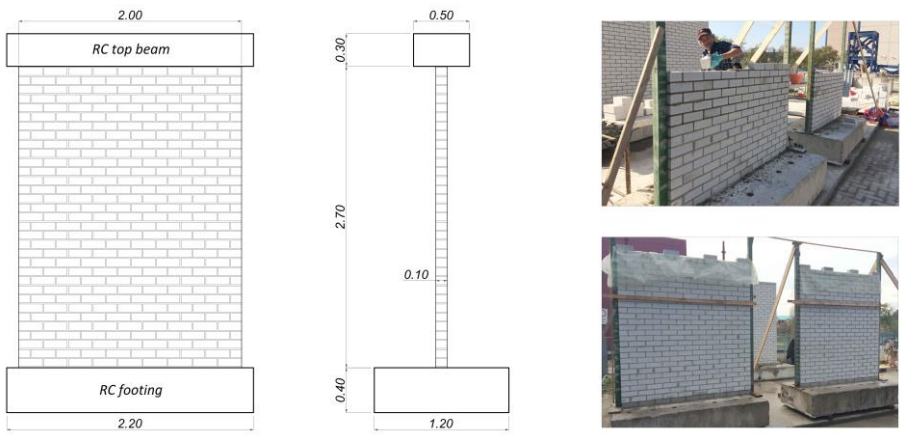

Figure 2.1 Bare masonry pier geometry. Units of m.

2.2.2 Retrofit system

The proposed masonry pier in-plane retrofit system consisted of a timber frame connected to the CS pier. It was conceived starting from the out-of-plane strengthening solution developed by Giaretton *et al.*, [2016] and Dizhur *et al.*, [2017], which relies on vertical timber strong-backs. Such solution was further expanded to increase also the pier in-plane force and displacement capacity. The frame included vertical timber posts, coinciding with the

strong-backs, and horizontal blocking (or nogging) elements. Timber sill plates allowed connecting the frame to the top reinforced concrete (RC) beam and to the footing. All timber elements had a cross-section of 80 x 60 mm, where the smaller dimension was oriented perpendicular to the masonry walls. 18-mm thick oriented strand boards (OSB) were fastened to the frame using 4-mm-diameter, 75-mm-long anker nails at 100-mm spacing, to increase the in-plane shear strength and stiffness of the specimen, following the American design guidelines for timber shear-walls (AWC, [2008]; Figure 2.2 and Figure 2.3). Member sizes were chosen to combine structural efficiency of the retrofit system with low invasiveness within real buildings. The effectiveness of the proposed solution depends on the connections between timber elements, masonry pier, and RC footing and top beam. Four connection types [Rothoblaas, 2015] were employed, as illustrated in Figure 2.3.

C1 indicates the tie-down anchorages that linked together posts, top and bottom sill plates, and top and bottom RC elements. They consisted of 340 x 182 mm steel angles with a cross section of 40 x 2 mm fastened to the timber posts by twelve 5-mm-diameter, 70-mm-long screws. The angles were connected to the RC elements through the sill plates by 12-mm-diameter class 8.8 threaded rods bonded to the concrete by an epoxy adhesive, pre-tensioned at 33 kN, with 40 x 160 x 15 mm rectangular steel anchor plates. C2 refers to additional connections between sill plates and RC elements through similar threated rods and anchor plates, designed to prevent shear sliding.

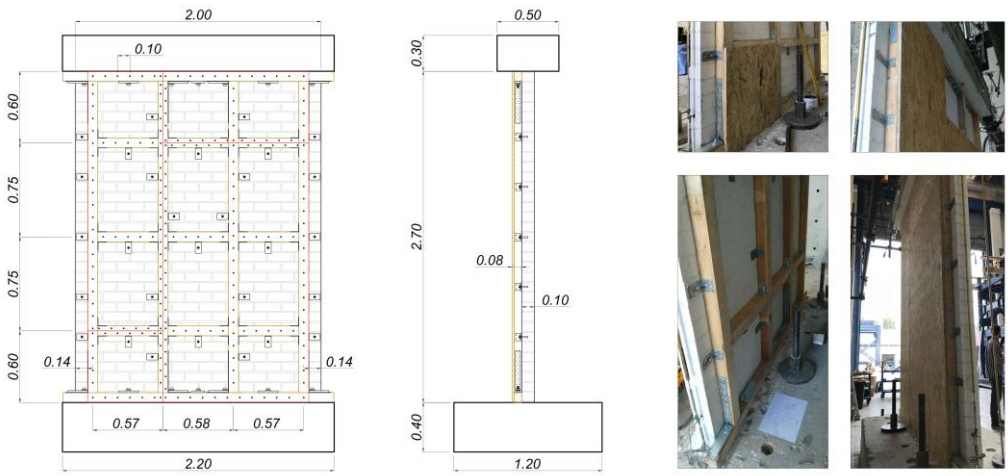

Figure 2.2 Retrofitted specimen geometry. Units of m.

C3 identifies the connection between timber frame and masonry pier. 90 x 50 mm steel angles with cross-section of 50 x 3 mm were connected to the timber members by four 5-mm-diameter, 70-mm-long screws and to the masonry by a 10-mm-diameter threated rod bonded by an epoxy adhesive. C4 indicates the connection between posts and blocking

elements provided by 70 x 70 mm steel angles with cross-section of 55 x 2 mm, connected to the timber members by five 5-mm-diameter, 70-mm-long screws on each leg. Four angles were provided at intersections with interior posts, while only two at intersections with edge posts.

The cost of the materials employed to strengthen the specimen was evaluated at approximately € 130 per square meter of wall surface, referring to Northern Italy market prices. The required installation time was estimated as 2.25 man-hours per square meter of wall surface, considering its application to an entire full-scale building prototype [Damiani *et al.*, 2019].

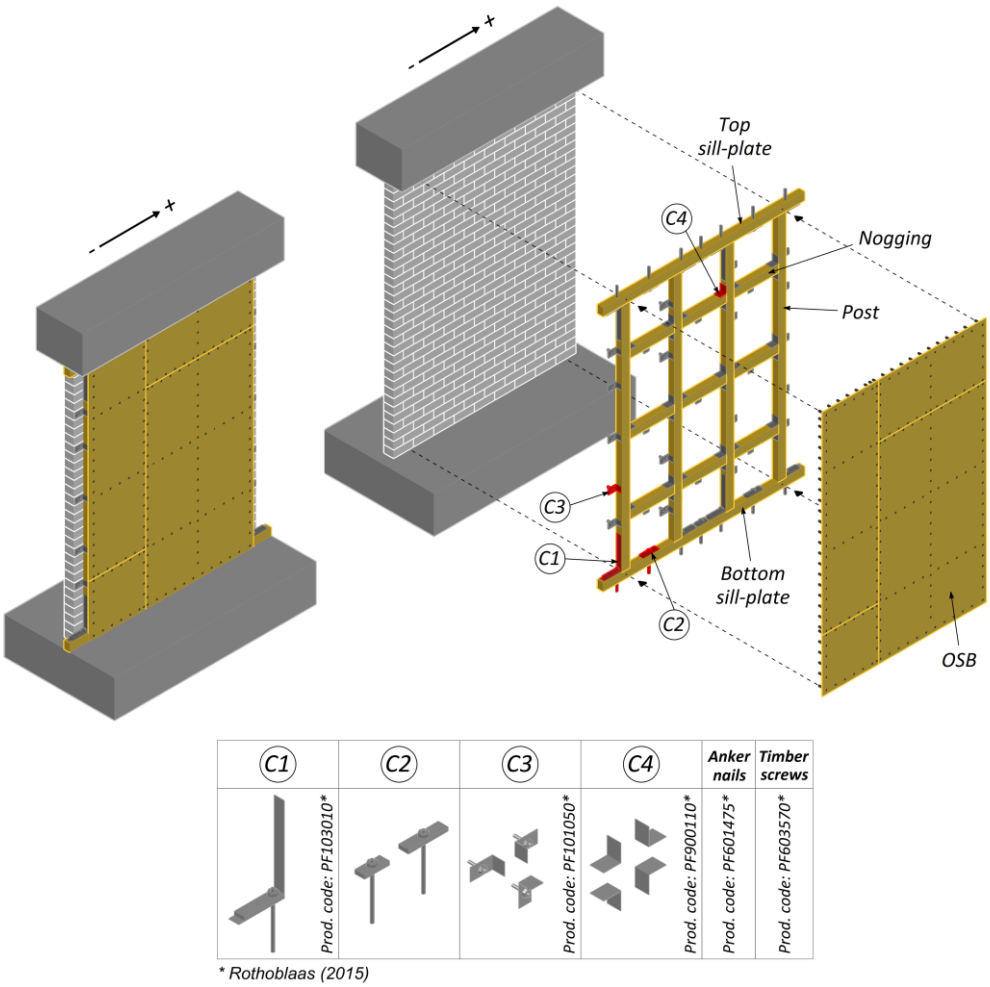

Figure 2.3 Retrofit system components.

2.2.3 Material mechanical properties

2.2.3.1 *Calcium-silicate masonry*

All mechanical characterisation tests on the masonry were performed at the DICAr laboratory of the University of Pavia in 2018 on specimens that were 28 d old. A detailed overview of the characterisation campaign can be found elsewhere [Miglietta et al., 2018].

The main material properties are summarised in Table 2.1. Calcium silicate bricks were tested in compression and bending according to BS EN 772-1:2011 [BSI, 2011] to obtain their compressive strength (f_b) and tensile strength (f_{bt}). The tensile (f_t) and compressive (f_c) strengths of the mortar were determined according to the prescriptions of BS EN 1015-11:2019 [BSI, 2006a]; sand was added to the mix to reproduce the properties measured in situ on existing buildings more closely. The compressive strength of the masonry (f_m) and the secant elastic modulus at 33% of compressive strength (E_m) were obtained by testing masonry wallettes in compression along the direction perpendicular to the horizontal bed-joints, according to BS EN 1052-1:1999 [BSI, 1998]. The initial shear strength (f_{v0}) and the friction coefficient (μ) were obtained according to BS EN 1052-3:2002 [BSI, 2002], while the masonry bond strength (f_w) was obtained following BS EN 1052-5:2005 [BSI, 2005a]. The masonry density (ϱ) was 1837 kg/m³.

Table 2.1 Masonry mechanical properties.

	Bricks		*Mortar*		*Masonry*					
	f_b [MPa]	f_{bt} [MPa]	f_c [MPa]	f_t [MPa]	f_m [MPa]	E_m [MPa]	f_w [MPa]	f_{v0} [MPa]	μ -	ρ [kg/m³]
Tested specimens	6	12	63	63	6	6	30	14	14	6
Avg.	19.8	2.5	5.06	1.74	10.1	6593	0.28	0.62	0.71	1837
C.o.V. [-]	0.18	0.09	0.24	0.28	0.06	0.09	0.32	-	-	0.01

2.2.3.2 *Retrofit components*

Red solid fir (Picea abies), with a density of 517 kg/m³ and belonging to category S10/C24 according to BS EN 14081- 1:2016 [BSI, 2016], was used to construct the timber frames. Its characteristic compressive strength parallel to the fibres ($f_{c,0}$) was 21 MPa, its characteristic tensile strength parallel to the fibres ($f_{t,0}$) was 14 MPa and its mean Young modulus ($E_{0,mean}$) was 11000 MPa. The OSB boards had a density of 572 kg/m³ and belonged to category OSB/3 according to BS EN 300:2006 [BSI, 2006b]. Only the densities were determined at the DICAr laboratory; all the other properties were taken as specified by the mentioned codes.

The steel angles used for tie-down connections C1 had a characteristic tensile strength of 11·6 kN, while those for the frame-to-masonry connections C3 had a characteristic shear strength of 3·3 kN [Rothoblaas, 2015]. The epoxy adhesive offered characteristic tensile and shear strengths of 41 kN and 20 kN respectively when applied to 10 mm dia. rods. These strengths increased to 59 kN and 30 kN respectively when used with 12 mm dia. rods. These values refer to embedment in uncracked concrete [Hilti, 2019].

2.3 TESTING PROCEDURE

2.3.1 Tests setup

The experimental setup used for the in-plane shear-compression cyclic tests on both specimens is illustrated in Figure 2.4. The RC footing was bolted to the laboratory strong floor. A steel beam was fastened to the top RC beam. To achieve continuous and uniform contact, a layer of self levelling high-strength shrinkage-controlled gypsum was placed between the RC footing and the strong floor and between the RC top beam and the steel beam.

Two vertical servo-hydraulic actuators, reacting against a steel frame fixed to the laboratory strong wall, were connected to the steel top beam, providing double-curvature boundary conditions. A horizontal servo-hydraulic actuator reacted against the strong wall and pushed/pulled the specimen through the top steel beam. A restraining system connecting the top steel beam to the strong wall limited the RC top beam rotations about its longitudinal axis and the out-of-plane displacements of the pier, forcing an in-plane response up to severe damage conditions.

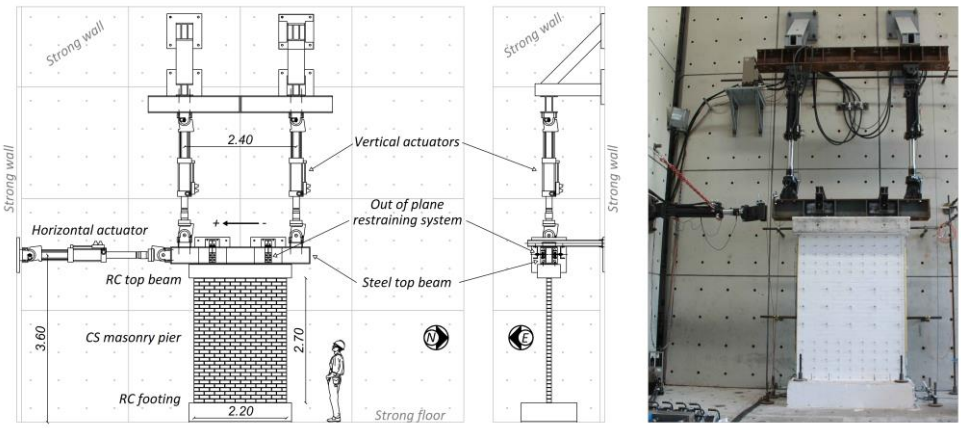

Figure 2.4 In-plane shear-compression cyclic tests setup. Units of m.

2.3.2 Instrumentation and data acquisition

The forces applied by the three actuators were continuously monitored by load cells. Horizontal, vertical, and diagonal displacements were recorded by transducers mounted at several locations throughout the specimen, allowing the determination of significant deformation parameters. In addition to load cells and potentiometers, an optical acquisition system with high-resolution cameras was used to monitor the three-dimensional trajectories of passive reflective markers, distributed over one surface of the specimens (grey dots visible in the photo of Figure 2.4).

2.3.3 Loading protocol

Both specimens were subjected to the same vertical overburden stress of 0.5 MPa at the top and were tested under double-curvature, consistent with the boundary conditions of masonry piers located in the first storey of a typical Dutch two-storey terraced house [Miglietta *et al.*, 2018]. The applied overburden stress represented an upper-bound scenario and was evaluated considering the axial-load increase due to rocking and uplift of the pier corners. In the first step, the vertical actuators applied the axial load with constant loading rate. In the case of the retrofitted pier, a gap of 10 mm was left between vertical posts and the top sill plate while the top row of nails had not yet been provided to the OSB during this loading phase. This allowed the vertical load to be carried by the masonry pier without significant participation of the frame, as would happen in real situations. Fastening operations were then completed after full application of the axial force. The horizontal loading history followed a force-controlled procedure for the firsts two sets of cycles, then continued in displacement-controlled mode Each set included three push–pull cycles of equal amplitude; the duration of the cycles was kept almost constant, varying the displacement rate proportionally to the target displacement. The target forces (F), displacements (δ) and drift ratios ($\theta = \delta / H$) of each cycle set for both specimens are provided in Table 2.2. The positive loading direction was associated with the actuator pulling the specimen southward and the negative direction was associated with pushing northward.

2.4 EXPERIMENTAL RESULTS

2.4.1 Unstrenghtened specimen

The bare specimen initially exhibited a rocking behaviour. The first horizontal crack was observed at the bottom of the pier (Figure 2.5a) at drift ratios $\theta_{cr}^{+} = \theta_{cr}^{-} = \pm 0.075\%$ in both positive and negative directions, along the first and second bed-joints above the base of the wall. The damage pattern at the end of the cycles when the maximum positive shear was achieved, i.e. $\theta_{Vmax}^{+} = 0.20\%$, is shown in Figure 2.5b.

Table 2.2 Nominal lateral loading protocol.

	Cycle set	F [kN]	δ [mm]	θ [%]	Velocity [mm/s]
Bare and retrofitted piers	1	15	-	-	-
	2	25	-	-	-
	3	-	0.50	0.02	0.01
	4	-	0.90	0.03	0.02
	5	-	1.30	0.05	0.03
	6	-	2.00	0.075	0.04
	7	-	2.70	0.10	0.05
	8	-	4.00	0.15	0.08
	9	-	5.40	0.20	0.10
	10	-	6.70	0.25	0.15
	11	-	8.10	0.30	0.15
	12	-	10.80	0.40	0.20
	13	-	13.50	0.50	0.30
Retrofitted pier	14	-	16.20	0.60	0.40
	15	-	21.50	0.80	0.50
	16	-	26.90	1.00	0.60
	17	-	40.40	1.50	1.00
	18	-	53.90	2.00	1.50

At a drift ratio of 0.25%, the top horizontal flexural crack extended throughout the whole length of the specimen, between the 32nd and 33rd brick courses above the base, allowing the onset of sliding at the top of the wall. The specimen began to behave asymmetrically in positive and negative directions during the cycles at a drift ratio of 0.40%: the wall kept sliding along the top crack when the actuator was pushing, while it rocked when the actuator was pulling.

During the cycles at a drift ratio of 0.50%, despite the presence of rotational restraints, the top beam started rotating about its longitudinal axis inducing out-of-plane displacements on the pier, probably due to extensive toe crushing at the base of the specimen and high out-of-plane slenderness. The test continued with a monotonic lateral loading procedure and was terminated when the specimen lost its vertical load-bearing capacity. The pier failed at an ultimate drift $\theta_u^+ = 0.75\%$ in the positive loading direction (Figure 2.5c).

The recorded hysteretic loops are displayed in Figure 2.6. The overall response of the specimen was characterised by rocking behaviour up to a drift ratio of 0.20%. The maximum negative shear, V_{max}^{-} = 74.5 kN, was reached at θ_{Vmax}^{-} = 0.15%, while the maximum positive shear, V_{max}^{+} = 77.9 kN, at θ_{Vmax}^{+} = 0.20%. After reaching the maximum positive resistance, the development of a continuous top horizontal crack at the pier top changed the behaviour to a shear-sliding mechanism. In fact, the hysteretic cycles became significantly wider, denoting greater energy dissipation due to friction between the brick courses sliding across the continuous crack. The asymmetrical behaviour observed during the test starting at a drift ratio of 0.40% was confirmed by the shape of the hysteretic cycles: wider, sliding-dominated cycles were obtained in the negative direction, as opposed to narrower, recentring, rocking-dominated cycles in the positive direction.

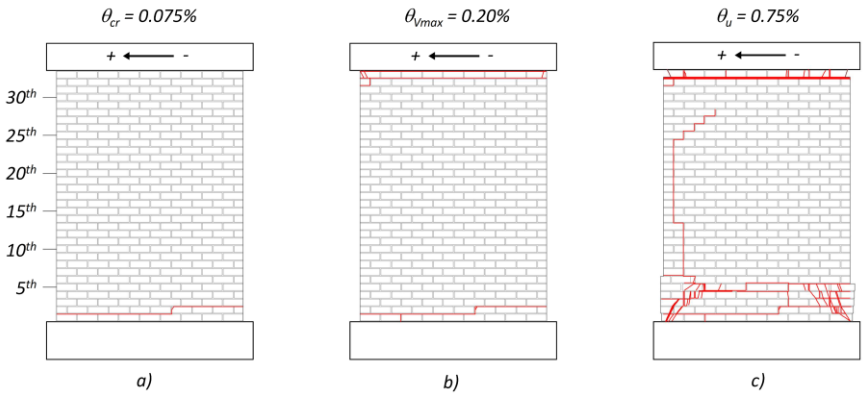

Figure 2.5 Bare pier crack pattern corresponding to: a) first cracking; b) maximum recorded shear; c) ultimate conditions.

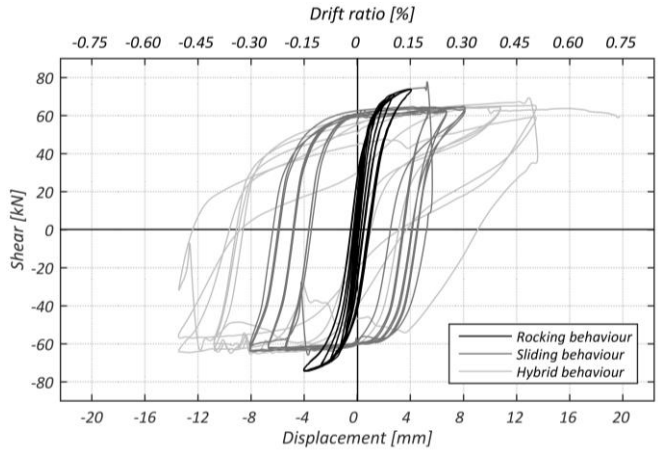

Figure 2.6 Bare pier hysteretic response.

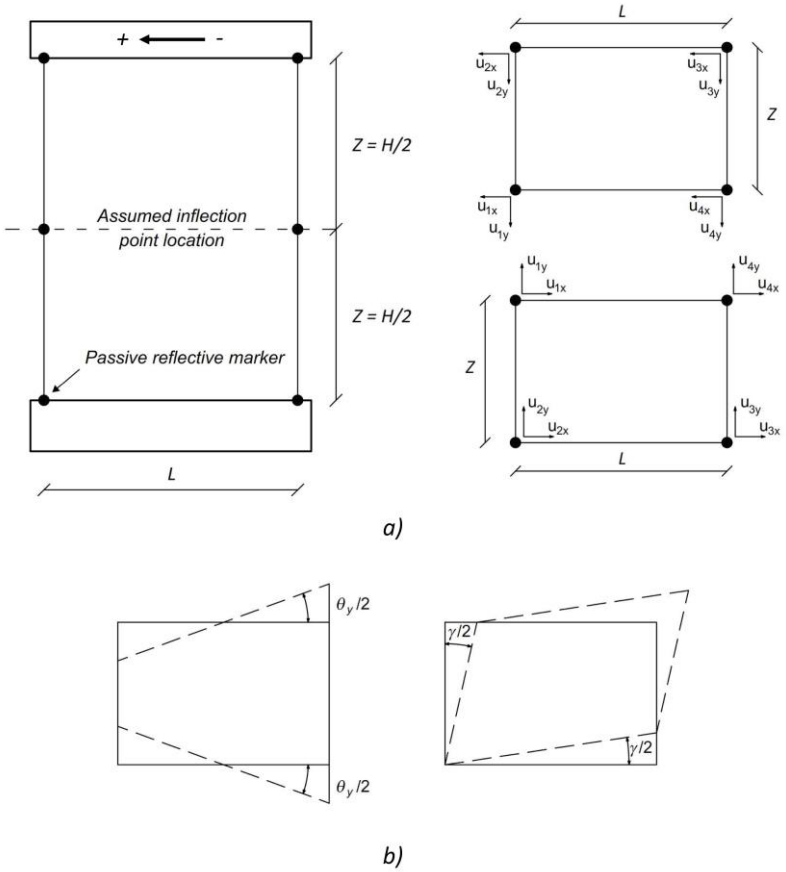

Figure 2.7 Displacement contributions: a) sub-elements with reference nodes; b) flexural and shear deformation modes.

The total lateral displacement was decomposed into the contributions of flexural (θ_y) and shear deformations (γ), following the procedure developed by Seible *et al.* [1991] as depicted in Figure 2.7. Because the test was performed under double-curvature conditions, the contributions were computed assuming the inflection point at mid-height of the specimen and analysing separately the top and bottom halves of the pier; accordingly, each half was characterised by height $Z = H / 2$. The displacements of six points (Figure 2.7), obtained from the trajectories of the passive reflective markers, were used to calculate the displacement components: two at the edges of the RC footing, two at the specimen mid-height, and two at the edges of the RC top beam.

Figure 2.8 shows the percentage of the lateral displacement contributed by flexural and shear deformations, recorded at maximum positive and negative displacements during the first cycle of each set of three. Some minor discrepancies were observed between the sum

of the two contributions and the total displacement (labelled "other" in Figure 2.8), likely due to instrumentation tolerances and inflection point deviations from mid-height. The two components were comparable up to a drift ratio of 0.15%. After that, the flexural effect dropped significantly while the shear component, which included sliding over the horizontal crack at the top of the specimen, became dominant.

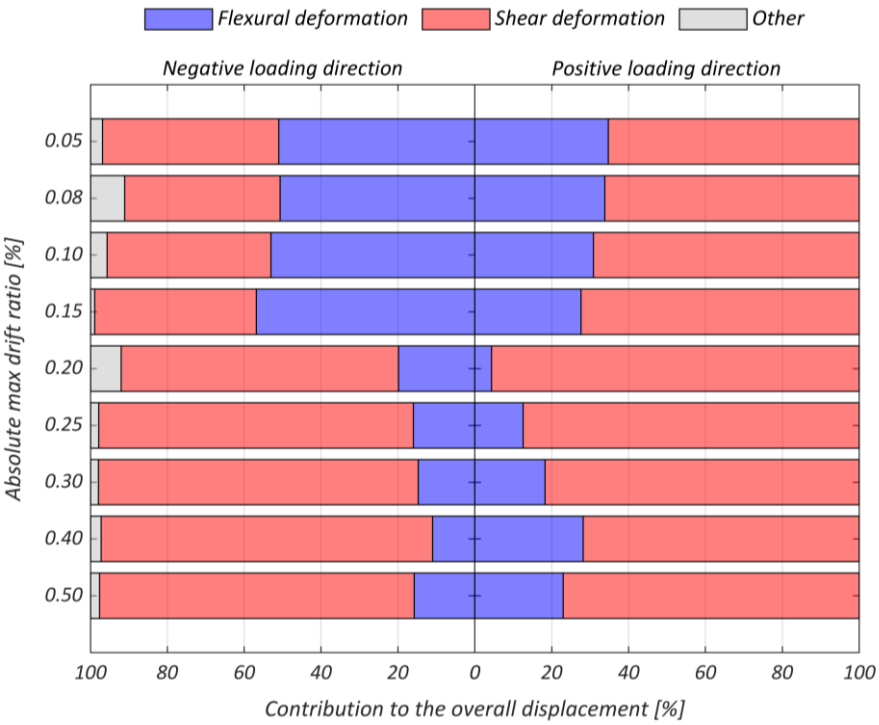

Figure 2.8 Bare pier displacement contributions.

2.4.2 Retrofitted specimen

The first two cracks developed above the second brick layer (Figure 2.9a), at drift ratios $\theta_{cr}^{+} = \theta_{cr}^{-} = 0.075\%$ in both positive and negative directions, as observed for the bare pier. The crack pattern characteristic of a toe crushing mechanism started developing at the bottom corners of the specimen after reaching a drift ratio of 0.15% and became evident after reaching 0.20% (Figure 2.9b). During these loading stages two horizontal cracks also extended continuously throughout the pier length: one above the second brick course and one above the fifth course, at the level of the lowermost timber post-to-masonry connections. It should be noted that at 0.20% drift ratio the bare pier exhibited its maximum shear strength with the onset of a sliding mechanism. The cycles at drift ratios of 0.25% and 0.30% were characterised by toe crushing propagation at both bottom corners, which caused also the expulsion of portions of bricks and mortar.

The first damage of a retrofit component was observed at a drift ratio of 0.60%: the steel angles of the tie-down connections (C1 in Figure 2.3) at the top corners of the specimen buckled in compression. Figure 2.9c shows the damage pattern detected after the specimen reached its maximum shear strength at drift ratios $\theta_{Vmax}^{+} = \theta_{Vmax}^{-} = \pm 0.80\%$, which also corresponded to the ultimate drift ratio of the unretrofitted pier: extensive toe crushing was visible, with dislocation and loss of significant portions of masonry at the lower corners. The following cycles at a drift ratio of 1.00% resulted in buckling of the tie-down steel angles also at the base of the specimen.

During the pulling phase at 1.50% a diagonal shear crack with slope of about 45° formed at the top half of the specimen. This was probably caused by the shear deformation reached by the pier, which could not be accommodated by the masonry. The last cycles were performed at $\theta_u^{+} = \theta_u^{-} = \pm 2.00\%$ and caused extensive damage to the specimen. During the pushing and pulling phases, new diagonal, vertical and horizontal cracks developed throughout the wall (Figure 2.9d). Tie-down steel angles visibly buckled, while the axial compression transferred by the posts resulted in dents in the top and bottom sill plates, with depth of few millimetres.

The test was stopped after completing two cycles at a drift ratio of ±2.00%: in fact, the masonry pier was no longer able to withstand the vertical load, which was likely almost entirely carried by the timber posts. The transfer of axial force from the masonry to the timber system was inferred by correlating the progressive lowering of the pier top with the cycle maximum drift ratios. As shown in Figure 2.10, the downward (negative) displacements became significant after overcoming the experimental ultimate drift ratio of the bare pier, reaching 22 mm at the end of the test.

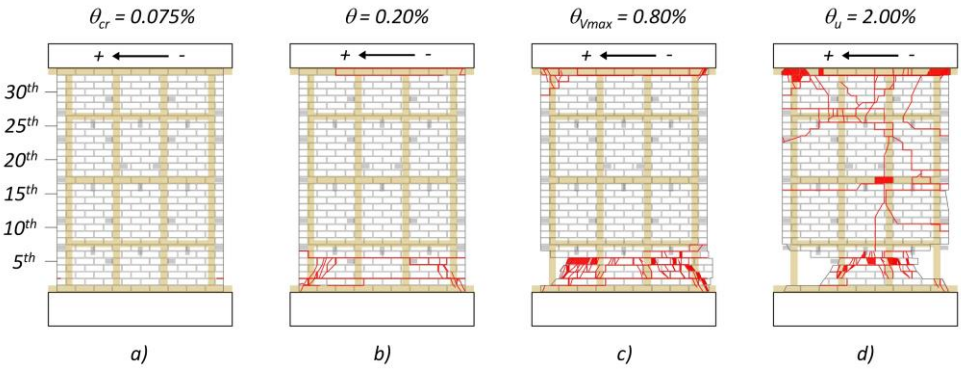

Figure 2.9 Retrofitted pier crack pattern corresponding to: a) first cracking; b) maximum recorded shear on the bare pier; c) ultimate conditions of the bare pier and maximum recorded shear on the retrofitted pier; d) ultimate conditions.

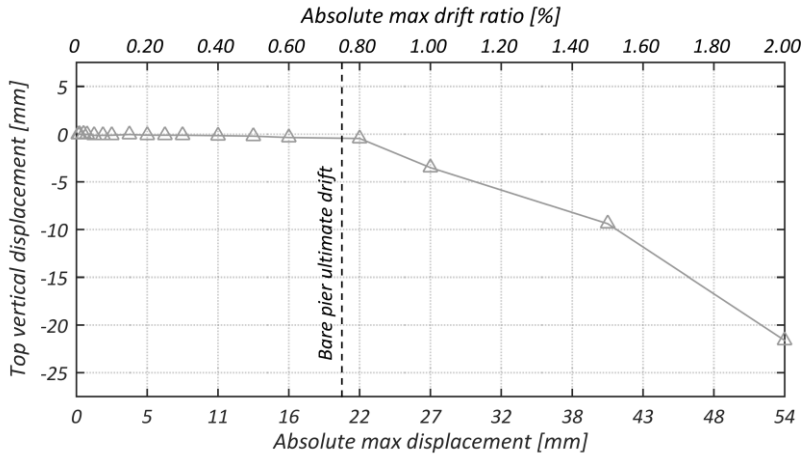

Figure 2.10 Retrofitted pier: vertical displacement of the pier top at zero lateral force.

The experimental hysteretic loops are represented in Figure 2.11. The specimen reached its maximum positive and negative shear strength, V_{max}^{+} = 104.7 kN and V_{max}^{-} = -109.6 kN, respectively, at drift ratios $\theta_{Vmax}^{+} = \theta_{Vmax}^{-} = \pm 0.80\%$ (Figure 2.9c). After these points, a progressive strength degradation was recorded when pulling, while the strength remained almost constant under pushing until it suddenly dropped during the second-last set of cycles upon diagonal shear cracking of the masonry.

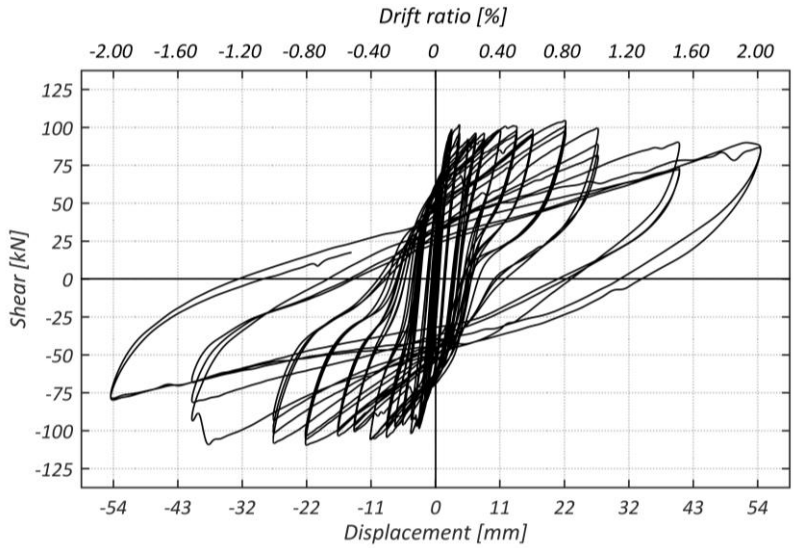

Figure 2.11 Retrofitted pier hysteretic response.

The total displacement was decomposed into flexural (θ_y) and shear (γ) deformation contributions, as discussed for the bare pier. Figure 2.12 shows their percentages recorded at maximum positive and negative displacements during the first cycle of each set of three. The proportions remained similar throughout the entire test without sudden changes, except for a slight reduction of the flexural contributions during cycles at 0.20% and 0.25% drift ratio: this may be associated with the formation of two continuous cracks in the lower portion of the pier, with possible onset of a sliding mechanism (as observed for the bare pier) partially inhibited by the stiffness of the timber retrofit.

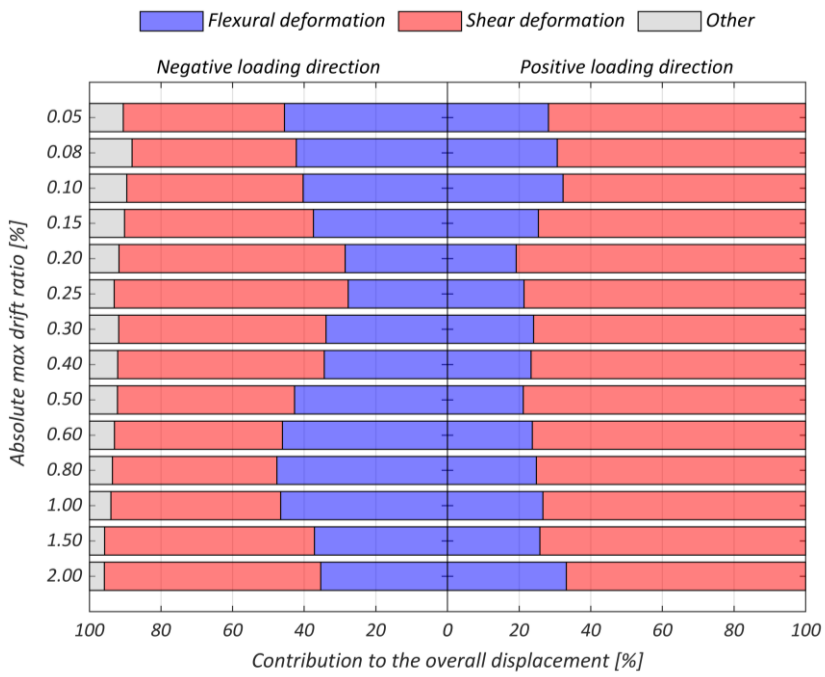

Figure 2.12 Retrofitted pier displacement contributions.

Figure 2.13 shows the axial deformation of the bottom-North tie-down connection and the shear deformation of a portion of OSB sheathing against the horizontal displacement history. Tie-down connections showed a stable tension-compression response up to a drift ratio of 0.80%; then a progressive shortening was observed, related to the extensive buckling of steel angles and to the denting of sill plates (Figure 2.13a). It is interesting to notice that the shortening of top and bottom tie-down connections, the denting of the sill plates, and the compressive axial deformation of the posts resulted in an overall shortening of the timber system compatible with the top beam 22-mm downward displacement shown in Figure 2.10. The shear deformation of the OSB became significant at a drift ratio of 1.50%, after reaching a value of 0.05% (Figure 2.13b): this corresponded to diagonal shear

cracking of the masonry and was consistent with the cracking shear deformation obtained for calcium-silicate squat piers by Graziotti *et al.*, [2016].

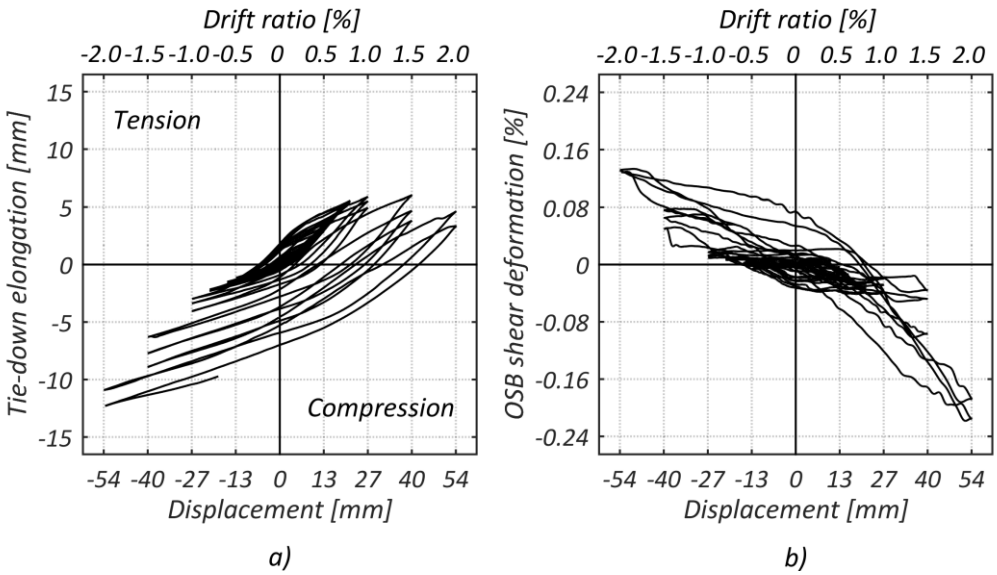

Figure 2.13 Retrofit system response: a) elongation of the tie-down connection at the bottom-North corner; b) OSB shear deformation.

2.4.3 Comparison of the test results

The experimental backbone curves of both piers in the positive loading direction and their bilinear idealisations are compared in Figure 2.14. The backbone curves include the maximum-force points for all cycles, and the maximum-displacement point for the last cycle. Table 2.3 provides a summary of the main experimental results for the positive loading direction, in terms of secant stiffness at 33% of the maximum shear force ($K_{33\%}^{+}$), first-cracking drift ratio (θ_{cr}^{+}), maximum shear force (V_{max}^{+}) with the corresponding drift ratio ($\theta_{V\,max}^{+}$), and ultimate drift ratio (θ_{u}^{+}) with the corresponding shear force (V_{u}^{+}).

The idealised bilinear relationships were defined according to Morandi *et al.* [2018]. The elastic stiffness (K_{bl}^{+}) was taken as the slope of the secant line through the experimental point at 70% of the maximum shear (V_{max}^{+}), while the ultimate drift ratio ($\theta_{u,bl}^{+}$) was set at a strength drop equal to 20% of V_{max}^{+}. The yield point ($\theta_{y,bl}^{+}$, $V_{y,bl}^{+}$) was obtained intersecting the secant line with a horizontal one, and imposing the equivalence of the areas below the experimental envelope and the idealised bilinear curve up to $\theta_{u,bl}^{+}$. The parameters defining the bilinear relationships are summarised in Table 2.4.

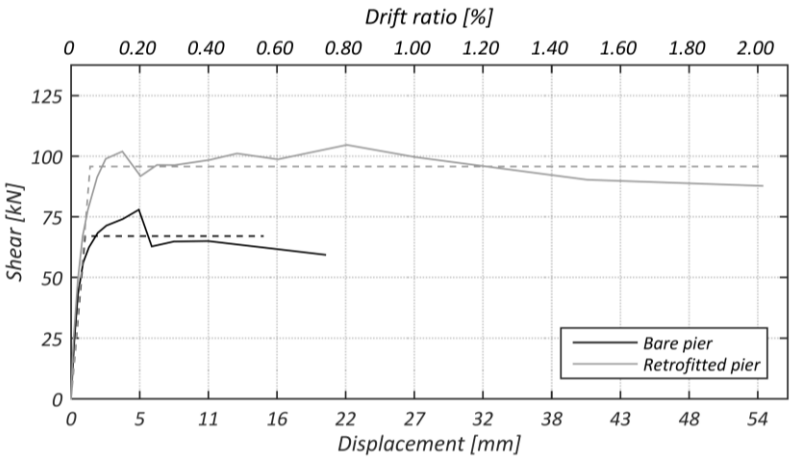

Figure 2.14 Bare and retrofitted pier backbone curves and bilinear idealisations, positive loading direction.

Table 2.3 Backbone curve parameters, positive loading direction.

Specimen	$K_{33\%}^{+}$ [kN/mm]	θ_{cr}^{+} [%]	θ_{Vmax}^{+} [%]	V_{max}^{+} [kN]	θ_{u}^{+} [%]	V_{u}^{+} [kN]
Bare pier	94	0.075	0.2	78	0.75	59
Retrofitted pier	106	0.075	0.8	105	2.00	88

Table 2.4 Bilinear idealisation parameters, positive loading direction.

Specimen	K_{bl}^{+} [kN/mm]	$\theta_{y,bl}^{+}$ [%]	$V_{y,bl}^{+}$ [kN]	$\theta_{u,bl}^{+}$ [%]
Bare pier	60.9	0.04	67.0	0.56
Retrofitted pier	64.3	0.06	95.7	2.00

It is interesting to note that the retrofit system, characterised by a stiffness equal to about 10% of the one of the masonry pier, began working after first cracking of the masonry, which happened at 0.075% drift ratio (Figure 2.14). For smaller displacements, the initial stiffness of the two specimens was nearly identical, as typically observed in reinforced masonry and reinforced concrete elements. Both specimens exhibited a sudden drop of strength at drift ratios of 0.20%, when horizontal cracks extended continuously throughout the pier length (Figure 2.15). However, while the bare pier did not recover this loss because of the transition from a rocking to a sliding behaviour, the stiffness of the timber retrofit

inhibited shear-sliding along the cracks and allowed the specimen to reach higher displacements gaining additional strength.

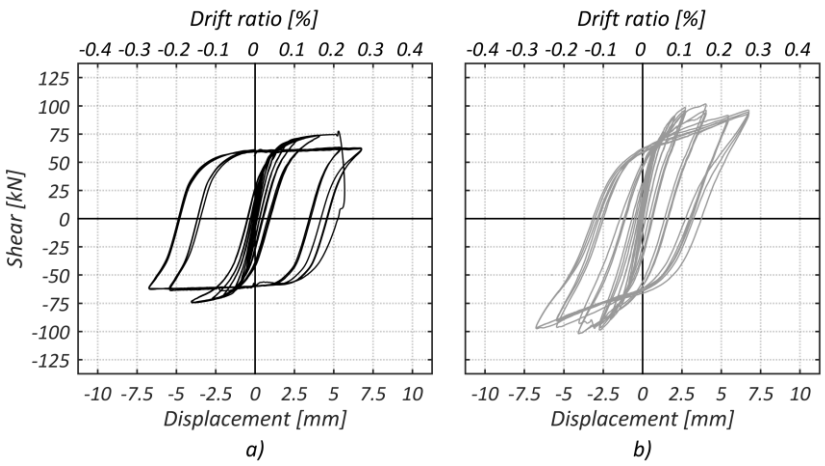

Figure 2.15 Hysteretic response up to 0.25% drift ratio: a) bare pier; b) retrofitted pier.

Figure 2.16a and Figure 2.16b show the ultimate conditions reached by the two specimens. Both of them presented significant toe crushing, more pronounced on the retrofitted wall. In fact, the bare pier failed due to out-of-plane distortion, induced by deterioration at the rocking/sliding interfaces, which limited its in-plane drift capacity. Instead, the retrofitted specimen sustained more than twice the lateral displacement, as the timber system allowed exploiting its full flexural-rocking capacity and gradually took over the masonry compression resistance.

At the end of the test, although the masonry was heavily damaged, the timber frame helped the retrofitted pier maintaining gravity load resistance, while the bare pier lost its vertical load-bearing capacity. Damage to the retrofit was localised within tie-down connections, where steel angles yielded in tension and buckled in compression (Figure 2.16c), and within top and bottom sill plates, where the posts transferred concentrated compressive forces.

The cumulative dissipated energy for the two piers is shown in Figure 2.17. Although they were characterised by different failure mechanisms and hysteretic loop shapes, the dissipated energy was quite similar up to failure of the bare pier. Indeed, the latter exhibited wider cycles with lower strength, governed by the shear-sliding mechanism, while the retrofitted one showed slightly thinner cycles with higher strength.

Figure 2.16 Ultimate conditions: a) bare pier; b) retrofitted pier; c) buckled tie-down steel angle.

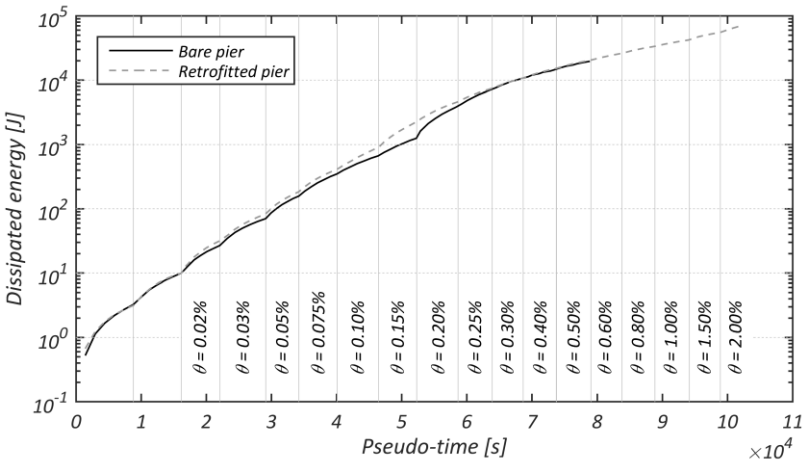

Figure 2.17 Bare and retrofitted pier hysteretic energy dissipation.

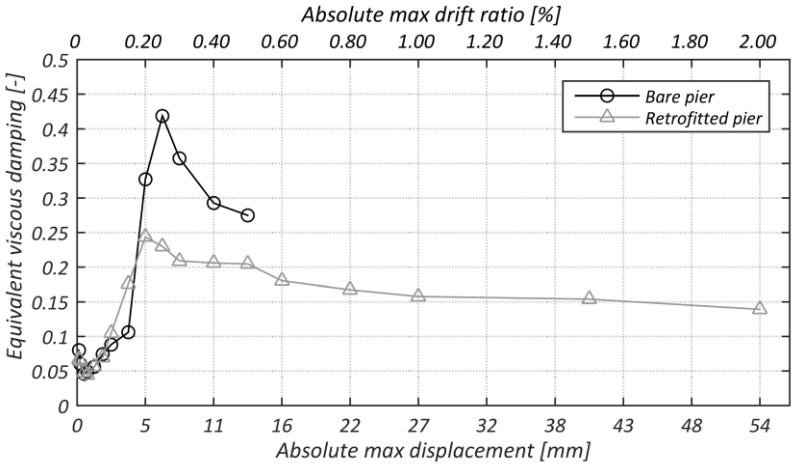

Figure 2.18 Bare and retrofitted pier equivalent viscous damping.

The dissipated energy was converted into equivalent viscous damping according to Jacobsen [1960], as shown in Figure 2.18 against the maximum drift ratio of each cycle. For each drift-ratio increment, the average area enclosed by the three cycles was first computed, then converted into equivalent viscous damping ratio. The bare pier offered higher equivalent viscous damping after the transition from rocking to shear-sliding behaviour at 0.20% drift ratio, because sliding-governed response results in wider hysteretic loops. On the other hand, the flexure-controlled retrofitted pier exhibited smaller equivalent viscous damping, slightly decreasing as damage progressed at larger drift ratios.

2.5 ANALYTICAL PREDICTION OF EXPERIMENTAL RESULTS

In this section, simple equations are proposed to capture the elastic stiffness and the strength of the retrofitted pier, which can be used for the design of the retrofit system. The analytical results are validated against the experimental ones obtained in the positive loading directions and summarised in Table 2.3.

2.5.1 Unretrofitted specimen

The masonry wall initial stiffness, for double-curvature boundary conditions, can be calculated as:

$$K_{mas} = \left(\frac{H^3}{E_m \cdot L^3 \cdot t} + 1.2 \frac{H}{G_m \cdot L \cdot t} \right)^{-1} \tag{2.1}$$

where E_m is the masonry modulus of elasticity, G_m is the shear modulus assumed equal to $0.35 \cdot E_m$ according to MIT (2018), while H, L, and t are respectively height, length, and

thickness of the pier, respectively. Substituting the dimensions and material properties of the bare pier into Equation (2.1) yields K_{mas} = 95 kN/mm. Thus, compared with the experimental secant stiffness at 33% of the maximum shear force (94 kN/mm), Equation (2.1) results in a negligible overestimation of the order of 1%.

The lateral strength associated with a flexural rocking mechanism can be obtained from the following equation [Magenes *et al.*, 1997]:

$$V_{R,mas,f} = \frac{2 \cdot M_{R,mas,f}}{H} \tag{2.2}$$

with the bending moment resistance ($M_{R,mas,f}$) of the end sections evaluated as:

$$M_{R,mas,f} = \frac{\sigma_v \cdot L^2 \cdot t}{2}\left(1 - \frac{\sigma_v}{\eta \cdot f_m}\right) \tag{2.3}$$

where σ_v is the vertical compressive stress evaluated on the gross masonry section at mid-height of the pier, t the wall thickness, and η the stress block magnitude parameter assumed equal to 0.85. For the tested pier, the vertical compressive stress of 0.524 MPa at mid-height results in an rocking shear strength $V_{R,mas,f}$ = 74 kN.

The estimated sliding-shear strength of the specimen, due to frictional ($V_{R,\mu}$) and cohesive ($V_{R,fv0}$) contributions, can be calculated as [Magenes *et al.*, 1997; Eurocode 6, 2005]:

$$V_{R,mas,s} = V_{R,\mu} + V_{R,f_{v0}} = \mu \cdot \sigma_v \cdot t \cdot L + f_{v0} \cdot t \cdot l_c \tag{2.4}$$

with the contact length (l_c) given by:

$$L \cdot \frac{\sigma_v}{\eta \cdot \lambda \cdot f_m} \leq \left[l_c = 1.5 \cdot L \cdot \left(1 - \alpha_v \frac{3 \cdot f_{v0} + 2 \cdot \mu \cdot \sigma_v}{\sigma_v + 3 \cdot f_{v0} \cdot \alpha_v} \cdot\right)\right] \leq L \tag{2.5}$$

where μ is the friction coefficient, σ_v the vertical compressive stress, f_{v0} the masonry initial shear strength, f_m the masonry compressive strength, and $\alpha_v = H / (2 \cdot L) = 0.67$ the shear-span ratio. The stress-block depth parameter λ, generally ranging from 0.7 to 1, can be taken equal to 0.85. The estimated sliding shear strength of the specimen is then $V_{R,mas,s}$ = 84 kN.

With the sliding-shear strength being slightly higher than the rocking lateral strength, the development of a flexural mechanism would be expected before the onset of sliding. In

fact, the minimum computed strength $V_{R,mas,f}$ = 74 kN provides a good estimation of the actual experimental strength of 78 kN, with an error of about 5%.

Moreover, the same equations can be used to estimate the residual shear strength after the sliding mechanism activation at 0.2% drift ratio, which resulted in a hybrid response of the specimen. This transition was caused by the opening of a full-length flexural crack at the top of the specimen, resulting in loss of cohesion and in an experimental residual strength of about 65 kN. Evaluating the frictional shear resistance only, $V_{R,\mu}$ = 75 kN, results in a 15% overestimation of this residual sliding shear strength.

2.5.2 Retrofitted specimen

The lateral stiffness and strength of the retrofitted pier can be calculated under the simplifying assumption that masonry and timber act as springs in parallel, thus directly summing their individual contributions. Accordingly, the elastic stiffness of the timber retrofit system can be computed with the following expression [Countryman, 1952]:

$$K_{tim} = \left(\frac{H^3}{6 \cdot E_p \cdot A_p \cdot L^2} + \frac{H}{K_{OSB} \cdot L} \right)^{-1} \tag{2.6}$$

where E_p is the timber post elastic modulus, A_p is the cross-sectional area of each outermost post, and K_{OSB} is the shear stiffness of nailed OSB panels. For the case under examination, an elastic modulus $E_p = E_{0,mean}$ = 11000 MPa and a nominal cross-section area A_p = 4800 mm² are adopted for the timber, while a nominal shear stiffness K_{OSB} = 15500 N/mm is assigned to the OSB according to the American specifications for timber shear-walls [AWC, 2008]. The in-plane elastic stiffness of the timber retrofit system becomes K_{tim} = 9.8 kN/mm. The experimental counterpart of 12 kN/mm can be obtained from Table 2.3, subtracting the stiffness of the bare pier (94 kN/mm) from the one of the retrofitted specimen (106 kN/mm). This results in a 18% underestimation of the retrofit stiffness. However, the timber retrofit accounts for only about 10% of the total lateral stiffness. Comparing the total predicted stiffness $K_{tot} = K_{mas} + K_{tim}$ = 105 kN/mm with the experimental one of the retrofitted pier (106 kN/mm), the error is only 1%.

The flexural rocking-strength of the retrofit system is provided by the vertical forces acting on the timber posts. All posts are assumed to be stressed by the same tensile force, except for an outermost post that carries compression. The rotational equilibrium can be written with respect to the compression post, since no axial load is assumed to be carried by the timber:

$$M_{R,tim,f} = \sum (T_i \cdot b_i) \tag{2.7}$$

where T_i is the tensile axial force in the ith post and bi its distance from the compression post. The tensile forces are the minimum between the tensile strength of the timber post and the yield strength of the vertical leg of the steel angle in connection C1 in Figure 2.3. The lateral strength associated with flexural failure can then be calculated using Equation (2.8):

$$V_{R,tim,f} = \frac{2 \cdot M_{R,tim,f}}{H} \tag{2.8}$$

For the tested pier, the tensile strength of the posts is $1.5 \cdot A_p \cdot f_{t,0}$ = 100.5 kN, while the mean yield capacity of the connection is 1.1·11.6 kN = 12.8 kN and controls the force on the posts. This results in $V_{R,tim,f}$ = 33 kN. Factors 1.5 and 1.1 account for mean-to-nominal (or mean-to-characteristic) strength ratio according to ASCE [2017].

The strength associated with a shear failure mode of the retrofit system is mainly provided by the OSB nailed to the timber frame. The shear strength can be predicted in accordance with the American specifications for timber shear-walls [AWC, 2008; ASCE, 2017], where it is a function of the nominal panel thickness, the fastener penetration into the framing members, and the panel edge fastener spacing. A shear strength $V_{R,tim,s}$ = 45 kN can be derived for the specific case. However, considering that such values are derived for shear-walls without blocking elements and nailed only along the panel edges, a slightly higher shear strength may be expected when intermediate nailing is also provided.

The retrofitted pier strength depends on the mechanism that will develop, controlled by either flexure or shear. The strength of the bare pier and of the retrofit system associated with the corresponding failure mode need to be summed together, and the smaller value indicates the correct mechanism. For the specific case, $V_{R,tot,f} = V_{R,mas,f} + V_{R,tim,f}$ = 107 kN and $V_{R,tot,s} = V_{R,mas,s} + V_{R,tim,s}$ = 129 kN: this anticipates a flexural failure mode, as observed experimentally, with an error of less than 2% on the actual strength of 105 kN (Table 2.3). The predicted strength of the retrofit system, $V_{R,tim,f}$ = 33 kN, is affected by a 22% error compared to the experimental value of 27 kN, obtained from Table 2.3 by difference between the retrofitted and bare pier strength.

2.6 CONCLUSIONS

A timber retrofit solution applied to a single-leaf unreinforced masonry pier built with calcium silicate bricks to enhance its in-plane seismic resistance was investigated. The proposed retrofit system consisted of a timber frame mechanically connected to the masonry pier, to the foundation and to the top beam, and OSB panels nailed to the frame.

Two specimens with the same masonry dimensions and material properties one a bare masonry pier and the other completed with the retrofit were subjected to cyclic in-plane shear–compression tests under the same level of axial compression and boundary

conditions. All the processed data and instrumentation schemes can be obtained elsewhere [Eucentre, 2020].

The unstrenghtened specimen showed a hybrid behaviour, developing first a flexural-rocking mechanism which then evolved in a sliding-shear mode. The first cracks appeared at a drift ratio of 0.075%, while ultimate conditions were reached at a drift ratio of 0.75% with out-of-plane distortion of the severely damaged specimen. The maximum recorded lateral strength was approximately 78 kN.

The retrofitted pier maintained a flexural behaviour up to 1.50% drift ratio, because the timber frame inhibited shear-sliding and allowed some flexural overstrength to develop. The first cracks appeared at a drift ratio of 0.075% as in the bare pier, while an ultimate drift ratio of 2.00% was reached when diagonal shear cracks formed within the masonry. Extensive toe crushing affected the base corners of the retrofitted masonry pier, with almost all vertical load carried by the timber frame at ultimate conditions. The only damage to the retrofit system was localised within the tie-down connection steel angles, which yielded and buckled, and within the timber sill plates, which were dented upon compression transfer from the posts. The maximum shear attained was about 105 kN.

Significant improvements of the seismic performance were achieved. Even though the timber retrofit did not delay first cracking, due to its high flexibility compared with the masonry pier, it allowed an increase in the specimen's ultimate displacement (by 167%) and its lateral strength (by 35%). The effectiveness of the proposed retrofit system depended on the good connection quality and on the top beam and foundation resistance to the transferred stresses.

Analytical predictions of the in-plane stiffness and strength of the two specimens resulted in good agreement with the experimental values, with errors always within 5%, and will serve for the future development of design guidelines.

For practical applications, the proposed retrofit system can not only enhance the in-plane behaviour of the piers, but also improve their out-of-plane resistance, as it stems from previous studies where the timber posts acted as strong-backs for out-of-plane response. To demonstrate its global effectiveness, the system was applied to a full-scale building prototype tested on the shake-table of the EUCENTRE laboratories in Pavia, Italy.

2.7 ACKNOWLEDGEMENTS

This work is part of the EUCENTRE project "Study of the vulnerability of masonry buildings in Groningen", within the research programme framework on hazard and risk of induced seismicity in the Groningen province, sponsored by the Nederlandse Aardolie Maatschappij BV (NAM). The data post-processing was also partially funded by the DPC-ReLUIS within the framework of the Work-Package-5 2019-2021: "Interventi di rapida

esecuzione a basso impatto ed integrati". The authors would like to thank all parties involved in this project: the DICAr Laboratory of the University of Pavia and the EUCENTRE Laboratory, which performed the tests, and the partner NAM. The valuable advice of R. Pinho, G. Magenes, and A. Penna was essential to the project and is gratefully acknowledged. Thanks also go to J. Uilenreef, I. Giongo, D. Dizhur, S. Kallioras, L. Grottoli, A. Boneschi and I. Nasso.

2.8 REFERENCES

Alcaino, P., Santa-Maria, H. [2008] "Experimental response of externally retrofitted masonry walls subjected to shear loading". *Journal of Composites for Construction*, 12(5): 489–498.

ASCE [2017] *ASCE/SEI 41-17: Seismic evaluation and retrofit of existing buildings*. American Society of Civil Engineers, Reston, Virginia, USA.

AWC [2008] *ANSI/AF&PA SDPWS-2008: Special design provisions for wind and seismic*. American Wood Council, Washington D.C., USA.

Babaeidarabad, S., Arboleda, D., Loreto, G., Nanni, A. [2014] "Shear strengthening of un-reinforced concrete masonry walls with fabric-reinforced-cementitious-matrix". *Construction and Building Materials*, 65: 243-253.

Bailey, S., Dizhur, D., Trowsdale, J., Griffith, M. [2014] "Performance of posttensioned seismic retrofit of two stone masonry buildings during the Canterbury earthquakes". *Journal of Performance of Constructed Facilities*, 29(4): 04014111.

Borri, A., Castori, G. Corradi, M. [2011] "Shear behavior of masonry panels strengthened by high strength steel cords". *Construction and Building Materials*, 25(2): 494-503.

Bourne, S.J., Oates, S.J., Bommer, J.J., Dost, B., van Elk, J., Doornhof, D. [2015] "A Monte Carlo method for probabilistic hazard assessment of induced seismicity due to conventional natural gas production". *Bulletin of the Seismological Society of America*, 105(3): 1721–1738.

BSI [1998] *BS EN 1052-1:1999: Methods of test for masonry. Determination of compressive strength*. British standards institution, London, UK.

BSI [2002] *BS EN 1052-3:2002: Methods of test for masonry units. Determination of initial shear strength.* British standards institution, London, UK.

BSI [2005a] *BS EN 1052-5:2005: Methods of test for masonry. Determination of bond strength by the bond wrench method.* British standards institution, London, UK.

BSI [2005b] *BS EN 1996: Eurocode 6: Design of masonry structures. Part 1-1: General rules for buildings. Rules for reinforced and unreinforced masonry*. British standards institution, London, UK.

BSI [2006a] *BS EN 1015-11:2019: Methods of test for mortar for masonry. Determination of flexural and compressive strength of hardened mortar*. British standards institution, London, UK.

BSI [2006b] *BS EN 300:2006: Oriented strand board (OSB). Definitions, classification and specifications*. British standards institution, London, UK.

BSI [2011] *BS EN 772-1:2011: Methods of test for masonry units. Determination of compressive strength*. British standards institution, London, UK.

BSI [2016] *BS EN 14081-1:2016: Timber structures. Strength graded structural timber with rectangular cross section. General requirements*. British standards institution, London, UK.

Calderini, C., Lagomarsino, S. Rossi, M. [2015] "Shaking table tests of an arch-pillars system and design of strengthening by the use of tie-rods". *Bulletin of Earthquake Engineering*, 13(1): 279–297.

Calderini, C., Piccardo, P. Vecchiattini, R. [2019] "Experimental characterization of ancient metal tie-rods in historic masonry buildings". *International Journal of Architectural Heritage*, 13(3): 425–437.

Cardoso, R., Lopes, M., Bento, R. [2004] "Earthquake resistant structures of Portuguese old 'pombalino' buildings". *Proceedings of the 13th WCEE, Vancouver, BC, Canada*, Paper No. 918.

Celik, O., Sesigur, H. Cili, F. [2009] "Importance of wood and iron tension members on seismic performance of historic masonry buildings: three case studies from Turkey". *SEI Conference on Improving the Seismic Performance of Existing Buildings and Other Structures*, San Francisco, CA, USA, pp. 1374–1383.

Countryman, D. [1952] "Lateral Tests on Plywood Sheathed Diaphragms": *Laboratory Report No. 55*. Douglas Fir Plywood Association, Tacoma, WA, USA.

Crowley, H., Pinho, R., van Elk, J, Uilenreef, J. [2018] "Probabilistic damage assessment of buildings due to induced seismicity". *Bulletin of Earthquake Engineering*, 17(8): 4495–4516.

D'Ambrisi, A., Mezzi, M. Caporale, A. [2013] "Experimental investigation on polymeric net-RCM reinforced masonry panels". *Composite Structures*, 105: 207–215.

Damiani, N., Miglietta, M., Mazzella L., Grottoli, L., Guerrini, G., Graziotti, F. [2019] "Full-scale Shaking Table Test on A Dutch URM Cavity-Wall Terraced-House end Unit – A Retrofit Solution with Strong-Backs and OSB Boards – EUC-BUILD-7". *Research report EUC052/2019U*, Eucentre foundation, Pavia, Italy.

Darbhanzi, A., Marefat, M.S., Khanmohammadi, M. [2014] "Investigation of in-plane seismic retrofit of unreinforced masonry walls by means of vertical steel ties". *Construction and Building Materials* 52: 122–129.

Derakhshan, H., Lucas, W., Visintin, P., Griffith, M.C. [2018] "Laboratory testing of strengthened cavity unreinforced masonry walls". *Journal of Structural Engineering*, 144(3): 04018005.

Dizhur, D., Giaretton, M., Giongo, I., Ingham, J.M. [2017] "Seismic retrofit of masonry walls using timber strong-backs". *SESOC Journal*, 30(2): 1–30.

Eucentre (2022) See http://www.eucentre.it/nam-project.

ElGawady, M.A., Lestuzzi, P., Badoux, M. [2007] "Static cyclic response of masonry walls retrofitted with fiber-reinforced polymers". *Journal of Composites for Construction*, 11(1): 50–61.

Damiani, N., Miglietta, M., Mazzella, L., Grottoli, L., Guerrini, G., Graziotti, F. [2019] "Full-scale shaking table test on a Dutch URM cavity-wall terraced-house end unit - a retrofit solution with strong-backs and OSB boards - EUC-BUILD-7". *Research report EUC052/2019U*, EUCENTRE foundation, Pavia, ITA,. www.eucentre.it/nam-project.

Facconi, L., Conforti, A., Minelli, F. Plizzari, G.A. [2015] "Improving shear strength of unreinforced masonry walls by nano-reinforced fibrous mortar coating". *Materials and Structures*, 48(8): 2557–2574.

Farooq, S.H., Ilyas, M., Ghaffar, A. [2006] "Technique for strengthening of masonry wall panels using steel strips". *Asian Journal of Civil Engineering (Building and Housing)*, 7(6): 621–638.

Galati, N., Tumialan, G., Nanni, A. [2006] "Strengthening with FRP bars of URM walls subject to out-of-plane loads". *Construction and Building Materials* 20(1–2): 101–110.

Giaretton, M., Dizhur, D., Ingham, J.M. [2016] "Shaking table testing of as-built and retrofitted clay brick URM cavity-walls". *Engineering Structures*, 125: 70–79.

Giaretton, M., Dizhur, D., Garbin, E., Ingham, J., da Porto, F. [2018] "In-plane strengthening of clay brick and block masonry walls using textile-reinforced mortar". *Journal of Composites for Construction*, 22(5): 04018028.

Giongo, I., Schiro, G., Piazza, M. [2017]" On the use of timber-based panels for the seismic retrofit of masonry structures". *Proceedings of Prohitech 3rd International Conference on Protection of Historical Constructions*, Lisbon, Portugal.

Graziotti, F., Penna, A., Magenes G [2014] "Influence of timber lintels on the cyclic behaviour of stone masonry spandrels". *Proceedings of International Masonry Conference*, Guimarães, Portugal.

Graziotti, F., Rossi, A., Mandirola, M., Penna, A., Magenes, G. [2016] "Experimental characterisation of calcium-silicate brick masonry for seismic assessment". *Proceedings of the 16th International Brick and Block Masonry Conference*, IBMAC, Padua, Italy, pp. 1619–1628.

Graziotti, F., Penna, A., Magenes G., [2018] "A comprehensive in situ and laboratory testing programme supporting seismic risk analysis of URM buildings subjected to induced earthquakes". *Bulletin of Earthquake Engineering*, 17(8): 4575–4599.

Gülkan, P., Langenbach, R. [2004] "The earthquake resistance of traditional timber and masonry dwellings in Turkey". *Proceedings of 13th WCEE*, Vancouver, BC, Canada, Paper No. 2297.

Hilti (2019) Hilti Technical Datasheet: HIT-RE 500 V3 Injection Mortar. Hilti, Schaan, Liechtenstein.

Horton Jr., J.W., Williams, R.A. (2012) "The 2011 Virginia earthquake: What are scientists learning?". *Eos*, 93(33): 317–318.

Ismail, N., Ingham, J.M. [2012] "Cyclic out-of-plane behavior of slender clay brick masonry walls seismically strengthened using posttensioning". *Journal of Structural Engineering*, 138(10): 1255–1266.

Ismail, N., Ingham, J.M. [2016] "In-plane and out-of-plane testing of unreinforced masonry walls strengthened using polymer textile reinforced mortar". *Engineering Structures*, 118: 167–177.

Jacobsen, L.S. [1960] "Damping in composite structures". *Proceedings of the 2nd World Conference on Earthquake Engineering*, Tokyo and Kyoto, Japan. vol. 2, pp. 1029–1044.

Kadam, S.B., Singh, Y., Li, B. [2015] "Out-of-plane behaviour of unreinforced masonry strengthened using ferrocement overlay". *Materials and Structures*, 48(10): 3187–3203.

Kariou, F.A., Triantafyllou, S.P., Bournas, D.A., Koutas, J.N. [2018] "Out-of-plane response of masonry walls strengthened using textile-mortar system". *Construction and Building Materials* 165: 769–781.

Kouris, L.A.S., Kappos, A.J. [2012] "Detailed and simplified non-linear models for timber-framed masonry structures". *Journal of Cultural Heritage*, 13(1): 47–58.

Laursen, P.T., Ingham, J.M. [2001] "Structural testing of single-storey post-tensioned concrete masonry walls. *The Masonry Society Journal*, 19(1): 69–82.

Luccioni, B., Rougier, V.C. [2011] "In-plane retrofitting of masonry panels with fibre reinforced composite materials". *Construction and Building Materials*, 25(4): 1772-1788.

Ma, R., Jiang, L., He, M. Fang, C., Liang, F. [2012] "Experimental investigations on masonry structures using external prestressing techniques for improving seismic performance". *Engineering structures*, 42: 297-307.

Magenes, G., Calvi, GM. [1997] "In-plane seismic response of brick masonry walls". *Earthquake engineering and structural dynamics*, 26(11): 1091-1112.

Mantegazza, G., Gatti, A., Barbieri, A. [2006]. Retrofitting concrete and masonry building: FRCM (fiber reinforced cementitious matrix) a new emerging technology. *Proceeding of the 12th Konferencja Naukowo-Techniczna Problemy Remontowe W Budownictwie Ogólnym i Obiektach Zabytkowych. REMO*, pp. 6-8.

Marcari, G., Manfredi, G., Prota, A., Pecce, M. [2007] "In-plane shear performance of masonry panels strengthened with FRP". *Composites Part B: Engineering*, 38(7-8): 887-901.

Meireles, H., Bento, R., Cattari, S., Lagomarsino, S. [2012] "A hysteretic model for "frontal" walls in pombalino buildings". *Bulletin of Earthquake Engineering*, 10(5): 1481-1502.

Miglietta, M., Mazzella, L., Grottoli, L., Guerrini, G., Graziotti, F. [2018] "Full-scale shaking table test on a Dutch URM cavity-wall terraced-house end unit – EUC-BUILD-6". *Research report EUC160/2018U*, Eucentre foundation, Pavia, Italy..

MIT [2018] *Norme tecniche per le costruzioni*. Ministero Infrastrutture e Trasporti, Italy.

Morandi, P., Albanesi, L., Graziotti, F., Lipiani, T., Penna, A., Magenes, G. [2018] "Development of a dataset on the in-plane experimental response of URM piers with bricks and blocks". *Construction and Building Materials*, 190: 593-611.

Moreira, S., Ramos, L.F., Oliveira, D.V., Lourenço P.B. [2014] "Experimental behavior of masonry wall-to-timber elements connections strengthened with injection anchors". *Engineering Structures*, 81, 98-109.

Moreira, S., Ramos, L.F., Oliveira, D.V., Lourenço P.B. [2016] "Design parameters for seismically retrofitted masonry-to-timber connections: injection anchors". *International Journal of Architectural Heritage*, 10(2-3), 217-234.

Mosallam, A., Banerjee, S. [2011] "Enhancement in in-plane shear capacity of unreinforced masonry (URM) walls strengthened with fiber reinforced polymer composites". *Composites Part B: Engineering*, 42(6): 1657-1670.

Papanicolaou, C., Triantafillou, T., Lekka, M. [2011] "Externally bonded grids as strengthening and seismic retrofitting materials of masonry panels". *Construction and Building Materials*, 25(2): 504-514.

Podestà, S., Scandolo, L. [2019] "Earthquakes and Tie-Rods: Assessment, Design, and Ductility Issues". *International Journal of Architectural Heritage*, 13(3): 329–339.

Popehn, J.R.B., Schultz, A.E., Drake, C.R. [2007] "Behavior of slender, posttensioned masonry walls under transverse loading". *Journal of Structural Engineering*, 133(11): 1541-1550.

Prota, A., Marcari, G., Fabbrocino, G., Manfredi, G., Aldea, C. [2006] "Experimental in-plane behavior of tuff masonry strengthened with cementitious matrix–grid composites". *Journal of Composites for Construction*, 10(3): 223-233.

Riccadonna, D., Giongo, I., Schiro, G., Rizzi, E., Parisi, M.A. [2019] "Experimental shear testing of timber-masonry dry connections for the seismic retrofit of unreinforced masonry shear walls". *Construction and Building Materials*, 211: 52-72.

Rothoblaas [2015] *Wood connectors and timber plates, Screws for wood*. https://www.rothoblaas.com/catalogue-rothoblaas

Seible, F., Igarashi, A. [1991] "Full scale testing of masonry structures under simulated seismic loadings". In: *Experimental and numerical methods in earthquake engineering*: Kluwer Academic Publishing, Dordrecht, the Netherlands, pp. 119–148..

Senaldi, I., Guerrini, G., Caruso, M., Graziotti, F., Magenes, G., Beyer, K., Penna, A. [2019] "Experimental Seismic Response of a Half-Scale Stone Masonry Building Aggregate: Effects of Retrofit Strategies". In: *Structural Analysis of Historical Constructions*. Springer, Cham, Switzerland: 1372-1381.

Sustersic, I., Dujic, B. [2014] "Seismic Shaking Table Testing of a Reinforced Concrete Frame with Masonry Infill Strengthened with Cross Laminated Timber Panels". *Proceedings of the World Conference on Timber Engineering (WCTE 2014)*, Quebec City, Canada.

Taghdi, M., Bruneau, M. Saatcioglu, M. [2000] "Seismic retrofitting of low-rise masonry and concrete walls using steel strips". *Journal of Structural Engineering*, 126(9): 1017-1025.

Tobriner, S. [1983] "La casa baraccata: Earthquake-resistant construction in 18th-Century Calabria". *Journal of the Society of Architectural Historians*, 42(2): 131-138.

Tomaževič, M., Gams, M., Berset, T. [2015] "Strengthening of stone masonry walls with composite reinforced coatings". *Bulletin of earthquake engineering*, 13(7): 2003-2027.

Valluzzi, MR. [2007] "On the vulnerability of historical masonry structures: analysis and mitigation". *Materials and Structures*, 40(7), 723-743.

Vintzileou" Effect of timber ties on the behavior of historic masonry". *Journal of Structural Engineering*, 134(6): 961-972.

Wight, G.D., Ingham, J.M., Kowalsky, M.J. [2006] "Shake-table testing of rectangular post-tensioned concrete masonry walls". *ACI Structural Journal*, 103(4): 587.

Willis, C.R., Seracino, R. Griffith, M.C. [2010] "Out-of-plane strength of brick masonry retrofitted with horizontal NSM CFRP strips". *Engineering structures*, 32(2): 547-555.

Yardim, Y., Lalaj, O. [2016] "Shear strengthening of unreinforced masonry wall with different fiber reinforced mortar jacketing". *Construction and Building Materials*, 102: 149-154.

3.FULL-SCALE SHAKE-TABLE TESTS ON TWO UNREINFORCED MASONRY CAVITY-WALL BUILDINGS: EFFECT OF AN INNOVATIVE TIMBER RETROFIT SYSTEM

In *Bulletin of Earthquake Engineering*, 19(6), 2561-2596.

ABSTRACT

Two full-scale building specimens were tested on the shake-table at the EUCENTRE Foundation laboratories in Pavia (Italy), to assess the effectiveness of an innovative timber retrofit solution, within a comprehensive research campaign on the seismic vulnerability of existing Dutch unreinforced masonry structures. The buildings represented the end-unit of a two-storey terraced house typical of the North-Eastern Netherlands, a region affected by induced seismicity over the last few decades. This building typology is particularly vulnerable to earthquake excitation due to lack of seismic details and irregular distribution of large openings in masonry walls. Both specimens were built with the same geometry. Their structural system consisted of cavity walls, with interior load-bearing calcium-silicate leaf and exterior clay veneer, and included a first-floor reinforced concrete slab, a second-floor timber framing, and a roof timber structure supported by masonry gables. A timber retrofit was designed and installed inside the second specimen, providing an innovative sustainable, lightweight, reversible, and cost-effective technique, which could be extensively applied to actual buildings. Timber frames were connected to the interior surface of the masonry walls and completed by oriented strands boards nailed to them. The second-floor timber diaphragm was stiffened and strengthened by a layer of oriented-strand boards, nailed to the existing joists and to additional blocking elements through the existing planks. These interventions resulted also in improved wall-to-diaphragm connections with the inner leaf at both floors, while steel ties were added between the cavity-wall leaves. The application of the retrofit system favoured a global response of the building with increased lateral capacities of the masonry walls. This paper describes in detail the bare and retrofitted specimens, compares the experimental results obtained through similar incremental dynamic shake-table test protocols up to near-collapse conditions, and identifies damage states and damage limits associated with displacements and deformations.

Keywords: Brick masonry cavity walls, Flexible diaphragm; Timber retrofit; Seismic performance, Damage states, Full-scale shake-table test.

3.1 INTRODUCTION

During the last few decades, gas extraction activities have exposed the region of Groningen, in the North-East area of The Netherlands, to induced seismicity. The affected area includes a stock of about 250.000 buildings, mainly consisting of unreinforced masonry (URM) structures not specifically designed for seismic resistance [Arup 2020]. Following a series of low-intensity earthquake events which caused minor, yet diffuse damage in the region, a comprehensive research project was conceived to assess and eventually mitigate the local seismic risk [Dost *et al.*, 2012; Dost and Kraaijpoel, 2013; Bommer *et al.*, 2016]. Within this framework, the seismic hazard [Bourne *et al.*, 2015], the local building stock fragility and fatality models [Crowley *et al.*, 2017, 2019] and the associated seismic risk [van Elk *et al.*, 2019] were to be analyzed and quantified.

Understanding the response of the local building stock to ground motions is essential for a complete regional seismic risk assessment. However, no specific studies or empirical data on Dutch buildings were available until 2014, since the country was not historically prone to natural seismicity. Therefore, an extensive experimental and numerical campaign was launched at the EUCENTRE Foundation laboratories (Pavia, Italy), to investigate the seismic behavior of Dutch URM buildings and to support the development of the regional seismic risk model. The campaign included static or quasi-static tests on materials, masonry assemblies, and structural components, as well as dynamic shake-table tests on full-scale buildings and subsystems [Graziotti *et al.*, 2019a, b], numerical simulations, and analytical formulations [Malomo *et al.*, 2018; Kallioras *et al.*, 2019; Tomassetti *et al.*, 2018]. Experimental tests were also conducted in parallel at the Delft University of Technology [Jafari *et al.*, 2017; Rots *et al.*, 2017; Esposito *et al.*, 2019].

Two-storey terraced houses built in the late '70s–early '80s (Figure 3.1) constitute one of the most common and earthquake-vulnerable building typologies within the Groningen region. This residential typology combines structurally-independent adjacent units, with discontinuous floors and roofs usually supported by single-wythe calcium-silicate (CS) walls. Since party walls consist of two independent CS leaves, each unit is structurally separated from the adjacent ones. A structural unit has typical dimensions of 5-to-6 m in the longitudinal direction, parallel to the front and back façades, and 7-to-9 m in the transverse one. The entire building is commonly enveloped by a continuous single-wythe clay (CL) veneer. The resulting cavity walls then consist of an inner CS leaf with load-bearing function and an outer CL veneer with architectural and insulation purposes, separated by an 80-mm air gap and connected with each other by steel ties. Large openings are irregularly distributed on the front and back façades. The first floor is typically built with precast reinforced concrete (RC) panels, completed by a cast-in-place topping slab. The second floor can be either a RC concrete slab or a timber structure. The roof usually consists of timber joists and planks, supported by CS masonry gables extending up from the transverse walls.

After a series of shake-table tests on a full-scale prototype and on subassemblies of a two-storey terraced-house end-unit with reinforced concrete slabs at both floors [Graziotti *et al.*, 2017; Tomassetti *et al.,* 2019a, b], information was still missing about the effects of highly irregular opening distributions and second-floor flexible timber diaphragms. Moreover, the development of an innovative sustainable, lightweight, reversible, and cost-effective retrofit technique appeared necessary, to tackle the sources of vulnerability proper of this specific building typology. Therefore, two identical full-scale specimens, representing the end-unit of a typical two-storey terraced house, with unfavorable construction details, were designed, built, and tested on the shake-table of the EUCENTRE Foundation. The first specimen was subjected to an incremental unidirectional ground-motion sequence up to its near-collapse limit state in June 2018, aiming to define its dynamic response and damage evolution without any retrofit intervention [Miglietta *et al.*, 2019]. The second building was retrofitted with an innovative timber system while in pristine conditions, then tested starting with the same protocol and up to twice the input acceleration amplitude during December 2018 [Damiani *et al.*, 2019].

This paper describes in detail the bare and retrofitted specimens, compares the two experimental dynamic responses up to near-collapse conditions, and identifies damage states and damage limits associated with displacements and deformations. All test results are available for free and can be downloaded upon request from http://www.eucentre.it/nam-project. Further details on the shared data can be found in Miglietta *et al.*, [2019].

Figure 3.1 Typical terraced house of the Groningen area: (a) front façade; (b) lateral façade.

3.2 CHARACTERISTICS OF THE SPECIMENS

3.2.1 General Overview

Both building specimens represented the end-unit of a Dutch two-storey URM cavity-wall terraced house of the late '70s–early '80s (Figure 3.1). The transverse walls of terraced houses generally do not present openings, except for some end-unit gables (Figure 3.1b), and can resist significant in-plane lateral forces. Given the high amount of openings in the front and back façades, these buildings are therefore more flexible and vulnerable in the longitudinal direction. The horizontal structures of adjacent units are discontinuous and

rest only on CS party walls, consisting of two independent CS leaves, making each unit structurally separated from the other ones. For these reasons, an individual end-unit prototype (Figure 3.2) could be easily isolated from the terraced house and tested uniaxially in the North-South direction, with the East and West longitudinal walls excited in their planes and the North and South transverse walls out-of-plane.

The plan dimensions were adapted to fit within the shake-table (Figure 3.3, Figure 3.4): in particular, the transverse length was reduced to 5.58 m, while the longitudinal one was set at 5.94 m. A total height of 7.83 m to the roof ridge was chosen. The first-floor RC slab and the second-floor timber joists spanned in the North-South direction, supported by the two transverse CS walls. Staircase openings were obtained in both floor diaphragms next to the North wall (Figure 3.4b, c). Two gables extending above the transverse walls supported a 39°-pitch timber roof, with joists spanning in the North-South direction. The roof was finished by battens, counter-battens, and clay tiles. Some timber frames and shutters were also installed in window openings, to study the damage to non-structural elements. The specimens were built directly on a composite steel-concrete foundation, fastened to the shake-table.

The experimental seismic behaviour of the bare specimen formed the basis of the retrofit concept and design. In particular, lack of connections between masonry walls and floors did not allow the development of a global seismic response, and a local mechanism resulted in the second-floor timber diaphragm sliding above the second-storey piers (see Sect. 4.2). The main objective of the proposed solution was to promote a box-type global response, by improving connections throughout the structure [Magenes *et al.*, 2014; Guerrini *et al.*, 2019; Senaldi *et al.*, 2020], enhancing in-plane and out-of-plane wall capacities, and stiffening the second-floor and roof flexible timber diaphragms [Senaldi *et al.*, 2014]. Moreover, desired features of the retrofit system were: (1) its sustainability, which led to the choice of timber as the main retrofit material; (2) its limited weight, promoted by using timber frames and oriented-strand board (OSB) panels rather than solid hardwood or glulam panels; (3) its reversibility, pursued by adopting dry connections between timber elements and existing masonry; and (4) its cost-effectiveness, associated with its ease of construction.

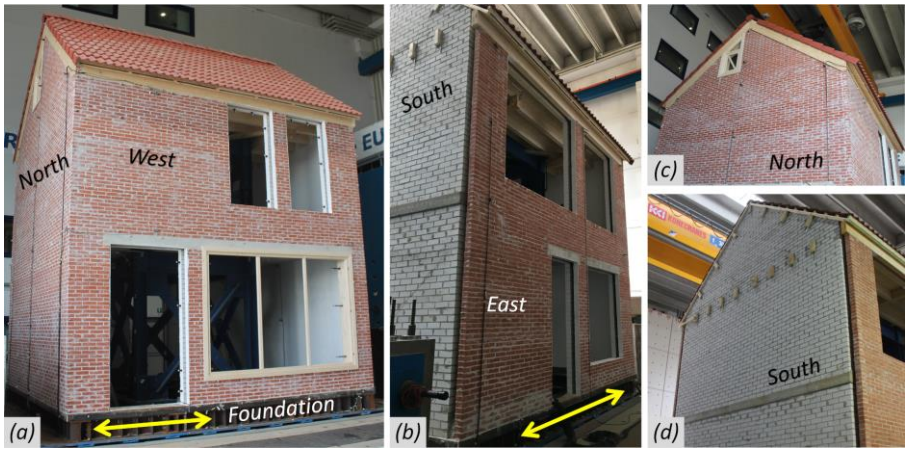

Figure 3.2 Overall photos of the specimens: (a) North and West façades; (b) South and East façades; (c) North façade; (d) South façade. Shaking direction indicated by yellow arrows.

3.2.2 Details of the bare structure

The structural details replicated common features of the Dutch two-storey URM cavity-wall terraced houses of the late '70s–early '80s. The masonry consisted of a single-wythe, 102-mm-thick CS inner leaf and a single-wythe, 100-mm-thick CL outer leaf, separated by a gap of approximately 80 mm (Figure 3.3, Figure 3.4). The CS bricks had dimensions of 212 × 102 × 71 mm while the CL bricks of 210 × 100 × 50 mm; mortar joints had thickness of 10 mm in both leaves. Only the inner CS leaf was continuous along the entire perimeter of the house; the outer CL leaf was not present on the South side, as in reality the adjacent residential unit would border with it (Figure 3.2, Figure 3.4). Steel ties granted connection between inner and outer leaves, distributed as shown in Figure 3.3 with a density of approximately 1 tie/m^2. This tie density was deemed representative of lower-bound conditions for the Groningen area, excluding cases of extreme and total corrosion. These ties had a diameter of 3.4 mm and a length of 200 mm. They were embedded in the horizontal mortar bed-joints during construction of the walls. The hooked end extended within the inner leaf for 60 mm, while the bent end was embedded in the CL veneers for 60 mm (Figure 3.5a).

Four pairs of precast reinforced concrete lintels were placed above the first-storey openings, supported for 100 mm on the masonry walls at each end (Figure 3.3a, b, Figure 3.5b). The lintels for the CS leaf had cross-section dimensions of 100 × 150 mm, corresponding to the height of two brick courses and one mortar joint, while those for the CL leaf had dimensions of 100 × 170 mm, as the height of three brick courses and two mortar joints.

The first floor consisted of a 160-mm-thick RC slab, reproducing the mass contributed by a hollow-core RC floor structure and by superimposed dead and live loads. The thickness was locally reduced to 150 mm over a 140-mm-wide strip along the perimeter, to match the height of two CS bricks and a horizontal mortar joint. The slab was monolithically precast aside and subsequently placed on a mortar layer above the CS masonry leaves. It rested on the North and South walls only, while a gap was left atop the East and West walls: this operation was intended to load the transverse walls, without applying any direct overburden to the longitudinal ones in static conditions (Figure 3.5c). The gap was then filled with mortar, after exhaustion of concrete creep deformations. Four 0.45 × 0.55-m holes were created in the RC slab, to fit a steel frame with collapse-safety and displacement reference functions (Figure 3.4b).

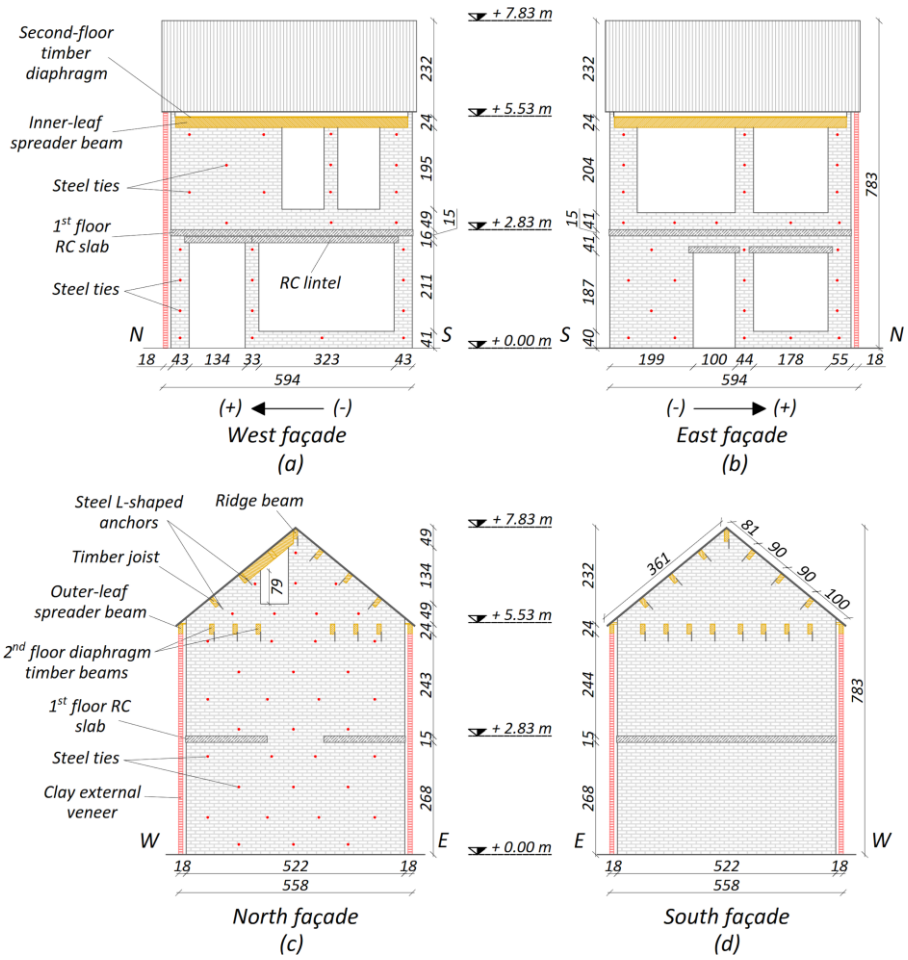

Figure 3.3 Elevations of the load-bearing CS inner leaves from the outside: (a) West façade, (b) East façade, (c) North façade, (d) South façade. Units of cm.

The second floor was made of 185 × 18-mm tongue-and-groove planks supported by eight 100 × 240-mm timber joists, spanning continuously between the North and South CS walls with an average center-to-center spacing of 600 mm (Figure 3.4c). Two pairs of 100 × 240-mm timber spreader beams were placed above the inner and outer leaves of the East and West façades, serving also as lintels for the second-storey openings (Figure 3.2, Figure 3.3, Figure 3.4). The planks were fastened to the joists by two 2-mm-diameter, 60-mm-long nails at each intersection. Four 0.45 × 0.75-m holes were provided to accommodate the safety and reference steel frame. 235 × 245-mm L-shape steel anchors, with a diameter of 14 mm, were fastened to each joist end by three 5-mm-diameter timber screws, passed through the CS wall, and bore against the exterior surface of the CS leaf, enhancing the wall-to-diaphragm connection (Figure 3.3c, d, Figure 3.5d).

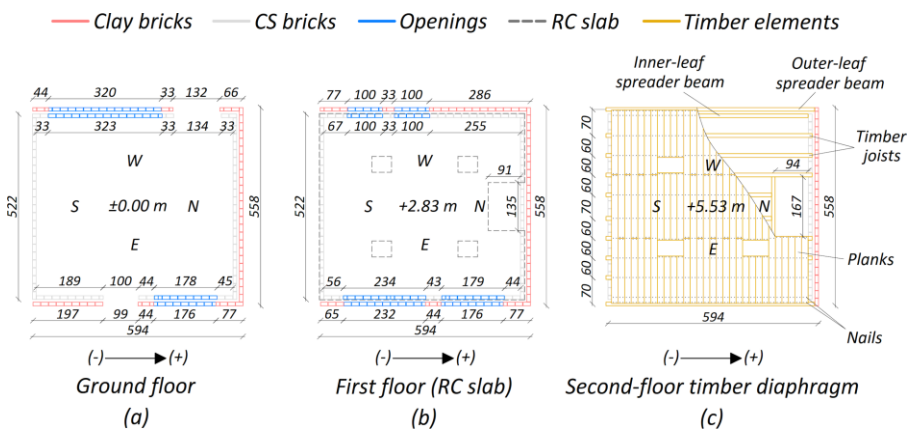

Figure 3.4 Plan views of the bare structure: (a) ground floor; (b) first-floor RC slab; (c) second-floor timber framing. Units of cm.

A 1.35 × 0.91-m staircase opening was provided on the North side of the RC slab (Figure 3.4b). Similarly, a 1.67 × 0.94-m hole was provided in the timber floor, with a transverse 100 × 240-mm timber beam supporting the joists interrupted by the opening (Figure 3.4c, Figure 3.5e); timber-to-timber connections were obtained with steel hangers fastened to the joists. The staircase holes left that region of the North CS wall locally unrestrained against out-of-plane actions and free from direct vertical loads except for those applied by the roof. The dimensions of these openings were chosen to allow continuity of the steel reinforcement or of the timber joists, while accommodating four additional holes in the diaphragms.

Two gables extended above the transverse North and South façades, supporting a 39° pitched timber roof. Openings can be frequently observed in the end-unit gables of typical terraced house of the Groningen region (Figure 3.1b). For this reason, the building prototype

presented a trapezoidal window at the top of the North side (Figure 3.2c, Figure 3.3c). A timber lintel, inclined as the roof pitches, provided support for the roof joist landing above the opening and was connected to them by the same steel hangers used for the staircase hole framing at the second floor (Figure 3.3c).

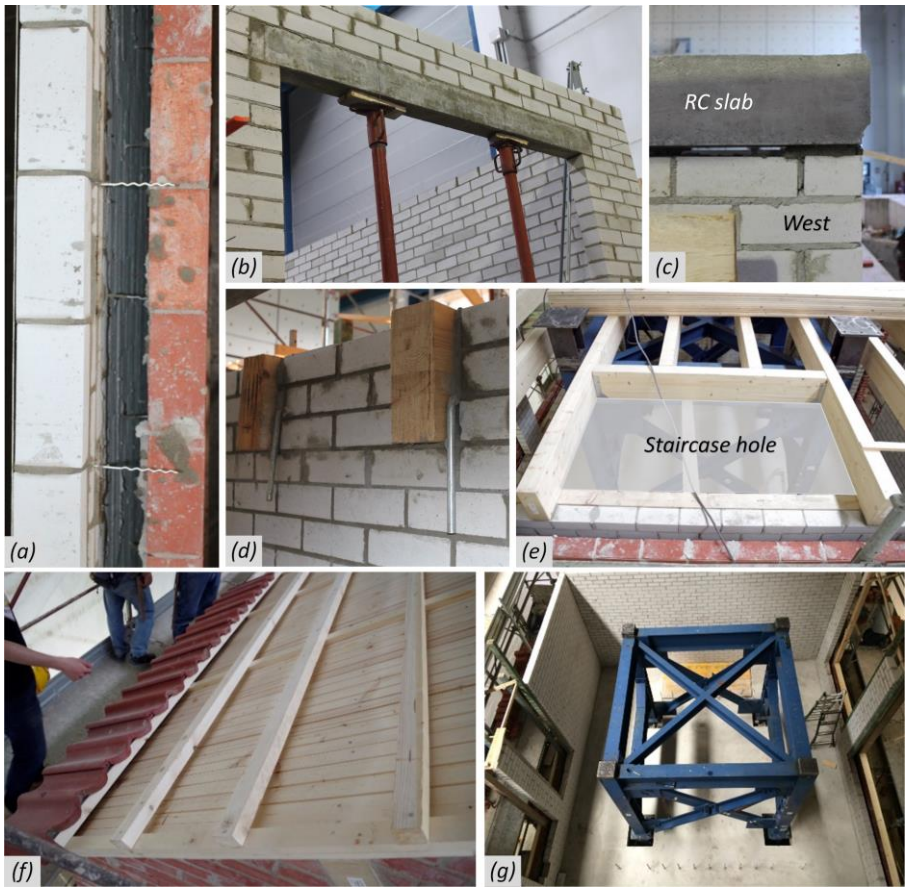

Figure 3.5 Bare structure construction photos: (a) top view of the cavity-wall section; (b) first-storey inner-leaf lintel; (c) first-floor RC slab connection detail above longitudinal CS leaves; (d) L-shape steel anchors between second-floor joists and transverse; (e) second-floor framing at staircase hole; (f) roof finishes; (g) internal steel rigid frame.

The timber roof structure consisted of a ridge-beam, two spreader beams above the longitudinal outer leaves (already mentioned in the second-floor description), and three intermediate joists on each side, with the same cross-section as the second-floor joists and spaced at approximately 0.9 m center-to-center (Figure 3.3c, d). Tongue-and-groove 185 × 20-mm planks were fastened with two 2-mm-diameter, 60-mm-long nails at each intersection with the roof joists. The connection between CS leaves and roof joists was

further improved by the same L-shape steel anchors used for the second-floor joists (Figure 3.3c, d, Figure 3.5d). The ridge beam and roof joists extended through the North façade CL outer leaf; two 20 × 240-mm timber cover plates hid their ends and were fastened to them by two 2-mmdiameter, 60-mm-long nails each (Figure 3.2c). However, two 6.5-mm-diameter, 240-mm-long screws, connected the cover plates to the spreader beams through the masonry leaf. Battens and counter-battens were nailed above the planks, while clay tiles completed the roof (Figure 3.5f).

Two window timber frames were installed in both building specimens: one in the large 3.23 × 2.11-m first-storey opening of the West façade, the other one in the North gable trapezoidal opening, as shown in Figure 3.2a, c. A 6-mm-thick anti-burst glass was provided to the southern shutter of the first-storey window. In the retrofitted specimen, a window frame was mounted also in one of the second-storey openings of the East-façade, because severe interstorey displacement demands were recorded at this location while testing the bare prototype.

A very stiff steel frame was firmly bolted to the shake-table, inside the building prototypes, with two main goals: providing a safety restraint in the event of partial or global collapse during the dynamic tests, and serving as a nearly rigid reference system to measure displacements with respect to the shake-table. The steel frame columns passed through four holes provided in both floor diaphragms (Figure 3.4, Figure 3.5g). Displacements allowances of ± 125 mm and ± 270 mm were left in the shaking direction at the first and second floor, respectively, and of ± 125 mm in the perpendicular one at both floors. Timber stoppers were provided to eventually absorb impacts. Loose steel cables connected the ridge-beam to the steel frame, preventing possible collapse of the roof which could severely damage the testing equipment. The cables allowed a maximum 200-mm displacement of the ridge-beam with respect to the steel frame in the North-South direction without interfering with the prototype response.

3.2.3 Details of the retrofit system

To match the objectives mentioned earlier, a timber retrofit solution was devised stemming from the out-of-plane strengthening of masonry piers investigated by Giaretton *et al.*, [2016], Dizhur *et al.*, [2017] and Cassol *et al.*, [2021], which relies on vertical timber posts working as "strong-backs" connected to the internal surface of the walls. The system was then extended to improve also the piers in-plane strength and displacement capacities, by adding horizontal nogging (or blocking) members between posts, and by nailing OSB panels to the resulting frame as done for timber shear-walls [AWC, 2008]. A preliminary study on the proposed system was carried out on two CS single-leaf piers, subjected to quasi-static in-plane shear-compression tests [Guerrini *et al.*, 2020].

Figure 6 shows the main details of the retrofit system installed on the second specimen. Top and bottom timber sill plates were provided along the entire wall lengths. Post-and-noggin frames were then built along the longitudinal East and West walls. Only vertical

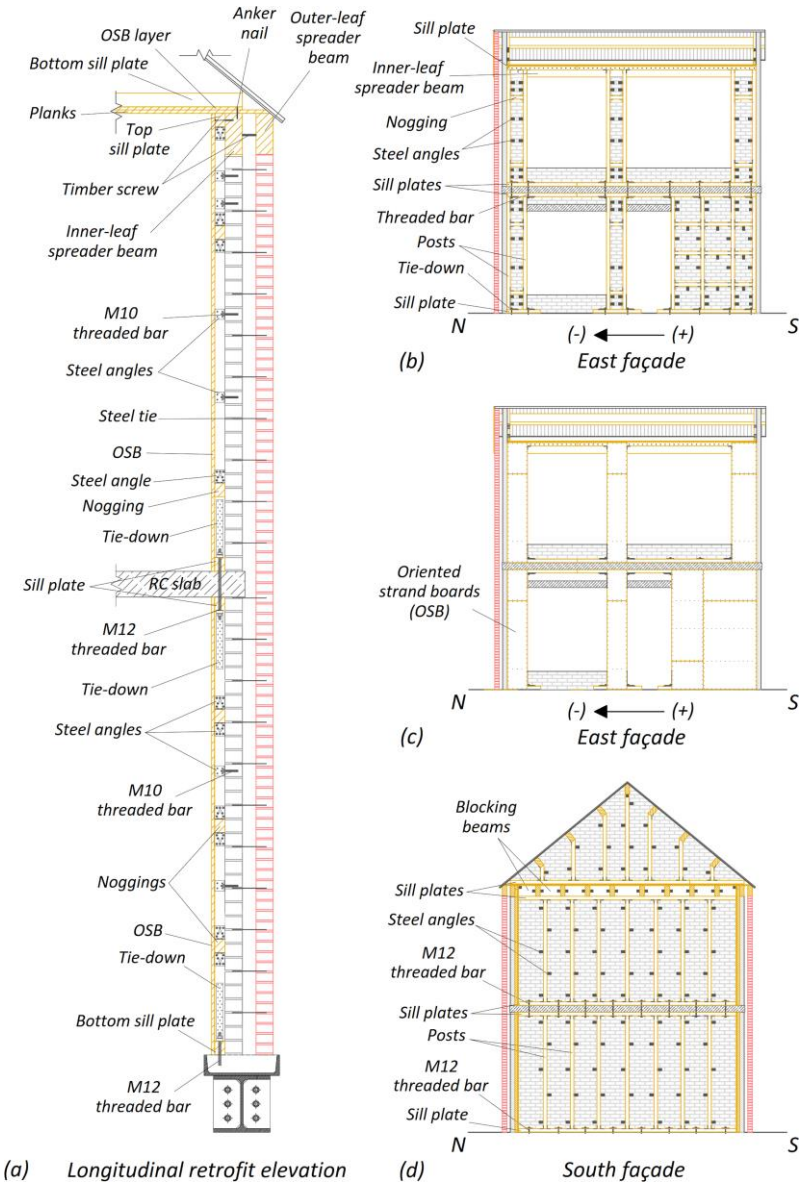

Figure 3.6 Retrofit system details: (a) vertical section of the typical longitudinal wall retrofit, (b) timber frame applied to the longitudinal East wall, (c) OSB panels nailed to the longitudinal East wall frame, (d) completed retrofit of the transverse South wall.

posts, without horizontal nogging, were used along the transverse North and South walls, where OSB panels were not applied. All timber elements had cross-sections of 80 × 60 mm, with the 60-mm side oriented perpendicular to the masonry walls. Timber posts were installed on the transverse and longitudinal sides at approximately 600-mm spacing, except for shorter slender piers, to achieve an in-plane strength increment of about 35% on the longest first-storey pier according to Guerrini *et al.*, [2020].

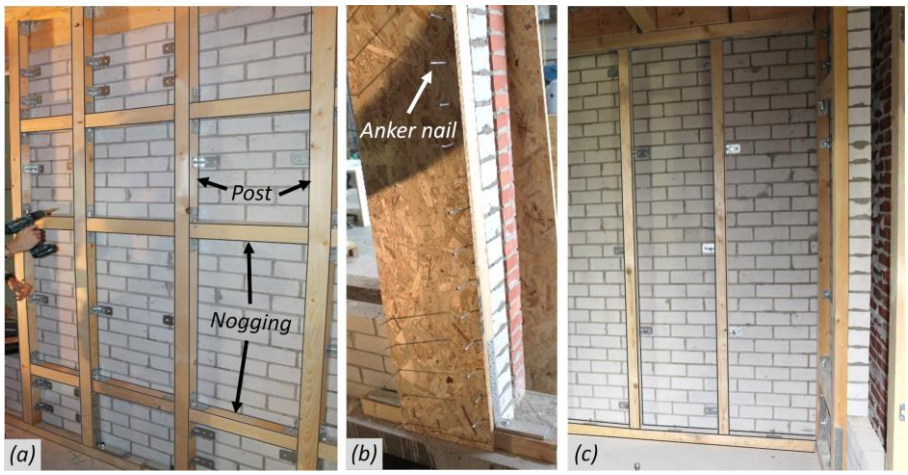

Figure 3.7 Retrofit system construction photos: a) longitudinal-wall timber frame, b) nailing of a OSB for in-plane strengthening of longitudinal walls, c) completed transverse walls retrofit not including OSB panels.

Posts and nogging members were connected to each other by 70 × 70-mm steel angles with cross-section of 55 × 2-mm, fastened to each timber element by five 5-mm-diameter, 70-mm-long screws (Figure 3.6a, Figure 3.7a). The frames were connected to the masonry through 90 × 50-mm steel angles, with cross-section of 50 × 3-mm, at 600-mm spacing for out-of-plane strengthening purposes [Giaretton *et al.*, 2016; Dizhur *et al.*, 2017]. The angles were fastened to timber by four 5-mm-diameter, 70-mm-long screws and to the masonry by M10 steel threaded bars of class 8.8 (Figure 3.6a, b, Figure 3.7a). These bars were anchored 50 mm inside the bricks with an epoxy adhesive.

Along the longitudinal East and West walls, 18-mm-thick OSB panels were applied to the timber frames with 4-mm-diameter, 75-mm-long anker nails, spaced at 100 mm along all edge and intermediate overlapping (Figure 3.6c, Figure 3.7b). These panels were intended to increase the in-plane shear resistance of piers. Nogging elements and OSB panels were not mounted on the transverse North and South masonry walls, which offered a significant in-plane resistance to lateral loads and were strengthened only for out-of-plane action (Figure 3.6d, Figure 3.7c). Moreover, coupling between inner and outer leaves was improved by building the second specimen with a tie density of approximately 5 ties/m2

(Figure 3.6a); in real applications, ties can be added by drilling through the masonry leaves and fastening new connectors to them before installation of the timber elements. This operation aimed at a better exploitation of the outer CL leaf structural resistance.

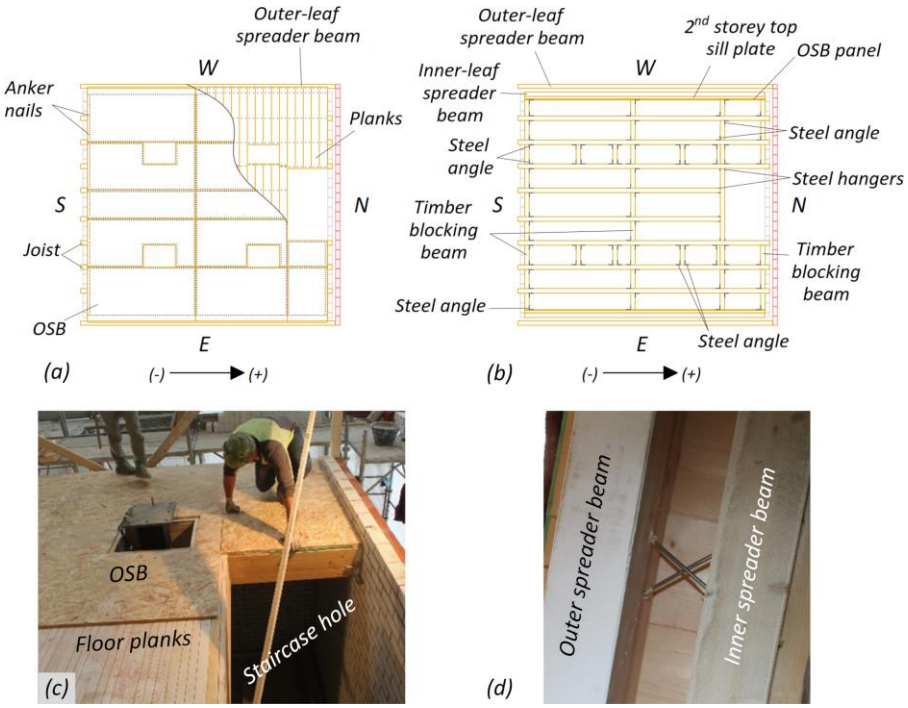

Figure 3.8 Second-floor diaphragm retrofit details: (a) OSB layout; (b) joists and blocking beams layout; (c) installation of OSB; (d) view from below of the connection between inner- and outer-leaf spreader beams.

In addition to the masonry wall retrofit, the second-floor timber diaphragm was stiffened and strengthened to transfer 50% of the seismic storey shear while preventing first cracking of the second-storey East-wall piers. 18-mm-thick OSB panels were nailed to the existing planks using the same anker nails spaced at 50 mm along all board edges (Figure 3.8a, c) following the American requirements for timber diaphragms [AWC 2008]. 100 × 240-mm timber blocking beams were inserted between existing joists, to allow fastening along board edges perpendicular to the timber joists (Figure 3.8b). Connection between blocking elements and joists was ensured by 70 × 70-mm steel angles with cross-section of 55 × 2-mm, fastened to each timber element by five 5-mm-diameter, 70-mm-long screws. Inner- and outer-leaf spreader beams were also connected to each other by pairs of diagonally crossing, 8-mm-diameter, 360-mm-long timber screws at 500-mm spacing (Figure 3.8d). This intervention promoted engagement of the outer CL leaf in the lateral resistance of the building.

The roof diaphragm was not retrofitted from the beginning on purpose. A detailed study on the gable-roof subsystem dynamic behaviour [Tomassetti *et al.*, 2019b] revealed that the displacement capacity of the timber roof is generally higher than the one associated with gable collapse. Therefore, only the masonry gables were initially retrofitted with timber posts for out-of-plane capacity, to investigate the response of the gable-roof system without the influence of a stiffened diaphragm. Loose diagonal steel cables, connecting the ridge beam to the second-floor joists, limited relative displacements to ± 200 mm. They were eventually tied during the latest test runs, when roof displacements became dangerously large, thus stiffening the inclined roof diaphragms in order to continue with the tests. Studying the response of the gable-roof system in two different retrofit conditions allowed the identification of a floor acceleration threshold that required roof stiffening.

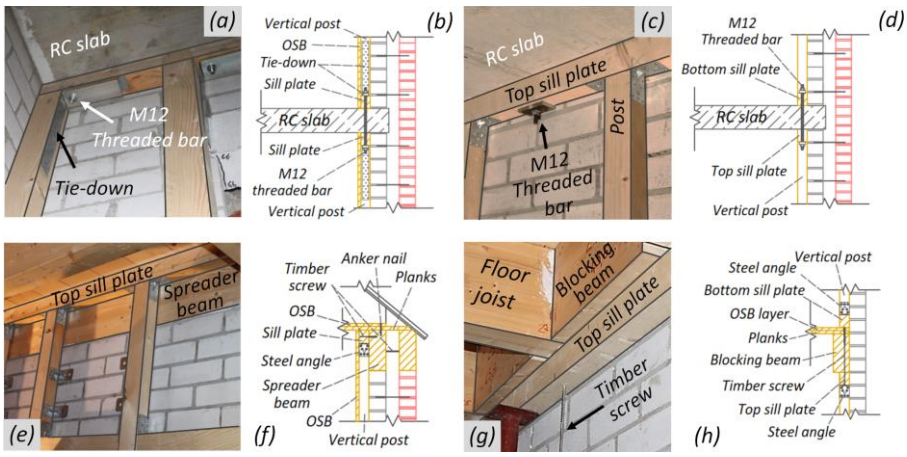

Figure 3.9 Retrofit system-to-floor connection details: (a, b) first-storey longitudinal-wall posts to RC slab; (c, d) transverse-wall sill plates to first-floor RC slab; (e, f) second-storey longitudinal-wall frame to inner-leaf spreader beam; (g, h) second-store

The longitudinal wall posts were anchored to the concrete foundation and to the first-floor diaphragm by steel tie-downs, to enhance the pier flexural resistance by providing tensile strength. One 340 × 182-mm, with cross-section of 40 × 2-mm-thick angle was fastened to each post by twelve 5-mm-diameter, 70-mm-long screws and to the concrete elements by class 8.8 M12 threaded bars bearing against the top or bottom sill plates (Figure 3.6a, b, Figure 3.9a, b). These bars developed into the foundation for 70 mm, bonded by an epoxy adhesive, while passed through the RC slab and connected together the first- and second-storey frames. In real applications, these connections can be installed independently above and below a given floor, as with the foundation. However, the dense reinforcement of the slab hampered the insertion of epoxy-bonded threaded bars. For this reason, holes were core-drilled through the slab, and passing bars were prestressed against the first-storey top and second-storey bottom sill plates. The applied prestressing force was capacity-designed

to prevent decompression at the interface between the sill plates and the slab, avoiding direct bending moment transfer between piers of different storeys.

The transverse North and South wall posts, instead, were fastened only to the top and bottom sill plates by pairs 70 × 70-mm steel angles with cross-section of 55 × 2-mm, fastened to each timber element by five 5-mm-diameter, 70-mm-long screws per element. The sill plates along the transverse walls were in turn anchored to the concrete foundation and RC slab by class 8.8, M12 threaded bars, with similar details as specified for the tie-down connections (Figure 3.6d, Figure 3.9c, d).

At the second-storey, top steel tie-downs could not be properly anchored to the timber diaphragm. For this reason, the second-storey longitudinal piers were assumed to behave as cantilevers, fixed at their bottom but not at their top. The longitudinal East and West posts were connected to the top sill plates by pairs of steel brackets, with similar details as used for the transverse wall posts; the sill plates were in turn fastened to the second-floor spreader beams with 6-mm-diameter, 110-mm-long screws at 100- mm spacing (Figure 3.9e, f). Along the transverse walls, the second-storey top sill plate and the gable bottom sill plate were connected to the timber diaphragm by 8-mm-diameter, 360-mm-long timber screws at 300-mm spacing; timber blocking beams were added between joists to accommodate these fasteners (Figure 3.9g, h). Gable posts were instead connected directly to the roof timber joists by 86 × 86-mm, 135°-bent steel angles, with cross-section of 40 × 3 mm, with six 5-mm-diameter, 70-mm-long screws per member.

Member sizes were chosen to reach a good compromise between structural efficiency and internal space saving. Connecting the timber frames to the masonry walls and to the floor diaphragms resulted also in improved wall-to-diaphragm connections, promoting a global box-type response. A detailed discussion on the design principles and analytical equations will be provided in a following paper focusing on the retrofit system mechanics.

The installation time and material cost of the masonry retrofit were estimated as 2.5 man-hours and €78, respectively, per square meter of wall surface, considering the net CS masonry area and market prices for Northern Italy. These values do not include the connection improvement between inner and outer leaves, which was obtained by building the specimen with an increased amount of steel ties. Similarly, the required time and material cost for the timber diaphragm retrofit were estimated as 0.6 man-hours and €17, respectively, per square meter of floor surface, excluding hole areas. It is interesting to note that the estimation of the retrofit material cost per square meter of wall surface considering the full-building specimen returns a value 40% less than the one obtained considering the retrofit applied to a single CS pier (approximately € 130 per square meter of wall surface, see par. 2.2.2). This because the single pier (EUC-COMP-2) was retrofitted to increase both in-plane and out-of-plane capacities, while in the retrofitted full-scale building only the longitudinal sides were retrofitted to increase both capacities, solid transversal walls were

retrofitted only to increase their out-of-plane capacity. As it can be observed in Figure 3.6, when the proposed timber system is applied to increase both in-plane and out-of-plane capacities of piers (Figure 3.6b and c), horizontal timber nogging elements are necessary to form the timber frame on which OSB can be nailed, as well as, a big amount of steel angles are necessary to connect horizontal and vertical elements. Differently, the application of the retrofit system for the sole improvement of the out-of-plane capacity of piers requires only vertical post, top and bottom sill plates, and a significantly less amount of steel angles. In accordance with these considerations, the cost estimated on the single CS pier per square meter of wall surface includes the in-plane and out-of-plane strengthening, while the cost estimated on the full-scale building is an average result related to the specific case. It is also worth to note that the full-scale building specimen EUC-BUILD-7 presented a total transversal wall area approximately equal to twice the longitudinal ones, therefore, the influence of the sole out-of-plane retrofit on the total cost estimation is prominent.

3.2.4 Masses

The average densities of CS and CL masonries were 1836 kg/m^3 and 1967 kg/m^3, respectively, for the bare specimen and 1862 kg/m^3 and 2072 kg/m^3 for the retrofitted one. Timber frame elements and OSB panels had densities of 517 kg/m^3 and 572 kg/m^3 respectively. The total mass of the bare building was 47.6 t, while the mass of the bare structure of the retrofitted specimen was 48.6 t. These values include a 1.2-t additional mass on the second-floor timber diaphragm, consisting of forty-eight 25-kg mortar bags to simulate the contributions of non-structural components and live loads. The retrofit system total mass was approximately 1.6 t, corresponding to 3% of the bare structure mass. This resulted in a 50.2-t mass for the strengthened specimen. Table 3.1 summarizes all mass contributions of the bare and retrofitted specimens.

3.2.5 Material mechanical properties

Characterization tests were performed at the Department of Civil Engineering and Architecture (DICAr) laboratory of the University of Pavia, Italy, to determine the mechanical properties of bricks, mortar, and masonry [Miglietta *et al.*, 2019].

Bending and compression tests were conducted on bricks and mortar samples according to EN 772-1 [CEN, 2015] and EN 1015-11 [CEN, 1999], to determine brick compressive (f_b) and tensile (f_{bt}) strengths, as well as mortar compressive (f_c) and tensile (f_t) strengths. Six masonry wallettes made of CS bricks and six made of CL bricks were tested in compression perpendicularly to the horizontal bed-joints, according to EN 1052-1 [CEN, 1998]; these tests allowed the determination of the masonry compressive strength (f_m) and the masonry secant elastic modulus at 33% of its compressive strength (E_m). Bond wrench tests on CS and CL masonry samples were performed in order to determine the bond strength of masonry (f_w), according to EN 1052-5 [CEN, 2005]. Specimens of both types of masonry were subjected to direct shear tests for the determination of cohesion or initial shear

strength (f_{v0}) and friction coefficient (μ), according to the guidelines given by EN 1052-3 [CEN, 2002].

Table 3.1 Prototype masses breakdown.

Component		Bare specimen [t]	Retrofitted specimen [t]
CS inner-leaf	North façade	6.0	6.2
	South façade	6.2	6.3
	West façade	2.8	2.8
	East façade	2.7	2.8
Clay veneers	North façade	7.1	7.5
	South façade	-	-
	West façade	3.4	3.5
	East façade	3.4	3.5
Floors	1st floor RC slab	11.2	11.2
	2nd floor timber structure	0.8	0.8
	Additional mass	1.2	1.2
Roof	Timber structure	0.7	0.7
	Tiles	2.1	2.1
	Total original structure	**47.6**	**48.6**
Timber retrofit system	North façade	-	0.20
	South façade	-	0.18
	West façade	-	0.43
	East façade	-	0.38
	2nd floor	-	0.45
	Total retrofit system	**-**	**1.64**
Total specimen		**47.6**	**50.2**

All characterization tests for masonry materials were performed at, or after, 28 days of maturation. Table 3.2 compares these values with the results obtained from in-situ testing on buildings in the Groningen, The Netherlands [Tondelli *et al.*, 2015]. It is worth noting that in-situ tests were conducted on different buildings; therefore, reported values of coefficient of variation (C.o.V.) are affected by both intra- and inter-building variability. Instead, the C.o.V. for the bare and retrofitted specimens include only intra-building variability.

The tensile ultimate capacity of the steel ties was determined as approximately 4.1 kN by TU Delft researchers [Esposito *et al.*, 2016; Messali *et al.*, 2016]. Their pull-out and push-in behaviour has been extensively analyzed by Arslan *et al.* [2020].

Concrete belonging to class C28/35 according to EN 206 [CEN, 2016a] and reinforcing steel with characteristic yield stress of 450 MPa formed the reinforced concrete first-floor slab and lintels. Glulam timber beams of class GL24h [CEN, 2013] and solid red fir planks were used to build the second floor and roof structures.

The timber frames used for the retrofit consisted of red solid fir (Picea-abies), belonging to class S10/C24 according to EN 14081-1 [CEN, 2016b]. They had characteristic compressive strength parallel to the fibers $f_{c,0}$ = 21 MPa, characteristic tensile strength parallel to the fibers $f_{t,0}$ = 14 MPa, and characteristic Young modulus $E_{0.05}$ = 7400 MPa. Oriented-strand-boards belonged to class OSB/3 according to EN 300 [CEN, 2006]. Only densities were determined at the DICAr laboratory.

Tie-down connections between timber posts and RC foundation or slab had characteristic tensile strength of 11.6 kN [Rothoblaas, 2015]. The epoxy adhesive characteristic tensile and shear strengths were respectively 41 kN and 20 kN when applied to 10-mm-diameter rods, 59 kN and 30 kN when applied to 12-mm-diameter rods. These values refer to embedment in uncracked concrete [Hilti, 2019].

3.3 TESTING PROTOCOL AND INSTRUMENTATION

3.3.1 Instrumentation

Several accelerometers and displacement transducers, installed inside and outside the buildings, monitored their responses. 46 accelerometers, with ranges of ± 2 g or ± 6 g, allowed measuring the total acceleration of the shake-table, masonry walls, first- and second-floor diaphragms, roof ridges, and rigid steel frame. A set of 15 wire potentiometers recorded out-of-plane displacements of the North and South façades (CS and CL leaves) with respect to the rigid frame while 5 wire potentiometers monitored in-plane deformations of the first-storey CS squat wall of the East façade. 4 wire potentiometers were added to monitor in-plane deformations of the second-storey CS squat wall of the West façade of the retrofitted building. 44 linear potentiometers were installed on both specimens to monitor floor displacements with respect to the rigid frame, and to record relative motion between structural elements. 30 linear potentiometers were added in the retrofitted building to record relative displacements of the strengthening system. Moreover, a 3D optical motion acquisition system was employed: passive reflective markers were attached to the external surface of the North, South and West clay walls, while 16 high-definition cameras recorded their trajectories. All recorded data are available for free and can be downloaded upon request at http://www.eucentre.it/nam-project. A detailed description of the sensor layout and of the data organization can be found in Miglietta *et al.*, [2019].

Table 3.2 Masonry mechanical properties of the bare and retrofitted prototype buildings. Comparison with estimates obtained from in-situ tests on buildings in the Groningen province [Tondelli *et al.*, 2015].

Material property [units]	Bare building				Retrofitted building				In-situ tests			
	Calcium-silicate		Clay		Calcium-silicate		Clay		Calcium-silicate (before 1985)		Clay (after 1945)	
	Avg.	C.o.V. [-]	Avg.	C.o.V. [-]	Avg.	C.o.V. [-]	Avg.	C.o.V. [-]	Avg.	C.o.V. [-]	Avg.	C.o.V. [-]
Density of bricks, ϱ_b [kg/m³]	1756	0.02	1994	0.01	Same batch				-	-	-	-
Density of masonry, ϱ [kg/m³]	1836	0.01	1967	0.01	1862	0.02	2072	0.02	-	-	-	-
Brick compressive strength, f_b [MPa]	19.8	0.18	50	0.1	Same batch				15.4	0.27	22.1	0.4
Brick tensile strength, f_{bt} [MPa]	2.5	0.09	8.8	0.08	Same batch				4.4	0.36	4.7	0.4
Mortar compressive strength, f_c [MPa]	5.1	0.24	2.4	0.47	4.0	0.41	3.0	0.38	-	-	-	-
Mortar tensile strength, f_t [MPa]	1.7	0.28	0.7	0.5	1.39	0.38	0.9	0.43	-	-	-	-
Masonry compressive strength, f_m [MPa]	10.1	0.06	11.6	0.29	10.0	0.11	17.6	0.21	10.8	0.37	15.1	0.47
Masonry Young's modulus, E_m [MPa]	6593	0.09	4436	0.44	7319	0.15	5686	0.31	7180	0.35	7140	0.48
Masonry bond strength, f_w [MPa]	0.28	0.32	0.24	0.52	0.33	0.37	0.14	0.59	0.18	0.33	0.43	0.51
Masonry (bed-joint) cohesion, f_{t0} [MPa]	0.62	-	0.30	-	0.49	-	0.18	-	0.14‡	0.71‡	0.45‡	0.57‡
Masonry (bed-joint) friction coeff., μ [-]	0.71	-	0.62	-	0.39	-	0.71	-	0.65‡	0.12‡	0.72‡	0.07‡

‡ Estimates from laboratory direct shear tests on triplets

3.3.2 Testing protocols

The specimens were subjected to incremental dynamic test sequences, by applying to their bases an input acceleration history that was increasingly scaled in amplitude up to near-collapse conditions of the buildings. In fact, the aim of the tests was to assess damage evolution, failure mode development, and ultimate capacity of the bare and retrofitted buildings.

A single-component earthquake signal, termed EQ-NPR, was used for both specimens to facilitate comparing their experimental performances. This ground-motion record was selected upon compatibility with the uniform hazard spectrum (UHS) with 2475-years return period, for the area of Ten Boer, The Netherlands [Brunesi *et al.*, 2019]. The selected record was characterized by a short significant duration $D_{s,5-75}$ = 1.37 s [Bommer and Martinez-Pereira, 1999; Kempton and Stewart, 2006] and a peak ground acceleration PGA = 0.30 g (Figure 3.10).

Table 3.3 and Table 3.4 show the sequences of main earthquake simulations applied to the bare and retrofitted buildings, respectively, with nominal amplitude scale factors and some significant intensity measures: recorded peak ground acceleration, *PGA*; recorded peak ground velocity, *PGV*; pseudo-spectral accelerations, *PSA*, and spectral displacements, S_D, for 5% viscous damping ratio at the fundamental period in undamaged ($T_{1,und}$) and damaged ($T_{1,i}$) state. The fundamental period $T_{1,i}$ was evaluated through dynamic identification procedures immediately before the ith main test. The PGA recorded for the bare building at 33% and 50% scale factors appear to be the same due to a shake-table overshoot for periods shorter than 0.3 s [Miglietta *et al.*, 2019].

Moreover, these tables list additional intensity measures correlated to the structural response in several seismic risk studies: geometric mean of the pseudo-acceleration spectral ordinates, PSA_{avg} [Bianchini *et al.*, 2009], in the period window from $T_{1,und}$ (undamaged structure) to $T_{1,dam}$ (at the end of the test run); the cumulative absolute velocity, *CAV* [EPRI, 1988]; the Arias intensity, I_A [Arias, 1970]; and the Housner intensity in its classical form, *HI* [Housner, 1952], and modified definition for short-period URM structures, *mHI* [Magenes *et al.*, 2014].

Between the main test runs listed in Table 3.3 and Table 3.4, low-amplitude random excitations covering a wide frequency band (0.1–40 Hz) with consistent energy content were performed for dynamic identification purposes. Moreover, low-intensity applications of the EQ-NPR signal were necessary between the main jolts, to calibrate the shake-table controller with the updated dynamic properties of the specimens.

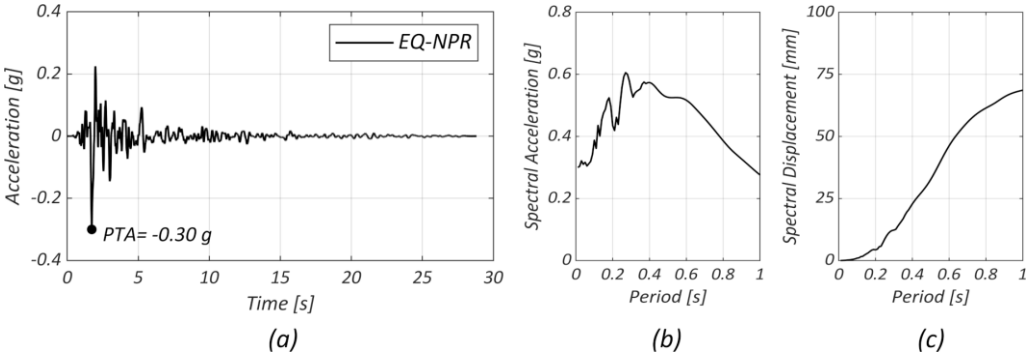

Figure 3.10 Input record EQ-NPR scaled at 100%: (a) acceleration time-series; (b, c) elastic pseudo-acceleration and displacement response spectra for 5% viscous damping ratio.

Table 3.3 Bare building main testing sequence with intensity measures.

Nominal scale factor	*PGA* [g]	*PGV* [m/s]	$PS_A(T_{1,und})$ [g]	$S_D(T_{1,und})$ [mm]	$PS_A(T_{1,i})$ [g]	$S_D(T_{1,i})$ [mm]	$PSA_{,avg}$ [g]	I_A [mm/s]	*CAV* [m/s]	*HI* [mm]	*mHI* [mm]
20%	0.06	0.05	0.10	0.75	0.10	0.75	0.11	15	0.8	140	19
33%	0.16	0.08	0.21	1.5	0.16	1.7	0.19	59	1.7	240	33
50%	0.16	0.13	0.26	1.9	0.23	2.5	0.26	86	1.7	350	45
66%	0.25	0.16	0.35	2.5	0.31	4.1	0.32	140	2.2	440	56
85%	0.26	0.21	0.43	3.1	0.42	6.0	0.42	230	2.8	570	74
100%	0.31	0.24	0.52	3.7	0.51	12	0.51	340	3.5	670	90
100%-rev*	0.30	0.26	0.62	4.5	0.53	37	0.54	340	3.2	670	95
133%-rev*	0.39	0.33	0.79	5.7	0.66	46	0.68	550	4.1	850	120

* Input motion applied with reversed polarity

Table 3.4 Retrofitted building main testing sequence with intensity measures.

Nominal scale factor	*PGA* [g]	*PGV* [m/s]	$PS_A(T_{1,und})$ [g]	$S_D(T_{1,und})$ [mm]	$PS_A(T_{1,i})$ [g]	$S_D(T_{1,i})$ [mm]	$PSA_{,avg}$ [g]	I_A [mm/s]	*CAV* [m/s]	*HI* [mm]	*mHI* [mm]
20%	0.06	0.05	0.09	0.64	0.09	0.64	0.1	13	0.75	120	18
33%	0.10	0.09	0.17	1.2	0.17	1.4	0.18	39	1.2	240	31
50%	0.17	0.13	0.29	2.1	0.30	2.4	0.29	110	2.0	370	50
66%	0.19	0.17	0.34	2.4	0.35	2.8	0.34	150	2.2	440	61
85%	0.25	0.21	0.42	3.0	0.34	3.3	0.41	220	2.8	560	73
100%	0.30	0.26	0.54	3.8	0.36	3.9	0.50	330	3.3	690	89
133%	0.41	0.36	0.79	5.7	0.61	6.7	0.74	690	4.8	960	130
133%-roof*	0.43	0.37	0.87	6.3	0.7	10	0.73	680	4.6	980	130
166%-roof*	0.51	0.41	0.9	6.4	0.9	15	0.84	910	5.5	1100	150
200%-roof*	0.66	0.47	1.1	7.6	0.94	24	1.0	1300	6.7	1300	180
266%-roof*	0.78	0.57	1.3	9.1	1.4	60	1.3	2100	8.7	1600	220

* Roof structure stiffened by diagonal steel cables

3.4 TEST RESULTS

3.4.1 General overview

At the end of each increment of the shake-table test sequence, the buildings were surveyed in detail and the crack patterns were accurately mapped to monitor the structural damage evolution. As emerged from these surveys, the two prototypes responded differently to the same base excitation, developing two distinct failure modes.

The bare building suffered a concentration of displacement demand and consequent damage at the second storey. In fact, the response of this prototype was mainly governed by a local mechanism: the second-floor timber diaphragm slid above the second-storey masonry piers, pushing the transverse walls out of their planes. Only minor structural damage was observed at the first storey at the end of the testing sequence.

On the other hand, the retrofitted building exhibited a global box-type behaviour during the entire testing sequence, with improved in-plane and out-of-plane capacities of the masonry piers. Enhanced connections between masonry piers and timber floor granted a top-to-bottom continuous flow of inertia forces and inhibited the onset of local sliding mechanisms. The final damage was mainly concentrated at the first storey, involving also the transverse walls because asymmetric stiffness distribution induced torsional response.

The following paragraphs discuss the observed damage pattern evolutions and the identification of the specimens damage states (DS) and damage limits (DL) throughout the incremental dynamic tests. A qualitative description of five damage states was chosen in accordance with the EMS-98 macro-seismic intensity scale [Grünthal, 1998]: DS1, no structural damage or slight non-structural damage; DS2, minor structural damage or moderate non-structural damage; DS3, moderate structural damage or heavy non-structural damage; DS4, heavy structural damage or very heavy non-structural damage; and DS5, very heavy structural damage with partial or total collapse.

Four damage limits were consequently defined as thresholds between damage states: DL1, the limit condition at which no structural damage was visible; DL2, the limit condition when only minor structural damage was detected; DL3, the limit condition when only moderate structural damage was reported; DL4, the limit condition when heavy structural damage was detected, before entering the near-collapse field. In other words, DL(i) constitutes the threshold between DS(i) and DS(i+1). For the identification of DL4, a statically unstable recorded dynamic response was considered equivalent to near-collapse damage conditions.

Each DL was then associated with a run of the testing sequence: specifically, DL(i) was associated with the last test that caused an overall building damage state of DS(i). Finally,

an engineering demand parameter value was assigned to each DL. To this end, the maximum global drift-ratio ($\tilde{\theta}$) recorded during the corresponding test increment was selected, defined as the maximum average second-floor displacement divided by the second-floor height above the foundation (5.4 m).

All processed data and videos of the tests are freely available and can be downloaded upon request at http://www.eucentre.it/nam-project.

3.4.2 Bare specimen damage evolution

Figure 3.11 illustrates the unretrofitted building damage evolution, relative to the CS inner leaf viewed from inside. Red marks identify cracks formed during the considered test run, while the black ones correspond to cracks that were already present. The figure shows only the runs when damage limits DL1 through DL4 were achieved.

The first hairline cracks were observed after test runs EQ-NPR-20% (*PGA* = 0.06 g) and EQ-NPR-33% (*PGA* = 0.16 g). They were located at the interfaces between timber joists or spreader beams and masonry walls. The ones visible on the East and West façades anticipated sliding between the timber diaphragm and the second-storey piers. However, these sliding cracks had not fully developed above all longitudinal piers, and the local mechanism was deemed not yet activated. For these reasons, the building was considered in DS1 up to run EQ-NPR-33% (*PGA* = 0.16 g), when damage limit DL1 was reached and associated with global drift ratio $\tilde{\theta}_{DL1}$= 0.037%. During the following run EQ-NPR-50% (*PGA* = 0.16 g) existing cracks extended moderately and a few new ones developed at the top and base of slender piers, denoting the onset of in-plane flexural-rocking responses. From this stage on, structural damage was considered of DS2 type.

During test run EQ-NPR-66% (*PGA* = 0.25 g), interface cracks extended completely between the second-storey longitudinal piers and the timber diaphragm, the local sliding mechanism of the second-floor diaphragm activated, and damage started concentrating at the upper storey. A full-length horizontal crack formed on the transverse South wall at the second-floor, due to relative displacement and pounding between the masonry wall and the timber diaphragm. This interaction accentuated the out-of-plane response of the transverse walls, which involved the corner piers of the longitudinal walls at the second storey: on the East side, both corner slender piers behaved as a return walls for the North and South ones (flange effect); similarly, on the West side, the South slender pier was interested by this flange effect, with a stair-stepped crack at its base, while the stiffer and stronger North squat pier started detaching from the North wall at the top. The central slender pier of the East wall showed signs of flexural-rocking behaviour. Only a few localized cracks could be observed on the first-storey longitudinal walls, while no damage was detected on the transverse ones. In all cases, residual crack widths were less than 1 mm, and no structural

element had been compromised yet. Therefore, the specimen was still classified in DS2 state, and damage limit DL2 was associated with this testing stage.

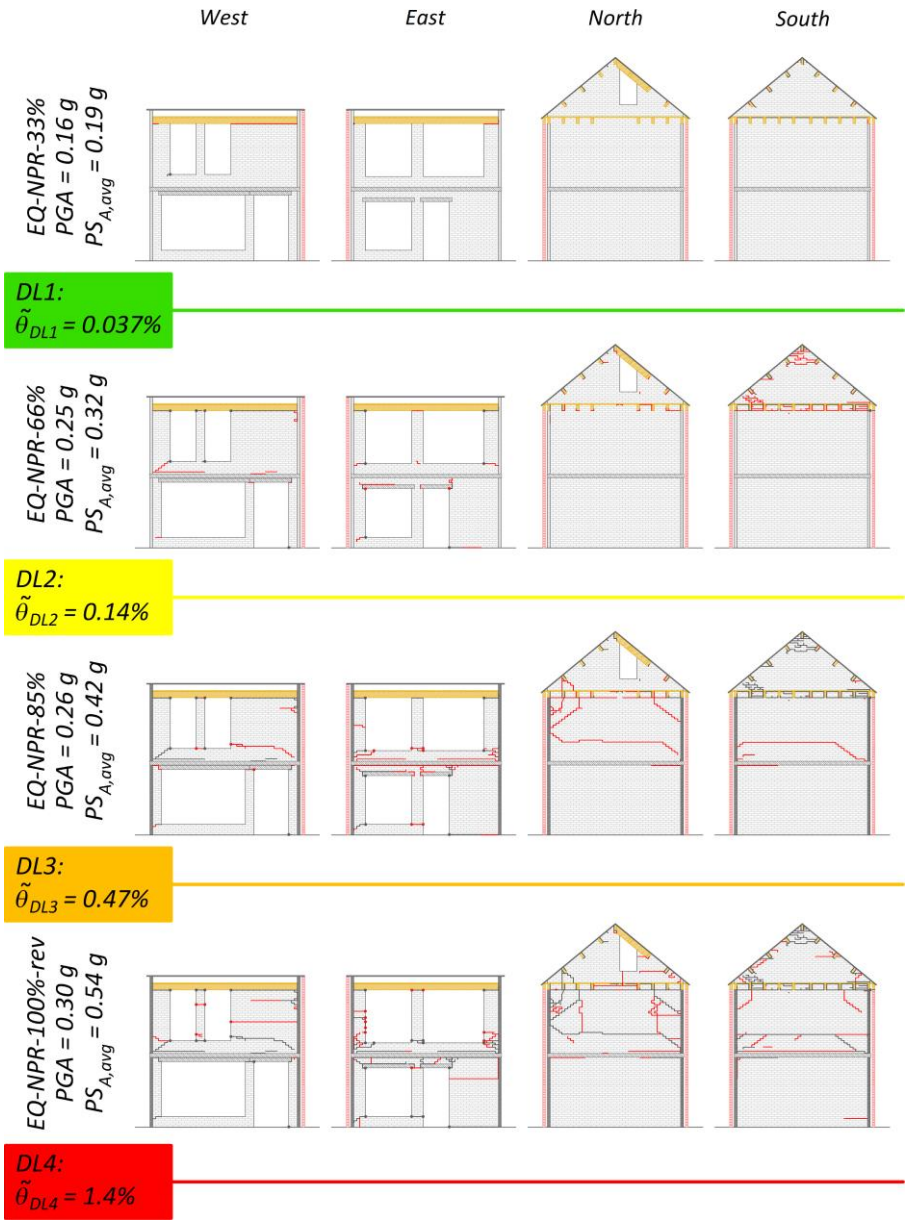

Figure 3.11 Bare masonry building damage pattern evolution on the load-bearing CS inner leaves, viewed from inside. New cracks in red, existing cracks in black.

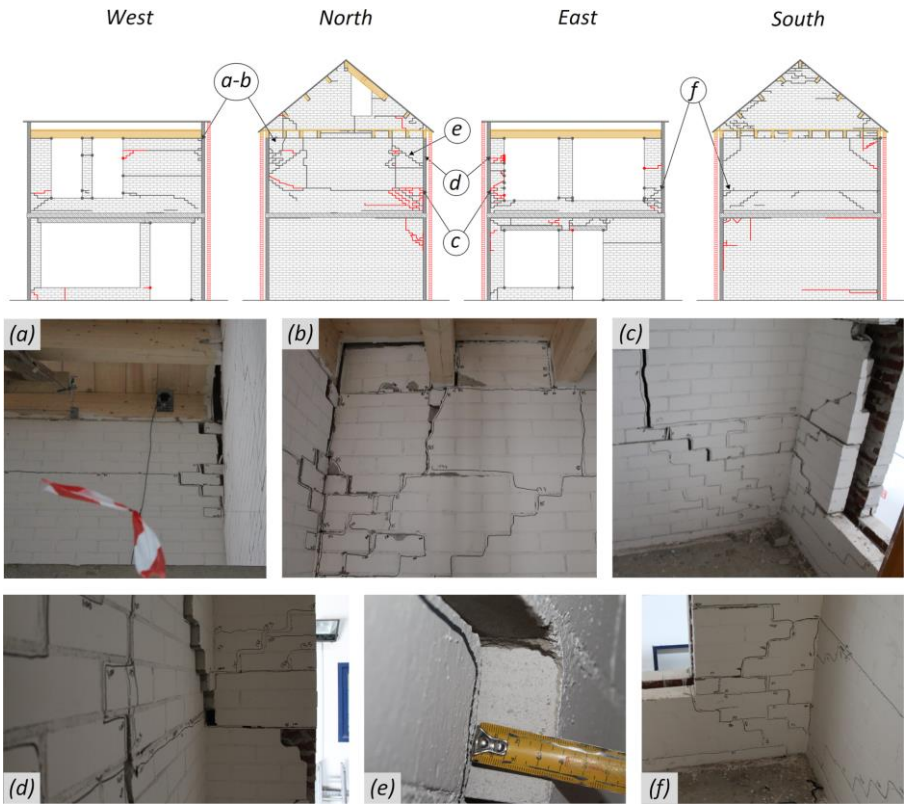

Figure 3.12 Bare masonry building final conditions: a, b second-storey North-West corner of the CS leaf, c, d second-storey North-East corner of the CS leaf, e brick dislocation on the North CS wall, f second-storey South-East corner of the CS leaf.

The corresponding maximum global drift ratio was $\tilde{\theta}_{DL2}$ = 0.14%. The subsequent test EQ-NPR-85% (*PGA* = 0.26 g) brought the specimen to a condition of widespread damage of DS3 type. The second-storey crack pattern of the longitudinal East and West walls evolved slightly, with all central and corner slender piers cracked at their top and bottom due to rocking and flange effect, respectively. Similar patterns were now visible also on the first-storey longitudinal walls. Focusing on the longitudinal squat piers, the second storey one of the West side tended to rock and slide while detaching from the North transverse wall; instead, the first-storey squat pier of the East side showed evidences of rocking but no damage at the interface with the South transverse wall. Several new cracks formed on the transverse walls at the second storey, due to out-of-plane flexural response amplified by pounding of the second-floor timber diaphragm. Each transverse wall developed a horizontal crack at about one third of the second-storey height, which extended diagonally towards the corners. Instead, no damage accumulated at the first-storey on the North and South walls. Residual crack widths after the test were still less than 1 mm, but they spread throughout the building. Only this run was assigned to DS3, thus damage limit DL3 was

associated with it and with the corresponding maximum global drift ratio $\tilde{\theta}_{DL3}$ = 0.47%. The application of EQ-NPR-100% (*PGA* = 0.31 g) caused the formation of several new cracks and the accumulation of significant residual displacements of the order of centimeters, classified as DS4. As damage became extensive, the following test runs were performed reversing the ground motion polarity (Table 3.3), with the hope to allow conducting more tests before reaching a near-collapse state. Moreover, some accelerometers were removed from the clay outer-leaf as a safety measure [Miglietta *et al.*, 2019].

The last two runs, EQ-NPR-100%-rev (*PGA* = 0.30 g) and EQ-NPR-133%-rev (*PGA* = 0.39 g), caused severe damage up to near-collapse conditions. Processed experimental data revealed that static stability of the building was lost during the final run: in fact, as the displacement was increasing in the negative direction, the base shear became positive. For this reason, the incremental dynamic test was terminated, and the specimen was considered in DS5 state during EQ-NPR-133%-rev. Indeed, collapse was likely prevented by acceleration sign inversions of the table dynamic input. Accordingly, damage limit DL4 was associated with the maximum global drift ratio recorded during EQ-NPR-100%-rev, $\tilde{\theta}_{DL4}$ = 1.4%, before losing static stability.

The final conditions of the specimen are depicted in Figure 3.12, where extensive damage can be observed: several masonry elements were cracked at multiple locations, in particular at the second storey. The survey detected significant extension of existing cracks, loss of some portions of masonry, and large residual crack widths or out-of-plane dislocations up to 50 mm. The damage pattern of the clay outer leaf followed very closely the one described for the CS inner leaf, demonstrating that even the adopted low density of steel ties was sufficient to couple the response of both leaves under the sustained level of acceleration demand. At the end of the incremental dynamic test, less damage was detected at the first storey compared to the second one, because the local mechanism of the second-floor timber structure sliding above the masonry piers dominated the response. The window timber frames installed on the North gable and on the West façade at the first storey did not show any significant damage: all shutters were properly opening at the end of the test sequence.

3.4.3 Retrofitted specimen damage evolution

Figure 3.13 illustrates the crack pattern evolution on the CS inner leaves of the retrofitted building detected from inside, limited to the runs when damage limits DL1 through DL4 were reached.

The surveys after test runs EQ-NPR-20% (*PGA* = 0.06 g) and EQ-NPR-33% (*PGA* = 0.10 g) did not reveal any damage to the building. A few localized hairline cracks at the interfaces between timber joists and load-bearing transverse walls formed during run EQ-

NPR-50% (*PGA* = 0.17 g). The following test EQ-NPR-66% (*PGA* = 0.19 g) caused only a moderate extension of the same interface cracks and no residual displacements were detected. Up to this run, the building was assigned to DS1 and damage limit DL1 was associated with it, resulting in maximum global drift ratio $\tilde{\theta}_{DL1}$ = 0.05%.

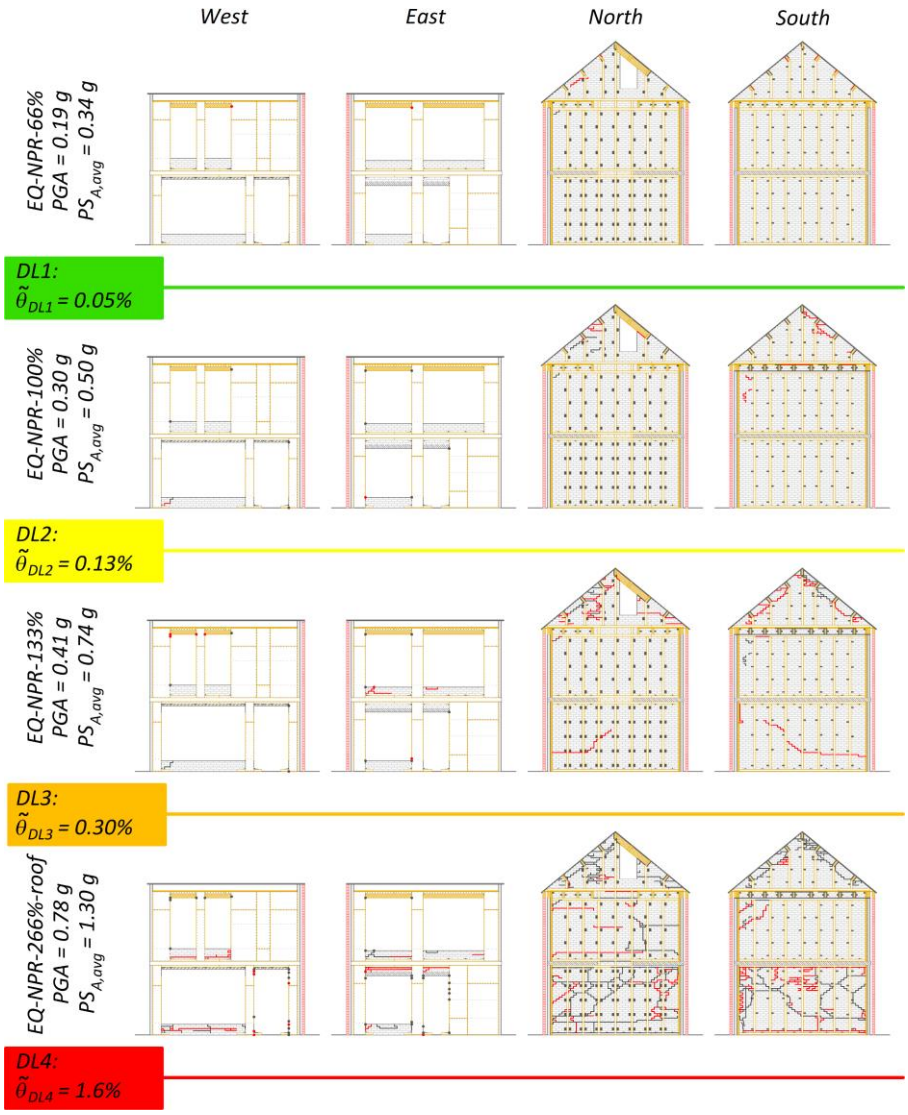

Figure 3.13 Retrofitted building damage pattern evolution on the load-bearing CS inner leaves, viewed from inside. New cracks in red, existing cracks in black.

The following runs EQ-NPR-85% (*PGA* = 0.25 g) and EQ-NPR-100% (*PGA* = 0.30 g) resulted in visible damage spreading only within the gable-roof subsystem, with DS2

classification of the overall specimen conditions. The building responded globally to the ground motion, but the higher flexibility of the gable-roof subsystem, characteristic of this building typology, became evident [Graziotti *et al.*, 2017; Tomassetti *et al.*, 2019b]. At this stage of the test, residual crack widths were less than 1 mm in the gables, while the first- and second-storey walls were still undamaged. During run EQ-NPR-100% (*PGA* = 0.30 g) the building was deemed to have reached damage limit DL2, with corresponding maximum global drift ratio $\tilde{\theta}_{DL2}$ = 0.13%. Up to this level of shaking the roof diaphragm did not require any stiffening interventions.

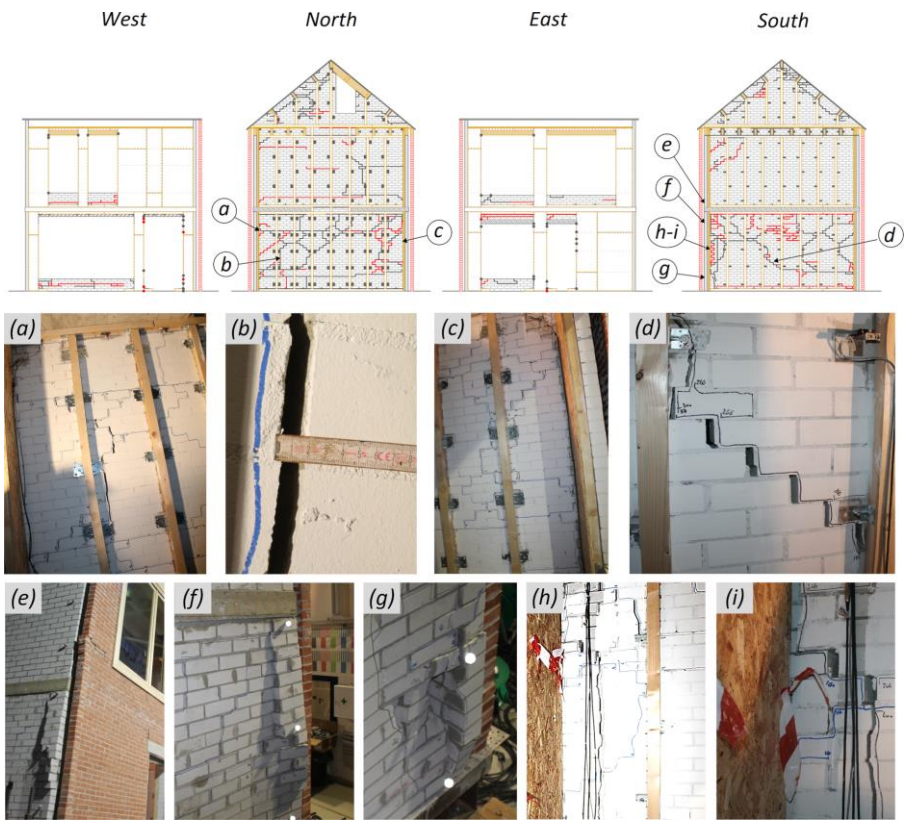

Figure 3.14 Retrofitted building final conditions: (a) first-storey North CS wall close to West corner; (b) brick dislocation on the North CS wall; (c) first-storey North CS wall close to East corner; (d) first-storey South CS wall close to the centre; (e, f, g) So

After test EQ-NPR-133% (*PGA* = 0.41 g), propagation of existing cracks in the gable-roof subsystem and formation of new ones in other structural elements were observed, leading to a DS3 damage condition. Minor cracks appeared at the edges of longitudinal CS piers, covered by the timber retrofit, probably due to in-plane flexural response: they were not localized only at the pier top and bottom, but spread away from the ends due to the

reinforcing effect of the timber posts. Two similar, long cracks were detected on both transverse walls at the first storey. They started as horizontal cracks at one edge of the wall, then continued following a stair-stepped path. These cracks were associated with the in-plane shear response of the transverse walls, triggered by the overall building torsional response: in fact, the two longitudinal walls offered very different stiffness and strength. This run was also associated with the attainment of damage limit DL3, with maximum global drift ratio $\tilde{\theta}_{DL3}$ = 0.3%.

At this stage of the incremental dynamic tests, due to extensive damage accumulated by the gables and large relative displacements between roof and second floor, the roof was stiffened by tightening the diagonal steel cables connecting the ridge-beam to the second-floor joists. A second-floor peak acceleration of 0.53 g was reached before retrofitting the roof diaphragm.

The test with the signal scaled at 133% of its amplitude was then repeated with the restrained roof (EQ-NPR-133%-roof, *PGA* = 0.43 g). The response of the building emphasized the first-storey damage due to torsional effects. The cracks propagated throughout the whole first-storey transverse walls, from edge to edge. The building could not be classified as moderately damaged anymore and, starting from this run, was associated with DS4 damage state. At this stage, the building had activated all its resisting mechanisms. Under further scaling of the ground motion for test runs EQ-NPR-166%-roof (*PGA* = 0.51 g) and EQ-NPR-200%-roof (*PGA* = 0.66 g) the first-storey damage due to torsional effects worsened, while only a few additional hairline cracks appeared at the second storey. The last run, EQ-NPR-266%-roof (*PGA* = 0.78 g) caused such severe damage that the specimen was deemed near partial collapse. Consequently, damage limit DL4 was associated with this run and its maximum global drift ratio $\tilde{\theta}_{DL4}$ = 1.6%.

At the end of the incremental dynamic test the building prototype was heavily damaged, especially at the first storey (Figure 3.14). Many cracks were detected at the edges of the first-storey piers, covered by the timber retrofit, of the East and West inner leaves. The North and South transverse walls were severely damaged at the first storey and accumulated residual crack widths up to 35 mm (Figure 3.14a-d), due to in-plane shear caused by the overall building torsional response. In particular, loss of masonry portions and significant residual dislocation of masonry units (up to 65 mm) were observed close to the East edge of the CS South wall, where it detached from the intersecting squat pier of the East wall (Figure 3.14e-i): uplift due to rocking of the longitudinal squat pier likely caused incompatible vertical displacements along the intersection with the transverse wall. Moreover, the overall building rotation about the vertical axis may have caused dislocations along this crack. The second-storey transverse walls presented lower levels of damage: a few horizontal cracks developed on the North wall at several heights, while two diagonal cracks formed on the South one, close to its top West corner.

Similarly to the case of the bare building, damage on the clay veneer generally followed the one observed on the CS inner leaf, revealing that the increased amount of steel ties ensured a coupled response of the two leaves throughout the test. The outer leaf was found undamaged up to EQ-NPR-66% (*PGA* = 0.19 g), when the building was still in DS1 conditions. Cracks, due to in-plane rocking and flange effect, started developing on the longitudinal East and West façades during EQ-NPR-85% (*PGA* = 0.25 g) and EQ-NPR-100% (*PGA* = 0.30 g), compatibly with DS2 damage state. At the end of the incremental dynamic test, all clay veneers presented widespread damage throughout their surfaces. Also the windows were affected by the large first-storey drift: the shutter of the West-side window fell during the last run, pushed off its pins by the shear deformation imposed to the timber frame, which however remained undamaged.

3.4.4 Hysteretic responses

This section discusses and compares the recorded experimental performances in terms of hysteretic responses, backbone curves, and cumulative energy dissipation. As already mentioned, the global drift-ratios ($\tilde{\theta}$) were obtained dividing the average second-floor displacements by the second-floor height above the foundation (5.40 m).

The base shears of the hysteretic loops (Figure 3.15) were computed multiplying the mass associated with each accelerometer times the recorded acceleration. The mass of the bottom half of the first storey was considered fixed to the shake-table: consequently, its contribution was neglected. The base-shear coefficients (BSC) were computed normalizing these base shears by the sum of the contributing masses of the corresponding building (40.6 t and 42.6 t for the bare and the retrofitted buildings, respectively). It is worth noting that the base-shear coefficient on Figure 3.15 (left vertical axis) is exact for both specimens, while the base shear in units of force (right vertical axis) is exact only for the bare building. However, since both specimens had very similar masses, it is a good approximation also for the retrofitted one.

Figure 15a compares the two hysteretic responses during test EQ-NPR-133%-rev (PGA = 0.39 g, last run for the bare building) and EQ-NPR-133% (PGA = 0.41 g, retrofitted building). After these runs with nearly the same PGA, the specimens presented clearly different crack patterns (Figure 3.11, Figure 3.13): while the bare building was severely damaged, the retrofitted one showed the first evidences of the activation of a global torsional mechanism. Moreover, Figure 3.15a shows evident strength degradation for the bare specimen, as its base shear became positive while the second-floor displacement was increasing in the negative direction: this proves that the building had lost static stability during this run, and collapse was likely prevented only by acceleration sign inversions of the table dynamic input. For this reason, damage state DS5 was associated with this test run for the bare specimen. Instead, the retrofitted building hysteretic loops evidence a response initially almost elastic, with minor excursions in the nonlinear range, slight

stiffness degradation, and no strength degradation, compatible with a DS3 damage state. The retrofitted specimen developed a base-shear coefficient BSC = 0.41, significantly higher than BSC = 0.25 offered by the bare building, while it underwent a global drift ratio $\tilde{\theta}$ = 0.3% in both directions, which is 15 of $\tilde{\theta}$ = 2.0% reached by the bare building in the negative direction.

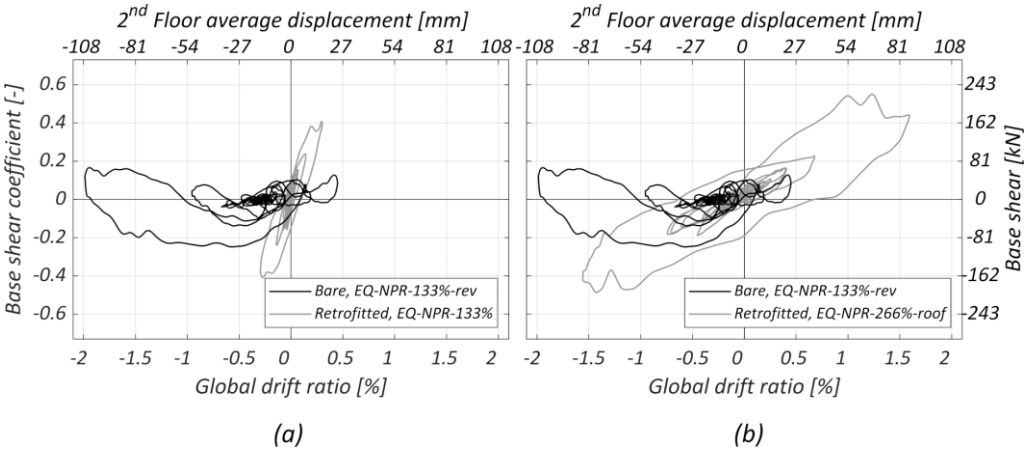

Figure 3.15 Hysteretic responses comparison: (a) with EQ-NPR signal scaled at 133% of its amplitude; (b) during the final test runs.

Figure 15b compares the experimental responses of the two specimens during the last test runs, EQ-NPR-133-rev (PGA = 0.39 g) for the bare building and EQ-NPR-266%-roof (PGA = 0.78 g) for the retrofitted one. The latter, as opposed to the former, maintained static stability throughout the testing sequence, with limited strength degradation and significant hysteretic energy dissipation, likely due to yielding of some steel connections. The retrofitted building sustained BSC = 0.55, more than twice the value of BSC = 0.25 resisted by the bare one, while it accommodated $\tilde{\theta}$= 1.6% in both directions, without reaching the value of $\tilde{\theta}$ = 2.0% recorded on the bare building in the negative direction.

Figure 16a shows the experimental backbone curves of the two buildings, highlighting the maximum global drift ratios associated with the damage limits mentioned in the previous sections. Since the specimens underwent higher displacements in the negative direction up to near-collapse conditions, the backbone curves were obtained by selecting for each run the point of maximum force with the corresponding displacement in that direction, from the hysteretic loops (hollow dots). The last point of the backbone curve is the one associated with maximum negative displacement from the hysteretic response during the last run (solid dots). The retrofit system did not influence the initial stiffness because of its high in-plane flexibility compared to the masonry walls. In light of this, it can be inferred that the retrofit system acts similarly to steel reinforcement in concrete or masonry elements: it becomes effective only after masonry first cracking.

This fact, combined with the small additional mass of the intervention, allows maintaining the initial dynamic properties of the bare masonry building nearly unchanged. One can observe from Figure 3.16a that the bare building could sustain its maximum BSC = 0.25 only up to $\tilde{\theta}$ = 0.57%; then it exhibited a fast strength degradation and finally lost static stability, as shown by the BSC sign inversion. The BSC of the bare specimen became zero around $\tilde{\theta}$ = 1.5%, which is very close to $\tilde{\theta}_{DL4}$ = 1.4% (i.e., associated with damage limit DL4) recorded during the second-last test run. Moreover, between $\tilde{\theta}$ = 0.28% and $\tilde{\theta}$ = 0.57%,

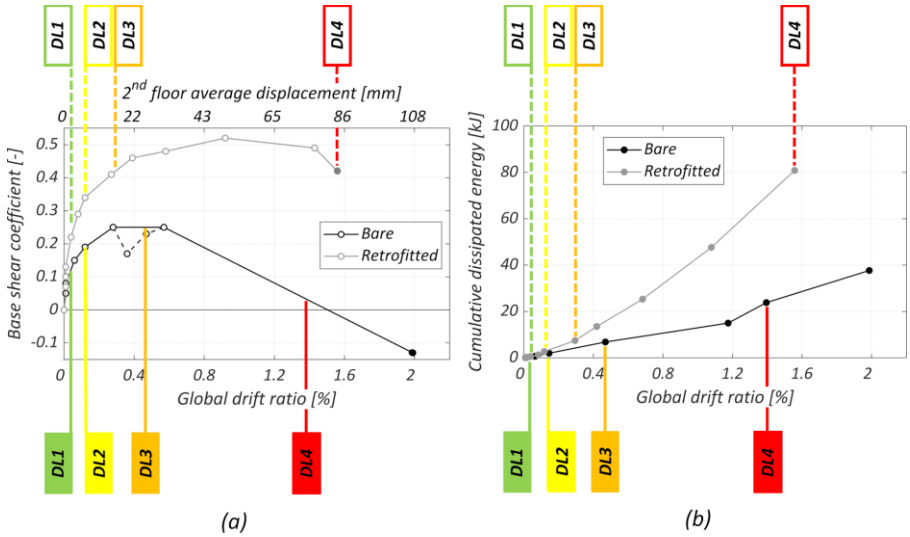

Figure 3.16 Experimental responses comparison: (a) backbone curves; (b) evolution of the equivalent viscous damping ratio.

the curve shows a local strength drop which is subsequently recovered (dashed black curve on Figure 3.16a). This apparent strength recovery was caused by reversing the input signal polarity after run EQ-NPR-100% (lowest point of the dashed line), to proceed with further testing in spite of extensive damage and residual displacements, as discussed earlier. Consequently, the solid black line represents the envelope of maximum recorded base shear for the bare building. Instead, the retrofit system allowed reaching a BSC ≈ 0.5 and maintaining it almost constant up to $\tilde{\theta}$ = 1.43% with negligible strength degradation, which became more evident only for larger global drift ratios during the last run.

Finally, the cumulative energy dissipated by the two specimens is associated with the maximum negative drift ratio (solid dots) experienced during each run in Figure 3.16b. The retrofitted building exhibited a higher energy dissipation capacity for given global drift ratio, and dissipated twice as much the energy of the bare building at the end of the entire sequence. The different amount of hysteretic dissipation is partially associated with the

higher strength of the retrofitted building, combined with the substantially different damage mechanisms. It is interesting to notice that both specimens dissipated nearly the same amount of energy when reaching the same damage limits up to DL3.

3.5 SUMMARY AND DISCUSSION OF THE TEST RESULTS

Figure 3.17 and Figure 3.18 summarize the experimental response evolution throughout the incremental dynamic tests in terms of peak displacements ($\delta_{i,j,x}$) of both floors or roof *i* along both longitudinal walls *j*, peak interstorey drift ratios ($\theta_{i,j,x}$) of both storeys *i* along both longitudinal walls *j*, peak average shear deformation ($\gamma_{R,x}$) of the roof pitches, peak interstorey drift ratios ($\theta_{i,j,y}$) of both storeys *i* along both transverse walls *j*, longitudinal acceleration amplification factors (AMP_i) of both floors or roof ridge *i*, and fundamental period of the damaged structure (T_1) at the end of each run.

Peak longitudinal displacements of the bare building (Figure 3.17) became significantly larger at the second floor than at the first floor, from test EQ-NPR-85% through the end of the testing protocol, as damage conditions of DS3 and DS4 type developed; at the same time, the roof displacement relative to the second floor slightly reduced. During the last test run, the second floor and roof moved by more than 100 mm, while the first one did not exceed 20 mm. Moreover, focusing on the displacement of the second-floor East and West sides, one can note some differences up to test EQ-NPR-66%: due to plan irregularity, the flexible timber diaphragm was initially deforming in shear as the building responded in DS1 and DS2 states. However, onset of the local second-floor mechanism during run EQ-NPR-85% prevented this distortion, as the diaphragm slid as a rigid body above the masonry piers in damage states DS3 and DS4.

These observations can be confirmed by the peak longitudinal interstorey drift ratio evolution, which concentrated at the second storey in DS3 and DS4 states: during the last test run, the second storey sustained interstorey drift ratios higher than 4%, as opposed to the values of the order of 0.7% recorded at the first storey and 0.3% at the attic one.

The development of the local second-floor sliding mechanism affected also the peak transverse interstorey drift ratios: in fact, despite remaining always below 0.3%, they increased on both transverse walls when the building responded in DS3 and especially DS4 damage states, most likely due to some rigid-body rotation of the whole timber diaphragm.

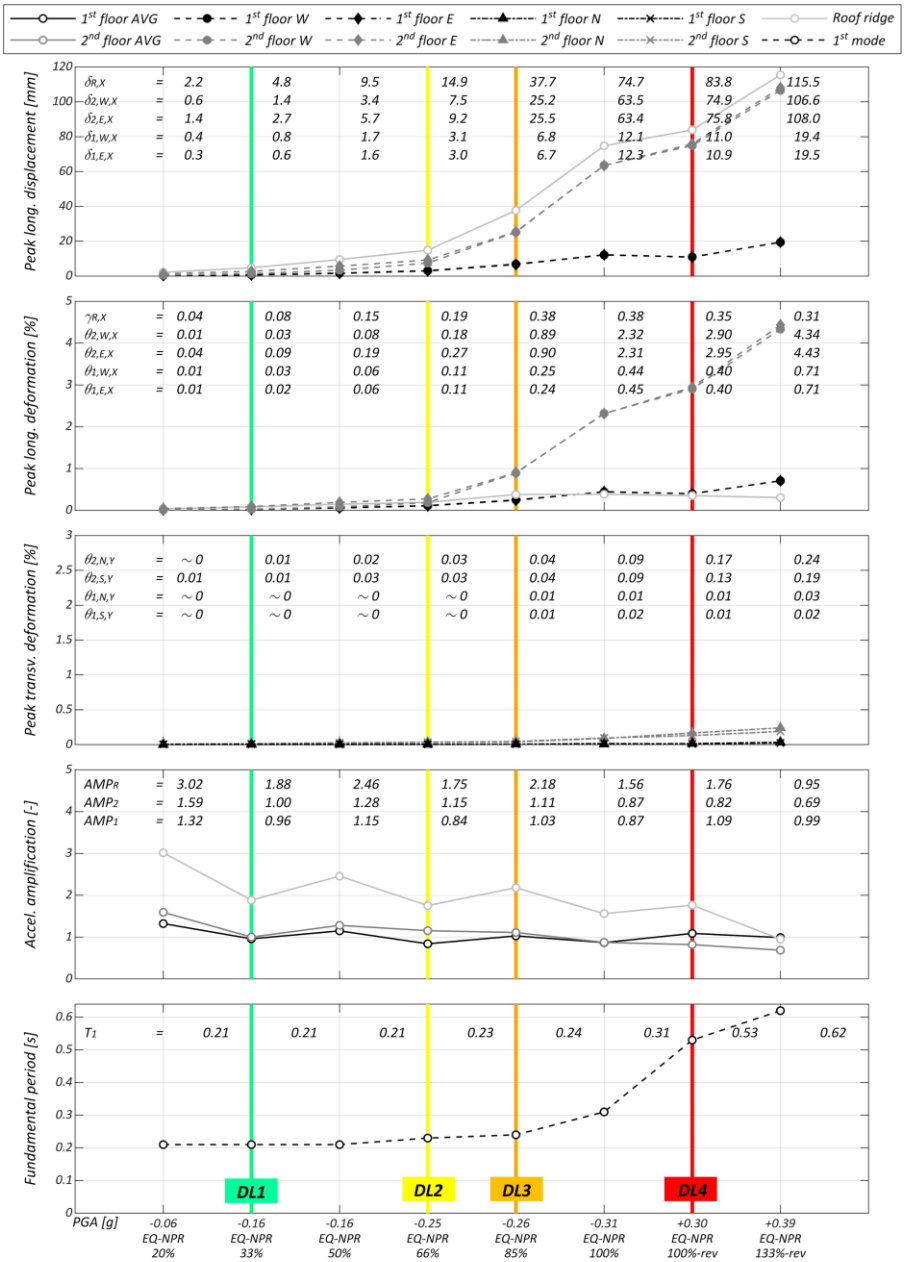

Figure 3.17 Evolution of the bare specimen response.

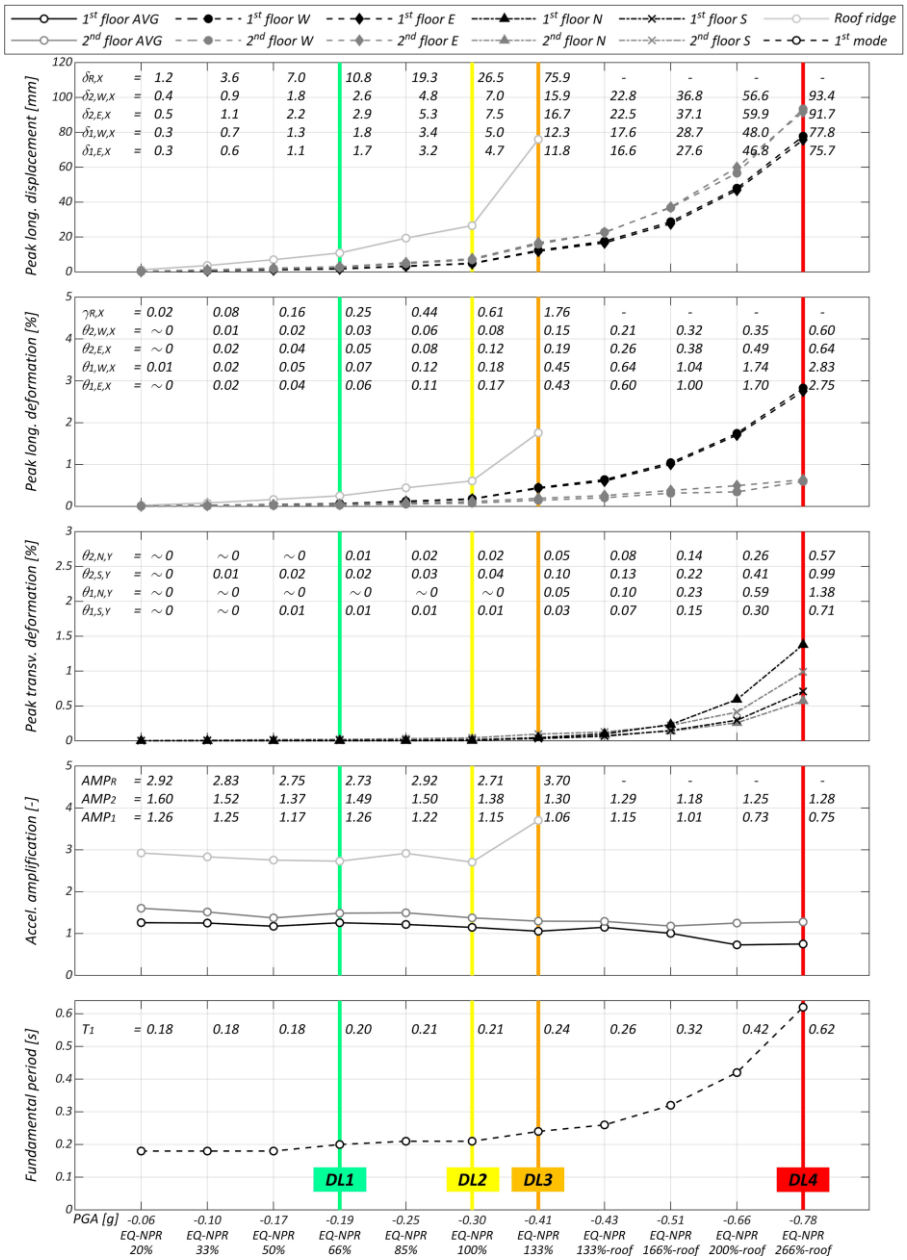

Figure 3.18 Evolution of the retrofitted specimen response.

A substantially different behavior was observed for the retrofitted building, as confirmed by the recorded data (Figure 3.18). The high flexibility of the gable-roof subsystem compared to the first and second storeys became evident, as the local second-floor

mechanism was inhibited: its longitudinal displacement and shear deformation were almost one order of magnitude larger than those of the storey below when DL3 was achieved (test run EQNPR-133%), after which the diagonal steel cables were tied. The first- and second-storey longitudinal displacements remained very close to each other also under high-intensity input motions. This resulted in interstorey drift concentration at the first storey starting from run EQ-NPR-133%, corresponding to DS3 and DS4 conditions: at the end of the test, the first-storey had experienced a maximum interstorey drift ratio of the order of 2.8% against the one of 0.6% recorded at the second storey. The peak transverse interstorey drift ratios confirmed a relevant torsional response of the building: the transverse North wall sustained a maximum in-plane interstorey drift ratio of about 1.4%, which is comparable with the one sustained on the longitudinal direction.

The roof and second-floor acceleration amplification of the bare building (Figure 3.17) progressively decreased to about 30% and 45% of the initial values, respectively: reaching the strength of the second-floor sliding interface limited the acceleration transmitted to the timber floor and roof. Instead, the first-floor amplification decreased only to 75% of the initial one, as the first-storey walls were far from reaching their strength. The retrofitted building (Figure 3.18) displayed a different response also in terms of floor acceleration amplifications, which remained nearly constant up to DL2 (test run EQ-NPR-100%). The roof presented a sudden increment to 27% of the initial amplification when DL3 was reached (test run EQ-NPR-133%), requiring the activation of steel cables during subsequent runs. The amplifications of the first and second floors, instead, progressively reduced in DS3 and DS4 conditions, to 60% and 80% of the initial values at the first and second floors, respectively. These decrements, not very pronounced, indicate that the structure maintained some reserve of lateral resistance and ability to transfer accelerations to upper floors.

Figure 3.17 and Figure 3.17 also compare the fundamental period evolution for both buildings. Both specimens were characterized by an initial fundamental period of 0.17 s in pristine conditions, because the retrofit system has negligible incidence on the overall mass and initial stiffness. Incidentally, they presented the same fundamental period of 0.62 s also at the end of the test sequences. Both specimens suffered the highest period elongation once entered in DS4 damage state, but the retrofitted building sustained a higher number of test runs and twice the ground acceleration amplitude to reach the same elongation. This finding can be extended considering the different number of runs sustained by the two buildings and the PGA associated with each DL (Figure 3.19): on average, the application of the retrofit system allowed increasing the PGA thresholds of each DL by factors of the order of 120–260%, with larger factors for higher DLs.

Table 3.5 shows the maximum interstorey drift-ratios (IDRs) recorded during the runs corresponding to each DL and compares them with those proposed by Tomassetti *et al.*

[2019a] for typical Dutch URM terraced houses. A good agreement was obtained in terms of IDRs associated to DL1. Focusing on DL2, the bare building IDR is significantly higher, specifically 180% of the proposed value, while the retrofitted building IDR is still consistent with the value proposed by Tomassetti *et al.* [2019a]. The same trend is evidenced by the IDRs associated with DL3: the bare and retrofitted building values are respectively 260% and 130% of the proposed value. However, it is fundamental to consider that the values proposed by Tomassetti *et al.* [2019a] were derived from tests on bare masonry buildings responding globally, without the activation of any local mechanism. Instead, the high values recorded for the bare building are the result of the local sliding mechanism of the second floor, which governed the overall seismic response of the building starting from DS2 (see Sect. 4.2); as such, in this case the second-storey drift ratio is not the most appropriate engineering demand parameter to be correlated with damage states of masonry walls.

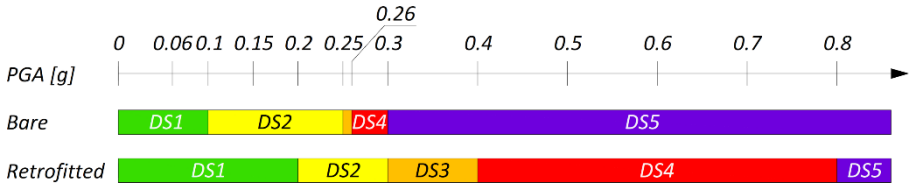

Figure 3.19 Relationship between experimental damage states and input PGA.

Table 3.5 Comparison of maximum longitudinal interstorey drift-ratios, corresponding to damage limits, with values proposed by Tomassetti *et al.* [2019a].

Specimen	θ_{DL1} [%]	θ_{DL2} [%]	θ_{DL3} [%]	θ_{DL4} [%]
Bare building	0.09	0.27*	0.90*	2.95*
Retrofitted building	0.07	0.18	0.45	2.83
Tomassetti *et al.*, [2019a]	0.1	0.15	0.35	0.9

* Governed by local sliding mechanism

Focusing on the interstorey drift ratios corresponding to DL4, both specimens sustained significantly larger values compared to the one proposed by Tomassetti *et al.* [2019a]. While the one associated with the bare building cannot be compared, due to the local sliding mechanism of the second-floor diaphragm, the one recorded for the strengthened building proved that the proposed retrofit solution is effective at increasing the ultimate strength and displacement capacity. Moreover, one can notice that the retrofit system did not affect significantly the interstorey drift ratios associated with the first three DLs: in fact, the masonry walls are characterized by higher stiffness than the timber structure, which becomes effective only after masonry cracking.

The in-plane response of the first-storey transverse walls of the retrofitted building, engaged by global torsional response, can be compared to that of a squat CS pier subjected to a quasi-static cyclic shear-compression test by Graziotti *et al.* [2016]. Similar double- fix

boundary conditions and overburden normal stresses of about 0.3 MPa were applied to both the transverse walls and the squat pier.

Table 3.6 Comparison of maximum transverse interstorey drift ratios, at first cracking and ultimate conditions, with values found by Graziotti *et al.* [2016].

Specimen	θ_{cr} [%]	θ_u [%]
Retrofitted building, South wall	0.03	0.71
Retrofitted building, North wall	0.05	1.38
Graziotti *et al.*, [2016]	0.05	0.30

Table 3.6 shows good agreement on the first-cracking interstorey drift ratio, θ_{cr}, recorded on both transverse walls during run EQ-NPR-133%, when overall DL3 was achieved. Graziotti *et al.* [2016] attained an ultimate drift ratio, θ_u, of 0.30%, which was reached by the South transverse wall during test run EQ-NPR-200%-roof. However, the North wall sustained 460% of this value during run EQ-NPR-266%-roof, when DL4 was attained. This larger displacement capacity was likely due to the lower number of cycles imposed on the building specimen, compared to the isolated pier, as well as some effect of the out-of-plane retrofit system, despite the absence of nogging elements and OSB panels on the transverse walls.

3.6 CONCLUSIONS

This paper discussed and compared the experimental seismic performance of two full-scale unreinforced masonry buildings with identical geometrical features, demonstrating the effectiveness of an innovative timber-based retrofit system applied to one of them.

The building prototypes reproduced some relevant features of an end unit of common Dutch terraced houses of the late '70s–early '80s, with perimeter cavity walls consisting of inner load-bearing calcium-silicate leaf and exterior clay veneer, connected by steel ties. The first floor consisted of a solid reinforced concrete slab, while the second floor and the roof were built as timber joist-and-plank structures.

Both specimens were subjected to a unidirectional, incremental dynamic shake-table test with similar input protocols. A ground-motion record, representative of induced seismicity in the Groningen region of The Netherlands, was imposed progressively scaling its acceleration amplitude and bringing the specimens to near-collapse conditions.

A sustainable, light-weight, reversible and cost-effective timber retrofit system was applied to the internal surface of the inner load-bearing masonry leaf of the second specimen to enhance out-of-plane and in-plane capacities of piers as well as wall-to-diaphragm connections. The proposed strengthening solution consists of timber frames mechanically

connected to the masonry and floor systems, with oriented-strand boards nailed to them. The cavity-wall retrofit was completed by increasing the density of steel ties between the two masonry leaves. Moreover, the timber diaphragm was stiffened and strengthened by nailing an additional layer of oriented-strand boards above the existing planks.

The bare building behaviour was governed by a local mechanism, with the second-floor timber diaphragm sliding upon the supporting masonry piers, facilitated by lack of wall-to-diaphragm connections. Displacement demand and structural damage concentrated at the second storey, preventing the development of a global building response. Despite the highly asymmetrical in-plan distribution of resisting piers, a global torsional response did not develop due to the activation of the local sliding mechanism. The incremental dynamic test was stopped after reaching a peak ground acceleration of 0.39 g, with the building in near-collapse conditions. Loss of static equilibrium was observed on the hysteretic response during the last test run, but collapse was inhibited by the dynamic nature of the base excitation.

The retrofit was effective at enhancing the walls in-plane and out-of-plane capacities, improving also the connections between structural elements, and thus inducing a global box-type behaviour on the second building, with full exploitation of the in-plane capacities of all masonry piers. Damage recorded on the perpendicular walls proved the triggering of a torsional response, which resulted in full utilization of the in-plane resistances of the transverse walls as well. The building reached its near-collapse state after sustaining a peak ground acceleration of 0.78 g. At the end of the incremental dynamic test, damage was fairly distributed throughout the building, even though it was more pronounced at the first storey. The roof diaphragm needed to be stiffened only after reaching a peak attic floor acceleration of 0.53 g when applying the input motion with a 133% scale factor.

Despite changing the failure mechanism and the overall lateral resistance of the building, the retrofit application did not affect the initial fundamental period of 0.17 s, thanks to its small mass and stiffness compared to those of the masonry structure. Both damaged specimens exhibited also the same period of 0.62 s at the end of the testing sequence, even though the retrofitted building sustained a larger number of test runs and twice the input intensity.

Damage states and damage limits were defined for both specimens based on the observed damage patterns, and were associated with global and interstorey drift ratios. These values were then compared with the ones found in literature for similar unreinforced masonry structures. The near-collapse thresholds were found to be greater than expected for both specimens. In fact, both bare and retrofitted buildings were able to sustain similar lateral displacements, but the latter resisted twice the input intensity when undergoing the same

displacement demand, developed a global response rather than a local sliding mechanism, and retained static stability throughout the test.

In light of these observations, the proposed retrofit solution effectively addresses and mitigates the main seismic deficiencies of unreinforced cavity-wall masonry buildings, typical of the Groningen region. Given the limited cost of the proposed interventions, they appear promising for a large-scale territorial application.

The results of this experimental campaign will form the basis for future numerical studies, to generate large-scale vulnerability models, to extend the proposed retrofit technique to other unreinforced masonry building typologies, and to perform cost/benefit and sustainability analyses of possible applications. An upcoming article will address the design concept and assumptions of the proposed retrofit system, as well as simplified equations for the analytical prediction of its structural effects.

All processed data and videos are freely available upon request at http://www.eucentre.it/nam-project.

3.7 ACKNOWLEDGEMENTS

This work is part of the EUCENTRE project "Study of the vulnerability of masonry buildings in Groningen", within the research programme framework on hazard and risk of induced seismicity in the Groningen province, sponsored by the Nederlandse Aardolie Maatschappij BV (NAM). The data post-processing was also partially funded by the DPC-ReLUIS within the framework of the Work-Package-5 2019-2021: "Interventi di rapida esecuzione a basso impatto ed integrati". The authors would like to thank the DICAr Laboratory of the University of Pavia and the EUCENTRE Laboratory, which performed the tests. The valuable advice of R. Pinho, G. Magenes and A. Penna was essential to the project and is gratefully acknowledged. Thanks also go to L. Grottoli for his essential contribution in data post-processing, J. Uilenreef, H. Crowley, F. Dacarro, A. Boneschi, L. Gandini, S. Girello, S. Kallioras, L. Mazzella, S. Peloso, and U. Tomassetti for the practical support.

3.8 REFERENCES

AWC [2008] *ANSI/AF&PA SDPWS-2008: Special design provisions for wind and seismic*. American Wood Council, Washington D.C., USA.

Arias, A. [1970] "A measure of earthquake intensity". In: Hansen RJ (editor) *Seismic design of nuclear power plants*. MIT Press, Cambridge, Massachusetts, United States, pp 438–483

Arslan, O., Messali, F., Smyrou, E., Bal, İ.E., Rots, J.G. [2020] "Experimental characterization of the axial behavior of traditional masonry wall metal tie connections in cavity walls". *Construction Building Materials*, 266, 121141. https://doi.org/10.1016/j.conbuildmat.2020.121141.

Arup [2020] "Groningen Earthquakes - Structural Upgrading, Exposure Database V7", *229746_031.0_REP2015*, ARUP, Amsterdam, The Netherlands.

Bianchini, M., Diotallevi, P., Baker, J.W. [2009] "Prediction of inelastic structural response using an average of spectral accelerations". *Proceedings of the 10th international conference on structural safety and reliability (ICOSSAR09)*, Osaka, Japan

Bommer, J.J., Martinez-Pereira, A. [1999] "The effective duration of earthquake strong motion". *Journal of Earthquake Engineering*, 3(2):127–172. https://doi.org/10.1080/13632469909350343

Bommer JJ, Dost B, Edwards B, Stafford PJ, van Elk J, Doornhof D, Ntinalexis M [2016] "Developing an application-specific ground - motion model for induced seismicity". *Bulletin of the Seismological Society of America*, 106(1):158-173. https://doi.org/10.1785/0120150184.

Bourne, S.J., Oates, S.J., Bommer, J.J., Dost, B., van Elk, J., Doornhof, D. [2015] "A Monte Carlo method for probabilistic hazard assessment of induced seismicity due to conventional natural gas production". *Bulletin of the Seismological Society of America*, 105(3):1721–1738. https://doi.org/10.1785/0120140302

Brunesi, E., Peloso, S., Pinho, R., Nascimbene, R. [2019] "Shake-table testing of a full-scale two-story precast wall-slab-wall structure". *Earthquake spectra*, 35(4):1583–1609. https://doi.org/10.1193/072518EQS184M

Cassol, D., Giongo, I., Ingham, J., Dizhur, D. [2021] "Seismic out-of-plane retrofit of URM walls using timber strong-backs". *Construction Building Materials*, 269:121237. https://doi.org/10.1016/j.conbuildmat.2020.121237

Crowley H, Polidoro B, Pinho R, van Elk J [2017] Framework for developing fragility and consequence models for local personal risk. Earthq Spectra 33(4):1325–1345. https://doi.org/10.1193/083116EQS140M

Crowley, H., Pinho, R., van Elk, J., Uilenreef, J. [2019] "Probabilistic damage assessment of buildings due to induced seismicity". *Bulletin of Earthquake Engineering*, 17(8):4495–4516. https://doi.org/10.1007/s10518-018-0462-1

Damiani, N., Miglietta, M., Mazzella, L., Grottoli, L., Guerrini, G., Graziotti, F. [2019] "Full-scale shaking table test on a Dutch URM cavity-wall terraced-house end unit—a retrofit solution

with strong-backs and OSB boards—EUC-BUILD-7". *Research report EUC052/2019U*, EUCENTRE foundation, Pavia, Italy. https://www.eucentre.it/nam-project.

Dizhur, D., Giaretton, M., Giongo, I., Ingham, J.M. [2017] "Seismic retrofit of masonry walls using timber strongbacks". *SESOC Journal*, 30(2): 1–30.

Dost, B., Goutbeek, T., van Elk, T., Kraaijpoel, D. [2012] "Monitoring induced seismicity in the North of the Netherlands: status report 2010". *KNMI Scientific Report WR 2012–2013*, Royal Netherlands Meteorological Institute, De Bilt, The Netherlands. http://bibliotheek.knmi.nl

Dost, B., Kraaijpoel, D. [2013] "The August 16, 2012 earthquake near Huizinge (Groningen)". *KNMI Technical Report*, Royal Netherlands Meteorological Institute, De Bilt, The Netherlands. http://bibliotheek.knmi.nl

Electrical Power Research Institute [1988] "A criterion for determining exceedance of the operating basis earthquake". EPRI, *EPRI Report NP-5930*, Palo Alto, California, United States.

Esposito, R., Messali, F., Rots, J.G. [2016] "Material characterization of replicated masonry and wall ties". *Final report 18 April 2016*. Delft University of Technology, Delft.

Esposito, R., Messali, F., Ravenshorst, G.J.P., Schipper, H.R., Rots, J.G. [2019] "Seismic assessment of a lab-tested two-storey unreinforced masonry Dutch terraced house". *Bulletin of Earthquake Engineering*, 17(8):4601–4623. https://doi.org/10.1007/s10518-019-00572-w

European Committee for Standardization [1998] *EN 1052-1: methods of test for masonry—part 1: determination of compressive strength*. CEN, Brussels, Belgium.

European Committee for Standardization [1999] *EN 1015-11: methods of test for mortar for masonry—part 11: determination of flexural and compressive strength of hardened mortar*. CEN, Brussels, Belgium.

European Committee for Standardization [2002] *EN 1052-3: methods of test for masonry—part 3: determination of initial shear strength*. CEN, Brussels, Belgium.

European Committee for Standardization [2005] *EN 1052-5: methods of test for masonry—part 5: determination of bond strength by the bond wrench method*. CEN, Brussels, Belgium.

European Committee for Standardization [2006] *EN 300: Oriented Strand Boards (OSB)—definitions, classification and specifications*. CEN, Brussels, Belgium.

European Committee for Standardization [2013] *EN 14080: timber structures—glued laminated timber and glued solid timber—requirements*. CEN, Brussels, Belgium.

European Committee for Standardization [2015] *EN 772-1: methods of test for masonry units—part 1: determination of compressive strength*. CEN, Brussels, Belgium.

European Committee for Standardization [2016a] *EN 206: Concrete - Specification, performance, production and conformity*. CEN, Brussels, Belgium.

European Committee for Standardization [2016b] *EN 14081-1: timber structures. Strength graded structural timber with rectangular cross section. Part I: general requirements*. CEN, Brussels, Belgium.

Giaretton, M., Dizhur, D., Ingham, J.M. [2016] "Shaking table testing of as-built and retrofitted clay brick URM cavity-walls". *Engineering Structures*, 125:70–79. https://doi.org/10.1016/j.engstruct.2016.06.032

Graziotti, F., Rossi, A., Mandirola, M., Penna, A., Magenes, G. [2016] "Experimental characterization of calciumsilicate brick masonry for seismic assessment". *Proceedings of the 16th international brick and block masonry conference: trends, innovations and challenges, IBMAC*, pp 1619–1628. https://doi.org/10.1201/b21889

Graziotti, F., Tomassetti, U., Kallioras, S., Penna, A., Magenes, G. [2017] "Shaking table test on a full scale URM cavity wall building". *Bulletin of Earthquake Engineering*, 15:5329–5364. https://doi.org/10.1007/s10518-017-0185-8

Graziotti, F., Penna, A., Magenes, G. [2019a] "A comprehensive in situ and laboratory testing programme supporting seismic risk analysis of URM buildings subjected to induced earthquakes". *Bulletin of Earthquake Engineering*, 17(8):4575–4599. https://doi.org/10.1007/s1051 8-018-0478-6

Graziotti, F., Tomassetti, U., Sharma, S., Grottoli, L., Magenes, G. [2019b] "Experimental response of URM single leaf and cavity walls in out-of-plane two-way bending generated by seismic excitation". *Construction Building Materials*, 195:650–670. https://doi.org/10.1016/j.conbuildmat.2018.10.076

Grünthal, G. (editor) [1998] *European Macroseismic Scale 1998 (EMS-98), Cahiers du Centre Européen de Géodynamique et de Séismologie 15*, Centre Européen de Géodynamique et de Séismologie, Luxembourg.

Guerrini, G., Senaldi, I., Graziotti, F., Magenes, G., Beyer, K., Penna, A. [2019] "Shake-table test of a strengthened stone masonry building aggregate with flexible diaphragms". *International Journal of Architectural Heritage (IJAH)*, 13(7):1078–1097. https://doi.org/10.1080/15583058.2019.1635661

Guerrini, G., Damiani, N., Miglietta, M., Graziotti, F. [2021]. "Cyclic response of masonry piers retrofitted with timber frames and boards". *Structures and Buildings*, 174(5), 372-388.

Hilti [2020] *Hilti technical datasheet: HIT-RE 500 V3 injection mortar*. https://catalogo.hilti.it/sistemi-ancoraggio/138/index.html.

Housner, G.W. [1952] "Intensity of ground motion during strong earthquakes". *Caltech Technical Report*, California Institute of Technology, Pasadena, California. http://authors.library.caltech.edu

Jafari, S., Rots, J.G., Esposito, R., Messali, F. [2017] "Characterizing the material properties of Dutch unreinforced masonry". *Procedia Engineering*, 193:250–257. https://doi.org/10.1016/j.proeng.2017.06.211

Kallioras, S., Graziotti, F., Penna, A. [2019] "Numerical assessment of the dynamic response of a URM terraced house exposed to induced seismicity". *Bulletin of Earthquake Engineering*, 17(3):1521–1552. https://doi.org/10.1007/s10518-018-0495-5

Kempton, J.J., Stewart, J.P. [2006] "Prediction equations for significant duration of earthquake ground motions considering site and near-source effects". *Earthquake Spectra*, 22(4):985–1013. https://doi.org/10.1193/1.2358175

Magenes, G., Penna, A., Senaldi, I., Rota, M., Galasco, A. [2014] "Shaking table test of a strengthened full-scale stone masonry building with flexible diaphragms". *International Journal of Architectural Heritage (IJAH)*, 8(3):349–375. https://doi.org/10.1080/15583058.2013.826299

Malomo, D., Pinho, R., Penna, A. [2018] "Using the applied element method for modelling calcium silicate brick masonry subjected to in-plane cyclic loading". *Earthquake Engineering & Structural Dynamics*, 47(7):1610–1630. https://doi.org/10.1002/eqe.3032

Messali, F., Esposito, R., Maragna, M. [2016] "Pull-out strength of wall ties". *Technical Report*, TU Delft, NL

Miglietta, M., Mazzella, L., Grottoli, L., Guerrini, G., Graziotti, F. [2019] "Full-scale shaking table test on a Dutch URM cavity-wall terraced-house end unit—EUC-BUILD-6". *Research report EUC160/2018U*, EUCENTRE foundation, Pavia, Italy. https://www.eucentre.it/nam-project.

Rothoblaas [2019] *Wood connectors and timber plates*. https://www.rothoblaas.com/catalogues-rothoblaas.

Rots, J.G., Messali, F., Esposito, R., Mariani, V., Jafari, S. [2017] "Multi-scale approach towards Groningen masonry and induced seismicity". *Key Engineering Materials*, 747:653–661. https://doi.org/10.4028/www.scientific.net/KEM.747.653

Senaldi, I., Magenes, G., Penna, A., Galasco, A., Rota, M. [2014] "The effect of stiffened floor and roof diaphragms on the experimental seismic response of a full-scale unreinforced stone masonry building". *Journal of Earthquake Engineering*, 18(3):407–443. https://doi.org/10.1080/13632469.2013.876946

Senaldi, I., Guerrini, G., Comini, P., Graziotti, F., Penna, A., Beyer, K., Magenes, G. [2020] "Experimental seismic performance of a half-scale stone masonry building aggregate". *Bulletin of Earthquake Engineering*, 18(2):609–643. https://doi.org/10.1007/s10518-019-00631-2

Tomassetti, U., Graziotti, F., Penna, A., Magenes, G. [2018] "Modelling one-way out-of-plane response of single-leaf and cavity walls". *Engineering Structures*, 167:241–255. https://doi.org/10.1016/j.engstruct.2018.04.007

Tomassetti, U., Correia, A.A., Candeias, P.X., Graziotti, F., Costa, A.C. [2019a] "Two-way bending out-of-plane collapse of a full-scale URM building tested on a shake table". *Bulletin of Earthquake Engineering*, 17(4):2165–2198. https://doi.org/10.1007/s10518-018-0507-5

Tomassetti, U., Correia, A.A., Graziotti, F., Penna, A. [2019b] "Seismic vulnerability of roof systems combining URM gable walls and timber diaphragms". *Earthquake Engineering & Structural Dynamics*, 48(11):1297–1318. https://doi.org/10.1002/eqe.3187

Tondelli, M., Graziotti, F., Rossi, A., Magenes, G. [2015] "Characterization of masonry materials in the Groningen area by means of in situ and laboratory testing". *Technical Report*, EUCENTRE Foundation, Pavia, Italy. Available at www.eucentre.it/nam-project

van Elk, J., Bourne, S.J., Oates S.J., Bommer, J.J., Pinho, R., Crowley, H. [2019] "A probabilistic model to evaluate options for mitigating induced seismic risk". *Earthquake Spectra*, 35(2):537–564. https://doi.org/10.1193/050918EQS118M

4. SEISMIC VULNERABILITY OF IRREGULAR DUTCH URM TERRACED HOUSE UNITS EXPOSED TO INDUCED SEISMICITY CONSIDERING GLOBAL AND LOCAL MECHANISMS – INFLUENCE OF THE NEW RETROFIT SYSTEM - A CASE-STUDY BUILDING

4.1 INTRODUCTION

When proposing a new structural retrofit solution, experimental tests are fundamental to assess the effectiveness of the intervention in improving the seismic capacity of the interested systems (i.e., irregular Dutch unreinforced masonry (URM) terraced houses). Once gathered sufficient knowledge on the lateral behaviour in bare and retrofitted configurations, numerical studies may assist in the seismic vulnerability assessment of a real case-study building, with typical dimensions and materials that can be found in-situ. To this end, numerical results can be interpreted in terms of damage accumulation and collapse of buildings through suitable limit thresholds, which can be experimentally identified. Numerical models can be calibrated on experimental tests, varied to be representative of an entire building typology, and subjected to several ground motions to assess the non-linear lateral response variability of the building category. Nevertheless, the seismic vulnerability of URM buildings may not be completely evaluated if local failure mechanisms are not considered. Out-of-plane (OOP) collapse of masonry elements are well-known to be one of the most significant contributors to economic losses and injuries caused by past earthquake events. Usually, results from global seismic vulnerability assessments are presented in terms of collapse or damage states fragility functions conditional on an intensity measure (IM), while OOP collapse mechanisms are separately verified. In engineering applications, it is not common to consider at the same time the two failure mechanisms. In this context, the present study presents single damage state fragility functions for bare and retrofitted configurations, that consider simultaneously global and local failure mechanisms, and could be used in practical applications.

In literature, the seismic vulnerability of structural systems is often presented in terms of fragility functions, which express the probability of exceedance of a certain threshold conditioned to an IM, which represents the external demand acting on the structure (often the PGA). To establish the probabilistic relationship between ground-motion intensities and nonlinear structural responses, a commonly used cost-effective methodology is the cloud method [Jalayer *et al.*, 2015]. It consists in subjecting a particular system to a set of

seismic excitations through Non-Linear Time-History Analysis (NLTHA) to collect a 'cloud' of intensity-response data points. These results can be then post-processed to provide the fraction of Ground Motions (GM) at each intensity level that caused collapse or exceedance a certain threshold. To this end, numerical models calibrated considering common practices and materials, capable to simulate the lateral response of the interested building typology, are the first requirements, together with a sufficiently large GM database representative of the area. Its extension is fundamental to take into account the uncertainties related to the record-to-record variability in the nonlinear response of the structures and has a great influence on the final results of the analysis [Crowley *et al.*, 2017], hence, it needs to be carefully evaluated. For instance, multiple earthquakes characterized by the same intensity measure can generate different displacement demands for the same structure, thus, the bigger the number of GMs with the similar intensity are available, the smaller the uncertainty on the structural responses to such intensity level. Nevertheless, the outcomes of the procedure can vary significantly not only based on the quality and extension of the GM database, but also on structural modelling assumptions. Several scientific authors demonstrated the difficulties in the appropriate selection of records and in the account for uncertainties inherent in the numerical modelling of the cloud method, and deemed them responsible for the limited applications of the method outside the research field [Miranda, 2000; Penna *et al.*, 2015; Martinelli and Faella, 2015]. As a results, there is a common agreement among researchers that fragility functions are strictly related to the building typology considered, as well as to the GM database used for the analysis, therefore, results should not be extended to different structures and/or different hazards. Numerous examples can be found in literature related to a wide variety of buildings typologies and seismic hazards [Rota *et al.*, 2010, Maio and Tsionis 2016, FEMA 2017], all of them share the interest on specific building typologies which can be typically found in regions with tectonic activity.

Simple numerical models that can guarantee an affordable computational load are essential to perform cloud analysis. The global seismic response of URM structures can be successfully modelled by means of the three-dimensional equivalent frame technique (e.g., Lagomarsino *et al.*, [2013]). This methodology neglects the OOP behaviour of walls, assuming that the OOP excitation has only local effects on the response of each wall, does not affect the global response of the building, and allows for a macroscopic interpretation of damage. Despite the simplifications, the approach is not suitable for a large amount of analysis due to the computational effort needed. Indeed, it is common practice to reduce real 3D structures into first-mode equivalent single-degree-of-freedom (SDOF) oscillators to perform NLTHA [Miranda, 2001]. The methodology has been widely used in literature for several different structural systems with very good results. However, in case of masonry buildings, the procedure is not trivial due to the difficulty in representing their hysteretic behaviour by means of simplified hysteretic shapes and their very short structural periods, which do not allow to use the so-called "equal displacement rule" [Kallioras *et al.*, 2019].

The aim of idealizing a 3D structure into a simplified SDOF system is to be able to synthetically represent the seismic response of a complex multi-degree-of-freedom (MDOF) model, provided that its response is governed by a single dominating mode of vibration. This assumption is usually acceptable when the structure is regular, low-rise, with sufficiently stiff diaphragms, efficient wall-to-diaphragm connections, and with a non-torsional global response. Whenever these conditions are not met by the building under consideration an equivalent SDOF idealization may not be possible. Despite all, the evaluation of URM buildings global lateral capacity may not be sufficient to have an exhaustive understanding of their weaknesses. Local OOP failures of masonry elements can represent a major cause of risk, both from the economical and safety point of views. Therefore, it is important to consider both mechanisms while assessing the seismic vulnerability of a masonry structure.

The aim of the present vulnerability assessment is to provide quantitative information on the impact of a new timber retrofit system on the seismic vulnerability of typical irregular Dutch URM terraced houses of late '70-early '80s, considering both global and local mechanisms. The study is carried out through the seismic assessment of a case-study building, with the overall features of the prototypes EUC-BUILD-6 and EUC-BUILD-7, transversal sides with typical length (8 m against 5.6 m of the experimental full-scale specimens), and average material properties that can be found in-situ. SDOF oscillators proposed by Graziotti *et al.*, [2016a] are used to assess the global vulnerability of the case-study building through NLTHA, while the model proposed by Tomassetti *et al.*, [2018] is used to perform OOP NLTHA of masonry piers. The capability of selected SDOF systems in reproducing the complex global behaviour of the interested buildings is firstly tested simulating the experimental responses of EUC-BUILD-6 and EUC-BUILD-7 [Miglietta *et al.*, 2021a]. Once demonstrated the reliability of oscillators, 3D MDOF systems are modelled through the equivalent frame techniques with the software TREMURI [Lagomarsino *et al.*, 2013], and calibrated on the experimental tests, aiming at extending transversal dimensions and generate the case-study building numerical models. These systems are then reduced to SDOF oscillators following the approach proposed by Casarotti and Pinho [2007] and subjected to NLTHA using the hysteretic models proposed by Graziotti *et al.*, [2016a]. Numerical results are used to produce global damage state fragility functions conditional on PGAs, while filtered accelerations THs are used to perform OOP NLTHA and generate collapse fragility functions for masonry piers. The results of global and local seismic vulnerability assessments are finally combined, and presented by means of single damage states fragility functions conditional on PGAs that account for global and local failure mechanisms.

The following paragraphs discuss first the SDOF and MDOF modelling approaches (par. 4.2), and the related simulations of experimental tests (par. 4.3). They are followed by the description of the methodologies used to derive fragility functions (par. 4.4) and the case-

study building. The seismic capacities of numerical models with typical and experimental features are discussed in par. 4.5 and 4.6, limit states and thresholds are defined in par. 4.7. The ground motions database used for NLTHA is presented in par. 4.8. Subsequently, the global seismic vulnerability assessments for bare and retrofitted conditions are discussed and followed by the local OOP ones (par. 4.9, par. 4.10). The integrated results for global and local vulnerability assessments are presented and discussed in terms of damage states fragility functions in par. 4.11 for the bare and retrofitted configurations. The conclusions of the study are reported in par. 4.12.

4.2 MODELLING APPROACHES

4.2.1 SDOF oscillators

The idealization of MDOF systems into first-mode equivalent SDOF oscillators is performed following the approach proposed by Casarotti and Pinho [2007]. The real MDOF systems are reduced to two-horizontal degrees of freedom systems, with lumped mass at each level. At the first one, the entire mass of the structure included between mid-first storey and mid-second storey height is placed, the above-remaining mass is lumped at the second level, while the non-oscillatory mass at the base of the buildings is disregarded. The choice of producing simplified SDOF systems from two-horizontal degrees of freedom MDOF systems, rather than three for first-, second-floor and roof levels, as one may intuitively expect, is dictated by the need to neglect the influence of the roof-gable subsystem dynamic properties in the overall response of the buildings. The mass and lateral stiffness of the roof interstorey would be too low compared to the other ones, hence, considering it in the transformation process, would affect the properties of the entire SDOF systems, altering the results of gamma coefficients and driving the oscillators far from the experimental results in terms of global parameters [Kallioras 2019]. Indeed, the gable-wall sub-system mode of vibration appear to be the building dominating one from modal analysis, jeopardizing the possibility to reduce the systems into a SDOF one for global assessment. By neglecting it and lumping its mass to the second-floor level, the experimental response of the buildings could be assumed as dominated by a single global mode of vibration. The high vulnerability of the roof-gable system, with respect to the rest of the building, could be observed since the very first dynamic test performed on full-scale prototypes of Dutch URM terraced houses [Graziotti *et al.*, 2017] and was specifically evaluated by Tomassetti *et al.*, [2019a].

The transformation factors Γ_j were computed as:

$$\Gamma_j = \frac{\sum m_i \Phi_{i,j}}{\sum m_i \Phi^2{}_{i,j}} = \frac{m^*{}_j}{\sum m_i \Phi^2{}_{i,j}} \tag{4.1}$$

where m_i is the mass associated to first- and second-floor levels and $\phi_{i,j}$ are floor displacements (normalised to the maximum one). They correspond either to the

experimental inelastic first-mode shape of a test run *j*, assumed constant within each of them, or to the numerical elastic dominant mode shape obtained with modal analysis. To transform the dynamic global backbone curve from MDOF into SDOF terms (i.e. from $\Delta_{2,j}$-$V_{b,j}$ into $\Delta_{SDOF,j}$-$a_{SDOF,j}$ format), the following equations are used:

$$\Delta_{SDOF,j} = \frac{\Delta_{2,j}}{\Gamma_j} \quad \text{and} \quad a_{SDOF,j} = \frac{V_{b,j}}{\Gamma_j m^* g} \tag{4.2}$$

The drift-ratio response of the equivalent SDOF systems are computed as:

$$\theta_{SDOF,j} = \frac{\Delta_{2,j}}{H_{eff}} \tag{4.3}$$

where:

$$H_{eff,j} = \frac{\sum m_i h_i \Phi_{i,j}}{\sum m_i \Phi_{i,j}} \tag{4.4}$$

The acceleration-displacement (AD) capacity curve is subsequently transformed into a bilinear relationship by preserving the energy below the curves, following the approach included in NPR-9998 [2020].

Another important aspect to be addressed in the SDOF idealization is the selection of the hysteretic model to be employed. The SDOF oscillators developed by Graziotti *et al.*, [2013, 2014, 2016a] were calibrated to match the elastic properties (i.e., initial stiffness and vibration period) and hysteretic responses of two benchmark MDOF systems, which in turn were calibrated on the experimental results of cyclic pushover tests [Magenes *et al.*, 1995]. The MDOF systems were able to match very well the cyclic response of two opposed building configurations: a structure with slender piers with flexure-dominated (FD) behaviour, and a case with squat piers and shear-dominated (SD) behaviour. Rayleigh viscous damping coefficients were appropriately set to maintain a viscous damping ratio nearly constant at 2% for periods ranging between the first-mode initial elastic period and the secant period at near-collapse conditions [Graziotti *et al.*, 2016a]. Therefore, two SDOF oscillators were generated by calibrating their elastic properties (i.e. initial stiffness and vibration period) and matching the hysteretic and viscous responses of the two benchmark MDOF models. The equivalent viscous damping ratio ξ_{hyst} by Jacobsen [1960] was used as a measure of the per-cycle hysteretic dissipation capacity of the two systems, resulting in 13.8% for the FD and 19.9% for the SD response. The viscous damping ratio ξ_{vd} associated with each SDOF oscillator was selected by maximising the correlation between the dynamic responses of the SDOF and corresponding MDOF systems, resulting in 3% and 5% for the FD and SD oscillators, respectively.

Besides the generation of the reduced systems to simulate these two extreme seismic behaviours, other five intermediate models were obtained through the combination and proportion of the responses of the two calibrated SD and FD SDOF systems. The procedure resulted in oscillators characterised by longer elastic periods T_0 and smaller ξ_{hyst} while transitioning from SD to FD response. Viscous damping ratios ξ_{vd} within the range 3-5% were assigned to each of the five intermediate models (Table 4.1). For example, the hysteretic acceleration-displacement response for the exact intermediate model between the two extreme cases is reported in Figure 4.1, together with the elastoplastic idealization of a monotonic AD response. The selected SDOF oscillators were used in literature for different studies, for instance by Mouyiannou *et al.*, [2014], who produced a set of SDOF systems based on the same models to derive state-dependent fragility functions for masonry structures considering existing damage. More recently, Guerrini *et al.*, [2017] performed a parametric study to compare different approximated methods to estimate the inelastic seismic displacement demands on short-period masonry structures. The same was carried out by Kallioras *et al.*, [2019], who tested the predictive capability in estimating earthquake-induced inelastic displacements on short-period masonry buildings of two well-established methods (the capacity-spectrum method included in the Dutch code NPR-9998 [2020], and the N2 method of Eurocode 8, [CEN, 2004]. The results of these studies evidenced the capability of the hysteretic behaviours to cover a broad range of low-rise masonry building typologies.

Table 4.1 Properties of the reference hysteretic models (reproduced from Kallioras *et al.*, [2019]).

Model	*General properties*		*Elastoplastic properties*			*Viscous damping*
	T_0 [s]	ξ_{hyst} [%]	T [s]	dy [mm]	ay [m/s2]	ξ_{vd} [%]
100% SD	0.150	19.9	0.165	2.1	3.03	5
80% SD	0.157	18.5	0.172	2.2	2.96	4.7
67% SD	0.162	17.7	0.177	2.3	2.91	4.4
50% SD	0.170	17.1	0.185	2.5	2.86	4.1
33% SD	0.179	15.4	0.195	2.7	2.80	3.8
20% SD	0.187	14.9	0.202	2.8	2.75	3.3
0% SD	0.202	13.8	0.212	3.1	2.68	3

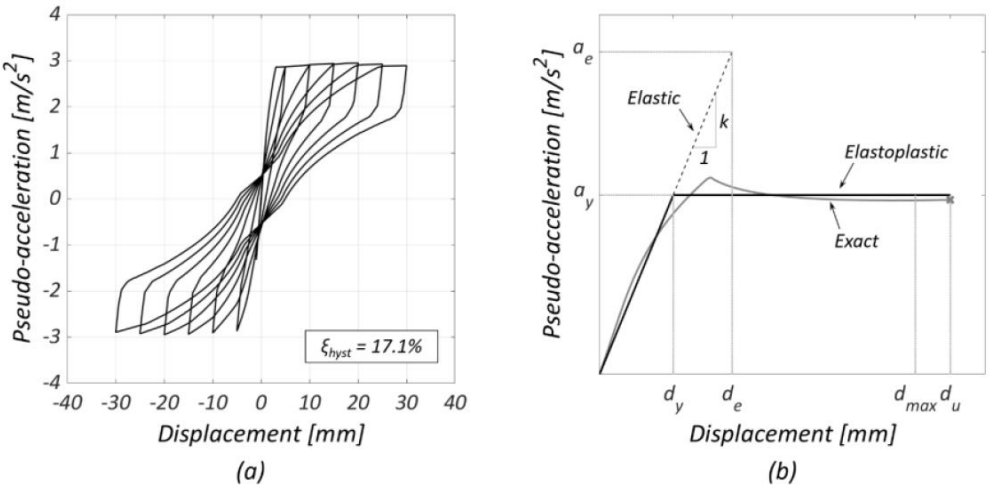

Figure 4.1 Reference SDOF models: (a) hysteretic AD response of system with ξ_{hyst} = 17.1% (50%SD); (b) elastoplastic idealisation of monotonic AD response, reproduced from Kallioras *et al.*, [2019].

4.2.2 MDOF systems

4.2.2.1 *Strategies and mechanical parameters*

MDOF numerical models are generated using macroelements with the software TREMURI [Lagomarsino *et al.*, 2013], which is based on the Equivalent Frame (EF) modelling method. This approach disregards the OOP response of walls, assuming negligible their effects on the overall structural responses. The TREMURI macroelement can simulate shear and flexural failures, including also transitions from one mode to the other as functions of the axial force [Penna *et al.*, 2014]. The implemented flexural behaviour relies on a nonlinear degrading model for rocking damage, allowing consideration of finite masonry compressive strength and stiffness degradation due to toe-crushing (Figure 4.2). The shear model is characterized by elastic, inelastic, and sliding ranges, with a post-peak softening branch that tends asymptotically to a residual static frictional strength. Parameters β (softening parameter, Figure 4.2) and G_{ct}, (nonlinear deformability parameter, Figure 4.2) control the transition from peak to residual shear strength and the displacement at peak strength, respectively. The macroelements shear resistance is implemented through an equivalent Coulomb-type criterion, with parameters (equivalent masonry cohesion, c_{eq}, and equivalent friction coefficient, μ_{eq}) properly calibrated to be macroscopically representative of different shear failure modes (i.e., diagonal cracking, shear sliding). Each macroelement is defined by: density, ρ; Young modulus, E_m; shear modulus, G_m; compressive strength, f_m; equivalent masonry cohesion, c_{eq}; equivalent friction coefficient, μ_{eq}; and, β and G_{ct}.

To simulate the experimental lateral response of the full-scale bare and retrofitted building specimens only the internal CS leaf of cavity walls, floors, and roof diaphragms were explicitly modelled. The choice of using the EF method and to disregard the explicit modelling of the clay outer leaf is motivated by mechanical considerations and by the observed experimental responses of EUC-BUILD-6 and EUC-BUILD-7, as well as by the ones observed during the formers full-scale tests on buildings belonging to the same typology tested within the present experimental campaign (EUC-BUILD-1 [Graziotti *et al.*, 2017], LNEC-BUILD-1, [Tomassetti *et al.*, 2019b]). At first, it is worth to recall that the cavity-wall system of the building typology under scrutiny is characterised by an internal CS leaf that sustain all the structural loads of the structure (floors and roof) and by an external clay veneer with no structural functions (self-standing), which are connected by a mesh of steel ties (see Figure 3.2b and d, Figure 3.5a to e and Figure 3.6a), which can be distributed with different densities, and are used to couple the two leaves. Throughout the present experimental campaign, the effect of different densities of steel ties were investigated, ranging from 1tie/m^2 to 5 ties/m^2. Regardless the configuration of the connection between inner and outer leaves, it was observed that the adopted steel ties are not able to offer a significant shear coupling effect for the in-plane response of cavity walls. Accordingly, the loadbearing CS internal structure of the tested building specimens moved independently from the clay outer leaves of the cavity walls excited in their plane. Conversely, it was observed that in case walls excited out-of-plane, all the configurations of steel ties offered an effective coupling between the two leaves, which mainly displaced simultaneously in all shake-table tests, as demonstrated by the experimental deformed shapes [Graziotti *et al.*, 2017, Tomassetti *et al.*, 2017a, Miglietta *et al.*, 2019, Damiani *et al.*, 2019]. However, being the outer leaf unloaded, it is expected to add a negligeable contribution to the OOP resistance of the cavity wall. Besides, the OOP detachment of the clay veneer from the CS one or its partial or total overturning due to the failure of tie connectors was never experimentally observed. In light of these considerations, it is deemed reasonable to neglect the explicit modelling of the clay external veneer while considering its seismic mass of the North façade by adding it as nodal forces (with nullified vertical component to avoid increasing the resistance of CS piers). In this way, the contribution of longitudinal clay veneers was fully disregarded due to the non-effective shear coupling between the two cavity wall leaves, while the inertia of the North clay outer leaf was not disregarded.

The bare case-study building is discretized through two-nodes macroelements, representing piers and spandrels, connected by nodes with associated rigid areas. The masonry density (ρ) and compressive strength (f_m) obtained from characterization tests (par. 3.2.5) are assigned to the macroelements. The shear modulus (G_m) is conventionally taken as $0.35*E_m$. As the axial and flexural response of a standard 2-node macroelement is lumped at the top and bottom interfaces, the elastic modulus of spandrels (E_m) was tripled to account for pier double-fixed boundary conditions, while the one of single piers was multiplied by 2.5 to

account for a non-perfect double-fixed condition [Penna *et al.*, 2014]. Equivalent masonry initial shear strength ($f_{v0,eq}$) and friction coefficient (μ_{eq}) were calibrated simulating the lateral responses of the full-scale specimen EUC-COMP-1 (see sect. 2, [Miglietta *et al.*, 2021b]). Since the experimental response was initially characterized by flexural rocking and followed by shear sliding failure (Figure 2.6, sect. 2, [Guerrini *et al.*, 2021]), the equivalent friction coefficient (μ_{eq}) was selected as the ratio between the residual shear strength (65 kN) and the applied vertical load at mid-height of the pier (106 kN), while the equivalent cohesion (c_{eq}) was evaluated as the ratio between the observed strength drop of 13 kN and the pier cross-sectional area. Finally, two parameters controlling the shape of the nonlinear shear model (β = 0.5 and Gct = 1.8) were selected to match the switch of governing behaviour from flexural to sliding at 0.20% drift ratio. The macroelement effective heights are selected using the methodology proposed by Dolce *et al.*, [1991], which allows to define pier heights consistently with the observed experimental crack patterns (Figure 4.3).

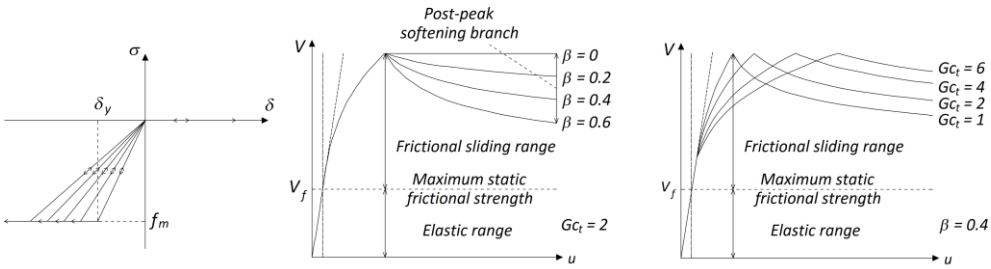

Figure 4.2 Nonlinear macroelement behaviour: nonlinear flexural degrading model; role of parameter β on the shear model; role of parameter G_{ct} on the shear model.

In retrofitted configurations, the macroelements are discretized into 6 two-nodes sub-elements of equal height, as proposed by Bracchi *et al.*, [2020] for modelling the lateral behaviour of reinforced masonry piers. This because the effect of the timber system on masonry piers lateral capacity is similar to a common steel reinforcement: it activates after masonry cracking and improve masonry strength and deformation capacities [Miglietta *et al.*, 2021a]. As for bare conditions, masonry density (ϱ) and compressive strength (f_m) obtained from characterization tests (par. 3.2.5) are assigned to the macroelements. Furthermore, the elastic moduli did not require any adjustment thanks to the macroelement discretisation. Equivalent masonry initial shear strength ($f_{v0,eq}$) and friction coefficient (μ_{eq}) were calibrated simulating the lateral responses of the full-scale pier specimen EUC-COMP-2 (see sect. 2). As opposed to the bare pier, the strengthened one exhibited a flexural response with yielding of tie-downs, followed by diagonal shear failure of the masonry (sect. 2, [Guerrini *et al.*, 2021]). The timber retrofit system inhibits the occurrence of sliding failure, as well as it forces the masonry to fail in diagonal shear fashion, regardless of the damage accumulated for toe-crushing. Equivalent cohesion (c_{eq}) and friction coefficient (μ_{eq}) were then calculated based on the diagonal shear criterion for regular

masonry of MIT (2018). Table 4.2 summarizes parameters assigned to CS masonry macroelements for bare and retrofitted conditions.

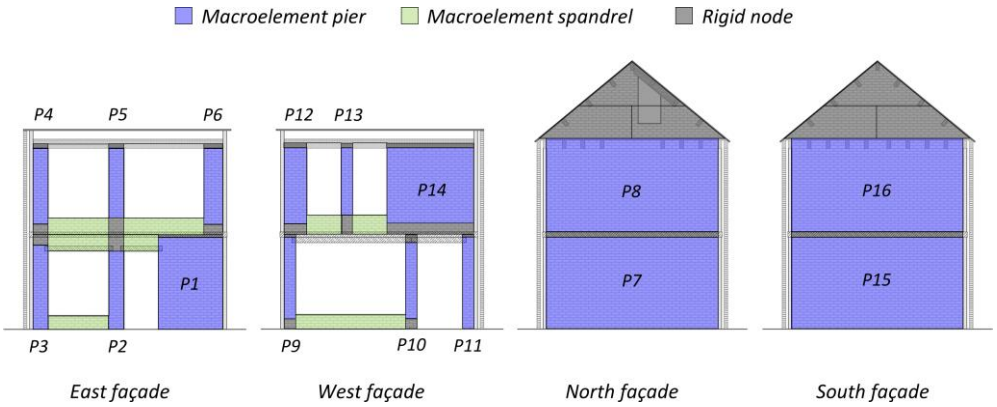

Figure 4.3 Bare building discretization and piers mapping (adapted from Damiani *et al.*, [2022]).

Table 4.2 Macroelements material properties, bare and retrofitted conditions.

Model	*Element*	E_m	G_m	f_m	c_{eq}	μ_{eq}	β	Gc_t
		[MPa]	*[MPa]*	*[MPa]*	*[MPa]*	*[-]*	*[-]*	*[-]*
Bare building	Longitudinal piers	16482**	2308	10.0	0.045	0.60	0.50	1.8
	Transversal piers	6593	2308	10.0	0.045	0.60	0.50	1.8
	Spandrels	13845**	1615	10.0	0.045	0.60	0.00	1.0
Retrofitted building	1st storey squat pier	7319	2562	10.0	0.200	0.22	0.25	1.8
	Slender piers	7319	2562	10.0	0.260	0.20	0.25	1.8
	Squat piers*	7319	2562	10.0	0.380	0.31	0.25	1.8
	Spandrels	15370**	1793	10.0	0.260	0.20	0.00	1.0

* Transverse piers and 2nd storey squat piers (P14).
** Values adjusted to consider piers boundary conditions [Penna *et al.*, 2014].

The contribution of the retrofit system is explicitly modelled using vertical and diagonal non-linear truss elements with zero moment of inertia and shear modulus and characterised by an elastic-perfectly plastic model. Specifically, the flexural contribution of the strengthening system is modelled by vertical truss elements, discretised into segments of equal length, and connected to the same nodes as the discretised macroelements (Figure 4.3). The intermediate segments of each post are characterised by cross-sectional area (A_p), mean elastic modulus (E_t) and mean tensile strength (f_t) of the timber members. Instead, top and bottom end-segments are modelled with the same cross-sectional area A_p but with equivalent Young modulus ($E_{eq,td}$) and strength ($f_{y,eq,td}$) to return the actual axial force-

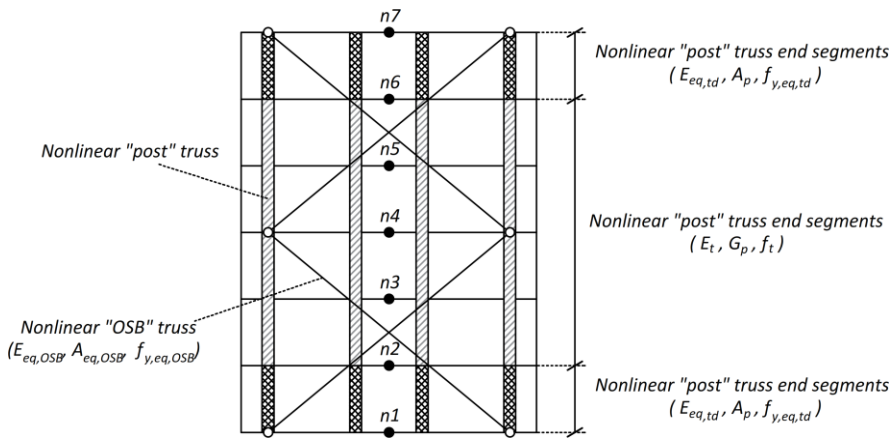

Figure 4.4 Retrofitted pier model scheme.

Table 4.3 Retrofit system nonlinear beams equivalent parameters.

Pier ID	A_p	$E_{eq,td(1)}$*	$f_{y,eq,td(1)}$*	$E_{eq,td(2)}$*	$f_{yeq,td(2)}$*	$A_{eq,OSB}$	$E_{eq,OSB}$	$f_{y,eq,OSB}$
	[mm²]	*[MPa]*	*[MPa]*	*[MPa]*	*[MPa]*	*[mm²]*	*[MPa]*	*[MPa]*
P1	4800	11724	2.66	13824	2.66	1200	10000	17.56
P2	4800	16071	2.66	21459	2.66	619	10000	5.29
P3	4800	16310	2.66	18409	2.66	769	10000	3.20
P4	4800	17735	2.66	509	2.02	717	10000	5.22
P5	4800	21593	2.66	479	2.02	630	10000	5.34
P6	4800	18467	2.66	504	2.02	774	10000	4.78
P7	4800	459	2.02	541	2.02	-	-	-
P8	4800	520	2.02	438	2.02	-	-	-
P9	4800	18163	2.66	12535	2.66	1044	10000	1.98
P10	4800	17856	2.66	15748	2.66	796	10000	3.99
P11	4800	11724	2.66	13824	2.66	1218	10000	1.70
P12	4800	18801	2.66	501	2.02	675	10000	5.73
P13	4800	23365	2.66	465	2.02	670	10000	4.80
P14	4800	18050	2.66	507	2.02	1933	10000	16.03
P15	4800	459	2.02	541	2.02	-	-	-
P16	4800	520	2.02	438	2.02	-	-	-

* Subscripts 1 and 2 indicates respectively the bottom and top segments of the "post" nonlinear beams.

displacement relationship of tie-down connectors. Similarly, the contribution to the shear resistance offered by OSB is modelled through four inclined nonlinear elastic-perfectly plastic truss elements connected to top, mid-height, and bottom nodes, allowing to capture the effects of double-curvature boundary conditions (Figure 4.4). For each pier, the additional contribution given by the nailed OSB to the shear strength was analytically evaluated following the prescriptions of AWC, 2015, therefore, starting from the assignment of the Young modulus of the elements, equivalent area and equivalent strength of the inclined trusses were calculated to return the actual shear-displacement relationship of nailed OSB. Table 4.3 summarizes the values assigned to each pier with reference to Figure 4.3.

4.2.2.2 *Diaphragms*

In TREMURI, diaphragms are modelled through two-dimensional orthotropic membrane finite elements, discretized by 4 nodes with 2 degrees-of-freedom in the global coordinate system (u_x, u_y). The mechanical parameters to be input in the software correspond to: the moduli of elasticity of the membrane along the two main directions (E_1, E_2), the shear modulus (G), the Poisson ratio (ν) and the equivalent thickness (t_{eq}). Among them, the most impacting on the behaviour of diaphragms is the shear modulus (G), which governs the capability to transfer shear forces from one side to the opposite of the building. The bare second-floor timber diaphragm is modelled using the approach suggested by Brignola *et al.*, [2009]. The additional contribution given by the installation of the OSB layer is computed following the recommendations of AWC [2015]. Concerning the roof diaphragms, they are calibrated on the experimental results of EUC-BUILD-7. In particular, a suitable value of shear stiffness is selected to be representative of the degrading effects that they underwent during the incremental test. A detailed discussion on the modelling of diaphragms can be found in Damiani *et al.*, [2022]. Table 4.4 summarized the employed mechanical parameters for diaphragm characterizations.

Table 4.4 Floor and roof diaphragms assigned properties.

Model	*Element*	E_1	E_2	G	ν	t_{eq}
		(MPa)	*(MPa)*	*(MPa)*	*(-)*	*(mm)*
Bare & Retrofitted building	1st floor RC slab	30000	30000	12500	0.2	200
	Roof diaphragm	17500	11000	27	0.3	18
Bare building	2nd floor diaphragm	26000	11000	5	0.3	18
Retrofitted building	2nd floor diaphragm & OSB	26000	11000	31	0.3	18

4.2.2.3 *Additional modelling considerations*

The complex behaviours exhibited by the full-scale specimens in bare and retrofitted configurations during the shake-table tests required additional considerations to be simulated. The bare building prototype lateral response was governed by the in-plane flexural behaviour of masonry longitudinal piers until the activation of the second-floor local mechanism, which activated during the run with EQ-NPR-66% (attainment of DL2), and emphasized lateral displacements at that height (par. 3.4.2). To take into account such behaviour, the rigid node areas on top of the second storey piers of the numerical model (Figure 4.3) are substituted by masonry macroelements with reduced coefficient of friction (μ_{eq}=0.1), and shear modulus calibrated to obtain a simultaneous rupture at the defined level of intensity. Focusing on the experimental lateral response exhibited by the retrofitted full-scale building prototype, it was characterized by a significant lowering of the overall stiffness with the increasing of the external excitation. This phenomenon could be initially explained discussing the results of the in-plane cyclic test performed on the full-scale bare and retrofitted CS piers (EUC-COMP-1 and EUC-COMP-2, par. 2), but also emphasized by the collapse mechanisms exhibited by EUC-BUILD-7. During the in-plane cyclic test, the timber frame inhibited the shear-sliding failure of the masonry, allowing some flexural overstrength to develop and forced the masonry to fail in diagonal shear mode. Its initial stiffness was very similar to the one of the bare specimen, while the timber system, characterized by a later stiffness equal about 10% of the one of the masonry, only after first cracking of the masonry began to work. The retrofitted pier was able to sustain twice the displacements sustained by the bare pier and to accumulate extensive damage at the base corners due to toe crushing, with the masonry no longer able to withstand vertical loads, which were gradually transferred to the timber frame. This effect was demonstrated by the progressive lowering of the RC top beam with the increasing of displacement as well as by top and bottom sill plates dented by the vertical post duo to axial compression forces. Overall, the retrofitted specimen sustained more than twice the lateral displacement sustained by the bare pier, as the timber system allowed to fully exploit the flexural-rocking capacity and gradually took over the masonry compression resistance. It is believed that this phenomenon also took place in the incremental dynamic tests performed on the retrofitted full-scale building. The repetition of test runs with the increasing scaling of the ground motion subjected the structure to increasing displacement demands and to extensive accumulation of damage. The building specimens was able to sustain such a high lateral displacements thanks to the retrofit system, which gradually took over the masonry causing the lowering of the overall stiffness. The modelling of this peculiar variation of building properties could not be simulated by only one numerical model through the software TREMURI since no degradation law are available for the purpose. Besides this complex mechanical behaviour, EUC-BUILD-7 during the last run of the incremental test exhibited the connection between two perpendicular resisting walls failed, leading to the separation of the two walls. This peculiar occurrence is hardly reproduceable through the

EF method. In light of these considerations, two MDOF macroelement models are generated, one to simulate the response of the retrofitted building specimen in DS1, DS2 and DS3, and one for the response in DS4. They differ in the masonry shear modulus of macroelements, which is reduced by 80% in the second model to simulate the building response in an advanced damage state. The reduction factor was found as the smallest value that allows to reach convergence of numerical results.

4.2.2.4 *Damping*

In dynamic analysis the definition of damping is fundamental to compute in the equation of motion the velocity dependent forces contribution, which could not be captured by hysteretic models. In the TREMURI program one of the most common approaches is implemented: the Rayleigh viscous damping model. It assumes that the damping matrix can be rewritten as the combination of a mass- and stiffness-proportional matrices, computed using the initial elastic stiffness matrix:

$$\bar{C} = \alpha_R \bar{M} + \beta_R \bar{K} \tag{4.5}$$

where $\bar{C}$, $\bar{M}$, and $\bar{K}$ are damping, mass and initial stiffness matrices, while α_R and β_R are the two Rayleigh damping coefficients. The methodology allows to define a relatively constant damping ratio ξ_{target} within a selected range of frequencies [Chopra 2012].

To simulate the dissipative behaviours observed during the incremental dynamic test on the bare building, three different values of damping ratio are used: 10% for the firsts two test runs (low damage), 7% for the second two test runs (intermediate damage), and 0.75% for the remaining runs (high damage). Instead, the use of two models for the retrofitted building test simulation allowed to keep a constant 5% damping ratio. Further details can be found in Damiani *et al.*, [2022].

4.3 SIMULATION OF THE INCREMENTAL SHAKE-TABLE TESTS

The numerical capabilities of the selected SDOF and MDOF modelling approaches, in simulating the global seismic behaviour of the interested building typology, is firstly investigated by simulating the experimental responses of the full-scale prototypes tested at the EUCENTRE laboratories, in bare and retrofitted configurations (EUC-BUILD-6 and EUC-BUILD-7, Miglietta *et al.*, [2021a]).

4.3.1 SDOF simulation

SDOF oscillators were generated to simulate the global responses of two irregular full-scale cavity-wall URM Dutch terraced houses incrementally tested on the shake-table at the EUCENTRE laboratories, one in bare condition and one retrofitted with a newly proposed timber system (EUC-BUILD-6 and EUC-BUILD-7, Miglietta *et al.*, [2021a]). The

calibration of numerical models pursued the best combination of dynamic parameters, and hysteretic models, that simulates the experimental global responses throughout the highest number of damage states. Dynamic properties were varied among the ones derived from single experimental runs (see sect. 4.2.1, eq. 4.1 to 4.4), while the hysteretic models were varied among the ones proposed by Graziotti *et al.*, [2013, 2014, 2016a] (from FD to SD, Table 4.1). Due to the pronounced and fast variation of mechanical properties observed during the experimental tests on EUC-BUILD-6 and EUC-BUILD-7, a pair of SDOF systems needed to be calibrated for the two configurations respectively, each pair including a first oscillator calibrated to simulate the experimental responses from damage state 1 (DS1) to the reaching of damage limit 3 (DL3) ($SDOF_b$ and $SDOF_r$), and a second one calibrated to simulate only the responses in DS4 ($SDOF_{b,DS4}$ and $SDOF_{r,DS4}$). This was necessary because, even neglecting the gable-roof sub-system, the specimens' experimental global responses in DS4 were very far from being dominated by their fundamental mode of vibration. In particular, with the increasing intensity of the GM, the bare building exhibited the local sliding of the second-floor diaphragm, while the retrofitted building was governed by a global torsional mode. Therefore, no oscillator could be calibrated to capture the evolution of the experimental response from the beginning of the incremental tests to the ends. The SDOF systems used to simulate the various stages of the experimental tests are summarised in Table 4.5 and Table 4.6, while their overall properties are reported in Table 4.7.

Table 4.5 Bare building (EUC-BUILD-6) test runs numerical models

EQ-NPR	**20%**	**33%**	**50%**	**66%**	**85%**	**100%**	**100%-rev**	**133%-rev**
Damage state	DS1	DS1	DS2	DS2	DS3	DS4	DS4	DS4
Numerical model	$SDOF_b$					$SDOF_{b,DS4}$		

Table 4.6 Retrofitted building (EUC-BUILD-7) test runs numerical models

EQ-NPR	**20%**	**33%**	**50%**	**66%**	**85%**	**100%**	**133%**	**133%-R**	**166%-R**	**266%-R**
Damage state	DS1	DS1	DS2	DS2	DS2	DS2	DS3	DS4	DS4	DS4
Numerical model	$SDOF_r$							$SDOF_{r,DS4}$		

The focuses to calibrate $SDOF_b$ and $SDOF_r$ are placed in the experimental test runs from EQ-NPR-33% (DL1) to EQ-NPR-85% (DL3), and from EQ-NPR-66% (DL1) to EQ-NPR-133% (DL3) respectively [Miglietta *et al.*, 2021a]. Instead, to calibrate $SDOF_{b,DS4}$ and $SDOF_{r,DS4}$ the focuses are placed in the experimental runs from EQ-NPR-100% to the end of the test and from EQ-NPR-166% to the end of the test, for the bare and retrofitted specimens respectively. To perform NLTHA, the selected GM signals are sequentially united into one to account for the incremental nature of the simulated tests and the consequent damage accumulation, global strength, and stiffness degradation. Between each

subsequent input motions, short time-windows with zero padding were inserted to ensure that the models start every simulation from rest conditions. The selected hysteretic AD response from Graziotti *et al.*, [2016a] corresponds to the intermediate model between the two extreme cases of FD and SD responses.

The outcomes of the simulation with $SDOF_b$ are reported in Figure 4.5, which shows the overlap of numerical and experimental results in terms of SDOF force-displacement hysteresis of the simulated test runs. The major differences between the curves lie in the negative branches of the hysteresis and become more evident with the increasing of the GM intensity. This is likely due to the occurrence of the local mechanisms during the experimental tests from the run EQ-NPR-66%, an aspect that could not be captured by a simplified SDOF oscillator. As expected, numerical results could not fully simulate the fast strength and stiffness degradation observed experimentally: simulating EQ-NPR-33% the model appears slightly more flexible than the experiment, as opposed to the run with EQ-NPR-66%. Focusing on numerical inelastic displacements, they are very close to reality up in positive direction while appeared underestimated in the negative one. However, it is worth to notice that the highest error is obtained with EQ-NPR-85%, where the experimental hysteresis shows a base shear sign inversion. This effect is motivated by the activation of the second-floor diaphragm local mechanism, which exasperated the recorded displacements at the second-floor level of the specimen. The experimental strength capacity is well captured in all runs. From an overall point of view, $SDOF_b$ reproduced the experimental global responses with a sufficient degree of accuracy.

Table 4.7 SDOF system properties.

SDOF	***Model (Table 4.1)***	***m**** ***[t]***	***Γ*** ***[–]***	H_{eff} ***[m]***	T_{SDOF} ***[s]***	a_{SDOF} ***[g]***	$\Delta_{y,SDOF}$ ***[mm]***	$\Delta_{u,SDOF}$ ***[mm]***
$SDOF_b$	50% SD	26.95	1.32	4.17	0.26	0.18	3.03	15.62
$SDOF_{b,DS4}$	50% SD	21.83	1.32	4.50	0.28	0.16	3.03	39.05
$SDOF_r$	50% SD	39.48	1.07	3.80	0.21	0.35	3.92	14.82
$SDOF_{r,DS4}$	50% SD	39.48	1.07	3.80	0.26	0.45	7.85	78.38

The simulation of test runs beyond DL3 using $SDOF_{b,DS4}$ are shown in Figure 4.6. It is evident that the level of accuracy reached by $SDOF_b$ simulating the experimental response of the specimen could not be reached as well simulating the experimental behaviour in DS4 using $SDOF_{b,DS4}$. As already mentioned, during the latest runs of the incremental dynamic tests the bare building was very far from being dominated by the first-vibration mode, accordingly, the focus of the calibration could be only the matching of maximum positive displacements, disregarding more detailed considerations on the nonlinear behaviour of the structure.

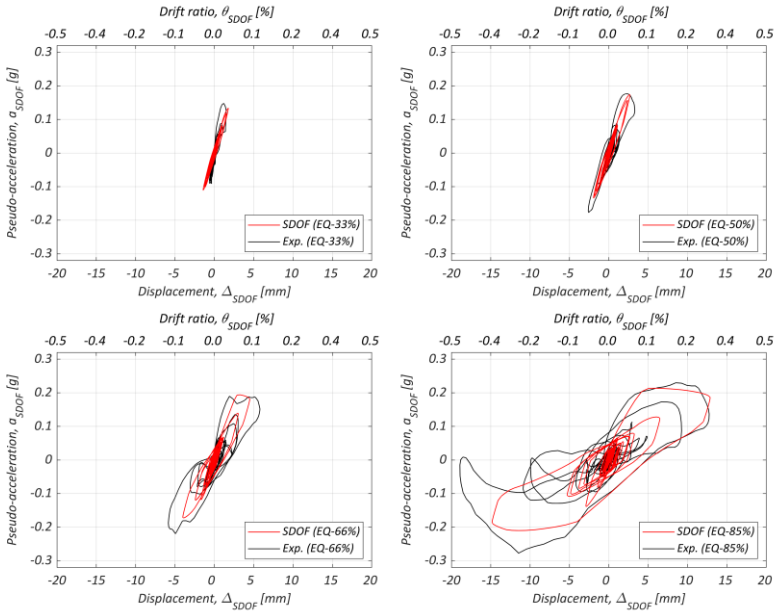

Figure 4.5 EUC-BUILD-6 incremental dynamic test simulation with *SDOF$_b$*: hysteresis overlap.

The hysteresis calibrated with *SDOF$_r$* overlapped with the experimental results are presented in Figure 4.7. From the stiffness point of view, the same conclusion of the previous case can be drawn. The model could not capture its degradation throughout the whole incremental dynamic test, even if the retrofitted building showed more regular stiffness degradation than the bare one. Focusing on the predicted inelastic displacements, a very good match was obtained up to DL2 (EQ-NPR-100%), while they were slightly overestimated in negative direction for DL3 (last simulated run). Figure 4.8 depicts the simulation of the retrofitted building experimental response in DS4 with *SDOF$_{r,DS4}$*. In this case, the SDOF system is able to fairly capture the evolution of global stiffness for the first three runs, while it could not simulate the experimental response in near collapse conditions. This because during the last run the retrofitted building response was mainly governed by the timber system due to the very high damage accumulated by the masonry, and such degraded behaviour could not be reproduced by the modelling approach. A very good match was obtained in terms of stiffness and strength up to the run EQ-NPR-200%-roof, where displacements in negative direction are only slightly underestimated. Overall, the simulation reached a sufficient degree of accuracy.

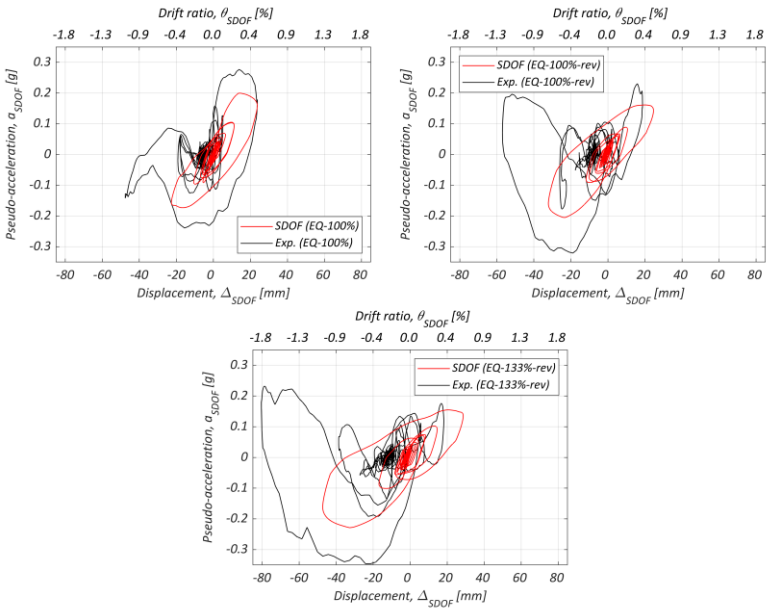

Figure 4.6 EUC-BUILD-6 incremental dynamic test simulation with $SDOF_{b,DS4}$: hysteresis overlap.

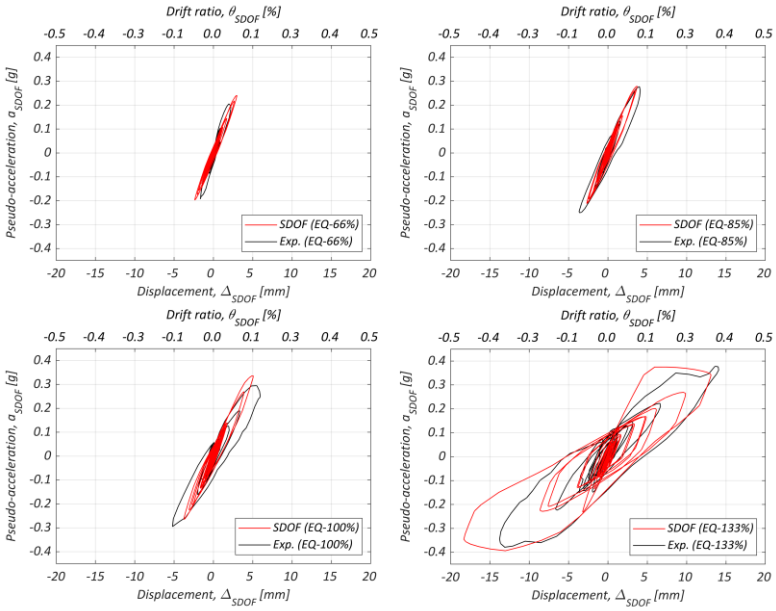

Figure 4.7 EUC-BUILD-7 incremental dynamic test simulation with $SDOF_r$: hysteresis overlap.

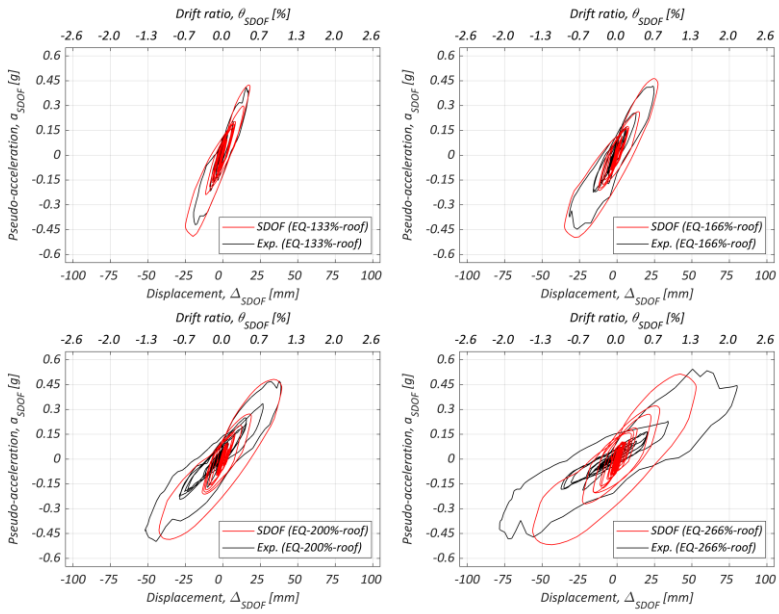

Figure 4.8 EUC-BUILD-7 incremental dynamic test simulation with *SDOF$_{r,DS4}$*: hysteresis overlap.

4.3.2 MDOF simulation

MDOF macroelement models are generated through the EF method with the software TREMURI [Lagomarsino *et al.*, 2013] and used to simulate the experimental responses of the full-scale specimens EUC-BUILD-6 and EUC-BUILD-7 [Miglietta *et al.*, 2021].

Figure 4.9 and Figure 4.10 show the overlap of numerical and experimental hysteretic behaviours of the bare building for each run of the incremental dynamic test. The model reproduces with a high level of accuracy the experimental responses up to the run with EQ-NPR-66% (DL2, Figure 4.9), which correspond to the activation of the local mechanism. Subsequently, the model returns a highly non-linear response which cannot fully capture the experimental one (Figure 4.10). The consistent simulation in positive direction is opposed by a non-reliable one in the negative direction. However, it has to be bear in mind that negative displacements are exaggerated by the local mechanism, which also determined base shear sign inversions, and that such behaviour cannot be simulated by the selected modelling approach. Focusing on acceleration and displacements THs, Figure 4.11 displays the overlap of experimental and numerical results from the attainment of DL2 to the attainment of DL4 (EQ-NPR-66% to EQ-NPR-100%-rev). Apart for the last reported run, in positive direction the main oscillations are well-captured. Instead, in negative direction, the error increases with the increase of the GM intensity. Looking at the comparison of first floor accelerations THs (Figure 4.12), a good match is obtained both in terms of maximum values and frequency content. A deeper look into the accuracy of

simulated maximum/minimum values of second-floor displacements, base shears, first- and second-floor accelerations, is provided in Figure 4.13. Overall, the model is stable in simulating base shears and accelerations at the first-floor level. The highest errors are lumped in the simulation of negative displacements and second-floor accelerations for the last 3 runs. Indeed, these are the parameters mostly affected by the local mechanism, which was fully developed during the last runs of the incremental dynamic test. In light of the obtained results, by hypothetically neglecting the effect of the local mechanisms on the building lateral response, it could be assumed that the numerical model is able to reproduce the experimental global response of the building with a sufficient degree of accuracy up to the attainment of DL3. When the building responds in DS4, experimental displacements are severely underestimated, hence, experimental damage limit thresholds are not used to post-process numerical results of NLTHA performed on this model or any derivation of it (further details in par. 4.5). Concerning OOP local failure verifications, the numerical model gives reliable estimations of input motions at the first-floor level.

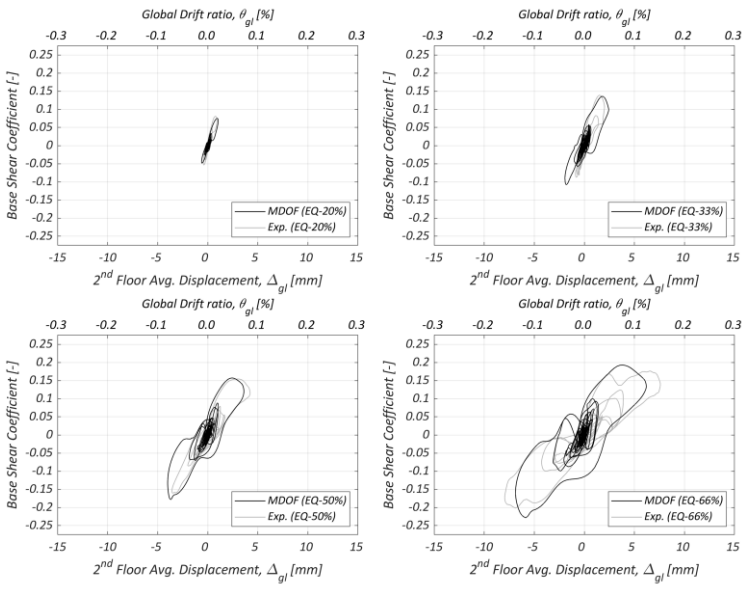

Figure 4.9 EUC-BUILD-6 incremental dynamic test simulation with EF system from run EQ-NPR-20% to EQ-NPR-66%: hysteresis overlap.

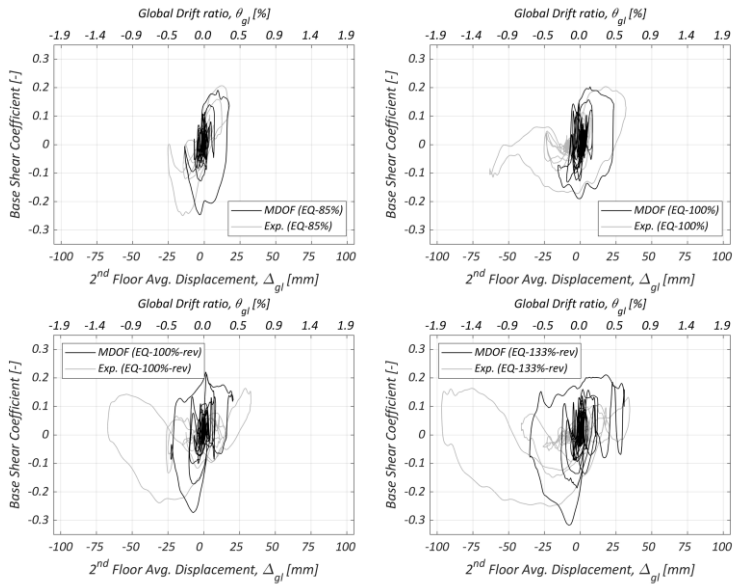

Figure 4.10 EUC-BUILD-6 incremental dynamic test simulation with EF system from run EQ-NPR-85% to EQ-NPR-133%-rev: hysteresis overlap.

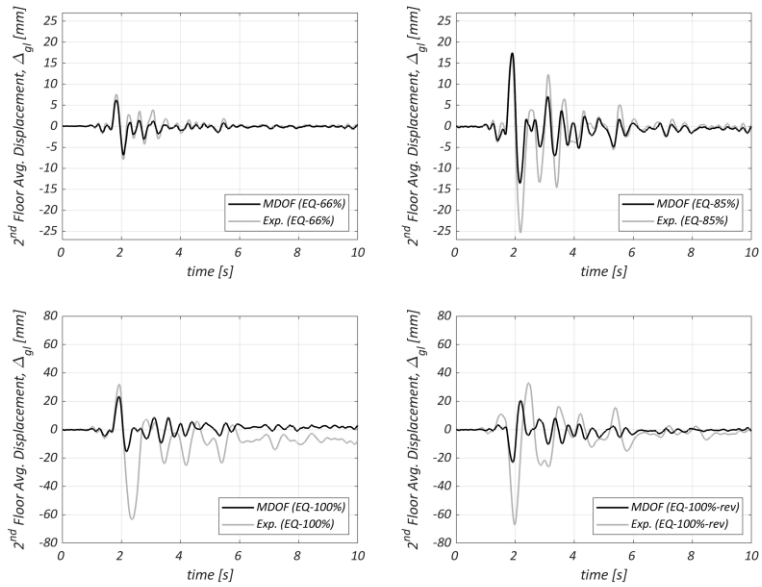

Figure 4.11 EUC-BUILD-6 incremental dynamic test simulation with EF system: displacement time histories overlap.

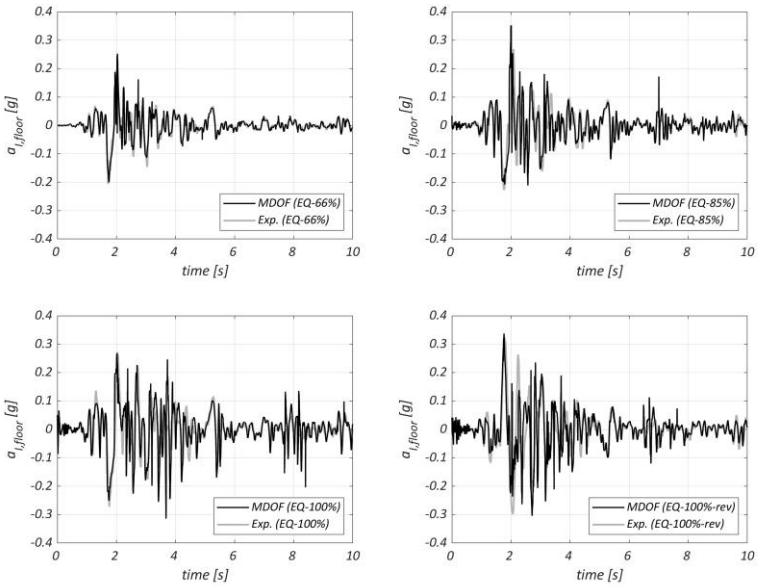

Figure 4.12 EUC-BUILD-6 incremental dynamic test simulation with EF system: displacement time histories overlap.

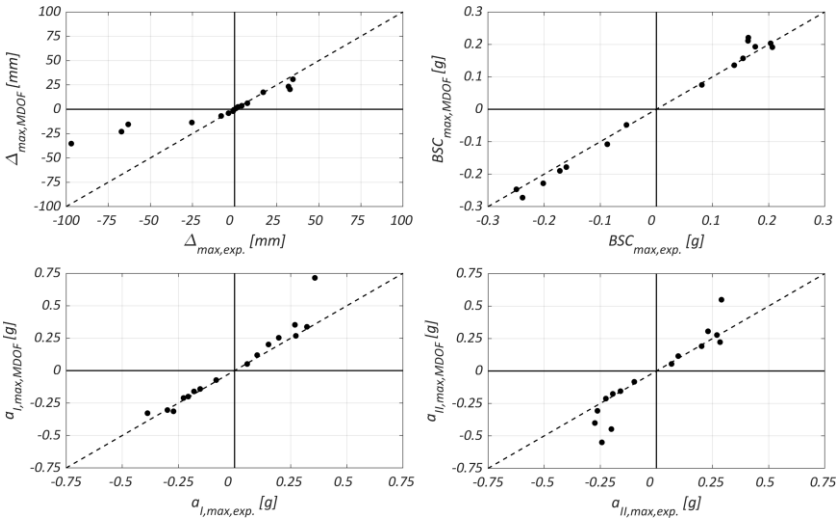

Figure 4.13 EUC-BUILD-6 incremental dynamic test simulation with EF system: experimental vs numerical maximum values.

Figure 4.14 shows the simulation results of the incremental dynamic test performed on the retrofitted full-scale building EUC-BUILD-7, from the run performed with EQ-NPR-66% (DL1) to the one with EQ-NPR-133% (DL3). The first three runs are not reported since they all belong to the experimental DS1 and are characterized by an approximatively linear response with no degradation of stiffness. Reported numerical results are very close to the reality, however, it can be observed that, with the increasing of the ground motion intensity, the overall stiffness of the prototype building decrease faster than the numerical one, despite the biggest loops preserve a very good match in all the simulations. Figure 4.15 and Figure 4.16 show the overlapping of numerical and experimental displacement and first-floor acceleration THs, also in this case a very good agreement between results can be observed. Overall, the model is able to reproduce the experimental responses with a very high level of accuracy up to the reaching of DL3, however, once the building prototype entered DS4, the experimental variation of dynamic properties could not be captured anymore by the same numerical model. This behaviour is likely due to the very high damage accumulated by the masonry during the experiment: in DS4 the global behaviour was almost entirely governed by the timber retrofit system, which gave to the structure very high flexibility and displacement capacities. This observation resulted also from the cyclic in-plane tests performed on two identical CS piers, in bare and retrofitted configurations (COMP-1 and COMP-2, par. 2, Guerrini *et al.*, [2021]). There, the masonry reached such an advanced level of damage that could accommodate very high horizontal displacements, while axial loads were gradually transferred to the timber system towards the latest cycles. Indeed, the test was interrupted at a high drift level due to diagonal failure of the masonry for displacement compatibility with the timber system. Such a complex interaction between a severely damaged masonry and the timber system required the generation of a new MDOF model with a lowered stiffness to simulate the experimental response of the building prototype in DS4 (from run with EQ-NPR-133%-roof). In particular, the shear stiffness of the masonry material is reduced to 20% of the experimental one, while all other parameters were kept unvaried.

Figure 4.17 shows the overlap of numerical and experimental global hysteresis for DS4. The model captures the experimental responses with a high level of accuracy for the first two run simulations, while the decreased stiffness showed during the last two runs is not reproducible despite a significantly lowered stiffness. As evidenced by the comparison of displacement THs (Figure 4.18), maximum values are slightly underestimated for the second to last run, while they are highly underestimated for the last one. Despite all, focusing on the simulate accelerations at the first-floor level (Figure 4.19) a good agreement between results can be observed.

To provide a closer look to the performances of the two generated MDOF models simulating the whole incremental dynamic test, Figure 4.20 and Figure 4.21 show the comparison between maximum values of global displacements, first- and second-floor

accelerations and base shear coefficient (BSC) for numerical and experimental results, using the model for DS1, 2, and 3, and the one for DS4, respectively. The main improvements given by the reduction of the shear modulus lie in the prediction of maximum displacements: while the experimental values recorded during the test runs beyond DS3 are severely underestimated by the first numerical model (Figure 4.20, empty dots), they are simulated with an appreciably higher level of accuracy by the numerical model explicitly calibrated to reproduce the lateral response in DS4 (Figure 4.21, filled dots). The choice of using two different MDOF models is mainly driven by the need to obtain reliable predictions of maximum displacements to allow the interpretation of NLTHA results from cloud analysis. However, it is taken into account that the numerical results underestimate the displacement capacity of the specimen in near collapse conditions, therefore, the experimentally defined DL4 would require to be reduced to interpret numerical dynamic responses.

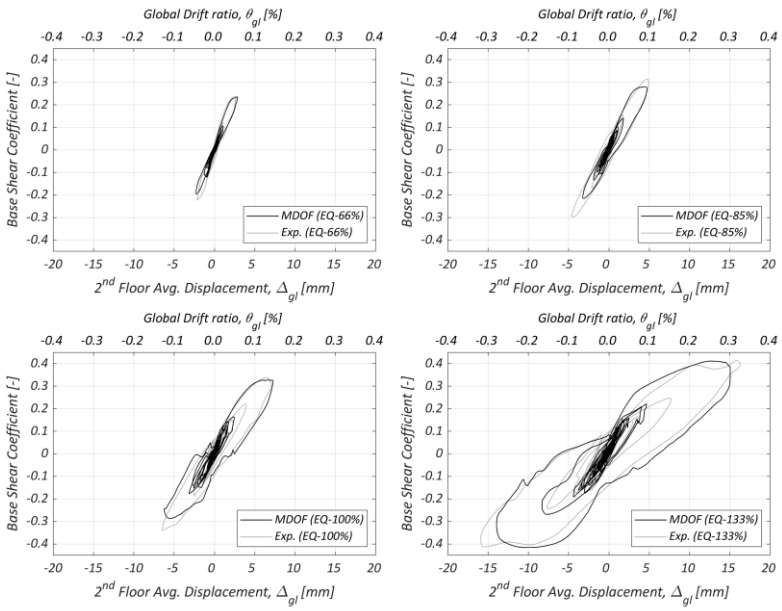

Figure 4.14 EUC-BUILD-7 incremental dynamic test simulation with EF system from EQ-NPR-66% to EQ-NPR-133%: hysteresis overlap.

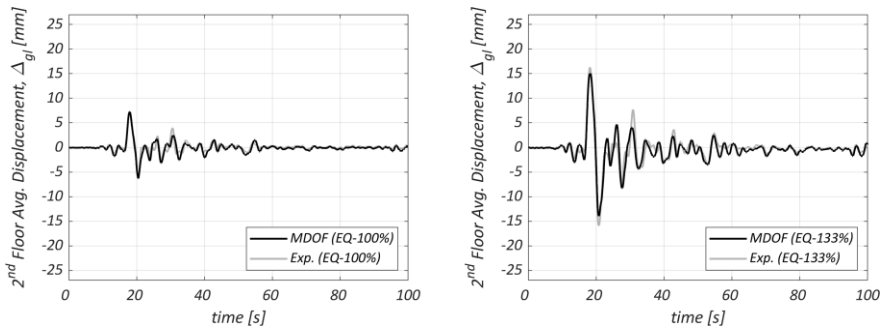

Figure 4.15 EUC-BUILD-7 incremental dynamic test simulation with EF system: displacement time histories overlap.

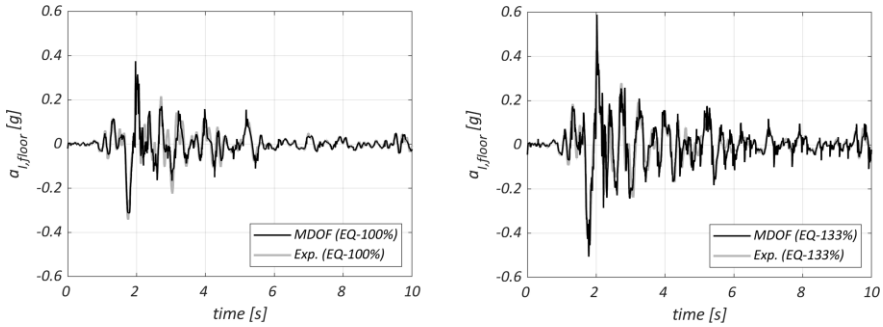

Figure 4.16 EUC-BUILD-7 incremental dynamic test simulation with EF system: 1st floor acceleration time history overlap.

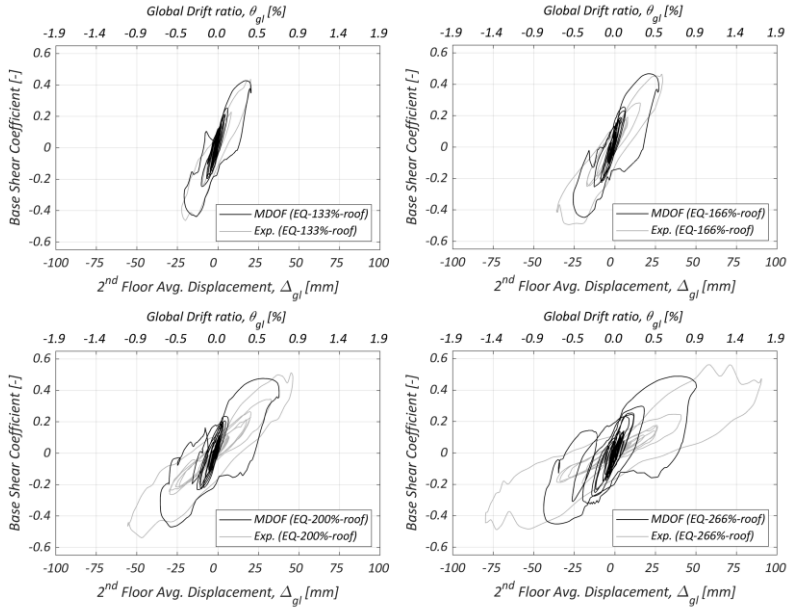

Figure 4.17 EUC-BUILD-7 incremental dynamic test simulation with EF system from EQ-NPR-133%-roof to EQ-NPR-266%-roof: hysteresis overlap.

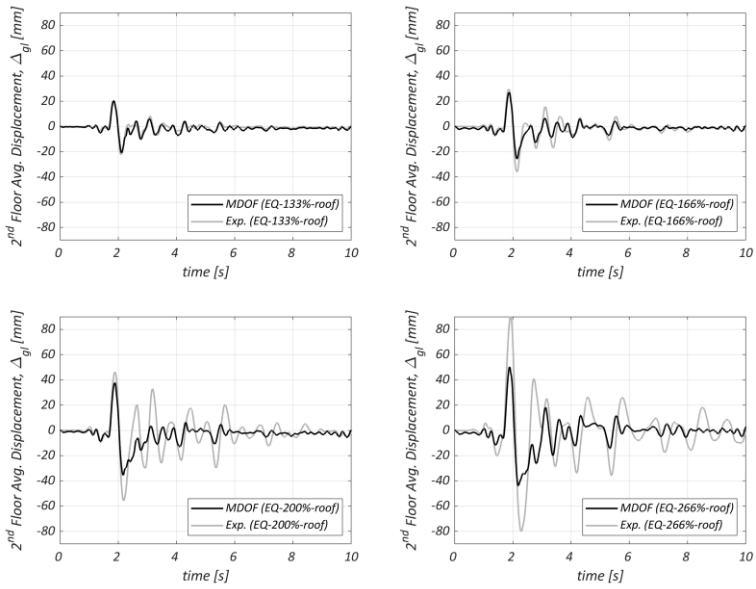

Figure 4.18 EUC-BUILD-7 incremental dynamic test simulation with EF system from EQ-NPR-133%-roof to EQ-NPR-266%-roof: displacement time histories overlap.

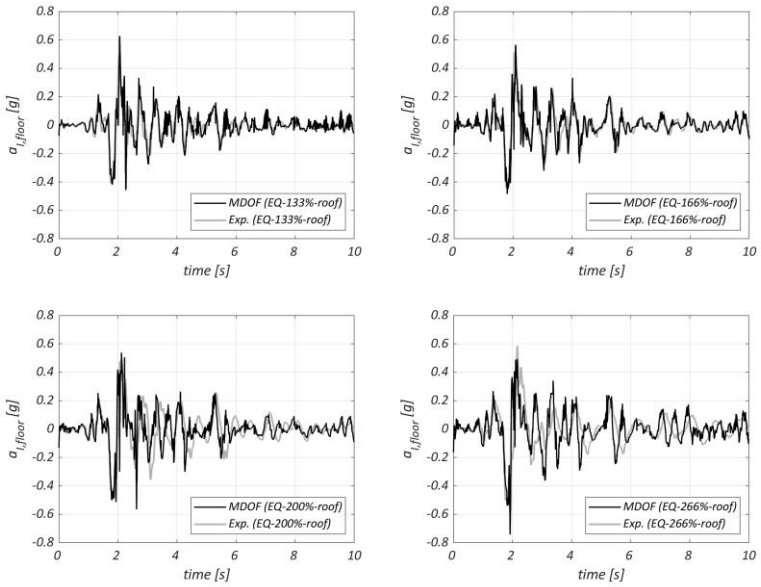

Figure 4.19 EUC-BUILD-7 incremental dynamic test simulation with EF system from EQ-NPR-133%-roof to EQ-NPR-266%-roof: 1st floor acceleration time history overlap.

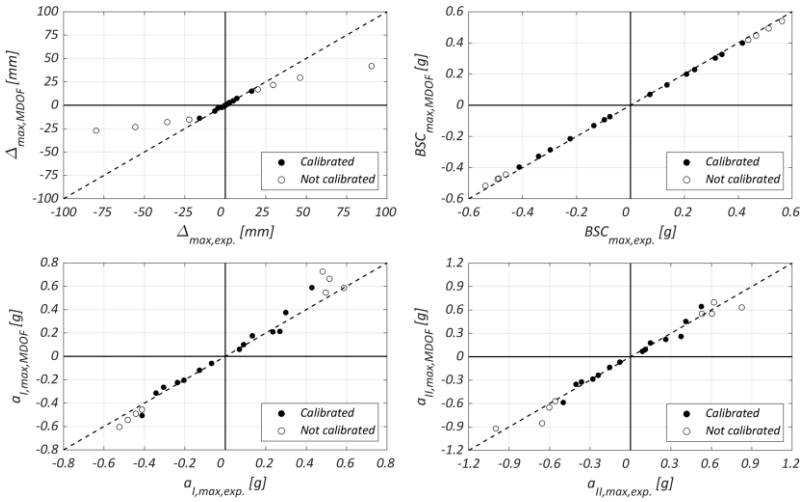

Figure 4.20 EUC-BUILD-7 incremental dynamic test simulation with EF system: experimental vs numerical maximum values (DS1, DS2, DS3).

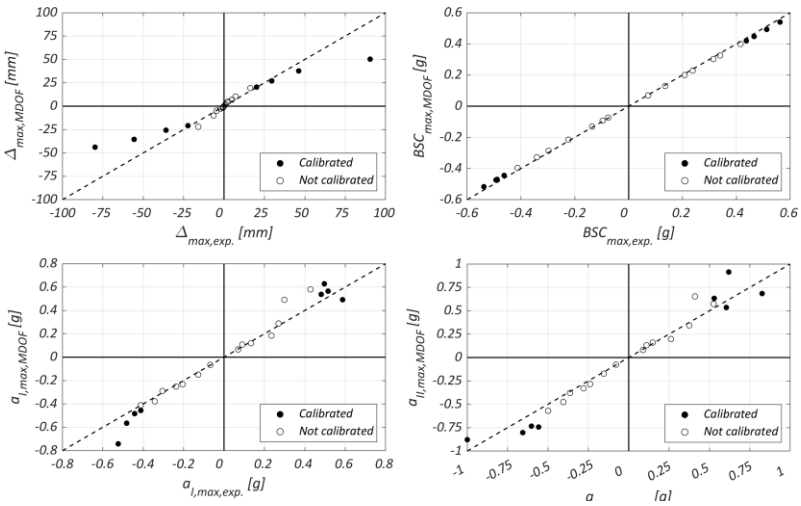

Figure 4.21 EUC-BUILD-7 incremental dynamic test simulation with EF system: experimental vs numerical maximum values (DS4).

4.4 FRAGILITY CURVES DERIVATION

In the seismic engineering field, fragility functions often express the probability of a structure (or of a structure typology) to exceed certain thresholds (i.e., displacement limits) as function of some GM IM. The methodology has been widely used during the last two decades and is increasingly popular in the structural assessment environment [Applied Technology Council, 2012, FEMA 2017]. Fragility relationships can be derived through several different approaches, for instance through fields observation of damage, engineering judgment, static analysis, or, as the present case, through NLTHA.

To define fragility functions from structural analysis, it is common to assume that for a given structure the IM values of ground motions causing the exceedance of the threshold are lognormally distributed. A lognormal cumulative distribution function can be written as:

$$P(E|IM = x) = \Phi\left(\frac{\ln(x/\theta)}{\beta}\right) \tag{4.6}$$

where $P(E|IM = x)$ is the probability that a ground motions with intensity x will cause the exceed of a certain threshold; $\Phi()$ is the standard normal cumulative distribution function (CDF); θ is the median of the fragility function (the *IM* level with 50% probability to cause the exceeding of the threshold); and β is the standard deviation of ln*IM* (also called dispersion of *IM*). In order to calibrate Equation 4.6, θ and β need to be estimated from structural analysis. Their randomness is given by the record-to-record variability since different ground motions with the same intensity level can generate very different

displacement demands for the same building. A possible way to find the best parameters that fit results is to use the maximum likelihood method, which find the parameters such that the resulting distribution has the highest likelihood of having produced the observed data. [Shinozuka *et al.*, 2000; Baker and Cornell 2005; Straub and Der Kiureghian 2008].

At each intensity level $IM = x_j$, the number of GM causing the exceedance of the displacement threshold out of a total number of seismic events is obtained through NLTHA. Assuming that observation of exceedance or not-exceedance from each GM is independent of observations from other GMs, the probability of observing z_j exceedance out of n_j GMs with $IM = x_j$ is given by the binomial distribution:

$$P(z_j \; exceedence \; in \; n_j \; GMs) = \binom{n_j}{z_j} {p_j}^{z_j} (1 - p_j)^{n_j - z_j} \tag{4.7}$$

where p_j is the probability that a GM with $IM = x_j$ will cause the structure to exceed the threshold. Taking the product of the binomial probabilities at each IM level, the likelihood of the entire dataset can be obtained:

$$Likelihood = \prod_{j=1}^{m} \binom{n_j}{z_j} {p_j}^{z_j} (1 - p_j)^{n_j - z_j} \tag{4.8}$$

where m is the number of IM levels and Π is a product over all levels. The independence of observations is assumed so that the overall likelihoods is the product of likelihoods at each IM level. By substituting Equation 4.6 in Equation 4.8, the fragility parameters θ and β are explicated in the likelihood function and their best estimates can be obtained maximizing the function:

$$Likelihood = \prod_{j=1}^{m} \Phi\left(\frac{\ln(x/\theta)}{\beta}\right)^{z_j} \left[1 - \Phi\left(\frac{\ln(x/\theta)}{\beta}\right)\right]^{n_j - z_j} \tag{4.9}$$

The procedure is particularly suitable since does not require multiple observations at each intensity level of interest (n_i can be equal to 1).

The NLTHA cloud data results are post-processed with the presented approach to assess global and local seismic vulnerabilities of the case-study building along its two main directions. Numerical maximum displacements (d_{max}) associated with each GM allowed to assign the building to a specific damage state and single piers to collapse or not collapse. By clustering these results into classes with the same PGA intensity level, the fraction of analysis producing the exceedance of a certain DL out of the total number of analysis can be derived for each PGA intensity. A lognormal cumulative distribution fragility function

can be then fitted to the obtained discrete cumulative frequency distributions through the maximum likelihood method.

4.5 Case study building numerical models (MDOF): Experimental vs real dimensions

The case-study building under scrutiny is a single end-unit of a typical irregular Dutch terraced house of late '70s – early '80s, located in the Groningen area (The Netherlands). It is characterized by a cavity-wall structural system with an internal CS loadbearing leaf and an external CL veneer with no structural functions, connected by steel ties. A RC slab is located at the first floor, while flexible timber diaphragms are located at the second floor and roof levels. Connection details and front and back façades geometrical properties are equal to the specimens tested at the EUCENTRE laboratories (EUC-BUILD-6 and EUC-BUILD-7, Miglietta *et al.*, [2021a], par. 3.2), transversal sides and material properties are assumed to present the typical characteristics that can be found in-situ. In particular, North and South façades extend for about 8 m (against 5.5 of the tested prototypes, see par. 3.2.2), while average material properties are taken from Tondelli *et al.*, [2015], who performed experimental characterization of materials in-situ. Figure 4.22 and Figure 4.23 show first interstorey plan view and elevations of the case study building, for connection details please refer to par. 3.2.2. Two orientations were considered to account for two angles of incidence of the seismic excitation for NLTHA (Figure 4.22a and b). Orientation 1 (Or_1) coincides with the one of experimental dynamic test, with the building excited along its weak direction (X). Orientation 2 (Or_2) is the building rotated by 90°, with the building excited along its strong sides (Y direction). Further details on the selected orientations are discussed in par. 4.8.

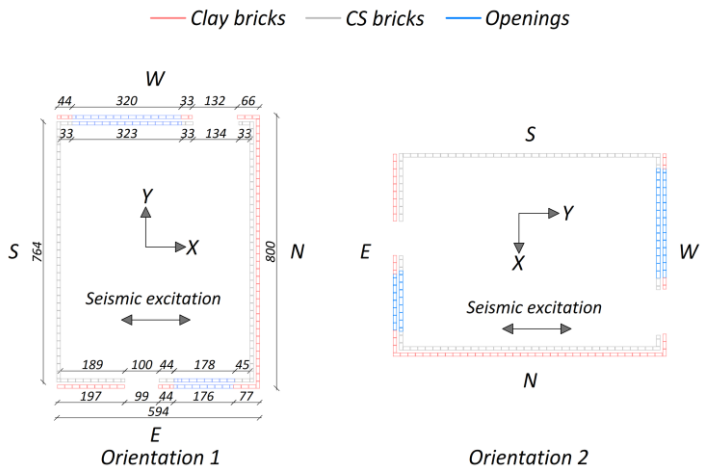

Figure 4.22 Plan view of the case-study building: Or_1, weak direction (left) and Or_2, strong direction (right).

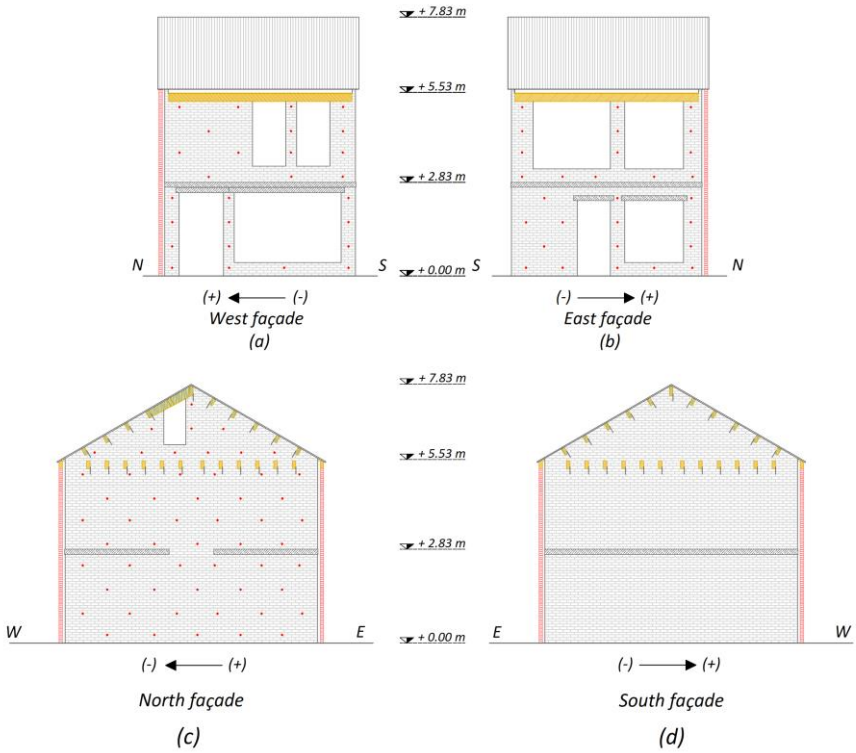

Figure 4.23 Case-study building elevations: (a) West; (b) East; (c) North; (d) South.

The case-study building MDOF numerical models are derived by extending the transversal wall lengths of the 3D equivalent frame models experimentally calibrated from 5.2 to 7.6 m (neglected clay outer-leaf, Figure 4.22a). This increase of dimensions leads to an increase of the total model mass of 42% (from 39.8 t to 56.6 t). Considering the high plan and elevation irregularity of the building under scrutiny, the influence of the increased wall lengths is investigated by subjecting the new models to the same protocols used to test EUC-BUILD-6 and EUC-BUILD-7 in both main orientations, using the experimental material mechanical properties.

Figure 4.24 shows the overlap of numerical global hysteresis for the building in bare conditions in Or_1, where the base shear is reported as BSC to consider the different masses. For the first two runs (EQ-NPR-50% and EQ-NPR-66%, corresponding to the attainment of DL2 during the shake-table test), the model with extended dimensions shows the same overall stiffness but developed a slightly lower displacement demands and BSC. The bigger difference in terms of developed strength capacities is obtained in negative direction by simulating the run with EQ-NPR-85% (attainment of DL3 during the experimental test). The simulation of the runs with the building in DS4 (from EQ-NPR-

100% to EQ-NPR-133%-rev) gave very similar results for the two models. Even if the responses are highly non-linear, the overall trends are characterized by similar displacement and strength demands. A deeper look into numerical results is proposed in Figure 4.25, where maximum and minimum displacements and base shear coefficients are plotted respectively in the same planes for the two models. Focusing on displacements (Figure 4.25a), for the first 4 runs the extended dimensions led to slightly lower demands, while from DS3 they led to higher and lower displacements for negative and positive directions respectively. Focusing on BSC values, Figure 4.25b shows that increasing the total mass and the lengths of walls perpendicular to the excitations lead numerical BSCs very similar to each other for the whole simulated incremental dynamic test. These results can appear in contrast with the expectations: intuitively, one may expect that increasing transversal piers lengths without improving the capacity of the building in the direction parallel to the seismic excitation, and increasing its total mass, will decrease the seismic capacity proportionally to the added seismic mass. However, due to the torsional response of the model, all resisting elements are excited in their plane and due to the higher capacity of transversal walls, the structure is able to redistribute higher forces between perpendicular elements. Accordingly, the increase of strength capacity perpendicular to the ground motion excitation did not translate into a decrease of the overall building capacity in X direction, despite the increased seismic mass.

Moving to the numerical model responses in Or_2, they remained elastic throughout the whole test simulation, with displacement demands lower than 1 mm. For illustrative purposes, Figure 4.26 shows the overlap of global hysteresis for the runs with EQ-NPR-85% and EQ-NPR-100%. The increased length of the walls excited in their principal plane produced a proportional increase in stiffness and strength of the whole building. Indeed, the hysteresis of the building with real dimensions show higher stiffness and strengths, and lower maximum displacements. This trend is highlighted in Figure 4.27, which compares maximum/minimum values of displacements and BSC of each simulation.

Figure 4.28 and Figure 4.29 show the numerical hysteresis obtained simulating the experimental test of EUC-BUILD-7 with the models with experimental and real dimensions in Or_1. In this case, the increased mass leads to an increase of the overall building flexibility which is in line with the expectations. In each single run, the model with real dimensions exhibited lower BSC and stiffness, denoting an increase of the overall seismic vulnerability. Maximum values of displacements and BSC are compared in Figure 4.30. In negative direction, the displacements are close to each other, while in positive direction a gradual increase for the model with real dimensions is highlighted by the graph (Figure 4.30a). Focusing on strength capacities (Figure 4.30b), the model with increased mass cannot develop values higher than 0.4, while the model with experimental dimensions reached BSC of 0.5 in both verses.

Moving to the simulations of the tests with the retrofitted buildings in Or_2, the same conclusions of the bare conditions can be drawn, therefore, results are not presented for the sake of brevity.

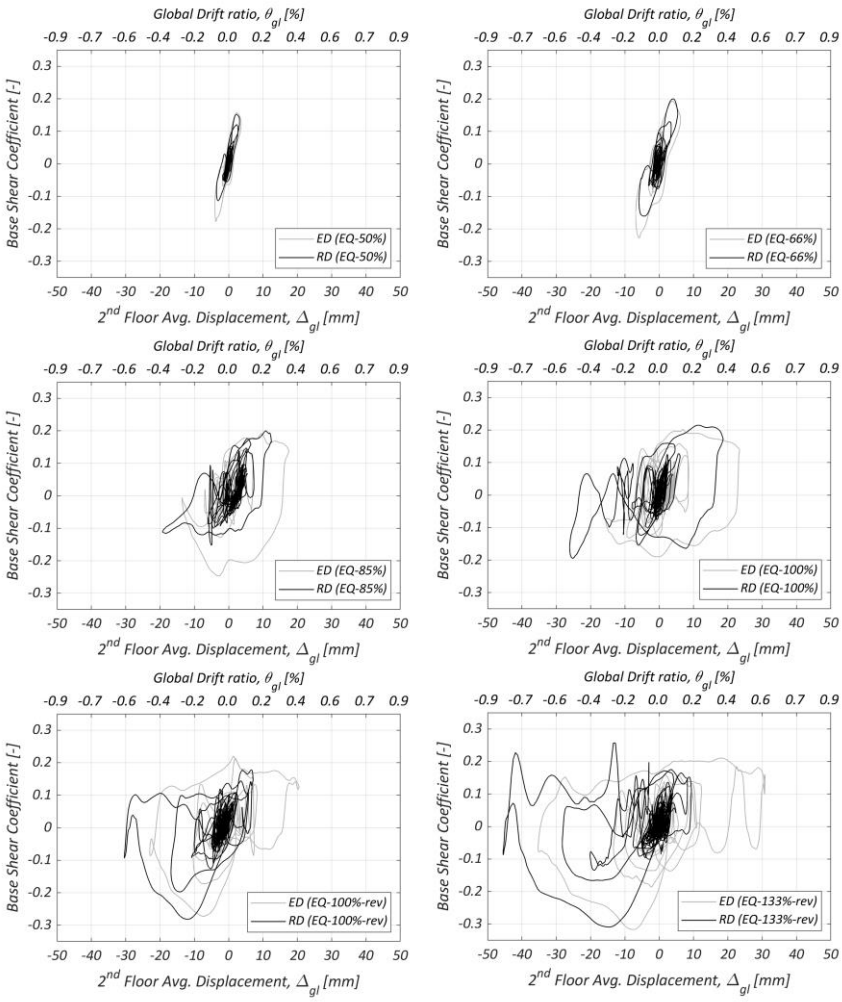

Figure 4.24 Numerical simulation of test EUC-BUILD-6: global hysteresis overlaps of EF model of case-study building and of experimental prototype (Or_1, weak direction).

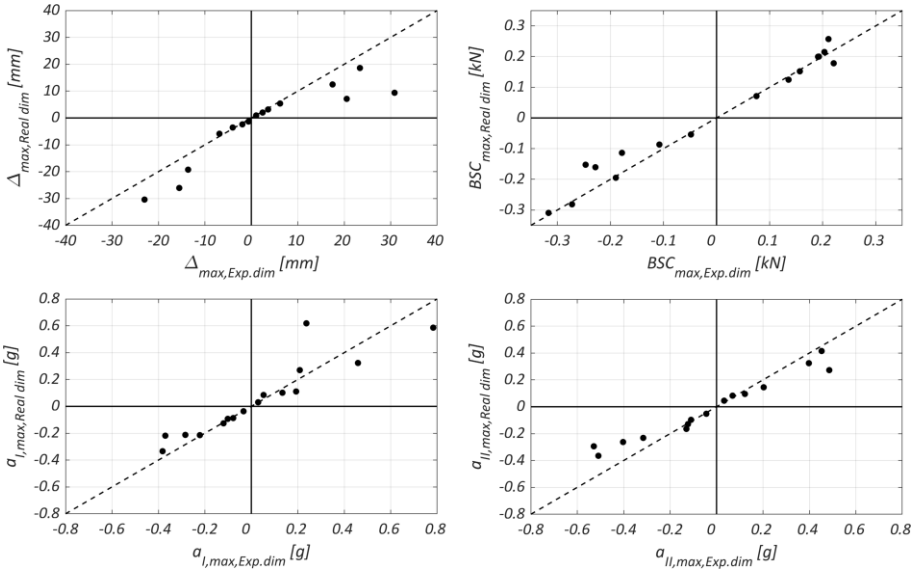

Figure 4.25 Numerical simulation of test EUC-BUILD-6: maximum values comparison of EF model of case-study building and of experimental prototype (Or_1, weak direction).

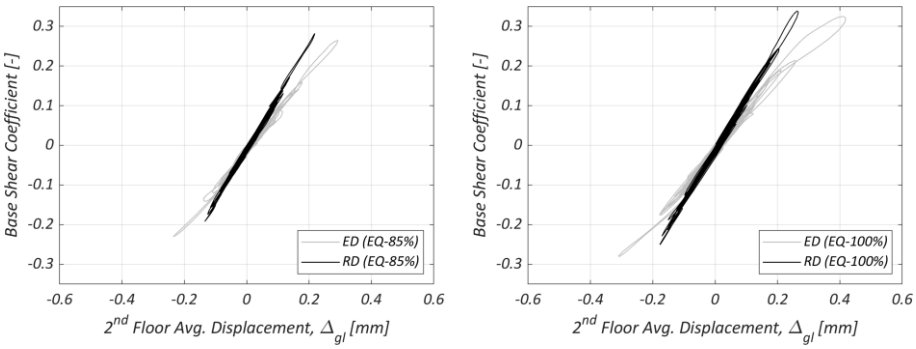

Figure 4.26 Numerical simulation of test EUC-BUILD-6: global hysteresis overlaps of EF model of case-study building and of experimental prototype (Or_2, strong direction).

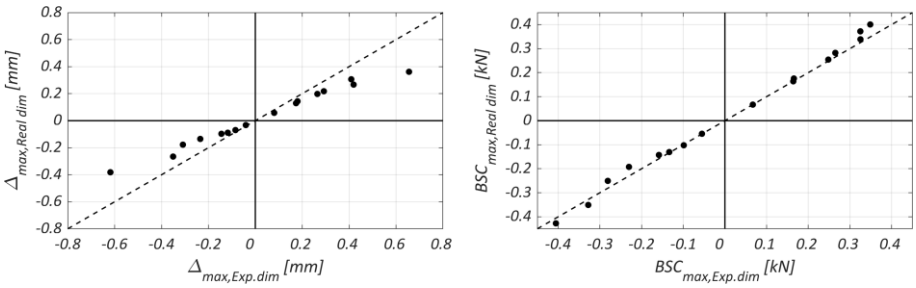

Figure 4.27 Numerical simulation of test EUC-BUILD-6: maximum values comparison of EF model of case-study building and of experimental prototype (Or_2, strong direction).

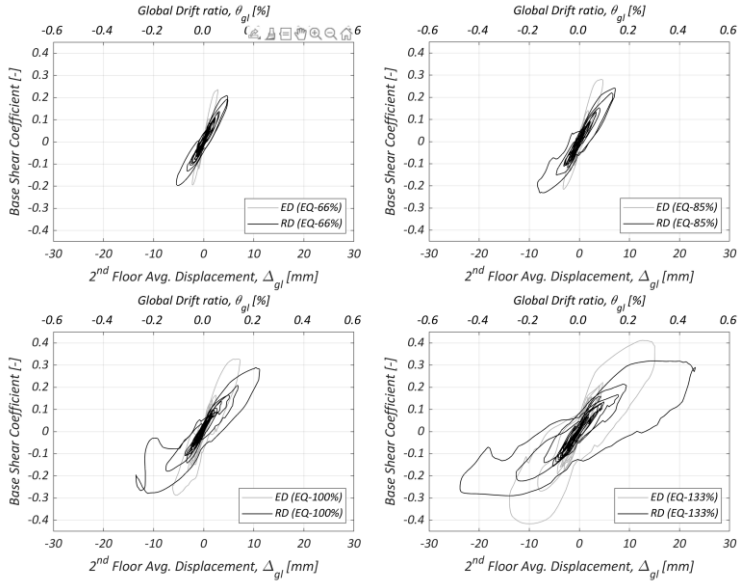

Figure 4.28 Numerical simulation of test EUC-BUILD-7: global hysteresis overlaps of EF model of case-study building and of experimental prototype (Or_1). Runs up to EQ-NPR-133% (DL3).

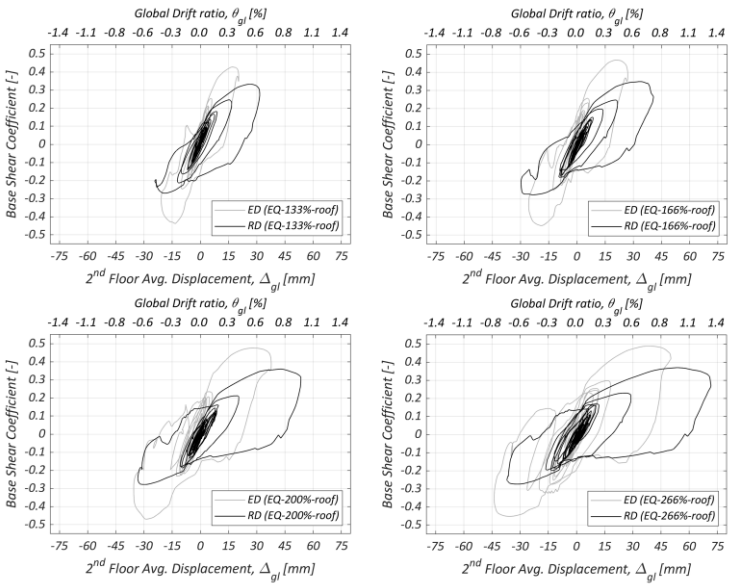

Figure 4.29 Numerical simulation of test EUC-BUILD-7: global hysteresis overlaps of EF model of case-study building and of experimental prototype (Or_1). Runs from EQ-NPR-133%-roof to EQ-NPR-266%-roof (DS4).

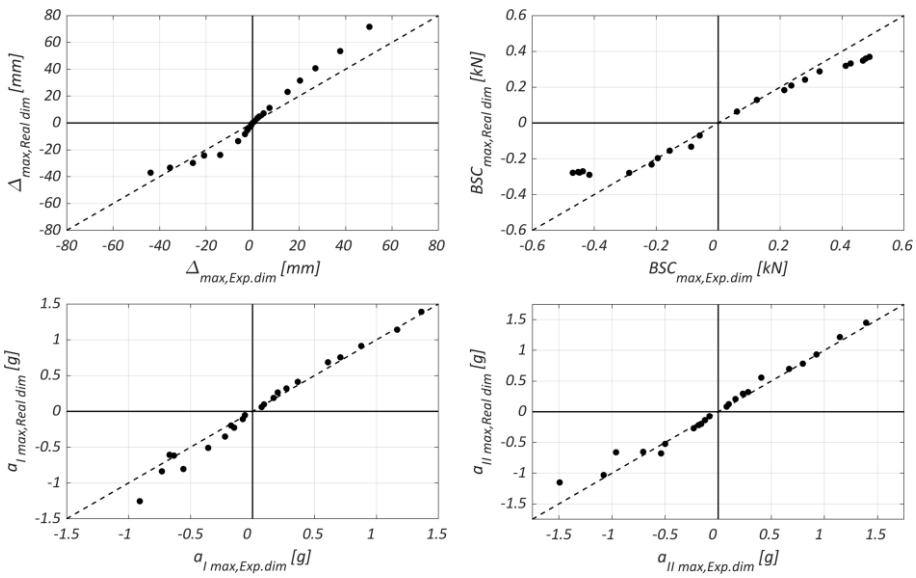

Figure 4.30 Numerical simulation of test EUC-BUILD-7: equivalent frame MDOF models with experimental and real transversal dimensions: maximum values comparison (Or_1).

4.6 CALIBRATED SDOF OSCILLATORS FOR CASE STUDY BUILDING IN BARE AND RETROFITTED CONFIGURATIONS

4.6.1 Bare conditions

The target SDOF oscillators for the case-study building in bare conditions are derived from the MDOF equivalent-frame models described in the previous paragraph, using the capacity curves resulting from the simulation of the test on EUC-BUILD-6 in X and Y directions, and the methodology presented in par. 4.2.1. The MDOF backbone curves are bi-linearized following the prescriptions of the Dutch seismic code [NPR9998, 2020]. The derived SDOF properties are calibrated to pursue the best match of results throughout the whole simulation, in terms of lateral strength, maximum displacements and accelerations, and global hysteresis. As occurred during the calibration of SDOF systems using experimental test results (see par. 4.3.1), also in this case a single oscillator cannot reproduce the experimental response in X direction throughout the whole damage states. Accordingly, two SDOF oscillators are produced: one to simulate the global response of the building in damage state DS1 and DS2 (up to the attainment of DL2), named $SDOF_{b,1,2}$; one for the building in damage states DS3 and DS4 (up to the attainment of DL4), named $SDOF_{b,3,4}$.

Figure 4.31 shows the overlap of global numerical hysteresis obtained simulating the shake-table test of EUC-BUILD-6 from EQ-NPR-20% to EQ-NPR-66%, with $SDOF_{b,1,2}$ and the equivalent-frame MDOF system. Overall, the TREMURI model is slightly stiffer than $SDOF_{b,1,2}$ at initial conditions, however, this difference is recovered approaching to DL2

(EQ-NPR-66%). While the SDOF oscillator is not able to capture the highly non-linear response and the energy dissipation simulated by the MDOF model, it returns reliable estimations of displacement and strength demands. This is also confirmed by the overlap of displacement and first-floor acceleration THs reported in Figure 4.32 and Figure 4.33, the numerical models are in good agreement in term of maximum values and frequency contents. However, focusing on displacements (Figure 4.32), it can be also noted that, with the increasing of the external excitation, the MDOF system is exhibiting an increasing negative displacement demand which could not be captured by the simplified oscillator. The comparison of maximum values (Figure 4.34) depicts a high reliability of the SDOF oscillator in terms of estimated displacements, strength and first-floor accelerations, while the second-floor ones appeared to be overestimated.

Moving to the case study building numerical responses in damage states DS3 and DS4, the hysteresis obtained simulating the runs from EQ-NPR-85% to EQ-NPR-133%-roof are overlapped in Figure 4.35. In this damage states, the non-linearity of the MDOF numerical response is increased and cannot be simulated by a simplified system. However, $SDOF_{b,3,4}$ returns good estimators of shear and displacement demands. Focusing on displacement THs (Figure 4.36), the models are in good agreement during the first two simulated runs, while, for the last two ones, the very good match in negative verse is opposed by an increasing difference in the positive one. Instead, focusing on first floor acceleration THs (Figure 4.37), an appreciable underestimation of $SDOF_{b,3,4}$ can be observed. With the aim of performing NLTHA on masonry piers located at the first-floor level, this limitation would result in unconservative OOP collapse assessments, therefore, second-floor accelerations are also evaluated (Figure 4.38). While the second-floor accelerations of the oscillator are increased with respect to the first-floor ones (approximately doubled amplitude), the ones of the MDOF system are comparable. This is likely due to the fact that the MDOF model concentrate most of the acceleration filtering effect at the ground storey. Consistently, the $SDOF_{b,3,4}$ second-floor filtered accelerations will be used to perform OOP NLTHA on masonry piers located at the first-floor level, to avoid an underestimation of the input motions. The mismatches between the models are also evidenced in Figure 4.39. Maximum displacements are very well captured in negative direction, while they are severely overestimated in positive direction during the last two simulations. A good match is obtained in terms of base shears while different levels of accuracy are obtained looking at the amplified accelerations at the first and second floor levels. The formers are very well predicted by the SDOF in negative direction, but underestimated in positive direction, as opposed to the second-floor ones, where they are well captured in both cases.

Focusing on the simulation of the experimental dynamic test with the case study building in Or_2, a SDOF model (named $SDOF_{b,Or2}$) is sufficient to reproduce the MDOF numerical response throughout the whole incremental dynamic test. As it can be noted by the overlap

of hysteresis reported in Figure 4.40, both models remained approximately linear elastic up to the last simulated run. Maximum/minimum values of displacements, base shears and accelerations, are in good agreement between the systems (Figure 4.41).

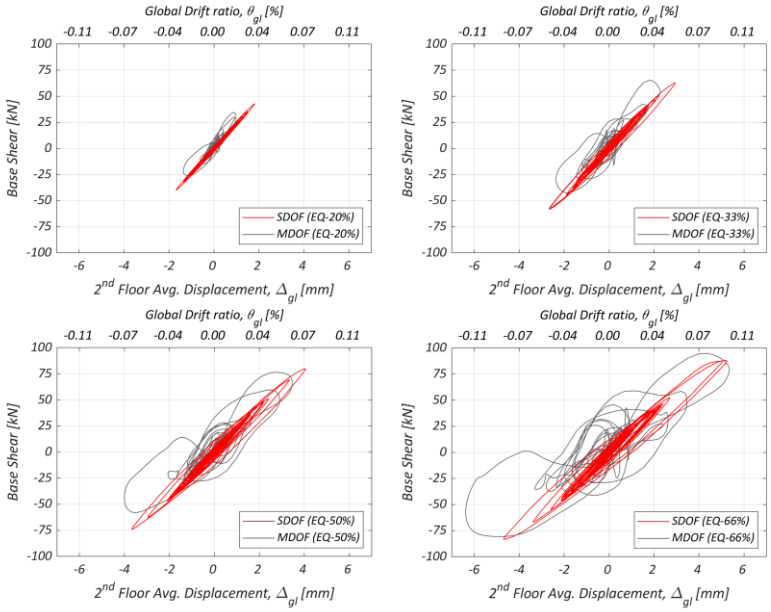

Figure 4.31 Simulation of the test on EUC-BUILD-6 with *SDOF*$_{b,1,2}$ and EF MDOF system in Or_1 from EQ-NPR-20% to EQ-NPR-66%: hysteresis overlaps.

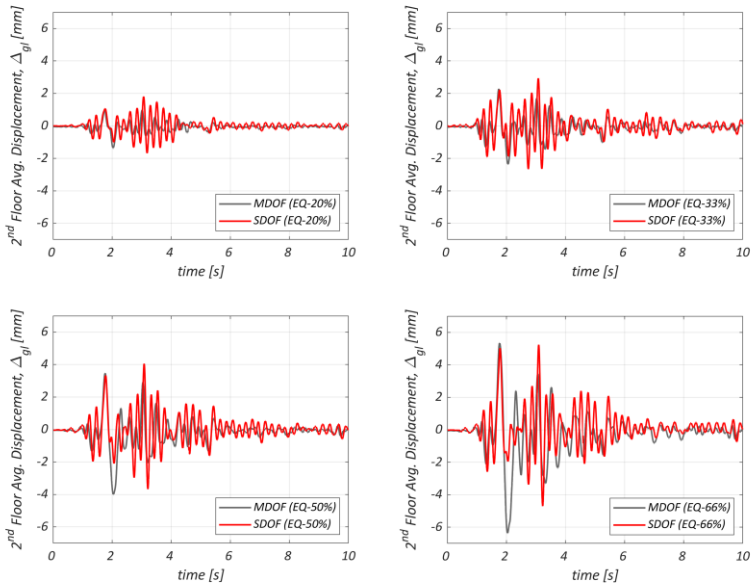

Figure 4.32 Simulation with *SDOF*$_{b,1,2}$ and with EF MDOF system in Or_1 of the EUC-BUILD-6 test runs from EQ-NPR-20% to EQ-NPR-66% (DL2): displacement TH overlaps.

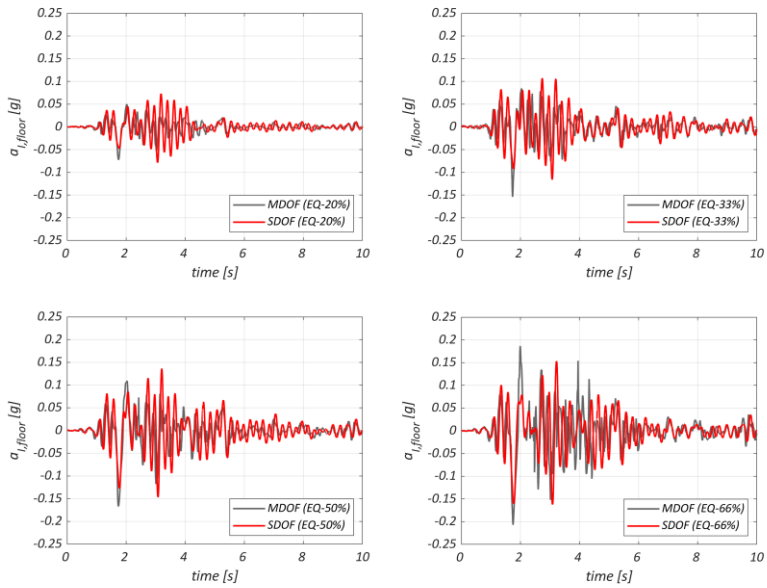

Figure 4.33 Simulation with *SDOF*$_{b,1,2}$ and with EF MDOF system in Or_1 of the EUC-BUILD-6 test runs from EQ-NPR-20% to EQ-NPR-66% (DL2): 1st floor acceleration TH overlaps.

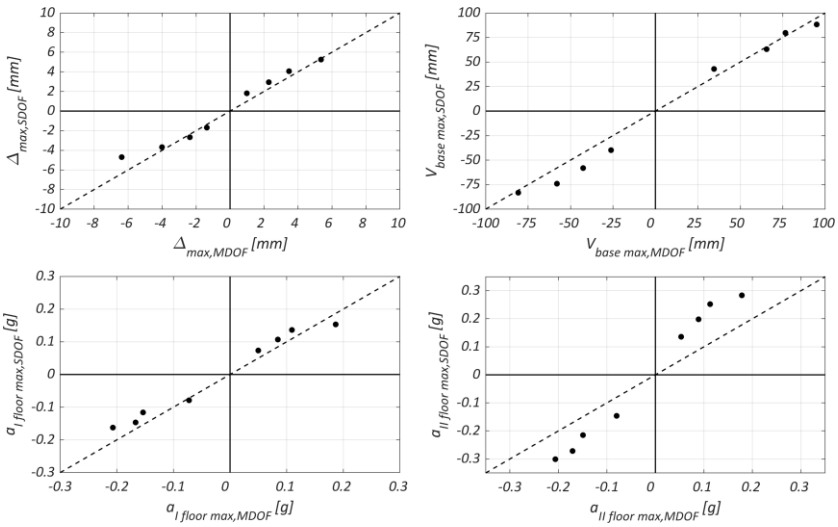

Figure 4.34 Simulation with *SDOF$_{b,1,2}$* and with EF MDOF system in Or_1 of the EUC-BUILD-6 test runs from EQ-NPR-20% to EQ-NPR-66% (DL2): maximum values comparison.

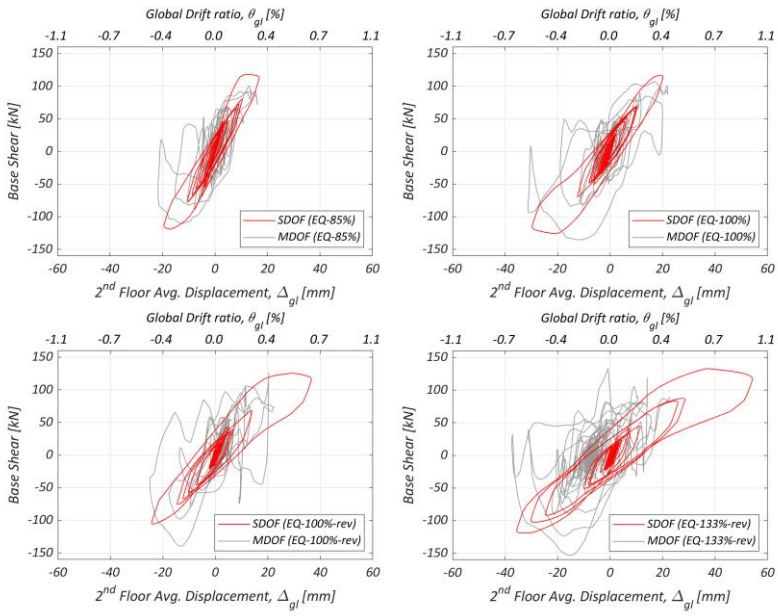

Figure 4.35 Simulation with *SDOF$_{b,3,4}$* and with EF MDOF system in Or_1 of the EUC-BUILD-6 test runs from EQ-NPR-85% (DL3) to EQ-NPR-133%-rev (DS5): hysteresis overlap.

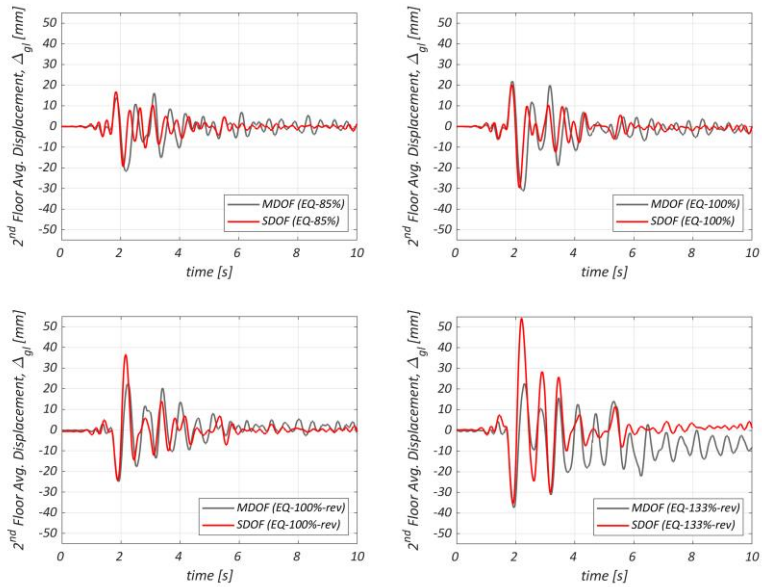

Figure 4.36 Simulation with *SDOF*$_{b,3,4}$ and with EF MDOF system in Or_1 of the EUC-BUILD-6 test runs from EQ-NPR-85% (DL3) to EQ-NPR-133%-rev (DS5): displacement TH overlap.

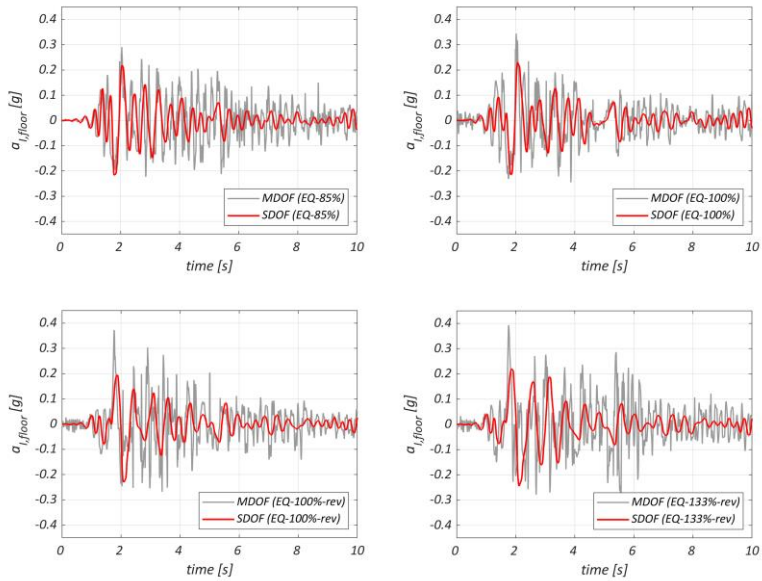

Figure 4.37 Simulation with *SDOF*$_{b,3,4}$ and with EF MDOF system in Or_1 of the EUC-BUILD-6 test runs from EQ-NPR-85% (DL3) to EQ-NPR-133%-rev (DS5): 1st floor accelerations TH overlaps.

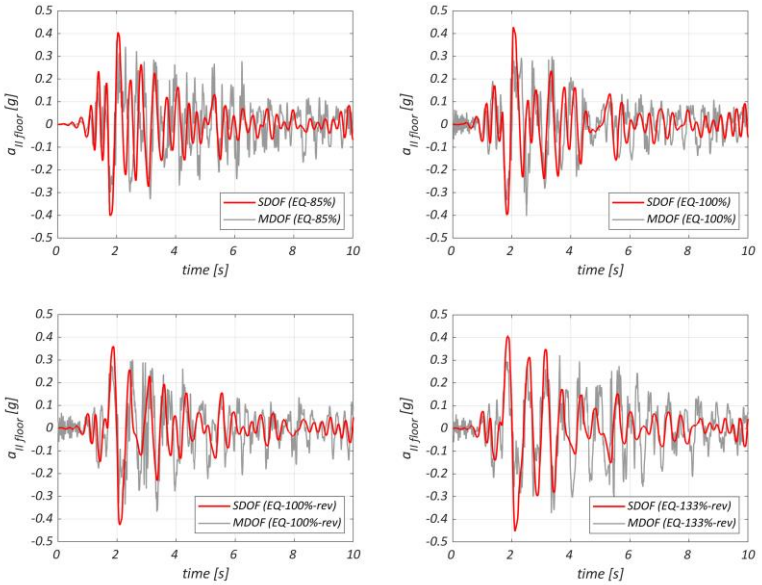

Figure 4.38 Simulation with *SDOF*$_{b,3,4}$ and with EF MDOF system in Or_1 of the EUC-BUILD-6 test runs from EQ-NPR-85% (DL3) to EQ-NPR-133%-rev (DS5): 2nd floor accelerations TH overlaps.

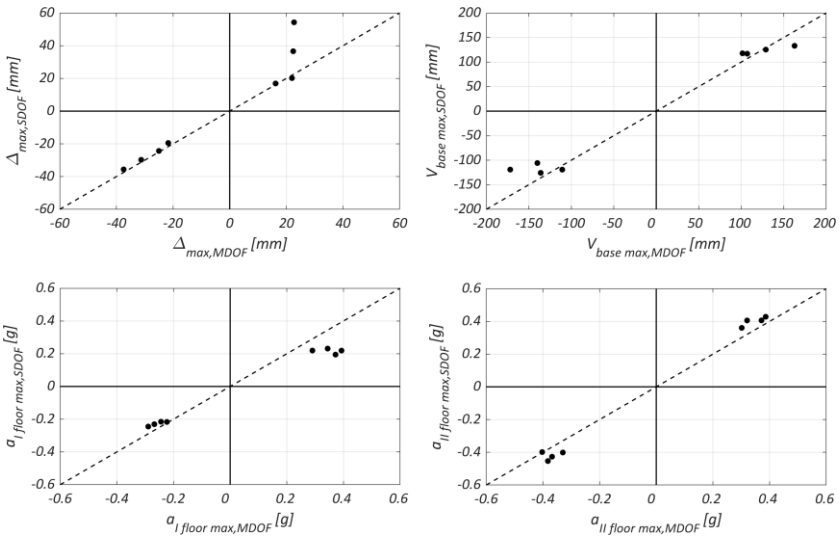

Figure 4.39 Simulation with *SDOF*$_{b,3,4}$ and with EF MDOF system in Or_1 of the EUC-BUILD-6 test runs from EQ-NPR-85% (DL3) to EQ-NPR-133%-rev (DS5): maximum values comparison.

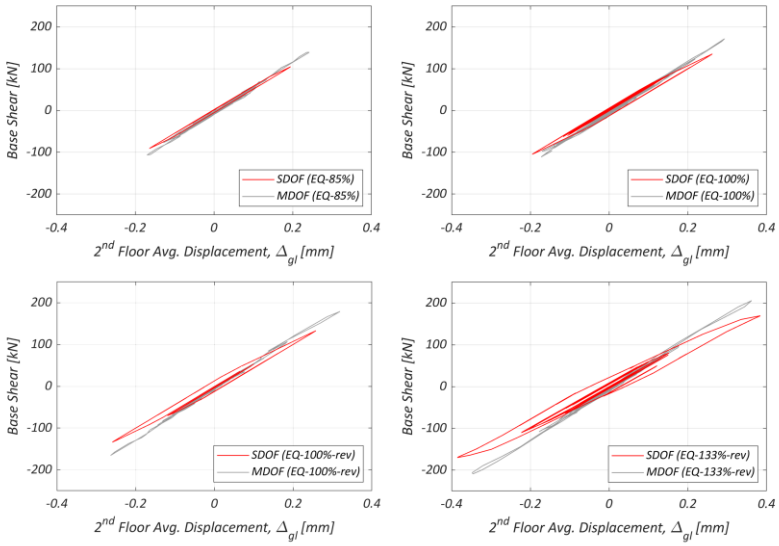

Figure 4.40 Simulation with $SDOF_{b,Or2}$ and with EF MDOF system in Or_2 of the EUC-BUILD-6 test runs from EQ-NPR-85% to EQ-NPR-133%-rev: hysteresis overlap.

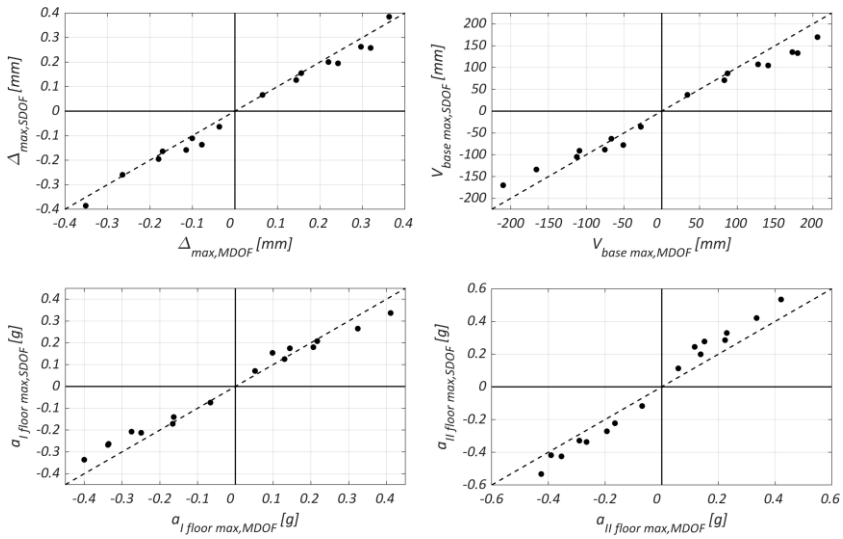

Figure 4.41 Simulation with $SDOF_{b,Or2}$ and with EF MDOF system in Or_2 of the EUC-BUILD-6 test: maximum values comparison.

4.6.2 Retrofitted conditions

The target oscillators representing the retrofitted case-study building are derived with the same procedure used for bare conditions. In particular, two SDOF systems are calibrated to simulate the lateral response of the MDOF equivalent-frame systems, one for the structure responding in DS1, DS2 and DS3 ($SDOF_{r,1,2,3}$) and one for the structure responding in DS4 ($SDOF_{r,4}$). Figure 4.42 shows the comparison between numerical results obtained simulating the experimental test performed on EUC-BUILD-7 up to the attainment of DL3 (EQ-NPR-133%). For the sake of brevity, the overlap of hysteresis is reported from the run corresponding to the experimental attainment of DL1 (EQ-NPR-66%). From an overall point of view, the two models present very similar strength and displacement capacities, and stiffnesses. Only slight overestimations of displacements in negative direction can be observed for the last two runs, as well as with EQ-NPR-133% the oscillator appear more flexible than the MDOF system. Nevertheless, the biggest loops preserve very good agreements throughout the presented runs. Such a good match of results is also highlighted by the comparison of displacements, first- and second-floor acceleration THs, reported in Figure 4.43, Figure 4.44 and Figure 4.45 respectively. Looking at maximum numerical values, plotted in Figure 4.46, it can be noticed that the highest errors are associated to the prediction of second-floor accelerations, while all the other parameters are well-estimated by the SDOF oscillator.

Moving to the results obtained with $SDOF_{r,4}$, the comparison of hysteresis with the one of equivalent-frame model is depicted in Figure 4.47. In this case, a minor level of agreement could be reached, compared to the results for previous DSs. However, the SDOF returns reliable approximations of MDOF results. The models show very similar global stiffnesses, shear and displacement capacities, the highest errors are obtained simulating the run with EQ-NPR-133%-roof. However, with the view of post-processing results from NLTHA, the most important run to be capture is the last one, corresponding to the attainment of DL4. In terms of THs, displacement and accelerations are well simulated by the SDOF system throughout the testing sequence (Figure 4.48, Figure 4.49 and Figure 4.50). Second-floor displacements are generally slightly overestimated in negative directions, while the accelerations at the first-floor level are almost perfectly estimated and the ones at the second floor only slightly overestimated during the last two runs. Such good results are highlighted also in Figure 4.51, where all points remained close to the bisector of graphs. With the aim of performing multiple NLTHA for global and local failure mechanisms, the SDOF oscillators are expected to return reliable maximum displacements and filtered accelerations.

Concerning the retrofitted case-study building in Or_2, a single SDOF (named $SDOF_{r,Or2}$)is sufficient to simulate the MDOF responses throughout the incremental dynamic test. The hysteresis of the last four runs of the simulated incremental test are showed in Figure 4.52.

The lateral response of the models remains linear, with very similar global stiffnesses, up to the run with EQ-NPR-166%, after which the structures entered the non-linear field. The most significant errors of the simulation can be seen for the last two runs. However, it is worth to notice the very low absolute values of global drift reached by both systems at high intensity. Figure 4.53 shows the comparison in terms of maximum values. Overall, the SDOF oscillator tends to slightly underestimate displacements, base shears, and accelerations at the first floor. Only the filtered accelerations at the second floor resulted slightly overestimated. Also in this case, it can be stated that the SDOF system approximate the response of the MDOF one with a sufficient degree of accuracy.

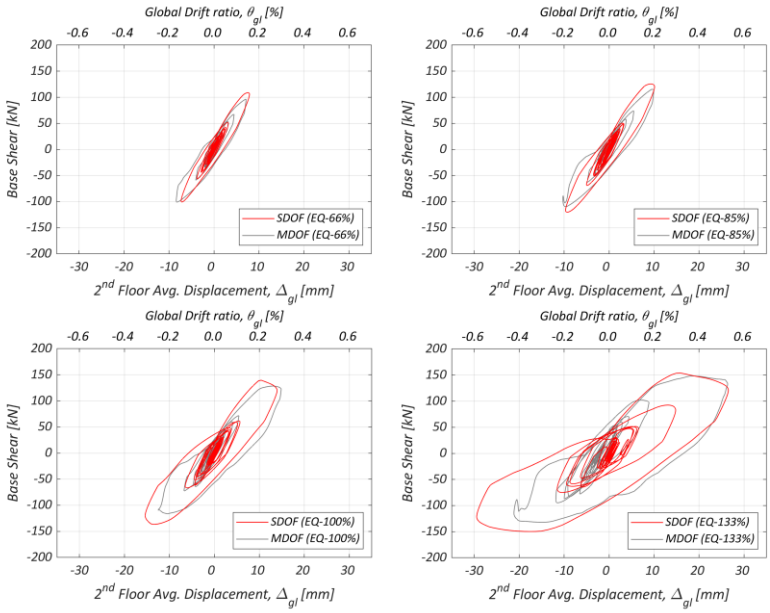

Figure 4.42 Simulation with *SDOF*$_{\eta,1,2,3}$ and with EF MDOF system in Or_1 of the of EUC-BUILD-7 test runs from EQ-NPR-66% (DL1) to EQ-NPR-133% (DL3): hysteresis overlaps.

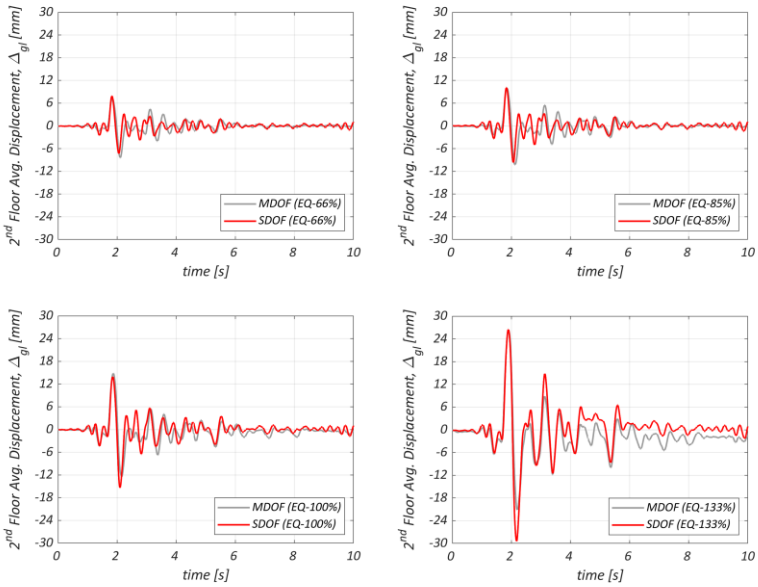

Figure 4.43 Simulation with *SDOF*$_{r,1,2,3}$ and with EF MDOF system in Or_1 of the of EUC-BUILD-7 test runs from EQ-NPR-66% (DL1) to EQ-NPR-133% (DL3): displacement TH overlap.

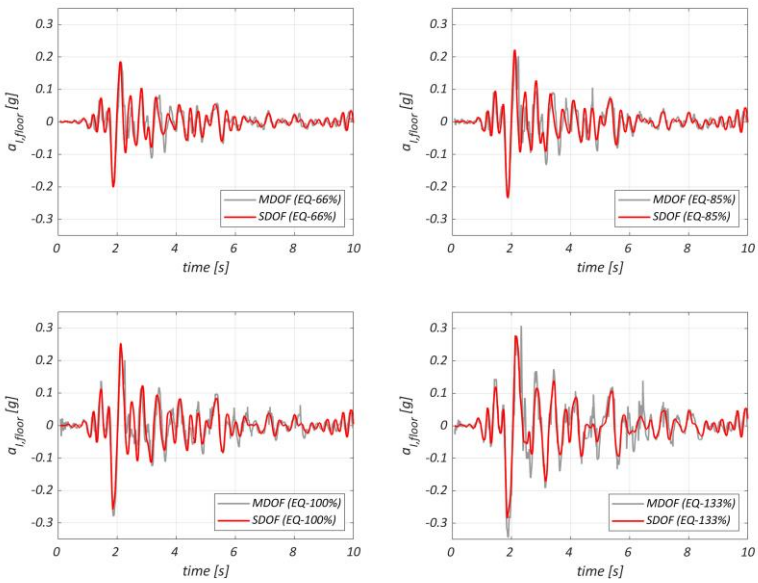

Figure 4.44 Simulation with *SDOF*$_{r,1,2,3}$ and with EF MDOF system in Or_1 of the of EUC-BUILD-7 test runs from EQ-NPR-66% (DL1) to EQ-NPR-133% (DL3): 1st floor acceleration TH overlap.

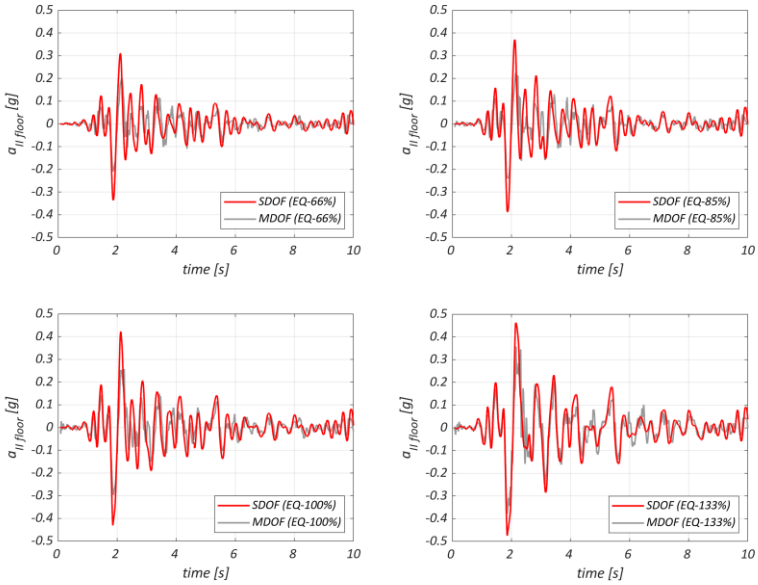

Figure 4.45 Simulation with *SDOF*$_{y,1,2,3}$ and with EF MDOF system in Or_1 of the of EUC-BUILD-7 test runs from EQ-NPR-66% (DL1) to EQ-NPR-133% (DL3): 2nd floor acceleration TH overlap.

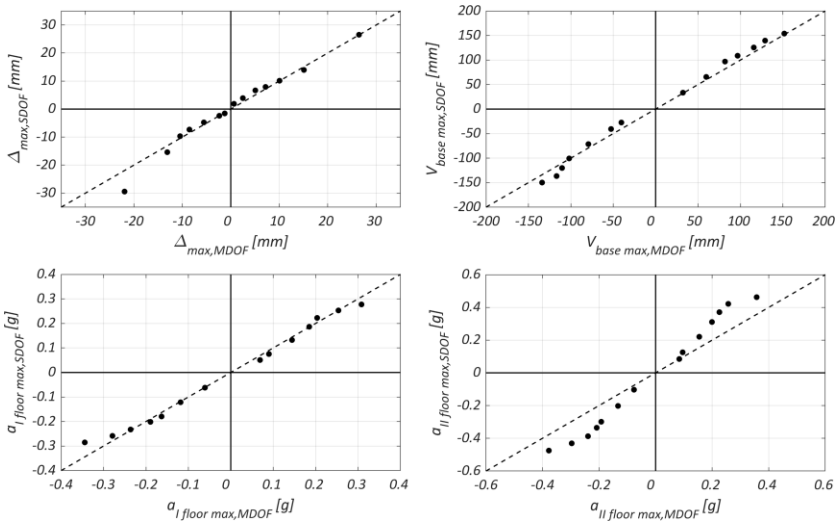

Figure 4.46 Simulation with *SDOF*$_{y,1,2,3}$ and with EF MDOF system in Or_1 of the of EUC-BUILD-7 test runs from EQ-NPR-66% (DL1) to EQ-NPR-133% (DL3): maximum values comparison.

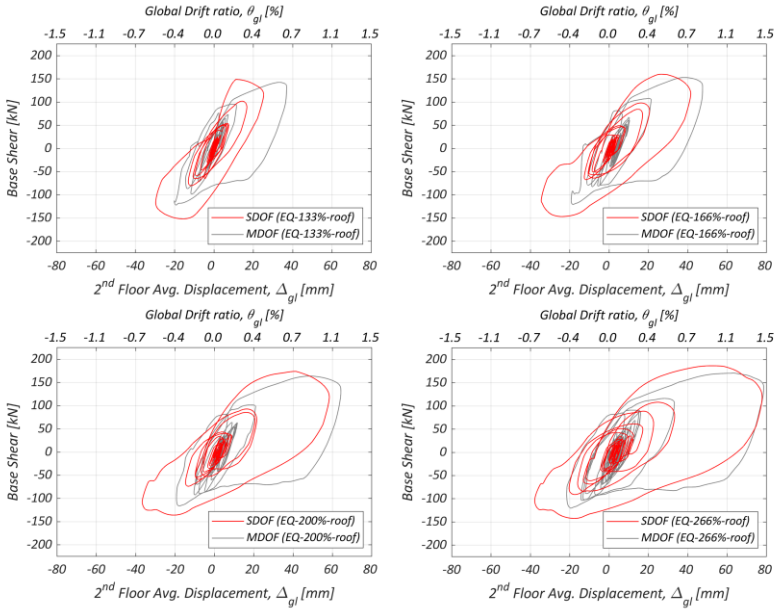

Figure 4.47 Simulation with $SDOF_{0.4}$ and with EF MDOF system in Or_1 of the of EUC-BUILD-7 test runs from EQ-NPR-133%-roof to EQ-NPR-266%-roof (DL4): hysteresis overlap.

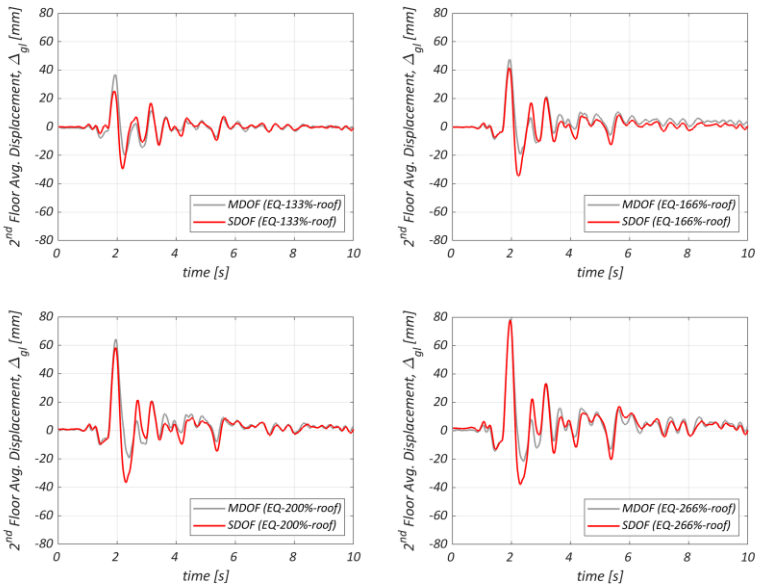

Figure 4.48 Simulation with $SDOF_{0.4}$ and with EF MDOF system in Or_1 of the of EUC-BUILD-7 test runs from EQ-NPR-133%-roof to EQ-NPR-266%-roof (DL4): displacement TH overlaps.

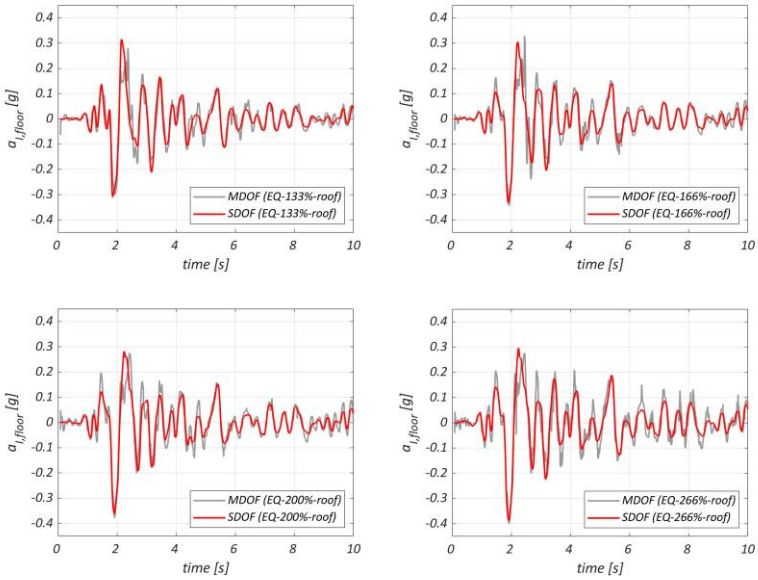

Figure 4.49 Simulation with *SDOF*$_{D,4}$ and with EF MDOF system in Or_1 of the of EUC-BUILD-7 test runs from EQ-NPR-133%-roof to EQ-NPR-266%-roof (DL4): 1st floor accelerations TH overlaps.

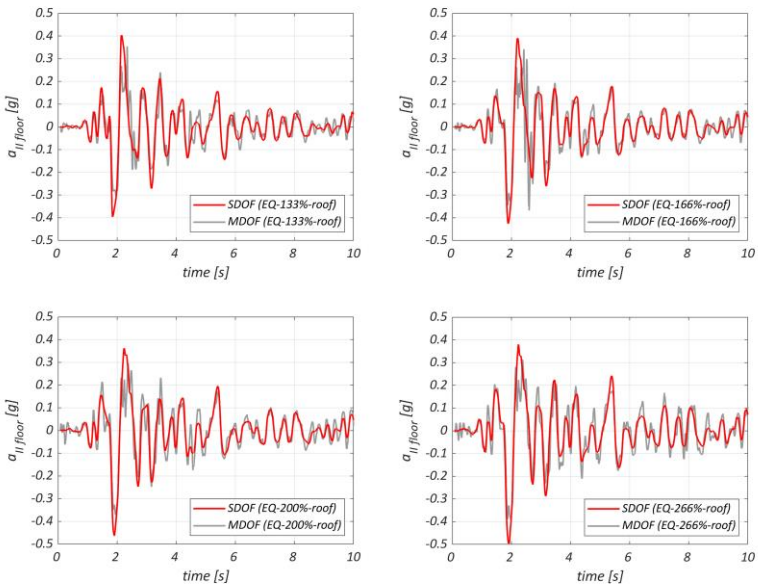

Figure 4.50 Simulation with *SDOF*$_{D,4}$ and with EF MDOF system in Or_1 of the of EUC-BUILD-7 test runs from EQ-NPR-133%-roof to EQ-NPR-266%-roof (DL4): 2nd floor accelerations TH overlaps.

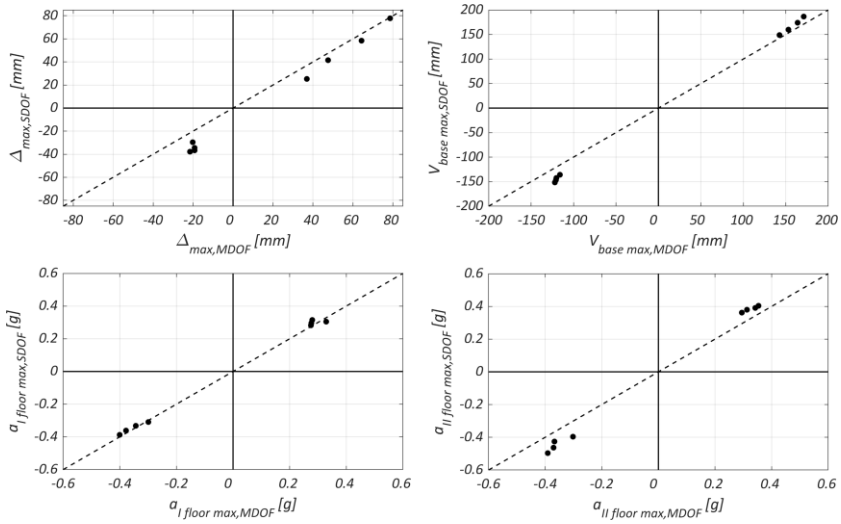

Figure 4.51 Simulation with *SDOF$_{r,4}$* and with EF MDOF system in Or_1 of the of EUC-BUILD-7 test runs from EQ-NPR-133%-roof to EQ-NPR-266%-roof (DL4): maximum values comparison.

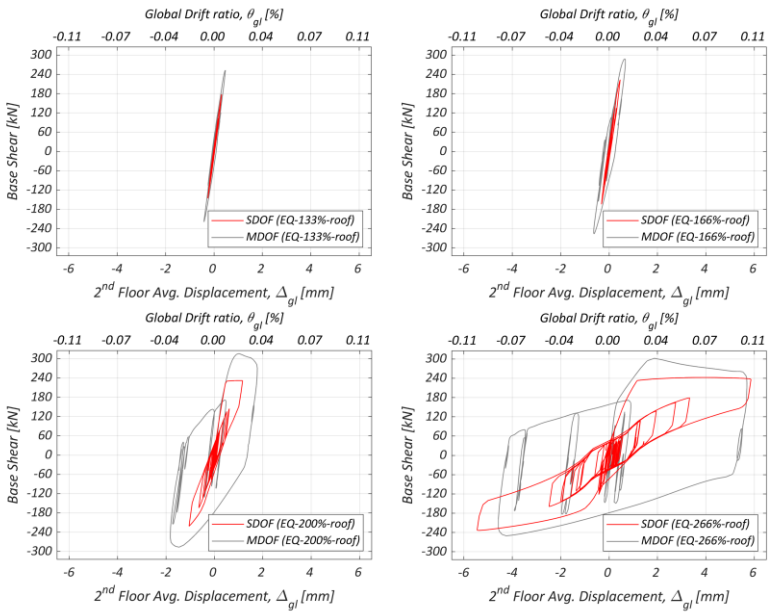

Figure 4.52 Simulation with *SDOF$_{r,Or2}$* and with EF MDOF system in Or_2 of the of EUC-BUILD-7 test runs from EQ-NPR-133%-roof to EQ-NPR-266%-roof (DL4): hysteresis overlap.

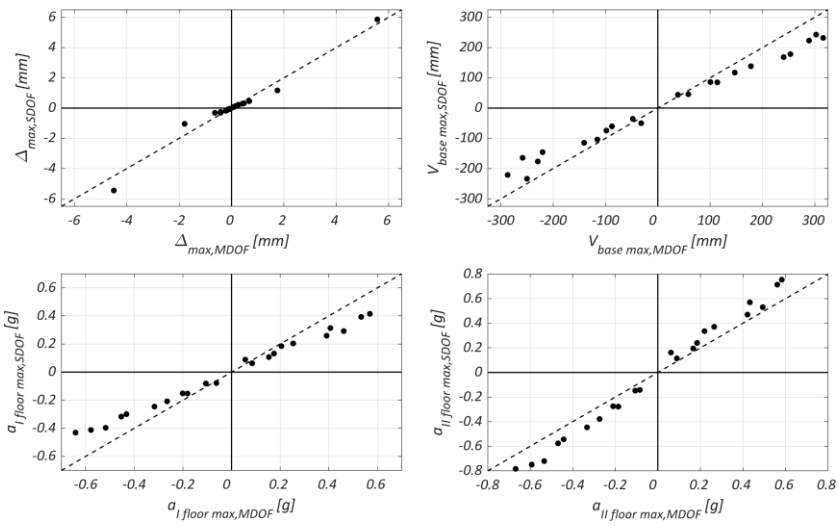

Figure 4.53 Simulation with $SDOF_{r,Or2}$ and with EF MDOF system in Or_2 of the of EUC-BUILD-7 test runs from EQ-NPR-133%-roof to EQ-NPR-266%-roof (DL4): maximum values comparison.

4.7 DEFINITION OF LIMIT STATE THRESHOLDS

One of the main scopes of the incremental dynamic tests performed on the bare and retrofitted building prototypes EUC-BUILD-6 and EUC-BUILD-7, is to define damage state thresholds in the weak direction of the specimen (Or_1) through a suitable engineering demand parameter, which allow for the interpretation of NLTHA results of buildings belonging to the same typology. During dynamic tests, it is impossible to continuously monitor the evolution of damage; therefore, damage states can only be defined between a finite number of runs [Graziotti *et al.*, 2019a]. The building prototypes are visually assigned to damage states based on the reconnaissance after each performed test run, and the maximum recorded second-floor global drift ratio (θ_{gl}) (i.e., the displacement of the second floor over its height above the foundations) is employed to link the global performances with the attained damage states. As deeply discussed in Sect. 3, it is worth to recall that two fundamentally different global seismic responses were experimentally exhibited by the bare and the retrofitted specimens: the former developed a local mechanism, while the latter exhibited a global box-type response with torsional effects. Considering that no local mechanism could be simulated through the equivalent frame method, the damage limits to be used for post-processing NLTHA results need to be carefully defined in both principal directions. Recently, Tomassetti *et al.*, [2019b] proposed damage limits interstorey drifts values to be associated to the weak direction of typical Dutch terraced houses with cavity walls. They were derived by multiple experimental dynamic tests on full-scale specimens with seismic responses not influenced by any local mechanism. These values needed to be updated, based on engineering judgement, in order to consider also the results of the last experimental dynamic test on an irregular prototype

[Miglietta *et al.*, 2021a]. Besides, interstorey drift limits associated to the perpendicular strong direction of the buildings (Or_2) needed to be defined for the first time. Before discussing the selection of DLs to be associated to bare and retrofitted configurations, it must be bear in mind the mechanical behaviour given by the interaction between timber system and masonry, in particular, that the retrofit system needs the masonry to be damaged in order to activate. Accordingly, the drift thresholds selected in the following are the same along the weak direction for both configurations up to DL3. This assumption is taken also to be always in the conservative side. It is also worth noting that the final values proposed are IDR, therefore, they are multiplied by the buildings second-floor height (5.4 m) to post-process NLTHA displacement results.

Focusing on Or_1, Table 4.8 collects the experimental maximum interstorey and global drift ratios (IDR and GDR) of the lastly tested buildings (EUC-BUILD-6 and EUC-BUILD-7), the values proposed by Tomassetti *et al.*, [2019b], and the ones finally identified for numerical results post-processing. For DL1, an interstorey drift of 0.05% is defined for both configurations, taken as the most conservative value. For DL2 and DL3, all reported values are comparable but the IDRs pertaining to the tested bare building, which are significantly higher since biased by the local mechanism, and therefore are neglected. DL2 and DL3 proposed in literature are placed in between the GDR recorded for the bare and retrofitted building specimens, while they are lower than the experimental IDR. Accordingly, the values proposed by Tomassetti *et al.*, [2019b] are selected to provide conservative results for both configurations. Moving to the collapse thresholds (DL4), the value proposed in literature is assigned to the bare building, given the unreliability of the experimental results, while a default approximation of it is assigned to the retrofitted configuration.

Concerning the perpendicular strong direction of the case study building, damage limits are derived from quasi-static cyclic tests on single piers in both configurations, recently performed at the EUCENTRE laboratories. The ones related to the masonry in bare condition are retrieved from Graziotti *et al.*, [2016b], who tested a single-whyte squat wall of 4 m length, 2.75 m height, under a vertical compression of 0.3 MPa. Specifically, they were visually defined based on the experimental damage pattern of each cycle. Moving to the retrofitted configuration, DL thresholds were visually defined based on the cyclic tests discussed in sect. 2 [Guerrini *et al.*, 2021]. Table 4.9 summarizes final selected values for both cases.

Table 4.8 Global damage limit thresholds for bare and retrofitted buildings in weak direction (Or_1).

Specimen	*DL1 (%)*	*DL2 (%)*	*DL3 (%)*	*DL4 (%)*
Bare (IDR) (Tomassetti *et al.*, [2019b])	0.1	0.15	0.35	0.9
Bare (IDR) (EUC-BUILD-6)	0.09	0.27*	0.90*	2.95*
Retrofitted (IDR) (EUC-BUILD-7)	0.07	0.18	0.45	2.83
Bare (GDR) (EUC-BUILD-6)	0.037	0.14*	0.47*	1.4*
Retrofitted (GDR) (EUC-BUILD-7)	0.05	0.13	0.30	1.6
Final Bare (IDR)	***0.05***	***0.15***	***0.35***	***0.9***
Final Retrofitted (IDR)	***0.05***	***0.15***	***0.35***	***1.5***

* Governed by local sliding mechanism

IDR = interstorey drift ratio; GDR = global drift ratio

Table 4.9 Global damage limit thresholds for bare and retrofitted buildings in strong direction (Or_2).

Specimen	*DL1 (%)*	*DL2 (%)*	*DL3 (%)*	*DL4 (%)*
Bare (IDR)	0.05	0.075	0.3	0.4
Retrofitted (IDR)	0.075	0.2	0.4	2.0

4.8 GROUND MOTION DATABASE

In the process of assessing the global and local seismic vulnerability of a building, the records to be employed for NLTHAs need to reflect the dynamic characteristics given by the interested area. The herein presented analyses are performed using the GMs database employed to derive the latest version of fragility functions for buildings exposed to the Groningen Gas-Field seismic hazard [Crowley *et al.*, 2020]. It is a further improvement of the database used for previous versions of fragility curves [Crowley *et al.*, 2019] since the duration of included records was not constraint in any way. The latest version collects 250 GM signals, clustered in groups of 50 based on the reference return period (i.e., 50 yr, 500 yr, 2500 yr, 10k yr, 100k yr), with the same spectra characteristics of the previous version. Figure 4.54 shows the database distributions of $PGAs$ and $D_{S5\text{-}75}$, while accelerations and displacements spectra are reported in Figure 4.55.

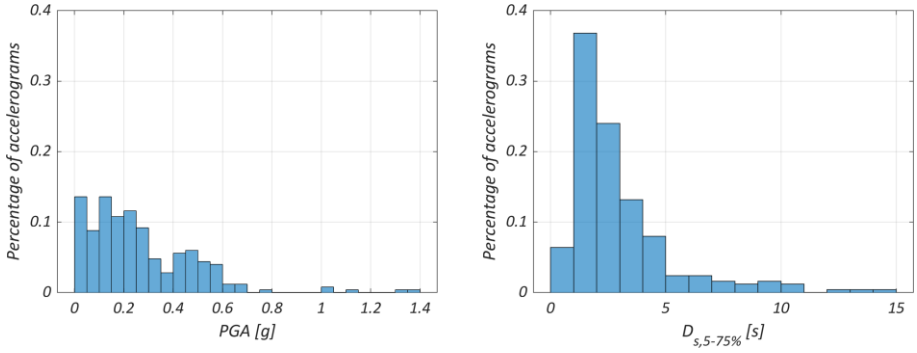

Figure 4.54 GM database intensity measure distributions: *PGA* (left), $D_{s,5-75}$ (right)

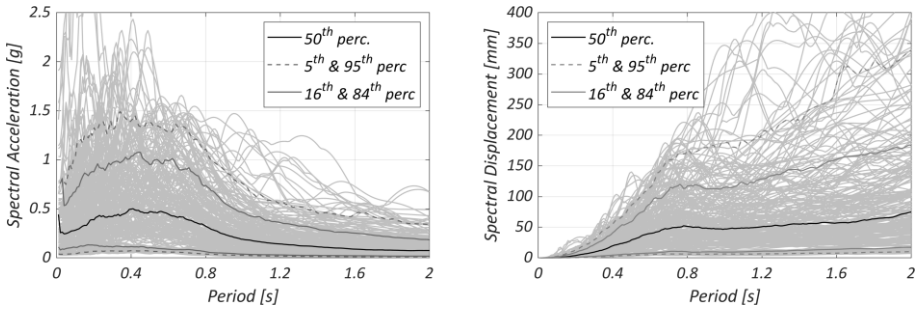

Figure 4.55 GM database acceleration and displacement spectra.

All records are unidirectional, and are applied only in X and Y directions for global and local vulnerability assessments, despite the examined structure is highly asymmetrical and torsional sensitive. For estimating the distribution of structural responses given a seismic hazard, a recurring issue is whether it is better to use few records varying several angles of seismic incidence, or using more records with less orientations. The choice to consider only two orientations of the case-study building is motivated by the need to reduce the computational effort of the numerical study, and based on findings from Giannopoulos *et al.*, [2018], also confirmed by Skoulidou *et al.*, [2020]. They demonstrated that the record-to-record variability has far more influence if compared to the orientation variability. Giannopoulos *et al.*, [2018] subjected several SDOF systems and one plan-asymmetric MDOF structure to a pulsive and a non-pulsive set of ground motions, combining record-set size and incident angle of rotations, and proved that the natural record-to-record variability of unrotated waveforms outweighed the influence of the orientation variability. More recently, Skoulidou *et al.*, [2020] quantified the effect of the GM database size and the record orientations used for NLTHA on the seismic demand of six multi-storey RC buildings. As a result, they recommend suitable amount of incidence angles of the GMs in relation with the number of records. In particular, they demonstrated that if only mean/median values of an EDP are to be evaluated, using 1 orientation of the GM can be

sufficient as long as a large enough ground motion group size is also considered (at least 30 ground motions depending on the level of admissible risk).

In the present study, considering the highly different seismic capacities of the case study building in the two main directions, and the availability of 250 reliable GMs representative of the seismic hazard of the area, the application of all seismic events in both main directions separately is considered sufficient to nullify the influence of the record orientations variability. For the sake of the presented study this assumption is considered acceptable, however, it is worth to underline that more research on the topic applied to masonry and irregular structures is needed to confirm such acceptability.

4.9 GLOBAL SEISMIC VULNERABILITY ASSESSMENT

The results of NLTHA performed with the SDOF oscillators representing the case study building in bare conditions are collected in Figure 4.56 and Figure 4.57, for Or_1 and Or_2 respectively. On the left, each discrete point of the graphs represents the numerical maximum absolute inelastic displacement of the models associated with the PGAs of the simulated events. On the right, the derived DS fragility curves conditioned to PGAs are reported. The presented results are the outcomes of two iterations: at first, the whole GM database is applied to $SDOF_{b1,2}$ for both orientations, then, all the GMs that generated displacement demands higher than DL2 are applied to $SDOF_{b3,4}$, and results used to overwrite the previous ones. It is immediate to see the highly different lateral capacities for the two principal directions. The high variability of results obtained in Or_1 is opposed to a significantly less one in Or_2. While for the former the 17,6% of the simulated earthquakes generated displacement demands beyond DL4 (collapse), for the latter the percentage decreased to 2.8%. Considering that both analysis are carried out using the same GM database, therefore with the same record-to-record variability, only the building responses in Or_1 appeared to be strongly influenced, while in Or_2 the building capacity is sufficient to guarantee a significantly minor response variability. Considering the PGA corresponding to 2475 years of return period (0.3g), the building in Or_1 is estimated to have 80% probabilities to overcome DL3, while in Or_2 to present no damage (DS0). The numerical results are in line with the expectations and with the experimental testing of Or_1 as weak direction of Dutch terraced house buildings [Miglietta *et al.*, 2021a]. Besides, recalling that the employed GM DB includes 250 GMs, clustered based on their return period (respectively 50, 500, 2500, 10000 and 100000 years), it is interesting to correlate the structural displacement demands of the weak direction (Or_1) with return periods. The exercise revealed that out of 63 GMs that caused the building collapse, 22 % of them belong to the GM group with 10k years of returning period, while the 78 % of them belongs to the one with 100k years of returning period. Instead, focusing on Or_2, all the GMs causing collapse have a return period of 100k years. These observations are in agreement with reality since no collapse was ever recorded in the Groningen area.

In order to further investigate the effect of increased transversal dimensions with respect to the prototype buildings tested on the shake-table, the global vulnerability assessment is also performed considering the case-study building with experimental dimensions. Figure 4.58 compares the DS fragility functions derived for each orientation of the bare case-study building, considering typical and experimental dimensions. Along the weak direction of the building (Or_1, Figure 4.58 left) the two configurations present very similar vulnerabilities. Overall, the typical dimensions lead to an increase of vulnerability apart from the probabilities of exceeding DL1. When hit by an earthquake event with a return period of 2475 years, corresponding to a PGA of 0.3g, both models show 100% of probability of being in DS3, over 60% and 70% of being in DS4 and around 20% and 30% of probability of being in DS4 and DS5 for the case-study building with experimental and real dimensions respectively. Focusing on DL fragility functions related to Or_2 (Figure 4.58 right), the two configurations present the approximately the same vulnerabilities. No damage risk was obtained for a PGA of 0.3 g, while the mean PGA associated to the overcoming of the first damage threshold is found to be around 0.5 g, significantly higher than the PGA associated to a return period of 2475 years.

The presented outcomes related to the vulnerability along the weak direction are in line with the experimental tests on Dutch terraced house end-units performed at the EUCENTRE laboratories (EUC-BUILD-1, Graziotti *et al.*, [2017] and EUC-BUILD-6, Miglietta *et al.*, [2020]). The former structure was a very regular prototype of a typical Dutch terraced house end-unit, as opposed to the latter. In both cases, the buildings were deemed to globally reach DL3 with the runs characterized by a PGA of 0.24 and 0.26g respectively, and to reach DL4 with PGAs of 0.31 and 0.30g. As depicted in Figure 4.58a, at a PGA of 0.25g the models show around 100% of probabilities of being beyond DL1, around 90% of being beyond DL2, around 50% to be beyond DL3, and around 15% of being in DS5. Instead, at a PGA of 0.3g, the structures have 100% of being beyond DL2, around 70% of being beyond DL3, and around 25% of being beyond DL4.

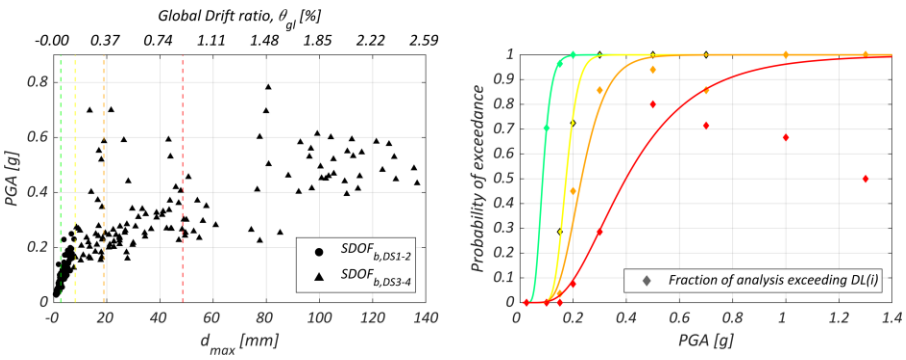

Figure 4.56 NLTHA outcomes, bare conditions (Or_1): cloud results (left) and DS fragility curves conditioned to PGA (right).

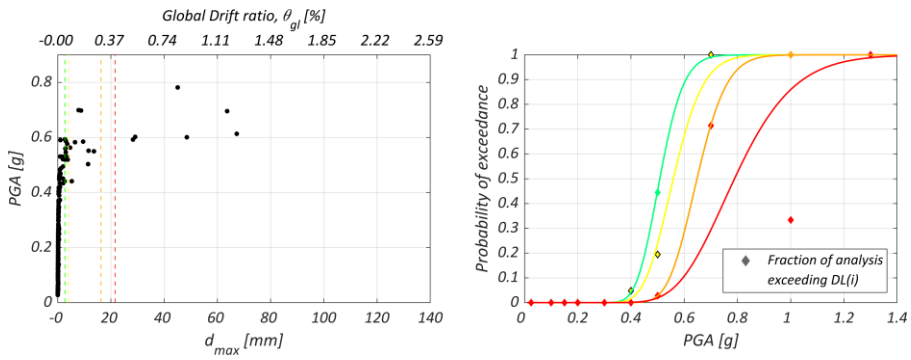

Figure 4.57 NLTHA outcomes, bare conditions (Or_2): cloud results (left) and DS fragility curves conditioned to PGA (right).

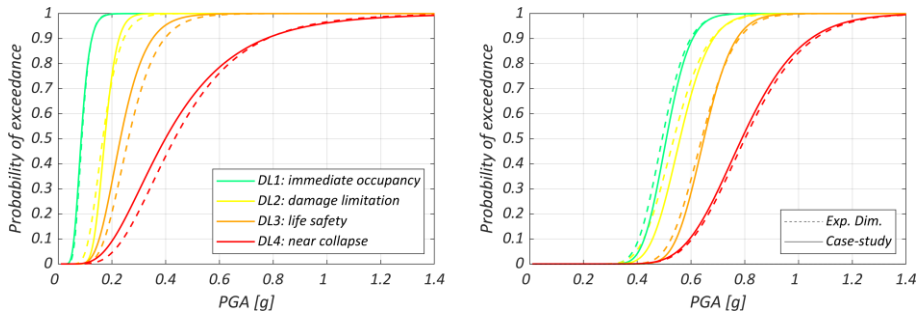

Figure 4.58 Damage states global fragility functions for experimental and real dimensions, bare conditions: case-study building in Or_1 (left) and in Or_2 (right).

Global seismic assessment results for the case-study building in retrofitted configuration are presented in Figure 4.59 and Figure 4.60 for Or_1 and Or_2 respectively. Even with the application of the retrofit system, the high response variability of the weak direction is opposed to a significantly lower one in the perpendicular direction. For Or_1, only the 3.6% of GMs cause the building to collapse, while 28.4% bring the building to DS4. Instead, for Or_2, the building is very unlikely estimated to accumulate damage with the seismic hazard of the region. In particular, the mean PGA associated to the overcome of DL1 is found to be around 0.72g, which is more than twice the PGA associated to a return period of 2475 yr, as well as no GM of the DB caused collapse of the structure, even with a return period of 100k years. Figure 4.61 summarizes and compares the cloud analysis results in terms of fragility functions conditioned to PGAs for the retrofitted building with experimental and typical dimensions. Along the weak direction (Or_1, Figure 4.61 left) increased dimensions results in increased fragility curves associated to DL2, DL3 and DL4. For instance, at a PGA level of 0.3g (2475 T_r) the retrofitted building with experimental dimensions presents the 25% of probabilities to overcome DL3, while with real dimensions this increase to around 45%. Along Or_2 (Figure 4.61 right), the only difference obtained between the two configurations is the minor dispersion of results associated to DL1 for

the case-study building, while the other fragility curves are overlapped. In both cases the probability of collapse associated to the seismic hazard of the region is 0%.

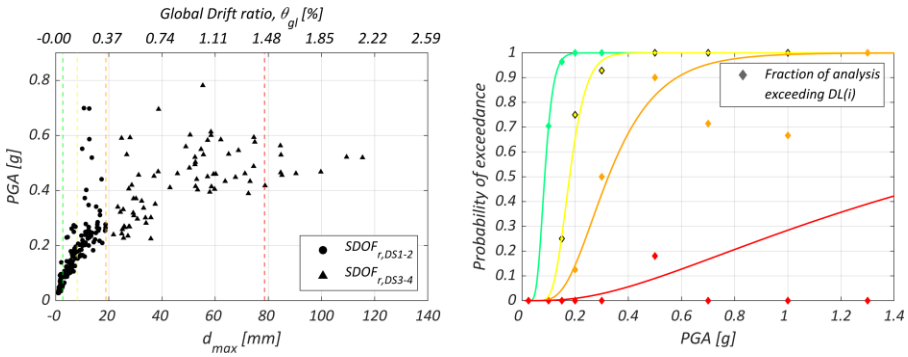

Figure 4.59 NLTHA outcomes, retrofitted conditions (Or_1): cloud results (left) and DS fragility curves conditioned to PGA (right).

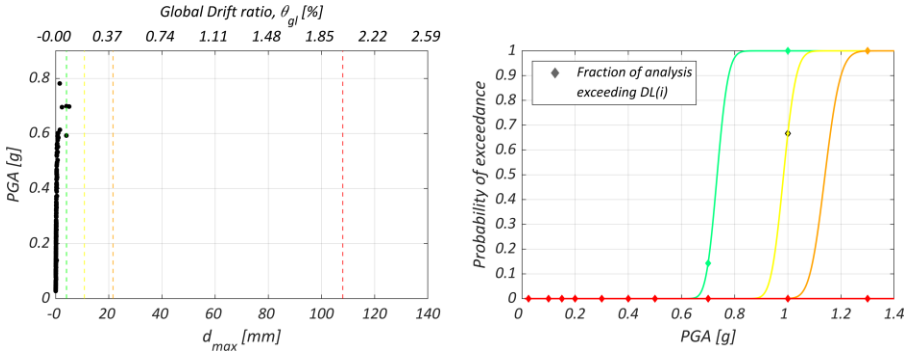

Figure 4.60 NLTHA outcomes, retrofitted conditions (Or_2): cloud results (left) and DS fragility curves conditioned to PGA (right).

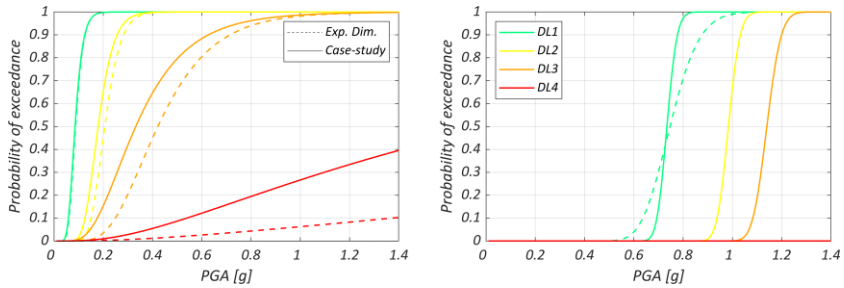

Figure 4.61 Damage states global fragility functions for experimental and real dimensions, retrofitted conditions: case-study building in Or_1 (left) and in Or_2 (right).

Figure 4.62 summarizes the global damage states fragility curves conditioned to PGAs derived for the case-study building, in bare and retrofitted configurations. Focusing on the

results related to the weak direction of the structure (Or_1, Figure 4.62 left), the influence of the retrofit system increases with the increase of damage (DL2, DL3 and DL4), rather than for low levels. The two configurations present the same fragilities associated with the overcome of DL1, while for DL2 the one associated with the retrofitted building is only slightly improved. Since the application of the timber system to URM consists in coupling two materials characterized by very different stiffnesses, the flexible timber needs the cracking of masonry to be activated, and as such, it cannot delay the accumulation of light damage to the structure. On the contrary, the strengthening system has a pronounced influence on the building lateral capacity if DL3 and DL4 are considered. The strengthening intervention increases the mean PGA value associated to the overcoming of DL3 of around 43% (from 0.23g to 0.33g), while it significantly reduced the possibility of having collapse with the considered seismic hazard. Moving to the strong direction of the building (Or_2, Figure 4.62 right), numerical results show a strong influence of the retrofit system. Fragility curves associated to the overcoming of DL1, DL2 and DL3 resulted shifted to significantly higher values of PGAs, with increased mean values of about 50%, while the probabilities of having collapse of the structure is nullified. The parameters used to fit lognormal distributions for all considered DLs for bare and retrofitted configurations are summarized in Table 4.10.

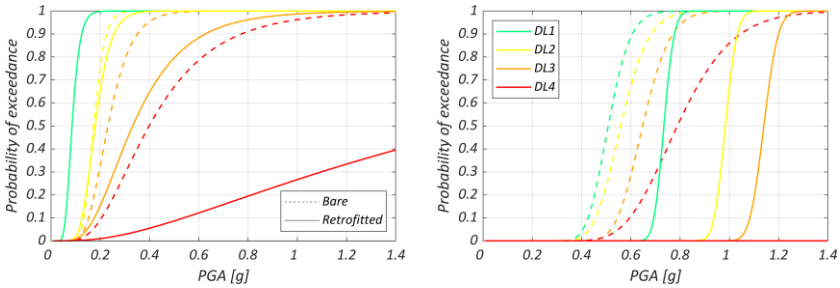

Figure 4.62 Damage states global fragility functions for bare and retrofitted conditions: case-study building in Or_1 (left) and in Or_2 (right).

Table 4.10 Parameters of fitted lognormal distributions (for all considered DLs) of the case-study building.

IM = PGA (g)	Bare				Retrofitted			
Damage limit	Or_1		Or_2		Or_1		Or_2	
	e^{μ} [g]	β	e^{μ} [g]	β	e^{μ} [g]	β	e^{μ} [g]	β
DL1	0.09	0.30	0.51	0.14	0.09	0.30	0.73	0.04
DL2	0.17	0.21	0.56	0.16	0.18	0.28	0.98	0.04
DL3	0.23	0.33	0.65	0.14	0.33	0.46	1.14	0.04
DL4	0.40	0.52	0.79	0.22	1.67	0.9	-	-

4.10 LOCAL VULNERABILITY ASSESSMENT

4.10.1 Introduction

In literature, the evaluation of the OOP seismic response of vertical spanning strip walls (VSSW) characterized by only horizontal or vertical edges restrained, and behaving in one-way bending (1WB), is usually performed representing them through semirigid-blocks, with a rocking dynamic response characterized by impacts, and an oscillation-amplitude dependent fundamental period of vibration. The simplification of assuming masonry elements as rigid blocks is acceptable if the masonry has good mechanical properties and can grant the development of such a mechanism. The OOP cracking resistance of walls is governed by the bond strength of masonry [CEN 2005] and is usually lower than the force needed to trigger the mechanism, hence it is reasonable to assume an initial cracked state in the assessment. However, it is scientifically recognized that walls segments have not infinite stiffness, and therefore researchers proposed bi-linear [Lagomarsino 2014], tri-linear [Doherty KT. 2000] and four-branch [Ferreira *et al.*, 2015] elastic non-linear curves to model their force-displacement (*F-u*) relationships. Another fundamental aspect to be addressed evaluating the OOP response of masonry elements is the energy dissipation, which is of major importance in elastic non-linear systems (i.e., rocking structures), since the damping phenomenon is dependent on the system frequency of vibration. The modelling of energy dissipation has been treated differently in literature: some researchers represented it with the coefficient of restitution, assuming that the overall reduction of energy is concentrated at the instant of the impact [Housner 1963, Sorrentino *et al.*, 2008]. Other authors simulated it as a velocity dependent force through a constant [Griffith *et al.*, 2003] and variable damping ratio (with cycle-to-cycle iterations) [Lam *et al.*, 2003]. In other works, the use of a constant or linear damping ratio-frequency ($\xi - \omega$) relationship was addressed [Lagomarsino 2014, Tomassetti *et al.*, 2017b], while other researchers developed MDOF models to analyse VSSW systems taking into account also the top diaphragm flexibility, and its interaction with the wall response [Simsir *et al.*, 2004, D'Ayala *et al.*, 2011, Costa *et al.*, 2015, Derakhshan *et al.*, 2015].

A limited number of studies can be found in literature regarding the OOP seismic assessment of two-way spanning walls characterized by both horizontal and vertical edges restrained, and responding to lateral loads in two-way bending (2WB) fashion. Among others, experimental quasi-static tests were carried out by Restrepo-Vélez *et al.*, [2014], by Vaculik *et al.*, [2004] or by Griffith *et al.*, [2007], while Walsh *et al.*, [2015] performed in-situ quasi-static airbag tests on walls in an existing building. The current state-of-art of design rules available to calculate the strength of URM wall panels in OOP two-way bending is based on the virtual work method, originally proposed by Lawrence and Marshall [2000], further developed by Willis [2004] and Vaculik [2012], and included in the Australian standards [AS 3700, 2008].

More recently, Graziotti *et al.*, [2019b] and Sharma *et al.*, [2020] performed experimental dynamic tests on full-scale masonry specimens with different configurations. In their work, they demonstrated that the assumption of an initially cracked section is suitable for VSSW, but it can be overly conservative in case of two-way spanning URM walls. All the tested specimens exhibited a peak cracking resistance (PCR) higher than the force needed to activate any kinematic mechanism. The authors also observed that once exceeded the peak cracking capacity of piers, non-linear kinematic methods (NLKM) [Derakhshan *et al.*, 2013, Derakhshan *et al.*, 2014], also present in NZSEE [2016], which do not consider the presence of cracked lateral supports (i.e., assume a one-way bending configuration) are suitable for a conservative simplified assessment of weak unit-strong joint URM walls [Graziotti *et al.*, 2019b, Sharma *et al.*, 2020]. In this way, the tendency of long two-way spanning walls, with supported vertical edges far apart from each other, to behave in OOP one-way bending is also considered. Moreover, they highlighted the possibility to loss the restraint along the top edge of a pier during an earthquake due to the uplift of the rigid floor slab in absence of mechanical connectors [Tomassetti *et al.*, 2019b], and proposed a simple check to take into account also this effect. This simplified methodology has been included in the latest version of the Dutch seismic code [NPR998, 2020], and therefore is taken as reference for OOP assessment of two-way-spanning walls.

In this section, all the case-study building piers are verified against OOP failure through NLTHA. For two-way spanning walls the PCR resistance is firstly checked against the seismic demand following the prescriptions of the Dutch seismic code, producing a first set of DL fragility functions. Subsequently another set is produced analysing them through NLTHA assuming a simple vertical bending failure mechanism. Details about the procedures are discussed in the following paragraph.

4.10.2 Methodology

To perform multiple OOP NLTHA, the availability of computationally efficient numerical models able to simulate cracking and collapse oscillation amplitudes of one-way bending URM walls is fundamental. Within the experimental campaign carried out at the EUCENTRE laboratories [Graziotti *et al.*, 2019a], a numerical model for one-way bending OOP analysis of bare single-leaf and cavity VSSW systems is developed and fine-tuned to the experimental tests performed by Graziotti *et al.*, [2016b], to provide the best tri-linear force-displacement relationships and damping parameters to simulate their dynamic behaviour (Tomassetti *et al.*, [2018], Figure 4.63). This model is here used to produce OOP collapse fragility functions of bare masonry piers through NLTHA. The original ground motions of the database are applied to structural elements located at the ground floor level, while the acceleration THs extracted from global analysis are applied to verify masonry piers at the first-floor level. The results of the assessment are finally presented in terms of fragility functions conditioned to PGAs. To carry out the same analysis on retrofitted piers,

the model required to be updated to consider the presence of the retrofit system. It is demonstrated that the application of timber strong-backs to URM walls significantly increases the OOP capacity, and that such increase is dependent on whether the strong-backs are on the compression or tension side of the wall under bending actions [Cassol *et al.*, 2021]. When the timber post in located the compression side, its presence only produces a slight shift of the neutral axis of the timber-masonry composite (TMC) section compared to the bare masonry one. Indeed, this configuration does not benefit from the tensile resistance of the timber post. Analytically the retrofit element is schematised as a double-pinned beam subjected to bending actions under a distributed lateral load with stiffness k_{SB}:

$$k_{SB} = \frac{384}{5} \cdot \frac{h^3}{E_{SB}J_{SB}} \tag{4.10}$$

where h is the wall height, and $E_{SB}J_{SB}$ is the flexural stiffness of the timber elements. Summing the contributions of the linear-elastic response of timber elements (k_{SB}) and the tri-linear response of the masonry wall (Figure 4.63), the tri-linear relationship approximating the response of the retrofitted system reported in Figure 4.64a can be obtained. Conversely, when the timber post in located the tension side, the tension-resisting timber elements significantly shift the position of the neutral axis of the TMC section, allowing to effectively exploits the strengths of both materials: the masonry is under compression, while the strong-backs take tension forces increasing the bending moment capacity of the entire system. As suggested by experimental results from airbag tests actions [Cassol *et al.*, 2021], the force-displacement behaviour of URM walls retrofitted with strong-backs on the tension side can still be idealised by a tri-linear relationship, but with increased strength and stiffness in comparison to the case where strong-backs are located on the compression side. The stiffness contribution offered by timber strong-backs ($k_{SB,TMC}$) is computed assuming a TMC element with double-pinned boundary conditions, subjected to a distributed load:

$$k_{SB,TMC} = \frac{384}{5} \cdot \frac{h^3}{\Delta EJ} \tag{4.11}$$

$$\Delta EJ = E_{SB}J_{SB} + \frac{1}{\frac{1}{\gamma \cdot E_{SB}A_{SB}} + \frac{1}{E_M A_M}} \cdot a^2 \tag{4.12}$$

where: $E_{SB}J_{SB}$ is the strong-back system flexural stiffness; $E_m A_m$ and $E_{SB}A_{SB}$ are, respectively, the masonry wall and strong-back system axial stiffness; γ is a coefficient ranging from 0 to 1 that accounts for the collaboration between masonry and timber; a is the distance between the barycentre of the masonry compressed zone to the barycentre of the timber section. Summing the contributions of the linear-elastic response of timber

elements ($k_{SB,TMC}$) and the tri-linear response of the masonry wall (Figure 4.63), the tri-linear relationship reported in Figure 4.64b can be obtained.

In another study, Tomassetti *et al.*, [2019c] addressed the modelling of energy dissipation for rocking systems, and proposed equations predicting equivalent viscous damping ratios. In particular, the authors considered equivalent viscous damping models based on: a constant damping coefficient, a constant damping ratio and a stiffness-proportional damping ratio. To model the OOP dynamic response of retrofitted pier, the stiffness proportional viscous damping model is employed, to take into account the dependence of the system stiffness on the location of timber posts with respect to bending actions.

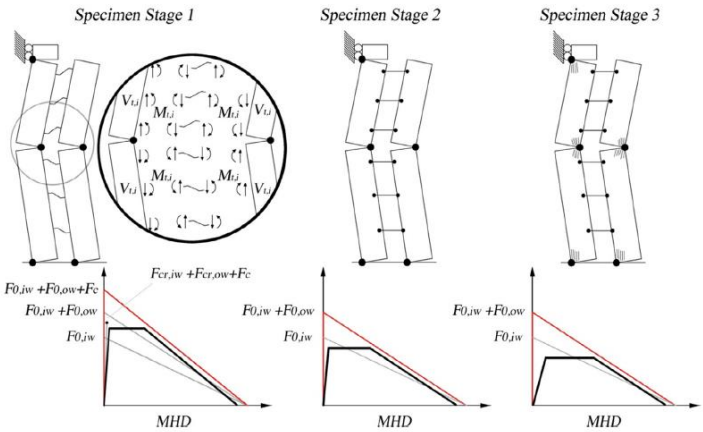

Figure 4.63 Schematic representation of the OOP response of cavity walls and associated F-u relationship (reproduced from Tomassetti *et al.*, [2018]).

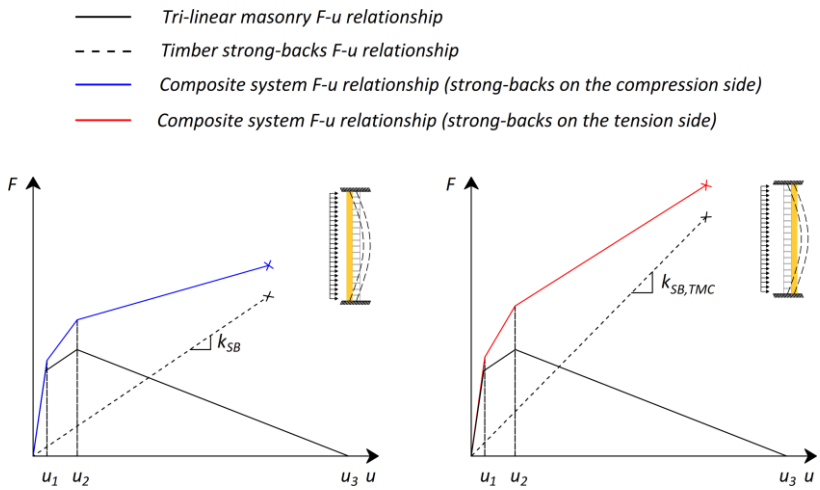

Figure 4.64 Tri-linear force displacement relationship for retrofitted masonry piers.

Moving to two-way-spanning walls, their vulnerability is firstly evaluated by computing their PCR, and comparing it with the seismic demand of each GM, computed as the spectral acceleration of the wall given by the average spectrum of top and bottom acceleration spectra, multiplied by the wall weights [NPR998, 2020]. A proper definition of the seismic demand acting on two-way spanning walls is strictly dependent on the correct evaluation of their fundamental period since it defines the acceleration spectral amplification at mid-height of the structural element. To this end, Sharma *et al.*, [2021] suggested to use the solution for the first mode of vibration of rectangular plates formulated by Janich [1962] and Warburton [1954]:

$$T_R = \frac{2 \cdot H^2}{\pi} \sqrt{\frac{\rho_s}{D}} \cdot C_t \tag{4.13}$$

Where D is the flexural rigidity calculated as $D = (E_m \cdot t^2)/12(1 - \nu^2)$, with t referring to the thickness of the wall, ν to the Poisson's ratio of masonry, and E_m to the modulus of elasticity of the masonry in tension and compression; H is the height of the wall; ρ_s is the mass density per unit area of the wall; C_T is a parameter that depends on the boundary conditions of the wall and on its aspect ratio *(L/H)* [Janich 1962, Warburton 1954]. The variation of this parameter is graphically given by Sharma *et al.*, [2021], who proposed different curves based on boundary conditions, as function of the wall aspect ratio *(L/H)*. Specifically, the authors derived C_T values required to obtain the experimentally measured periods of all tested specimens.

The PCR of two-way spanning URM piers can be determined preselecting a two-way bending failure mechanism (Figure 4.65 left) through the formulation proposed by Lawrence and Marshall [2000]:

$$w_c = \frac{2a_f}{L_d^2}(k_1 M_{ch} + k_2 M_{cd}) \tag{4.11}$$

where:

a_f is the aspect factor calculated as per Table 4.11;
k_1, k_2 are coefficients calculated as per Table 4.11;
L, H are the length and height respectively of the wall panel being assessed;
L_d is the design length, which need to be computed based on boundary conditions (Figure 4.65 right);
M_h is the horizontal bending capacity of the URM pier (computed with equation 4.14);
M_d is the diagonal bending capacity of the URM pier (computed with equation 4.15);

$$M_h = lesser\ of \begin{cases} \frac{1}{2(h_u+t_j)}\left[(f_m - \nu \cdot \sigma) \cdot h_u \cdot \frac{{t_u}^2}{6}\right] \\ \frac{1}{h_u+t_j}\left[\tau_u \cdot k_b \cdot 0.5(l_u + t_j) \cdot {t_u}^2\right] \end{cases} \tag{4.12}$$

$$M_d = \frac{\sin\varphi}{h_u+t_j}\left[(\sin\varphi)^3 \cdot \tau_u \cdot k_b \cdot 0.5\left(l_u + t_j\right) \cdot {t_u}^2 + (\cos\varphi)^3 \cdot (f_{mt} + \sigma) \cdot \frac{0.5(l_u+t_j)}{6}\right] \tag{4.13}$$

Where l_u, t_j, t_u, h_u are geometrical properties of masonry as depicted in Figure 4.66, τ_u is the torsional shear strength of a masonry bed joint, which can be calculated as reported in Sharma *et al.*, [2021]. k_b is a numerical constant whose value depends on the approach adopted to calculate τ_u and can be graphically determined with the plots provided in Sharma *et al.*, [2021].

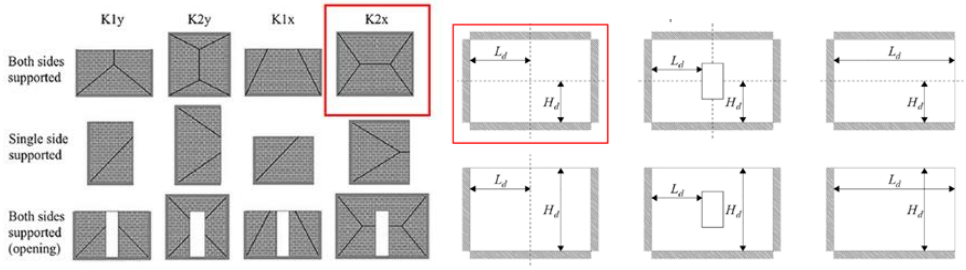

Figure 4.65 Preselected failure mechanisms and boundary conditions (reproduced from Vaculik, [2012]).

In Table 4.11, G_n is the slope of a diagonal crack based on unit geometry, (Figure 4.66); α is a slope factor calculated as G_nL_d/H_d, controlling the association with K1X or K1Y mechanisms, with $\alpha = 1$ being the limiting case between the complementary X and Y mechanisms; R_{f1} and R_{f2} are restraint factors for the first and second vertical edges of the wall, respectively. These factors assume a value of 0 if no rotational restraint is present (i.e. simply supported), a value of 1 if the supported edge is fully restrained against rotation (i.e. fully fixed) and intermediate values in case of partial rotational restraint. The methodology validation against experimental results can be found in Graziotti *et al.*, [2019b], Sharma *et al.*, [2020], Griffith *et al.*, [2007], and Vaculik *et al.*, [2017], who obtained well-matched analytical results using a value of 0.5, as recommended also by Sharma *et al.* [2021].

Masonry walls at the ground storey of North and South façade are also checked against the possible loss of horizontal top restrain due to slab uplift (Figure 4.67). In case the vertical deflection caused by the overburden load of the rigid slab is lower than the uplift caused by longitudinal piers, the top edge of the wall below the slab can no longer be assumed as effectively restrained. The maximum deflection of the slab, obtained considering a strip

idealized to be a uniformly loaded and simply supported, can be equated to the uplift caused by drift of the in-plane piers using the following equation:

$$EI = \frac{5 \cdot q \cdot l_s^{\,4}}{384 \cdot \theta \cdot l_p} \tag{4.14}$$

where q is the load per unit length and unit width of the floor system parallel to the wall; EI is the stiffness of a strip of unit width of the floor system parallel to the wall; l_s is the span length of the floor system in the transverse direction (perpendicular to the out-of-plane direction of the wall being assessed) (Figure 4.67); θ is the drift demand of longitudinal piers; l_p is the effective length of the longitudinal pier (Figure 4.67). Sharma *et al.*, [2021] also included a graphical way to perform the abovementioned check (Figure 4.68). Four different charts are provided for longitudinal piers of aspect ratios h_p/l_p ranging from 1.5 to 3.0, a vertical load from 2 to 8 kNm, and adopting a drift demand of θ = 1.25%. This value is reasonably considered in codes as an upper bound associated with the in-plane rocking/flexural failure capacity of URM piers.

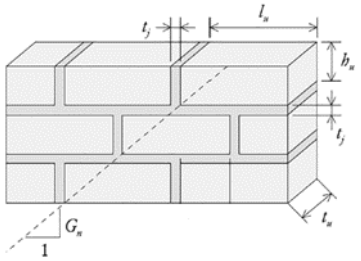

Figure 4.66 Masonry wall geometrical properties (reproduced from Sharma *et al.*, 2021)

Table 4.11 Coefficients to calculate PCR for two-way-spanning walls (reproduced from AS 3700 [2018])

Op.	*NVE*	*α [-]*	*a_f [-]*	*k_1 [-]*	*k_2 [-]*	*Mechanism* (Figure 4.65a)
No	2	≤1	$\frac{1}{1-\frac{\alpha}{3}}$	$\frac{R_{f1}+R_{f2}}{2}+1-\alpha$	$\alpha\left(1+\frac{1}{G_n^{\,2}}\right)$	K2Y
No	2	>1	$\frac{1}{1-\frac{1}{3\alpha}}$	$\frac{R_{f1}+R_{f2}}{2}$	$1+\frac{1}{G_n^{\,2}}$	K2X
No	1	≤1	$\frac{1}{1-\frac{\alpha}{3}}$	R_{f1}	$\alpha\left(1+\frac{1}{G_n^{\,2}}\right)$	K1Y
No	1	>1	$\frac{1}{1-\frac{1}{3\alpha}}$	R_{f1}	$1+\frac{1}{G_n^{\,2}}$	K1X
No	2	≤1	$\frac{1}{\left(1-\frac{\alpha}{3}\right)+\left(1-\frac{\alpha}{2}\right)\frac{l_0}{l_d}}$	R_{f1}	$\alpha\left(1+\frac{1}{G_n^{\,2}}\right)$	K1Y
No	2	>1	$\frac{1}{\left(1-\frac{\alpha}{3}\right)+\frac{l_0}{2l_d}}$	R_{f1}	$1+\frac{1}{G_n^{\,2}}$	K2X

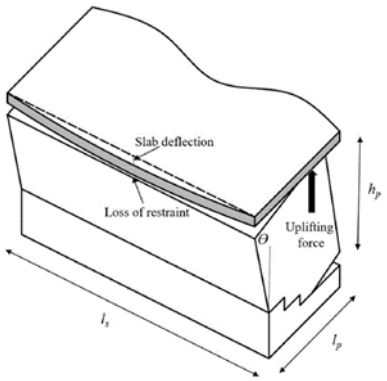

Figure 4.67 Loss of horizontal top restrain mechanism, notation (reproduced from Sharma *et al.*, [2021]).

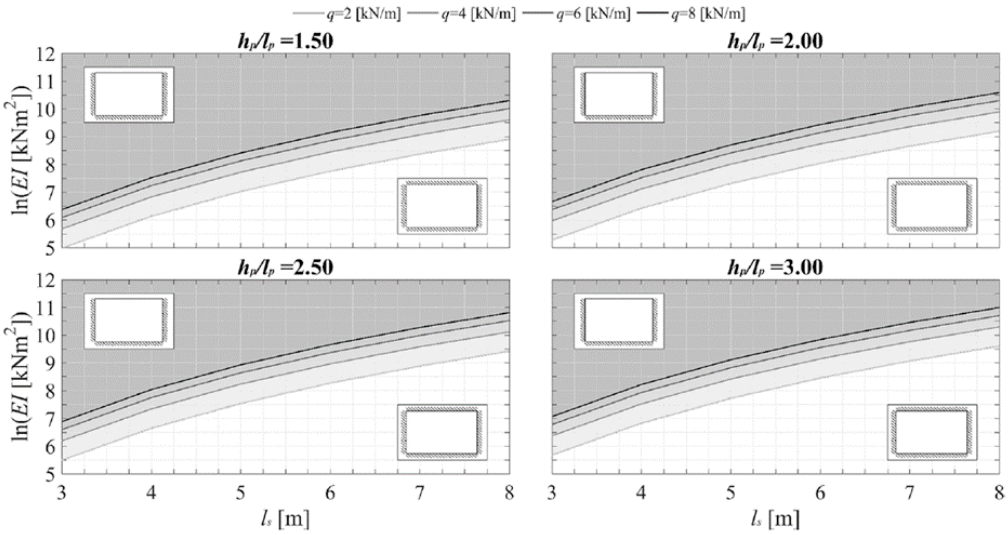

Figure 4.68 Charts for assessing restraint at the top edge of URM walls as a function of the geometry and stiffness of the floor system (plotted for θ = 1.25%) (reproduced from Sharma *et al.*, [2021]).

4.10.3 Bare building

With the case-study building in Or_1, the slender piers of East and West sides are excited along their principal plane, while solid squat piers of North and South façades are excited out-of-plane. They are approximately 7.5 m long, and 2.68 m and 2.55 hight at the first and second storey respectively. Moreover, the ones on the South side are single-leaf CS piers, while the others are cavity walls. The structural elements under consideration, named as N_1, S_1, N_2 and S_2, are depicted in Figure 4.69. It is worth to note that the piers at the ground floor level and the one at the first-floor level are distinguished not only by the

different heights, but also by the boundary conditions (rigid RC slab at the first floor and flexible timber diaphragm at the second one). Based on the results obtained by Sharma *et al.*, [2021], in case of cavity walls, it is assumed a sufficient density of steel ties (i.e., 2/m^2) to allow the consideration of the two leaves acting together, and offering a total OOP resistance given by the sum of the two contributions. This behaviour was experimentally observed during the test performed by Graziotti *et al.*, [2019b].

The OOP seismic assessment of two-way-spanning walls is performed based on Sharma *et al.*, [2021], following the procedure described in the previous paragraph. A first set of fragility functions conditioned to the PGA of the simulated events is produced based on the probability to exceed the PCRs. To this end, it is assumed that all walls are vertically fully restraint at their edges, due to the interlocking with perpendicular walls ($R_{1,f}$ and $R_{2,f}$ =1). Then, a second set of fragility functions conditioned to the same IM are produced based on NLTHA, assuming the walls behaving in one-way bending. The original ground motions of the GM DB are applied perpendicularly to the main direction of the structural elements located at the ground-floor level, while the input motions applied to the piers at the upper floor level are extracted from global SDOF NLTHA. The obtained acceleration and displacement spectra are reported in Figure 4.70, for each direction and floor level.

With reference to Tomassetti *et al.*, [2018], three parameters are to be defined for NLTHA in order to characterize the horizontal restraints of VSSW: α_t and α_b, to describe the degree of restraint at the top and bottom of the wall, ranging from 0 for pinned connection to 1 for fixed one; and β, a parameter affecting the mid-span deflection of a double-supported elastic beam, which may vary between 5, from solid mechanics in pinned-pinned configuration (α_t=α_b=0), and 2, empirically well representative of a fixed-fixed condition (α_t=α_b=1). For the specific cases, the walls at the ground-floor level were assumed in between a double fixed and pinned-pinned condition at top and bottom (αa_t=α_b=0.5 and β = 3.5). The ones at the first-floor level are assumed as pinned at the top (due to the presence of the timber diaphragm (a_t=0) and in between fixed and pinned at the base (α_b=0.5), while β is selected as per pinned-pinned double-supported elastic beam (β=5). In presence of cavity walls, the outer leaf has been assumed as pinned-pinned (α_t=α_b=0). Table 4.12 summarizes geometrical features, applied vertical loads, horizontal and vertical constraints coefficient, and fundamental vibration periods computed with equation 4.15, for one way bending (α_t, α_b and β) and for two-way-bending ($R_{1,f}$, $R_{2,f}$) verifications of the walls under scrutiny.

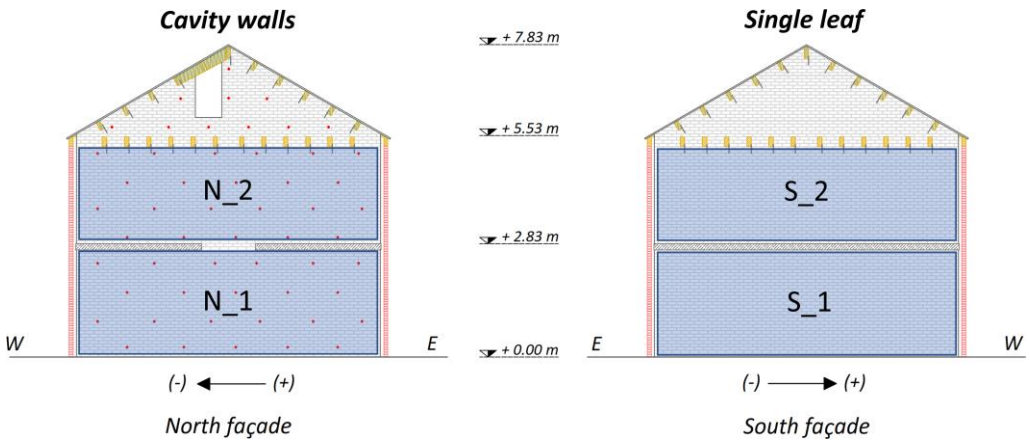

Figure 4.69 Vertical elevation of North and South sides. Notation for OOP seismic assessment.

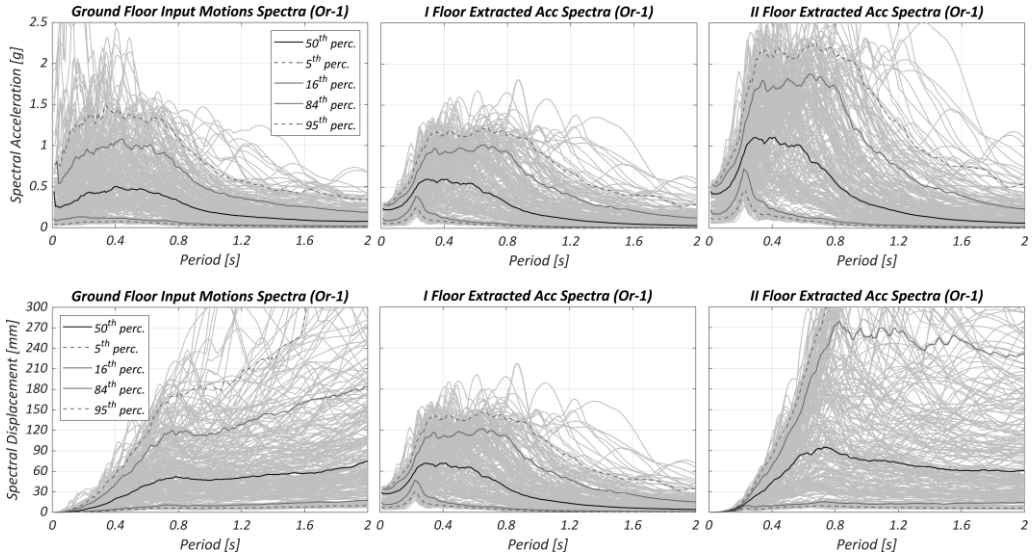

Figure 4.70 Floor acceleration and displacement spectra for Orientation 1 OOP assessment, bare conditions.

Table 4.12 Overall characteristics of North and South facade piers for OOP seismic assessment, bare conditions

						One-way bending			*Two-way bending*	
Wall	***L***	***H***	$\sigma_{v,CS}$	$\sigma_{v,CL}$	T_R	α_b	α_t	β	R_{1f}	R_{2f}
	[m]	*[m]*	*[MPa]*	*[MPa]*	*[s]*	*[-]*	*[-]*	*[-]*	*[-]*	*[-]*
N_1	7.54	2.68	0.24	0.24	0.11	0.5	0.5	3.5	1.00	1.00
S_1	7.54	2.68	0.24	-	0.11	0.5	0.5	3.5	1.00	1.00
N_2	7.54	2.44	0.07	0.07	0.09	0.5	0.0	0.5	1.00	1.00
S_2	7.54	2.44	0.07	-	0.09	0.5	0.0	0.5	1.00	1.00

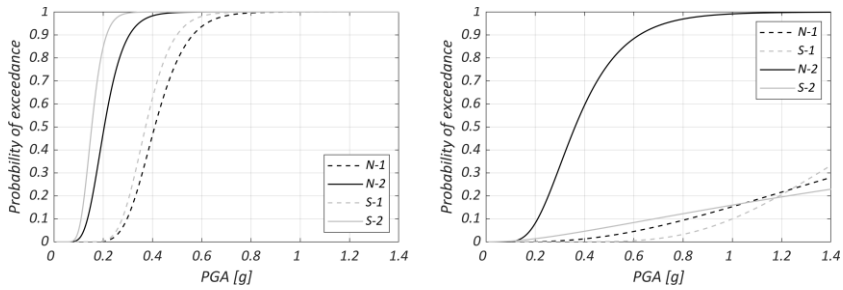

Figure 4.71 OOP collapse fragility functions for bare conditions: derived through virtual work method (PCR, 2WB, left) and derived by NLTHA for one-way bending failure mechanism (right).

The outcomes of the assessment are reported in Figure 4.71, in terms of collapse fragility functions conditioned to the PGA of simulated events, assuming 2WB and 1WB failure mechanisms. Results show that this assumption strongly affects the final vulnerabilities of the considered piers. When the exceedance of the PCRs is considered (Figure 4.71 left), the mean PGAs associated to collapses range between 0.15g and 0.4g, instead, considering the exceedance of the instability displacements in 1WB fashion (Figure 4.71 right), the probability of collapse are nullified for all piers but the one at the first-floor level of the North façade (cavity wall). Nevertheless, the mean PGA associated to 1WB collapse of N_2 is approximately doubled compared to the one associated to 2WB collapse. These results confirm that the attainment of the PCR does not imply the collapse of the wall. Considering the highest PGA recorded in the interested region is around 0.3g, and that the fragility functions computed for S_2 and N_2 present mean PGAs of 0.18g and 0.22g respectively, some heavy damage or collapse should have been observed in-situ. Also, during the experimental tests on EUC-BUILD-6, the ground motion was scaled up to a PGA of around 0.4g without causing any OOP collapse of the North and South façades.

In case of Or_2, the strong sides of the case-study building (North and South) are excited along their principal plane, and the piers of East and West sides need to be verified against OOP failure. The structural elements under consideration are four slender piers and two

squat ones, as depicted in Figure 4.72. The one-way spanning piers (W_1, W_2, E_1 and E_2) are assessed through NLTHA (Tomassetti *et al.*, [2018]), assuming a one-way bending failure mechanism. Instead, the squat ones are verified as performed for Or_1 for two-way spanning walls. No vertical stress is considered acting on the piers since floor diaphragms of Dutch terraced houses of late '70s-early '80s were typically laid on solid walls only, without loading front and back façades of the buildings. The effective height of slender piers at the first-floor level is assumed as the height of openings (W_2, E_2), while the one of slender piers at the ground floor level (W_1, E_1) is obtained using the methodology proposed by Dolce *et al.*, [1991]. The full storey height is assigned to squat walls (W_3 and E_3). Regarding boundary conditions, horizontal constraints of slender piers at the ground floor level are assumed as in between pinned-pinned and fixed-fixed (α_t=α_b=0.5 and β = 3.5, W_1, E_1). The same is assumed at the base of piers at the second-floor level, while no constraints were assumed at the top of them (α_b=0.5, α_t=0 and β = 5, W_2, E_2). These assumptions related to piers located at the ground or first floor level is applied also to the squat piers W_3 and E_3. The outer leaf is assumed as pinned-pinned (α_t=α_b=0, β = 5). Table 4.13 summarizes geometrical features, applied vertical loads, horizontal and vertical constraints coefficient, and fundamental vibration periods computed with equation 4.15, for one way bending (α_t, α_b and β) and for two-way-bending ($R_{1,f}$, $R_{2,f}$) verifications of the walls under scrutiny. Figure 4.73 shows the acceleration and displacement spectra for each floor level derived by applying the original GM database records to the entire building for global assessment.

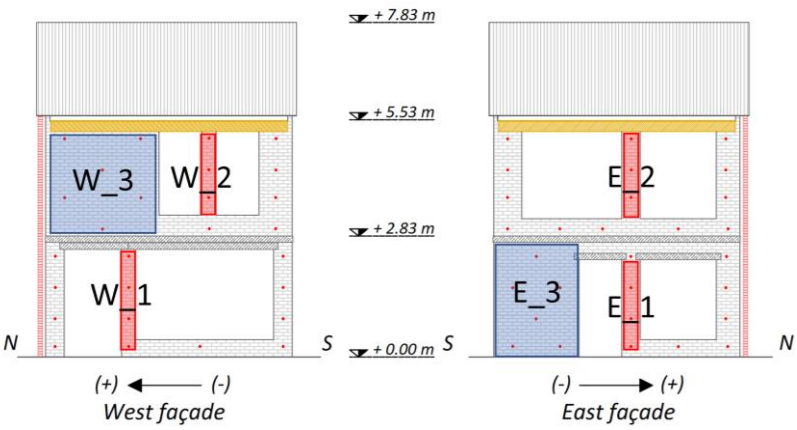

Figure 4.72 Vertical elevations of West and East walls. Notation for OOP seismic assessment.

Table 4.13 Overall characteristics of West and East façade piers for OOP seismic assessment, bare conditions.

						One-way bending			*Two-way bending*	
Wall	***L***	***H***	$\sigma_{v,CS}$	$\sigma_{v,CL}$	T_R	α_b	α_t	β	R_{1f}	R_{2f}
	[m]	*[m]*	*[MPa]*	*[MPa]*	*[s]*	*[-]*	*[-]*	*[-]*	*[-]*	*[-]*
W_1	0.33	2.31	0.00	0.00	-	0.5	0.5	3.5	-	-
E_1	0.44	2.07	0.00	0.00	-	0.5	0.5	3.5	-	-
E_3	1.99	2.68	0.00	0.00	0.35	0.5	0.5	3.5	1.00	1.00
W_2	0.33	1.95	0.00	0.00	-	0.5	0.0	0.5	-	-
E_2	0.44	2.03	0.00	0.00	-	0.5	0.0	0.5	1.00	1.00
W_3	2.60	2.44	0.00	0.00	0.35	0.5	0.0	0.5	-	-

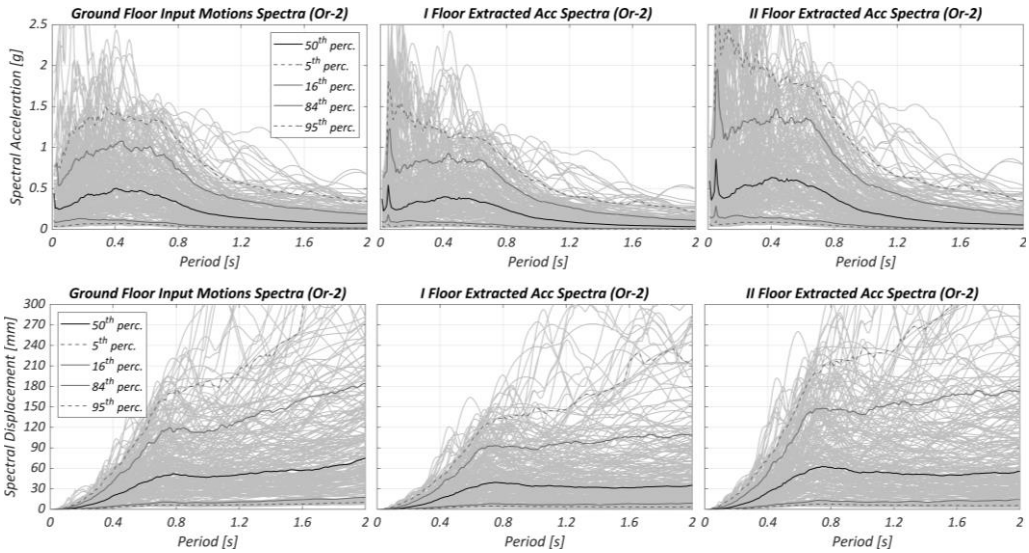

Figure 4.73 Floor acceleration and displacement spectra for Orientation 2 OOP assessment, bare conditions.

Figure 4.74 shows the OOP collapse fragility functions derived for squat walls assuming 2WB and 1WB failure mechanisms. Even in this case, the vulnerabilities obtained considering the exceedance of PCRs are significantly higher than the one obtained considering the exceedance of the instability displacement. Focusing on the formers, the fragility associated to the squat wall located at the first-floor level of the West side (W_3) is characterised by a mean PGA of around 0.1g, while the one located at the ground floor of the East side presents a mean PGA of around 0.25g. These values increase to around 0.4g when considered a 1WB failure mechanism, passing from the probabilities to collapse with an intensity of 0.3g from 100% to less than 20%, and from 60% to less than 10%, for

W_3 and E_3 respectively. Moving to the assessment of the OOP vulnerability of slender piers (Figure 4.75 left), results estimate a low probability of collapse with the seismic hazard of the region. Fragility curves mean PGAs range between 0.45g and 0.85g, which are significantly higher than the one associated to a 2475 year of return period (0.3g). At that PGA, the probabilities of collapse of all piers lie below 5%. The summary of results is depicted in Figure 4.75 (right), where all the obtained collapse fragility functions considering one-way bending failure mechanisms are overlapped. It emerges that the squat piers are the most vulnerable structural elements to OOP actions, nevertheless, for an intensity level corresponding to a return period of 2475 years, all the structural elements present a probability of collapse below 30%.

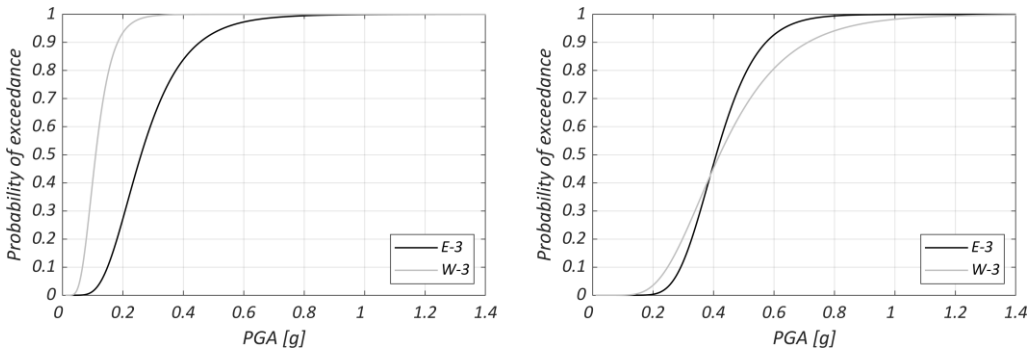

Figure 4.74 Collapse fragility functions for squat walls, bare conditions: derived by virtual work method (PCR, left) and derived through NLTHA (right).

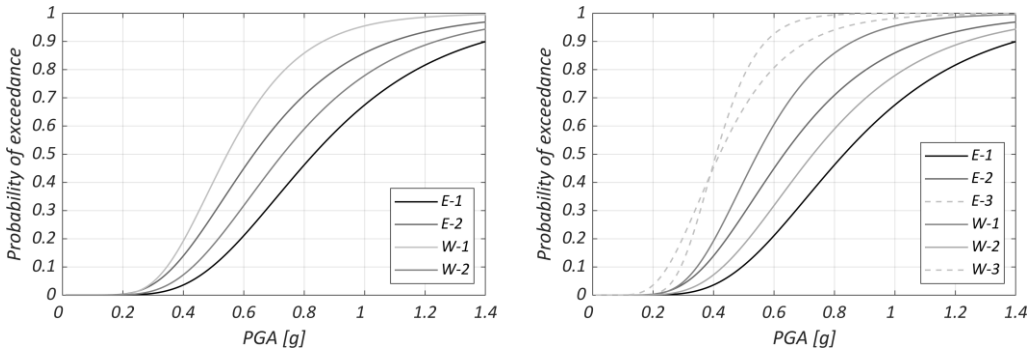

Figure 4.75 Collapse fragility functions, bare conditions: slender piers (left) and for all piers in 1WB for Or_2

4.10.4 Retrofitted building

In case of retrofitted piers, the OOP verifications based on the assumption of a 2WB failure mechanism are not carried out since the occurrence of such failure mode is deemed inhibited by the retrofit system. Figure 4.76 and Figure 4.77 show the acceleration and displacement spectra of the input motions used at different building levels for the two

orientations. The results of NLTHA related Or_1 are depicted in Figure 4.78 (left). Over the 250 GMs, only a few of them characterised by very high PGA cause collapse of the piers located at the ground-floor level, while no risk of collapse is obtained for the piers at the first-floor level. Focusing on Or_2 (Figure 4.78 right), only a few collapses are exhibited by the pier E_3, while no risk of collapse is estimated for the other retrofitted piers.

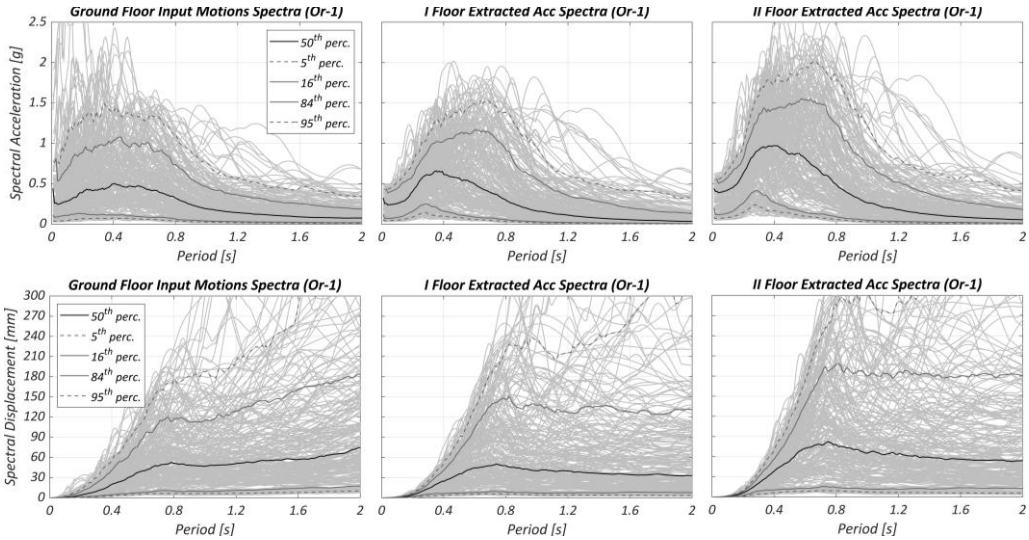

Figure 4.76 Floor acceleration and displacement spectra for Orientation 1 OOP assessment, retrofitted conditions.

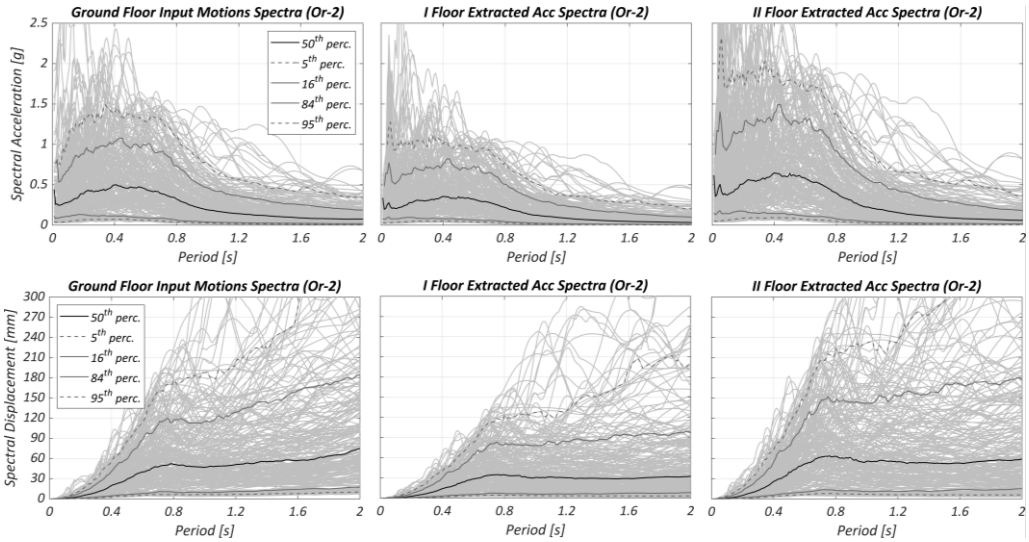

Figure 4.77 Floor acceleration and displacement spectra for Orientation 2 OOP assessment, retrofitted conditions.

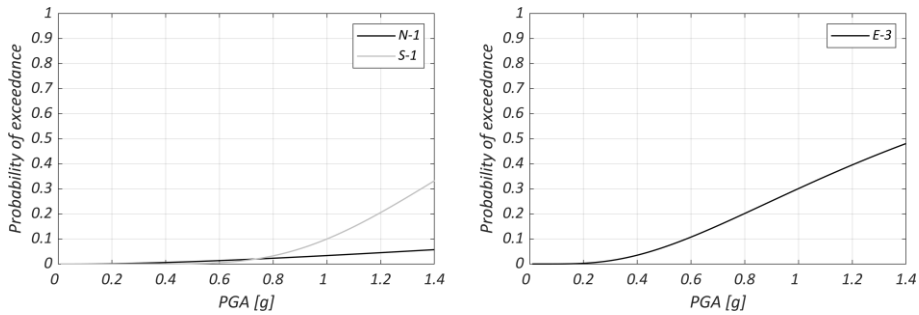

Figure 4.78 OOP collapse fragilities for retrofitted configuration in Or_1 (left) and Or_2 (right).

4.10.5 Results comparison

As a results, the OOP collapse fragility functions derived for bare and retrofitted configurations of all the case-study building piers are compared in Figure 4.79. Overall, numerical results suggest that the application of the retrofit system to URM piers make extremely unlikely that any OOP failure could occur with the seismic hazard of the area. As depicted in Figure 4.79 (left), considering the case-study building in Or_1, no risk of collapse is estimated for the retrofitted pier S_1, while the one of the retrofitted pier N_1 is practically nullified. However, already in bare conditions the piers presented low OOP vulnerabilities, apart from N_2, of which risk of collapse is nullified by the retrofit system. Focusing on Or_2 (Figure 4.79 right), all bare piers presented appreciable vulnerabilities, with mean PGAs ranging from 0.41g to 0.83g, associated with the squat pier E_3 and the slender pier E_1 respectively. The strengthening intervention nullified the estimated risk of collapse for all piers but for the retrofitted squat wall E_3, of which collapse is however estimated extremely unlikely to occur (mean PGA higher than 1.4g). The performed numerical study estimates the proposed retrofit intervention applied to the case-study building to inhibit the probability of occurrence of piers OOP local collapses, regardless the orientation of the GM. In the following paragraph, the presented results are combined with the ones from global assessment to derive single damage states fragility functions, which take into account simultaneously global and local failure mechanisms for the case-study building in bare and retrofitted configurations.

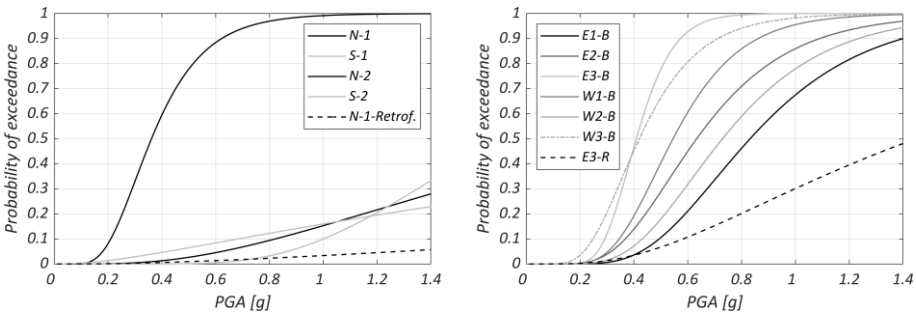

Figure 4.79 OOP collapse fragility functions for bare and retrofitted configurations in Or_1 and Or_2.

4.11 DISCUSSION

The fragility curves representing the vulnerability of the case-study building in bare and retrofitted configurations, considering both global and local failure mechanisms, are derived by assigning to each possible pier OOP collapse a consequence on the global damage state of the structure. The definition of such consequences is based on the classification of damage provided by Grünthal [1998], and on engineering judgement. Peculiarly, a local collapse of any solid wall in the North or South façades is categorized as total or partial collapse, and therefore, brings the whole structure to DS5. The same is assigned to any collapse of the squat walls located at the ground and first floor level of the East and West façades respectively. Instead, any collapse of slender piers of East and West façades is deemed responsible to bring the structure to DS4, assuming such collapses slightly less impacting on the global damage state. Concerning squat walls exceeding their PCRs assuming a 2WB failure mechanisms, their failure is interpreted as a first cracking check, therefore, they bring the structure to DS2. For each of the 250 input motions of the GM database, the initial global damage state assigned to the structure is the higher between the ones associated to Or_1 and Or_2 through global assessment. Then, if the GM also causes the OOP collapse of a masonry pier, and the assigned consequence increases the global level of damage, the global damage state is overwritten.

The results of the procedure related to the bare case-study building are summarised in Table 4.14 and depicted in Figure 4.80, where the combined fragility curves considering global and local failure mechanisms are overlapped with the ones derived only through global assessment. Clearly, the curves mostly penalized by combining the vulnerabilities are the ones related to the strong direction of the case-study building (Or_2, Figure 4.80 right), since the responses in the perpendicular direction drove the association of global damage states for the 99% of the performed NLTHA. Instead, focusing on the weak direction (Or_1, Figure 4.80 left), it can be observed that local failure mechanisms mainly affected the fragility associated to the exceeding of DL4. Specifically, they caused a decrease of 4% and 45% of runs bringing the structure to DS3 and DS4, respectively, while increased the runs associated to the collapse of the structure of about 38%. Therefore, while the fragility

curves associated to DL1 are identical, the ones associated to DL2 and DL3 present the same mean PGAs but with slightly increased dispersion, and the one associated to near collapse (DL4) shows decreased mean PGA and dispersion (more runs associated to collapse) (Table 4.14). The local failure mechanism most impacting on the global damage states is found to be the collapse of the squat walls of the East and West façades. They determined the update of DS4 to DS5 for the 5.2% of GMs, increasing the percentage of analysis bringing the structure to collapse from 26% to 31%. Instead, focusing on the other pier collapses, they are not found to be as influent since for all cases the structure is already evaluated as in an advanced damage state through global analysis.

Moving to the retrofitted configuration of the case-study building in Or_1 (Figure 4.81 left), also in this case the combined fragility curves most affected by the consideration of OOP failures is the one related to the exceedance of DL4. The collapse of a squat wall determined the passage from DS4 to DS5 for 3.6% of the total analysis performed. Considering that 3.2% of them are initially estimated to cause collapse from global analysis, with the accounting for local failures the percentage is doubled. In terms of fragility parameters (Table 4.14), the same overall trend observed for bare conditions is obtained, the curves related to first and second damage limits are not influenced by considering local failures, as opposed to the ones related to DL3 and DL4. The former presents slightly decreased mean PGA and dispersion, while the latter is characterized by a halved mean PGA and a decreased dispersion. Focusing on Or_2 (Figure 4.81 right), the same conclusion outlined for the case-study building in bare conditions can be drawn.

Figure 4.82 compares the fragility functions conditional on the GM PGAs, considering simultaneously global and local failure mechanisms, for the case-study building in bare and retrofitted configurations. The impact of the timber retrofit system on the first two damage states fragility functions is practically absent. This is in line with the mechanical behaviour given by the interaction between masonry and timber: due to the significantly different stiffnesses of the two materials, the retrofit system needs the cracking of masonry in order to activate. On the other hand, the intervention has a clear beneficial effect on the vulnerability of the case-study building to high level of damage, and partial or total collapse (DS3, DS4 and DS5). The DL3 fragility function derived for retrofitted conditions almost coincides with the one of DL4 derived for the bare ones. The possibility of reaching DS4 by the retrofitted case-study building with the considered hazard is significantly decreased, while the probability of reaching total or partial collapse is practically nullified. Considering the PGA associated to a return period of 2475 years, the bare case-study building is estimated to have more than 90% of probability of being in DS3, around 75% of being in DS4 and almost 50% of being in DS5 (collapse). In retrofitted configuration, the percentages of being in DS3 are approximately unvaried, while the one associated to DS4 is decreased to 45%, and the one associated to collapse reduced to less than 5%. Comparing the parameters used to fit fragility functions (Table 4.15), it can be observed that the retrofit

intervention increases of about 39% and 193% the mean PGA associated to the bare case-study building exceeding DL3 and DL4, respectively.

In order to contextualize the obtained results within the research campaign launched at the EUCENTRE laboratories, damage states fragility functions are also derived for the building prototypes EUC-BUILD-6 and EUC-BUILD-7, in order to compare results with the ones provided by Kallioras *et al.*, [2019] for regular buildings belonging to the same typology, excited along their weak direction. Focusing on bare conditions in Or_1 (Figure 4.83 left), it can be noted that the regular configuration presents higher mean PGAs for each considered damage limit. Therefore, it appears reasonable to assume the fragility curves derived in the present study as lower bound for the entire building typology. Furthermore, when comparing the retrofitted irregular building fragility functions for Or_1 with the ones proposed by Kallioras *et al.*, [2019], the same conclusions emerged in the previous paragraph can be drawn. Qualitatively, the application of the retrofit system to a regular building is not expected to be able to delay the occurrence of light damage (DL1, DL2), however, it is estimated to appreciably increase the mean PGA associated to the exceedance of DL3, as well as to nullify the probability of having collapse with the considered hazard.

The presented assessments results could be also integrated with the ones provided by Tomassetti *et al.*, [2019a] for the gable-roof subsystem of typical URM Dutch terraced houses of late '70s – early '80s. In their work, the authors estimated the probability of the system to reach a certain damage state as function of the global one reached by the structure.

Table 4.14 Parameters of fitted lognormal distributions (for all considered DLs) for bare and retrofitted conditions, with and without the consideration of local failure mechanisms.

IM = PGA (g)	**Bare**				**Retrofitted**			
Damage limit	**Global**		**Global and local**		**Global**		**Global and local**	
	e^{μ} [g]	β	e^{μ} [g]	β	e^{μ} [g]	β	e^{μ} [g]	β
DL1	0.09	0.30	0.09	0.30	0.09	0.30	0.09	0.30
DL2	0.17	0.21	0.17	0.33	0.18	0.28	0.18	0.28
DL3	0.23	0.33	0.23	0.39	0.33	0.46	0.31	0.41
DL4	0.40	0.52	0.30	0.43	1.67	0.9	0.88	0.61

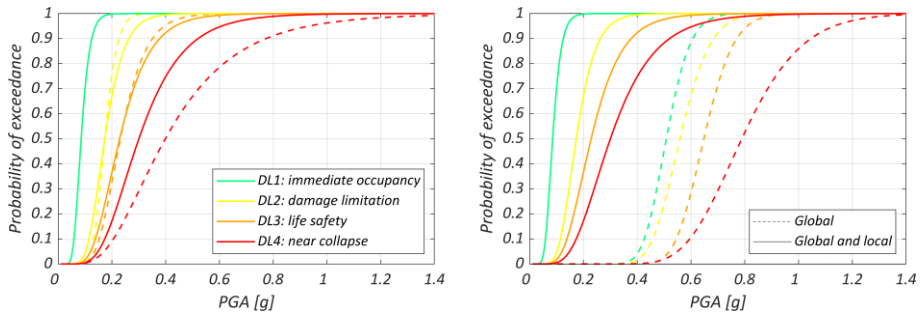

Figure 4.80 Fragility curves comparison with and without consideration of OOP verifications, bare conditions: global results for Or_1 (left) and Or_2 (right).

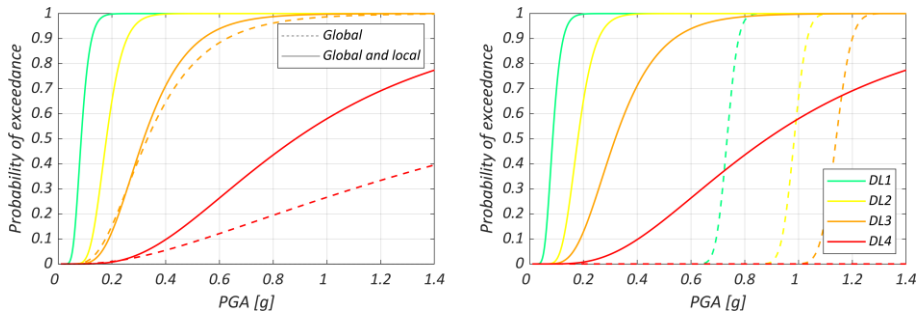

Figure 4.81 Fragility curves comparison with and without consideration of OOP verifications, retrofitted conditions: global results for Or_1 (left) and Or_2 (right).

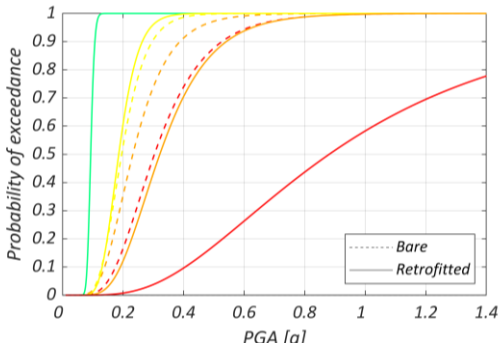

Figure 4.82 Combined damage states fragility functions for bare and retrofitted configurations considering global in-plane and local OOP vulnerabilities.

Table 4.15 Parameters of fitted lognormal distributions (for all considered DLs) for the case-study building in bare and retrofitted conditions considering global and local mechanisms.

IM = PGA (g)	Bare		Retrofitted	
Damage limit	e^{μ} [g]	β	e^{μ} [g]	β
DL1	0.09	0.11	0.09	0.11
DL2	0.20	0.33	0.19	0.27
DL3	0.23	0.40	0.32	0.40
DL4	0.30	0.43	0.88	0.61

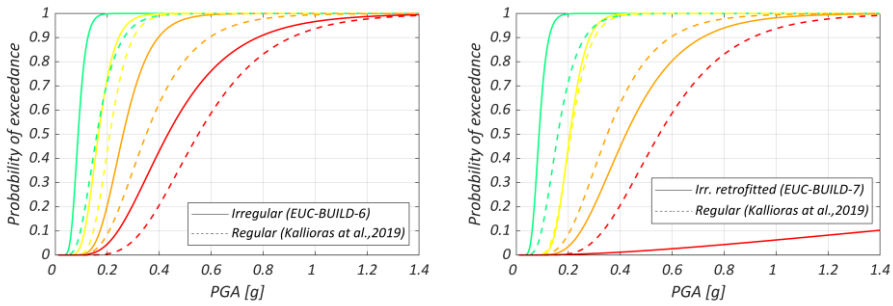

Figure 4.83 Global damage states fragility functions derived for EUC-BUILD-6 [Miglietta *et al.*, 2020] compared with results provided by Kallioras *et al.*, [2019] for regular buildings

4.12 CONCLUSIONS

The seismic vulnerability assessment of a case-study building representing an end-unit of an irregular URM Dutch terraced houses of late '70s – early '80s in the Groningen region (The Netherlands) in bare and retrofitted configurations is carried out considering simultaneously global and local failure mechanisms, aiming to quantify the benefits of a newly proposed timber retrofit system. MDOF numerical models based on the equivalent-frame method are derived from the full-scale experimental tests performed at the EUCENTRE laboratories on two replicas of a highly asymmetric reference building, one in bare and one in retrofitted configuration [Miglietta *et al.*, 2021a]. These systems are then used to derive the numerical models of a case-study building in bare and retrofitted configurations, characterized by typical features that can be found in-situ, such as geometrical characteristics and material properties (the tested building prototypes presented reduced transversal dimensions to fit on the shake-table). They are subsequently reduced to SDOF oscillators and cloud NLTHA is carried out using the latest available GM database of the Groningen region. NLTHA results are then statistically post-processed to obtain global damage states fragility functions conditioned to the PGAs of GMs. Similarly, the OOP collapse vulnerability of URM piers is assessed through NLTHA using the same GM DB, and results used to produce collapse fragility functions. Local and global

assessments are finally combined into singular damage states fragility functions by assigning consequences on the predicted global damage state due to local OOP collapses.

The reliability of the selected approaches for numerical modelling is addressed simulating the global responses recorded during the experimental tests on EUC-BUILD-6 and EUC-BUILD-7 [Miglietta *et al.*, 2021]. The procedure required several dynamic considerations and assumptions, for instance, the neglecting of the gable-roof system in the SDOF reductions due to its low mass and high flexibility compared to the rest of structure, as well as the procedure itself selected to reduce MDOF systems into SDOF oscillators or the modelling strategy adopted for retrofitted masonry. Once produced reliable MDOF systems calibrated on experimental tests, geometrical properties and dimensions are varied to generate a case-study building in bare and retrofitted configurations with typical features that can be found in-situ. Therefore, the impact of the new retrofit system on the global seismic capacity of the building is evaluated through NLTH cloud analysis using a GM database representative of the study area. The outcomes of NLTHA, interpreted using damage limit thresholds experimentally defined, allow to generate global damage states fragility functions. Numerical results provided also filtered acceleration THs used for the dynamic assessment of masonry piers located at the first-floor level. The OOP behaviour of walls is simulated with the model proposed by Tomassetti *et al.*, [2018], which is also updated with a new routine to allow the modelling of timber retrofitted masonry piers. The outcomes of the procedure are presented in terms of fragility functions conditional on the PGAs. As last step, global and local vulnerability assessments are combined into single damage states fragility functions, for bare and retrofitted conditions. The study showed that results from the global NLTHA along the strong direction of the case-study building could be neglected for both building configurations, since the exceedance of damage limit thresholds is entirely governed by the vulnerability along the weak direction. Instead, it suggested that is important to assess the local OOP vulnerability of masonry elements along both main directions and to combine them with global results in order to obtain conservative vulnerability results. It also suggested that local OOP behaviours have small influence on the building vulnerability associated to low level of damage (DL1 and DL2), while they can have non-negligible effects on high levels (DL3 and DL4). Overall, it appears fundamental to consider local OOP failure mechanisms for the exhaustive vulnerability assessment of irregular Dutch URM cavity-wall terraced houses of late '70s – early '80s, especially in bare conditions. Moreover, it is estimated that the application of the newly proposed retrofit system has significant positive effects on their seismic vulnerability to high level of damage and collapse, while it does not affect the occurrence of light damage.

The final results of the numerical study represent an overall view of the vulnerability of typical irregular Dutch URM terraced houses in bare and retrofitted configurations, which is in line with post-earthquake observations from the Groningen area. Considering the highly unfavourable features of the case-study building under scrutiny, with respect to more

regular buildings belonging to the same typology that can be found in-situ, the obtained curves could be assumed as lower bound for the entire typology. Nevertheless, they are not intended to be representative of the entire URM building stock of the considered area. The presented results provide useful quantitative information that are highly affected by the assumptions and approximations made. Especially for the presented case, due to the irregularity of the building and the complexity of its lateral response, in both configurations, several assumptions are needed to overcome limits of the used methodologies. Besides, MDOF numerical models are derived by experimental tests on prototypes featuring a certain combination of construction details, materials, and subjected to a certain dynamic testing protocol. However, different types of Dutch URM terraced houses can be characterized by a variety of materials and material properties, especially depending on the period of construction. More studies on similar buildings are needed to confirm the general validity of presented results.

4.13 REFERENCES

Applied Technology Council [2012] *Guidelines for Seismic Performance Assessment of Building, ATC-58 100% Draft*, 266 pp, Redwood City, CA.

AS 3700 [2018] *Masonry Structures*, Australian Standard, Sydney, Australia.

AWC [2008] *ANSI/AF&PA SDPWS-2008: Special design provisions for wind and seismic*. American Wood Council, Washington D.C., USA.

Baker, J.W., Cornell, C.A. [2005] "Vector-Valued Ground Motion Intensity Measures for Probabilistic Seismic Demand Analysis", *Report No. 150*, John A. Blume Earthquake Engineering Center, Stanford, CA, 321 pp.

Bracchi, S., Mandirola, M., Rota, M., and A. Penna. [2020] "A new macroelement-based strategy for modelling reinforced masonry piers". In *Brick and Block Masonry-From Historical to Sustainable Masonry*, 900-907. CRC Press.

Brignola, A., Pampanin, S., Podestà, S. [2009] "Evaluation and control of the in-plane stiffness of timber floors for the performance-based retrofit of URM buildings". *Bulletin of the New Zealand Society for Earthquake Engineering*, 42(3): 204-221. doi: 10.5459/bnzsee.42.3.204-221.

Casarotti, C., Pinho, R. [2007] "An adaptive capacity spectrum method for assessment of bridges subjected to earthquake action". *Bulletin of Earthquake Engineering*, 5(3), 377-390.

Cassol, D., Giongo, I., Ingham, J.M., Dizhur, D. [2021] "Seismic out-of-plane retrofit of URM walls using timber strong-backs". *Construction and Building Materials*, 269, 121237.

Chopra, A.K. [2012] *Dynamics of Structures: Theory and Applications to Earthquake Engineering (4th edition)*, Prentice Hall, One Lake Street, Upper Saddle River, New Jersey, United States.

Costa, A.A., Penna, A., Arede, A., Costa, A. [2015] "Simulation of masonry out-of-plane failure modes by multi-body dynamics". *Earthquake Engineering and Structural Dynamics*; 44(14).

Crowley, H., Polidoro, B., Pinho, R., van Elk, J. [2017] "Framework for developing fragility and consequence models for local personal risk". *Earthquake Spectra*, 33(4), 1325-1345.

Crowley, H., Pinho, R., Cavalieri, F. [2019] "Report on the v6 Fragility and Consequence Models for the Groningen Field", *Technical report*. Available at https://www.nam.nl/over-nam/onderzoeksrapporten.html.

Crowley, H., Pinho, R. [2020] "Report on the v7 Fragility and Consequence Models for the Groningen Field", *Technical report*. Available at https://www.nam.nl/over-nam/onderzoeksrapporten.html.

Damiani, N., Miglietta, M., Mazzella, L., Grottoli, L., Guerrini, G., Graziotti, F. [2019] "Full-scale shaking table test on a Dutch URM cavity-wall terraced-house end unit—a retrofit solution with strong-backs and OSB boards—EUC-BUILD-7". *Research report EUC052/2019U*, EUCENTRE foundation, Pavia, Italy. https://www.eucentre.it/nam-project.

D'Ayala, D., Shi, Y. [2011] "Modeling masonry historic buildings by multi-body dynamics". *International Journal of Architectural Heritage*, 5(4–5):483–512.

Derakhshan, H., Griffith, M.C., Ingham, J.M. [2013] "Out-of-Plane Behavior of One-Way Spanning Unreinforced Masonry Walls". *Journal of Engineering Mechanics*, 139:409–17. https://doi.org/10.1061/(ASCE)EM.1943-7889.0000347.

Derakhshan, H., Dizhur, D., Griffith, M.C., Ingham, J.M. [2014] "Seismic Assessment of Out-of-Plane Loaded Unreinforced Masonry Walls". *Bulletin of the New Zealand Society for Earthquake Engineering*, 47:119–38.

Derakhshan, H., Griffith, M.C., Ingham, J.M. [2015] "Seismic out-of-plane seismic response of vertically spanning URM walls connected to flexible diaphragms". *Earthquake Engineering and Structural Dynamics*, 45(4):563–80.

Doherty, K.T. [2000] "An investigation of the weak links in the seismic load path of unreinforced masonry buildings", *PhD Dissertation*, University of Adelaide, Australia.

Dolce, M. [1991] "Schematizzazione e modellazione degli edifici in muratura soggetti ad azioni sismiche". *L'industria Delle Costruzioni*, 25(242):44–57 (in Italian).

European Committee for Standardization [2004] *Eurocode 8: Design of Structures for Earthquake Resistance - Part 1: General Rules, Seismic Actions, and Rules for Buildings, EN 1998-1*, CEN, Brussels, Belgium.

European Committee for Standardization [2005] *EN 1052-5: Methods of test for masonry – Part 5: Determination of bond strength by the bond wrench method*. CEN, Brussels, Belgium.

Federal Emergency Management Agency [2017] *HAZUS-MH MR4 multi-hazard loss estimation methodology: earthquake model, Technical Manual*, FEMA, Washington DC, United States.

Ferreira, T.M., Costa, A.A., Vicente, R., Varum, H. [2015] "A simplified four-branch model for the analytical study of the out-of-plane performance of regular stone URM walls". *Engineering Structures*, 83:140–53.

Giannopoulos, D., Vamvatsikos, D. [2018] "Ground motion records for seismic performance assessment: To rotate or not to rotate?". *Earthquake Engineering & Structural Dynamics*, 47(12), 2410-2425.

Graziotti, F. [2013] "Contributions towards a Displacement-Bases Seismic Assessment of Masonry Structures", *PhD Dissertation*, University School for Advanced Studies (IUSS), Pavia, Italy.

Graziotti, F., Penna, A., Bossi, E., Magenes, G. [2014] "Evaluation of displacement demand for unreinforced masonry buildings by equivalent SDOF systems", *Proceedings of 9th International Conference on Structural Dynamics (EURODYN 2014), European Association for Structural Dynamics*, Porto, Portugal, pp. 365-372.

Graziotti, F., Penna, A., Magenes, G. [2016a] "A nonlinear SDOF model for the simplified evaluation of the displacement demand of low-rise URM buildings", *Bulletin of Earthquake Engineering*, Vol. 14, No. 6, pp. 1589-1612. https://doi.org/10.1007/s10518-016-9896-5.

Graziotti, F., Tomassetti, U., Penna, A., Magenes, G. [2016b] "Out-of-plane shaking table tests on URM single leaf and cavity walls". *Engineering Structures*, 125:455–70. http://dx.doi.org/10.1016/j.engstruct.2016.07.011

Graziotti, F., Tomassetti, U., Kallioras, S., Penna, A., Magenes, G. [2017] "Shaking table test on a full scale URM cavity wall building". *Bulletin of Earthquake Engineering*, 15:5329–5364. https://doi.org/10.1007/s10518-017-0185-8

Graziotti, F., Penna, A., & Magenes, G. [2019a] "A comprehensive in situ and laboratory testing programme supporting seismic risk analysis of URM buildings subjected to induced earthquakes". *Bulletin of Earthquake Engineering*, 17(8), 4575-4599.

Graziotti, F., Tomassetti, U., Sharma, S., Grottoli, L., Magenes, G. [2019b] "Experimental response of URM single leaf and cavity walls in out-of-plane two-way bending generated by seismic excitation". *Constructions Building Materials*, 195:650–70. https://doi.org/10.1016/j.conbuildmat.2018.10.076.

Griffith, M.C., Magenes, G., Melis, G., Picchi, L. [2003] "Evaluation of out-of-plane stability of unreinforced masonry walls subjected to seismic excitation". *Journal of Earthquake Engineering*, 7:141–69.

Griffith, M.C., Vaculik, J., Lam, N.T.K., Wilson, J., Lumantarna, E. [2007] "Cyclic testing of unreinforced masonry walls in two-way bending". *Earthquake Engineering & Structural Dynamics*, 36:801–21. https://doi.org/10.1002/eqe.654.

Grünthal, G. (editor) [1998] *European Macroseismic Scale 1998 (EMS-98), Cahiers du Centre Européen de Géodynamique et de Séismologie 15*, Centre Européen de Géodynamique et de Séismologie, Luxembourg.

Guerrini, G., Graziotti, F., Penna, A., Magenes, G. [2017] "Improved evaluation of inelastic displacement demands for short-period masonry structures", *Earthquake Engineering & Structural Dynamics*, Vol. 46, No. 9, pp. 1411-1430. https://doi.org/10.1002/eqe.2862.

Guerrini, G., Damiani, N., Miglietta, M., Graziotti, F. [2021] "Cyclic response of masonry piers retrofitted with timber frames and boards". *Structures and Buildings*. https://doi.org/10.1680/jstbu.19.00134

Housner, G.W. [1963] "The behavior of inverted pendulum structures during earthquakes". *Bulletin of Seismological Society of America*, 53(2): 403–17.

Jacobsen, L.S. [1960] "Damping in composite structures". *Proceedings of the 2nd World Conference on Earthquake Engineering*, Tokyo and Kyoto, Japan. vol. 2, pp. 1029–1044.

Jalayer, F., De Risi, R., Manfredi, G. [2015] "Bayesian Cloud Analysis: efficient structural fragility assessment using linear regression". *Bulletin of Earthquake Engineering*, 13(4), 1183-1203.

Janich, R. [1962] *Die N¨aherungsweise Berechnung Der Eigenfrequenzen VonRechteckigen Platten Bei Verschiedenen Randbedingungen*. Die Bautechnik. 3:93–9.

Kallioras [2019] Contributions to the seismic vulnerability assessment of unreinforced masonry buildings under induced seismicity. *PhD dissertation*. University School for Advanced Studies (IUSS), Pavia, Italy.

Lagomarsino, S., Penna, A., Galasco, A., Cattari, S. [2013] "TREMURI program: an equivalent frame model for the nonlinear seismic analysis of masonry buildings". *Engineering structures*, 56: 1787-1799.

Lagomarsino, L. [2014] "Seismic assessment of rocking masonry structures". *Bulletin of Earthquake Engineering*, 13:97–128.

Lam, N.T.K., Griffith, M., Wilson, J., Doherty, K. [2003] "Time-history analysis of URM walls in out-of-plane flexure". *Engineering Structures*, 25(6):743–54.

Lawrence, S., Marshall, R. [2000] "Virtual work design method for masonry panels under lateral load". *Proceedings of the 12th international brick and block masonry conference, IBMAC*. p. 1063–73.

Maio, R., Tsionis, G. [2016] "Seismic fragility curves for the European building stock: review and evaluation of analytical fragility curves", *EUR 27635 EN*, Joint Research Centre (European Commission), Ispra, Italy. Available at https://doi.org/10.2788/586263.

Magenes, G., Calvi, G., Kingsley, G. [1995] "Seismic testing of a full-Scale, two-story masonry building: test procedure and measured experimental response. Experimental and numerical investigation on a brick masonry building prototype – Numerical Prediction of the Experiment", *Research Report*, University of Pavia, Department of Structural Mechanics, Pavia, Italy.

Martinelli, E., Faella, C. [2015] "Nonlinear static analyses based on either inelastic or elastic spectra with equivalent viscous damping: a parametric comparison", *Engineering Structures*, Vol. 88, pp. 241-250. Available at https://doi.org/10.1016/j.engstruct.2015.01.035.

Miglietta, M., Mazzella, L., Grottoli, L., Guerrini, G., Graziotti, F. [2019] "Full-scale shaking table test on a Dutch URM cavity-wall terraced-house end unit—EUC-BUILD-6". *Research report EUC160/2018U*, EUCENTRE foundation, Pavia, Italy. https://www.eucentre.it/nam-project.

Miglietta, M., Damiani, N., Guerrini, G., Graziotti, F. [2021a] "Full-scale shake-table tests on two unreinforced masonry cavity-wall buildings: effect of an innovative timber retrofit". *Bulletin of Earthquake Engineering*, 19(6), 2561-2596.

Miglietta, M., Damiani, N., Bracchi, S., Guerrini, G., Graziotti, F., Penna, A. [2021b] "Macroelement Numerical Simulation of the Seismic Response of a Timber-Retrofitted Masonry Pier". In proceedings of the 12th International Conference on Structural Analysis of Historical Constructions (SAHC). https://www.scipedia.com/public/Miglietta_et_al_2021a

Miranda, E. [2000] "Inelastic displacement ratios for structures on firm sites", *Journal of Structural Engineering* (ASCE), Vol. 126, No. 10, pp. 1150-1159. Available at https://doi.org/10.1061/(ASCE)0733-9445(2000)126:10(1150).

Miranda, E. [2001] "Estimation of inelastic deformation demands of SDOF systems". *Journal of Structural Engineering*, 127:1005–1012

Mouyiannou, A., Penna, A., Rota, M., Graziotti, F., Magenes, G. [2014] "Implications of cumulated seismic damage on the seismic performance of unreinforced masonry buildings", *Bulletin of the New Zealand Society for Earthquake Engineering*, Vol. 47, No. 2, pp. 157-170.

NPR 9998 [2020]. *Beoordeling van de constructieve veiligheid van een gebouw bij nieuwbouw, verbouw en afkeuren - Geïnduceerde aardbevingen -Grondslagen, belastingen en weerstanden*. Dutch Practical Guideline, NEN, Delft, The Netherlands:.

NZSEE [2016]. *Section C8 – Seismic assessment of unreinforced masonry buildings, The seismic assessment of existing buildings: Technical guidelines for engineering assessment*. New Zealand.

Penna, A., Lagomarsino, S., & Galasco, A. [2014] "A nonlinear macroelement model for the seismic analysis of masonry buildings". *Earthquake Engineering & Structural Dynamics,* 43(2): 159-179.

Penna, A., Rota, M., Galasco, A., Mouyiannou, A. [2015] "Towards the use of time-history analysis for the seismic assessment of masonry structures". *In: Psycharis, I.N., Pantazopoulou, S.J., Papadrakakis, M. (editors) Seismic Assessment, Behavior and Retrofit of Heritage Buildings and Monuments*, Springer International Publishing, Switzerland, pp. 83-111.

Restrepo-Vélez, L.F., Magenes, G., Griffith, M.C. [2014] "Dry stone masonry walls in bending - Part I: Static tests". *International Journal of Architectural Heritage*, 8:1–28. https://doi.org/10.1080/15583058.2012.663059.

Rota, M., Penna, A., Magenes, G. [2010] "A methodology for deriving analytical fragility curves for masonry buildings based on stochastic nonlinear analyses", *Engineering Structures*, Vol. 32, No. 5, pp. 1312-1323. Available at https://doi.org/10.1016/j.engstruct.2010.01.009.

Sharma, S., Tomassetti, U., Grottoli, L., Graziotti, F. [2020] "Two-way bending experimental response of URM walls subjected to combined horizontal and vertical seismic excitation". *Engineering Structures*; 219:110537. https://doi.org/10.1016/j.engstruct.2020.110537.

Sharma, S., Tomassetti, U., Graziotti, F., & Magenes, G. [2021] "Simplified methodologies for assessing the out-of-plane two-way bending seismic response of unreinforced brick masonry walls: lessons from recent experimental studies". *Structures*, Elsevier, Vol. 33, pp. 2839-2854.

Shinozuka, M., Feng, M. Q., Lee, J., and Naganuma, T. [2000] "Statistical analysis of fragility curves". *Journal of Engineering Mechanics*, 126, 1224–1231.

Simsir, C.C., Aschheim, M.A., Abrams, D.P. [2004] "Out-of-plane dynamic response of unreinforced masonry bearing walls attached to flexible diaphragms". *Proceedings of the 13th World Conference on Earthquake Engineering*, Vancouver, BC, Canada.

Skoulidou, D., & Romão, X. [2020] "The significance of considering multiple angles of seismic incidence for estimating engineering demand parameters". *Bulletin of Earthquake Engineering*, 18(1), 139-163.

Sorrentino, L., Masiani, R., Griffith, M.C. [2008] "The vertical spanning strip wall as a coupled rocking rigid body assembly". *Structural Engineering and Mechanics*, 29:433–53.

Tomassetti, U., Correia, A. A., Graziotti F., Marques, A. I., Mandirola, M., Candeias, P. X. [2017a] "Collapse shaking table test on a urm cavity wall structure representative of a Dutch terraced house". *Research report*, EUCENTRE foundation, Pavia, Italy. https://www.eucentre.it/nam-project.

Tomassetti, U., Graziotti, F., Penna, A., Magenes, G. [2017b] "Energy dissipation involved in the out-of-plane response of unreinforced masonry walls", *Proceedings of the 6th Compdyn conference*, Rhodes, Greece. http://dx.doi.org/10.7712/120117.5622.18454.

Tomassetti, U., Graziotti, F., Penna, A., Magenes, G. [2018] "Modelling one-way out-of-plane response of single-leaf and cavity walls". *Engineering Structures*, 167, 241-255.

Tomassetti, U., Correia, A. A., Graziotti, F., Penna, A. [2019a] "Seismic vulnerability of roof systems combining URM gable walls and timber diaphragms". *Earthquake Engineering & Structural Dynamics*, 48(11), 1297-1318.

Tomassetti, U., Correia, A. A., Candeias, P. X., Graziotti, F., & Costa, A. C. [2019b] "Two-way bending out-of-plane collapse of a full-scale URM building tested on a shake table". *Bulletin of Earthquake Engineering*, 17(4), 2165-2198.

Tomassetti, U., Graziotti, F., Sorrentino, L., & Penna, A. [2019c] "Modelling rocking response via equivalent viscous damping". *Earthquake Engineering & Structural Dynamics*, 48(11), 1277-1296.

Tondelli M, Graziotti F, Rossi A, Magenes G [2015] "Characterization of masonry materials in the Groningen area by means of in situ and laboratory testing". *Technical Report*, EUCENTRE Foundation, Pavia, Italy. Available online at www.eucentre.it/nam-project

Vaculik, J., Griffith, M.C., Hogarth, B., Todd, J. [2004] "Out-of-plane flexural response tests using dry-stack masonry". *Proceedings of a conference held by the Australian Earthquake Engineering Society*, Mt. Gambier, South Australia.

Vaculik J. [2012] "Unreinforced masonry walls subjected to out-of-plane seismic actions". *PhD Dissertation*, University of Adelaide, Australia.

Vaculik, J., Griffith, M. C. [2018] "Out-of-plane shaketable testing of unreinforced masonry walls in two-way bending". *Bulletin of Earthquake Engineering*, 16(7), 2839-2876.

Walsh, K.Q., Dizhur, D., Shafaei, J., Derakhshan, H., Ingham, J.M. [2015] "In Situ Out-of-Plane Testing of Unreinforced Masonry Cavity Walls in as-Built and Improved Conditions". *Structures*, 3:187–99. https://doi.org/10.1016/j.istruc.2015.04.005.

Warburton, G.B. [1954] "The vibration of rectangular plates". *Proceedings of the Institution of Mechanical Engineers*, 168(1), 371-384. https://doi.org/10.1243/PIME_PROC_1954_168_040_02.

Willis, C. [2004] "Design of unreinforced masonry walls for out-of-plane loading". *PhD Dissertation*, University of Adelaide, Australia.

5. PRELIMINARY CONSIDERATIONS ON THE SUSTAINABILITY OF THE RETROFIT INTERVENTION

5.1 INTRODUCTION

In recent times, the global warming effects are becoming a major issue worldwide, their evidence are not anymore constrained to scientific studies, but clear to the whole population. Storms, floods, hurricanes, drought, fires, and in general extreme meteorological events, are increasing in frequency and their associated energy is growing with their occurrence rate. Such events can have devastating effects on entire regions, from life safety, economical, and environmental point of views. Nowadays it is well-known that the main drivers of climate changes lie on the human activities and the amount of carbon emitted in the atmosphere, which cannot be naturally adsorbed by the planet anymore. Consequently, radical actions are required to change human habits towards a sustainable life, in equilibrium with nature, to guarantee to the next generations the life that we know. The concept of "sustainable development" was firstly introduced in 1987 at the General Assembly of the United Nations, where the Bruntland Commission defined it as the "meet of the needs of the present without compromising the ability of future generations to meet their own needs" [WCED, 1987]. Such an objective can only be achieved from simultaneously addressing economic, environmental, and social issues, i.e., the so-called "three pillars" of sustainability [United Nations, 1997], or sustainability triple bottom line. The conclusion of the Paris Agreement at COP 21 establishes the worldwide shared commitment to face the climate change effects by limiting the global warming to 1.5°C (below 2°C). The European Community set the first de-carbonisation target in 2030, with the objectives of reducing of 40% the green-house gasses (GHG) emissions compared to 1990, of consuming at least 32% of renewable energy in the energy mix and to reach at least the 32% of energy savings [European Union 2018/1999]. Each member state is asked to set its own strategic plan to go towards this direction. Subsequently, the European Union set an even more ambitious long-term target consisting of reaching carbon neutrality by 2050, through the reduction of 50% of the final energy consumption compared to 2005 [EU COM, 2018].

To pursue a sustainable development, the human production sectors with the highest environmental impacts need to be identified and firsts actions must be related to them. Within this context, it is well recognised that the pursued reduction of energy consumption is primarily driven by the building sector. 40% of the total European energy consumption is imputable to existing buildings, of which the 25% is imputable to the residential ones

[Tsemekidi Tzeiranaki *et al.*, 2019]. The European building stock is characterised by aged constructions, of which around 45% were built before the first thermal regulations (1970) and present exhausted service life, the 40% was built before 2000, while only the 15% after 2000 [European Building Observatory]. Moreover, it is estimated that the 75% of the existing buildings will be still standing in 2050 [Ürge-Vorsatz *et al.*, 2016]. The existing European building stock has a large energy efficiency potential which cannot be exploited unless deep energy renovation actions are undertaken [IPCC, 2018]. The upgrading of energy performance of a building reduces its operational emissions and the associated pollution, and from the household's viewpoint, it reduces energy bills, increases the disposable income, reduces energy poverty, and improves internal house comfort.

Existing buildings can present several structural and energy issues, for instance, exhausted service life, high seismic vulnerability due to absence of regulation or of seismicity at the time of construction, non-efficient operational energy consumptions, and low internal comfort. At present, the main efforts to move towards a sustainable construction sector have been the promulgation of national and European incentives, as well as the publication of protocols for the construction of new eco-efficient buildings (e.g., LEED and GBC protocols). The big limitation of these measures is that they regard only new constructions, which could be either realized in unspoiled areas or in substitution of existing buildings (to be demolished). Preservation Green Lab, [2012] and UCL Urban Lab, [2014] demonstrated that none of the solutions is viable: while the use of unspoiled lands increases the burden on the environment, the demolition of existing buildings generates additional waste to be disposed, increasing more the pressure on landfills. In both cases, the environmental impact of unsafe and energy-consuming existing buildings is not decreased. Considering the low rate of new constructions (around 1.5%, [Baek and Park, 2012]), it appears evident that the solely construction of new eco-efficient buildings is not sufficient to develop an appreciable decrease in the GHG emissions associated to the sector. In light of these findings, the renovation of existing buildings became recently a prior need to foster an appreciable decrease of the construction sector environmental impact. Therefore, the European community promoted the deep renovation of existing buildings and new investments in energy efficiency through the Energy Performance of Buildings Directive (EU) 2018/844 [Directive (EU), 2018b] and the revised Energy Efficiency Directive (EU) 2018/2002 [Directive (EU), 2018a]. Improved financial instruments and new financial models, as well as the development of supporting mechanisms is fundamental to foster sustainable energy projects within the economical and social development of the member states [Bertoldi *et al.*, 2021].

In the last 20 years, several European scientific groups focused their attention on the reduction of the operational energy consumptions and on the use of low-carbon materials in the building refurbishment process. However, the commonality of these studies is that no natural hazard is taken into account, while nowadays it is recognized that the

environmental impact of the structural retrofits required after an earthquake event can undermine any prior energy refurbishment [Belleri *et al.*, 2016]. In other words, the target of nearly-zero-energy building, promoted by International Standards, cannot be pursued if adequate energy efficiency interventions are applied to structurally unsafe constructions. To face this issue, the European SAFESUST (safety + sustainability) commission has established the basis for a "Roadmap for the improvement of earthquake resistance and eco-efficiency of existing buildings and cities" [Caverzan *et al.*, 2016]. These concepts are broadly shared by engineers, who recently published numerous studies on the environmental impact of the seismic hazard related to the built environment [e.g., Wei *et al.*, 2016, Menna *et al.*, 2019]. Some of them proposed life-cycle frameworks for the identification of optimal building renovation strategies considering concurrently structural, economic, and environmental impacts [Clemett *at al.*, 2022, Caruso *et al.*, 2020]. The common idea is that the three pillars of sustainability must be considered simultaneously within a building retrofit intervention to determine the most sustainable solution, from the material extraction to the building end of life (cradle-to-grave), independently from the specific reasons that led the owner to invest.

Remarkably, Caruso *et al.*, [2020] also proposed a new index (named Life Cycle Performance Metric – LCPM) that allows to classify building upgrade interventions integrating the economic and environmental aspects throughout the entire life cycle of a structure. The authors fostered a framework for a sustainable development that considers natural hazard and does not condense costs into environmental impacts or vice-versa. By computing LCPM values for different intervention alternatives for a specific structure, one can classify them into a double entrance table (Figure 5.1). So far, as stated by the authors, the classification methodology has only been applied to their case studies, therefore, additional investigations are required to evaluate ranges of values for the different classes. However, the system could serve as basis for a communitarian classification scheme that goes beyond the economical aspects, and help practitioners in the selection of optimal retrofit interventions to mitigate seismic vulnerability and energy consumptions.

Passoni *et al.* [2020] proposed a new Life-Cycle-Thinking(LCT)-based design framework to foster the Sustainable Building Renovation (SBR), embracing holistic perspectives throughout all the steps of the design process. In their work, the authors carried out a thorough review of the state of art, highlighting that previous works are often ex-post methods and could be clustered into four main groups based on the three sustainability pillars: methods combining environmental and economic sustainability; methods combining safety and economic sustainability; methods combining safety and environmental sustainability; and, only recently, methods combining safety, environmental, and economic sustainability. Their proposal, named Sustainable Building Renovation Design framework (SBR-D), is an innovative LCT-based approach aiming at overcoming the gaps found in literature and at offering a holistic design procedure for sustainable

retrofit interventions. It is intended to be applied from the very initial stage of the project, before the design of the possible interventions themselves, and to promote the choice of the best retrofit option considering the three main aspects of sustainability: economical, social/cultural, and environmental. Within the selection and realization of an intervention, being structural, energetic, or integrated, the major barriers to be addressed are mainly identified in high initial construction costs, long duration of works, and impairing construction sites [BPIE, 2011, La Greca and Margani, 2018]. To overcome these issues the SBR-D framework introduced a "pre-screening" of possible retrofit solutions right after the identification of structural and energetic deficiencies of the building under scrutiny in as-built conditions. At this stage, the engineer can evaluate the suitability of different alternatives (either structural or energetic or combined interventions) under the lens of LCT principles, considering building specific needs and barriers to the renovation (e.g., inability to relocate the inhabitants during the construction works, low budget, etc.). This preliminary qualitative assessment of the range of possibilities connected to the specific project represents the main innovation of the framework and involves all parties in the definition of qualitative social, economical, and structural decision variables to be considered throughout the whole project stages. In this way, LCT principles could be applied before the selection of possible alternatives, which by themselves could be not always sustainable.

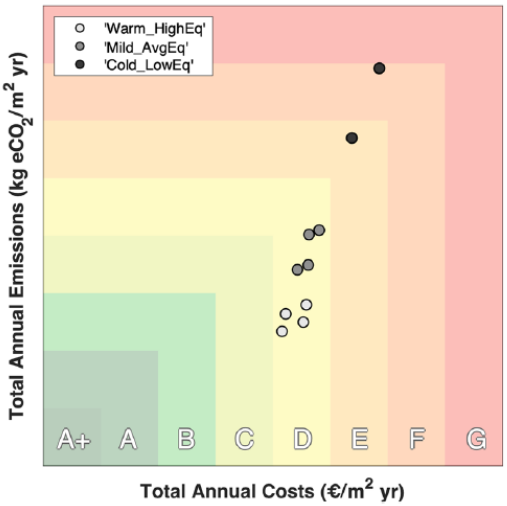

Figure 5.1 Example of double entrance table for classification of buildings. Qualitative image reproduced from Caruso *et al.*, [2020])

Given the recent development in the construction field research, nowadays several methods can be used to estimate environmental impacts and costs of retrofit solutions, being them structural or energetic, or combined. However, very variable levels of accuracy

can be reached by combining the different method to analyse the life-cycle stages of a building. For instance, the environmental impacts of construction, retrofit and demolition of a building can be determined through process life-cycle assessment (LCA) or through the economic input-output LCA (EIO). The former is the most rigorous. It requires the collection of all the industrial processes behind the production of all materials used and related environmental impact data, and therefore an advanced level of knowledge to be applied. It is the bottom-up procedure, but can also be susceptible to significant truncation bias, which happen when some processes are left outside the considered system boundaries [Majeau-Bettez *et al.*, 2011, Säynäjoki *et al.*, 2017, Ward *et al.*, 2018]. The latter is based on economic input-output tables which effectively model economic transactions between different sectors of economy. From them, the user can retrieve how much dollars an industrial sector of the economy spends in each other sectors to produce 1 dollar worth of its own product. Once known the EI of each industrial sector for dollar of product produced, the corresponding environmental impacts can be determined. The robustness of the different methodologies available for the environmental impact assessment has been investigated by researchers in literature [e.g., Majeau-Bettez *et al.*, 2011, Junnila, 2006, Lenzen, 2000]. They focused on different aspects or stages of the building life cycles, aiming at highlighting deficiencies or bias, and convey on the fact that assumptions are the main drivers on this type of analysis. European guidelines for LCA are the ISO 14040:2006 [BSI, 2006], ISO 14044:2008 [BSI, 2008a] and ISO 1539-2008 [BSI, 2008b], that define the instruments to estimate environmental impacts as relative tools, which provide "relative expressions and do not predict impacts on category endpoints, the exceeding of thresholds, safety margins or risks". The most sustainable alternative among a selected set of options to resolve the same issue can always be quantitatively determined. However, the meaning of the assessment is firstly established by the selection of the options to be compared. It is therefore required a qualitative evaluation of the possible choices under the light of a sustainable approach before the study on the sustainability of the solutions themselves. For instance, an engineer could propose multiple retrofit systems for the same structural/energy retrofit, which all use a non-sustainable material, and compute the one that would be responsible of less emissions in the environment. There are also many other non-quantifiable aspects of a retrofit intervention, i.e., characteristics of reversibility, low invasiveness, standardization, ease of assembly, speed of installation.

During the conception of the new timber-based retrofit system, not all the above-mentioned aspects could be covered due to time constraints. However, the *a-posteriori* analysis of the proposed retrofit intervention under the light of LCT principles could allow to decrease the environmental impacts of the intervention by making it entirely reversible and optimizing the use of material. To this end, the present section reviews the technologies used in the timber structural retrofit system and proposes a new dry solution to connect the timber elements to the existing masonry. The mechanical characterisation of the new connection is followed by the assessment of environmental and economical benefits given

by the substitution of the original one in the intervention applied to the case-study building discussed in the previous section (par. 4.5). The environmental impacts of the two solutions are compared through the computation of the GHG emission associated to the employed material.

5.2 RE-ENGINEERING OF THE RETROFIT SYSTEM

Beyond structural and economical point of views, a new strengthening system compliant with LCT principles should be ideally standardizable, reversible, reparable, recyclable, integrable with energetic retrofit systems, and should be able to address the building-specific main barriers to renovation. However, often time constraints do not allow to cover all the aspects during the conceiving phase of an intervention, as well as the progress of technology could offer new techniques to be employed with the advance of time. In order to meet higher objectives in terms of environmental sustainability with the proposed timber retrofit system, it is *a-posteriori* critically examined under the lens of LCT.

Overall, the proposed solution already complies some of the LCT principles: it can be easily installed since no specialized expertise is required, and it can be standardized and repaired. Also, it is based on unprocessed wood, that does not require chemical processes (or glue) to be produced, and by itself is a low-carbon material. The focus of the examination was placed on the connection details between timber elements and the existing structure. As described in detail in par. 2.2.2, the retrofit system includes four types of connections: the timber-to-timber and the timber-to-masonry, and the anchorage of horizontal and vertical timber elements to floors and foundations. The connection of first-storey top sill plate and second storey bottom sill-plate with the first floor RC slab (see Figure 3.7) relies on passing through threaded bars that allow the clamping of timber elements to the floor slab. At the second floor, the connections with the timber diaphragm could be entirely realized with steel angles and screws. Both solutions are completely reversible, and the composing elements could be entirely recycled at end of life. The same characteristics cannot be associated to the solution used to connect the timber frame system with foundations and existing masonry. In both cases, threaded bars were embedded into the existing structure and bonded by an epoxy glue, which prevent the possibility to recycle the connection at end of life, jeopardizing the reversibility of the system.

In the experimental test, the building specimen was built directly on the shake-table of the EUCENTRE laboratory, supported by a composite steel-concrete foundation. The walls were all founded on a 110-mm-thick concrete layer (Mapei Mapefill 50 with gravel), contained in UPN 400 steel profiles (see Figure 3.7). Given the characteristics of the foundation, which clearly does not present the typical features that could be found in situ, and severely limited the usable length to anchor threaded bars, no suitable dry connection was found available in the market, therefore the use of an epoxy bond was deemed the only viable alternative. However, with no limitations on the anchoring length, the connection

could potentially be substituted by a dry solution. The main attention was placed on the connection between the timber frames and the existing masonry. As discussed in par. 2.2.2, the retrofit system was conceived starting from the research work carried out by Giaretton *et al.*, [2016] and Dizhur *et al.*, [2017], who investigated the use of vertical timber posts (named "strongbacks") to increase the out-of-plane capacity of masonry walls. With the following up experiments, they also investigated different solutions to connect timber elements to the masonry. Specifically, they investigated the characteristics of steel connectors that could be screwed from the internal surface of the timber posts into the masonry, that would grant a proper connection between the two materials. Their work resulted in new fasteners named PYTHON MT fixings, [www.pytonfixings.co.nz], characterized by a diameter of 8 mm, a total length of 230 mm, with a first threaded length to hold to timber (70 mm), and a second one to hold to masonry (160 mm) (Figure 5.2). This is an example of a new solution that was not available in the market at the time of conceiving the interventions but could increase the sustainability of the proposed system, by avoiding the use of non-recyclable materials and by making it completely reversible.

The new screws, specifically designed to the strong hold on timber/steel to brick and concrete masonry, were tested only on clay specimens, which during the EUCENTRE experimental campaign were demonstrated to have better mechanical properties than calcium-silicate bricks [Sharma *et al.*, 2020], which are very sensitive to drilling. Accordingly, the new dry solution to connect timber posts and masonry walls needed to be experimentally characterised to preliminary assess: (i) the possibility to screw the connectors without cracking CS bricks, and (ii) the effectiveness of the mechanical bond between screw and brick.

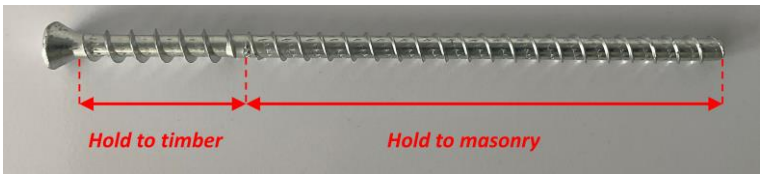

Figure 5.2 Python screw.

5.2.1 Mechanical characterization of the improved connection

A series of six withdrawal tests were performed at the Department of Civil Engineering and Architecture (DICAr) of the University of Pavia. The specimens consisted in single CS bricks, on which a Python fastener is screwed in the centre for a length of 70 mm. To avoid cracking the brick and to facilitate the fastening process, pre-drilled holes with a diameter of 6 mm were realised. The testing procedure consisted in pulling the screws outside the bricks under displacement control by clamping them at the head (Figure 5.3). The specimens were tested using the machine MTS 810, which is able to develop a force range between 10 and 500 kN (Class I based on UNI-ISO 7500-1), with a velocity of 0.05 mm/s.

Figure 5.3 Test setup.

Pre-drilled holes were initially realized with a diameter of 5 mm, which correspond to the internal diameter of the screw, but the bricks were cracking during the fastening, hence they were enlarged to 6 mm. The recorded force-displacement relationships of all the specimens are reported in Figure 5.4. The connection exhibited quite good ductility properties and on average resisted a pull-out force of 5.3 kN. The maximum resisted forces appear promising for the application of the new connection, especially considering that no experimental evidence from COMP-2 [Guerrini *et al.*, 2021] and EUC-BUILD-7 [Miglietta *et al.*, 2021] highlighted any damage due to the development of pull-out forces. Obviously, the performed tests are not exhaustive for the mechanical characterization of the connection, they were designed only to investigate if Python screws can be used to connect timber elements to CS masonry without compromising the integrity of bricks. At the same time, it is worth to underline that within the proposed retrofit system the fasteners under scrutiny are mainly subjected to shear forces that develop for displacement compatibility between timber and masonry, rather than pull-out ones. In this regard, experimental tests on the shear behaviour of different timber-to-masonry dry connections for the seismic retrofit of URM walls were performed by Riccadonna *et al.*, 2019. In their work, they investigated two different masonry typologies (brick and rubble stone masonry) using five different screw anchor fasteners with variable geometry and materials. The results suggested that the choice of fastener typology have lower impact on the strength and stiffness parameters of the connection in comparison with the selection of timber panel product or masonry elements. Accordingly, even if one the tested fasteners is very similar to PYTHON screws, experimental results could be extended to the connection under scrutiny, due to the significantly lower strength and stiffness properties of calcium silicate bricks and unprocessed solid fir compared to the investigated systems. Moreover, further full-scale experimental tests on retrofitted components and buildings are needed to gather insights on the structural effectiveness of the proposed retrofit system with replaced connections timber-to-masonry.

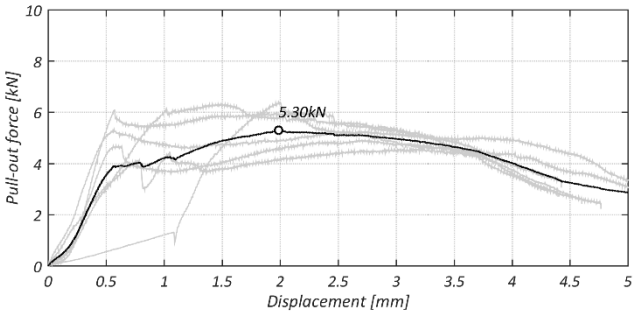

Figure 5.4 Experimental force-displacement curves

5.3 ENVIRONMENTAL IMPACT COMPARISON

The GHG emissions of buildings throughout their life cycle can be divided into three phases: the first includes the emissions due to the construction process, the second the emissions produced during the operational phase, while the third the emissions due to demolition/disposal and/or recycle. The emissions of first and third phases, and the ones of the operational phase, contribute on average for 30% and 70% respectively to the entire building life cycle emissions [Hammond and Jones, 2008].

Since the arise of concerns in reducing the building construction sector emissions, the consumption during the operational phase is assumed as the most important contributors to the overall environmental impact, considering its significant duration within the life span of a building. Consequently, the main actions undertaken so far regards innovations and regulations aiming at decreasing the operational energy consumption of buildings, while no comparable actions were undertaken to measure, to monitor, and to decrease the emissions related to construction and demolition/recycle (embodied emissions). As a result, considering an entire building life cycle, the prominent relative fraction of building emissions due to the operational phase is decreasing while the relative fraction due to embodied emissions is growing [Moncaster *et al.*, 2013]. Recent studies brought even more attention to the topic demonstrating that new efficient materials have a significant impact in reducing the operational energy consumptions, but at the same time their production require increasing energy, hence, their associated embodied emissions are increasing as well [Ibn-Mohammed *et al.*, 2013, Giesekam *et al.,* 2017]. Regarding refurbishment interventions, depending on the solution adopted in terms of materials and components, the complexity of the structural system and the depth of the intervention, the associated embodied emissions can reach the 50% of the embodied emissions related to the construction phase [Norton *et al.*, 2021]. Therefore, considering the urgent need to deeply renovate the existing building stock, embodied impacts associated to retrofit interventions are important to be assessed and minimized.

Embodied impacts include GHG emissions from the energy used to produce, transport, and install materials, components, and systems when they are built, maintained, renovated,

and eventually demolished (Norton *et al.*, 2021). Recurring embodied impacts are the GHG emissions related to repair or retrofit interventions, being structural, energetic, or integrated. To assess and make comparisons in terms of environmental impacts, all GHG emissions are converted into their carbon dioxide equivalent (CO_2e). To compute the embodied equivalent carbon of a specific material quantity the most common way is using the so-called embodied carbon factors (ECF), which express the amount of emissions released in the atmosphere for the realisation of a single unit of that material ($kgCO_2e/kg$). While the procedure is straightforward, there are many issues related to the assumptions behind the employed ECF. While there are now standards and regulations for the calculation of operational energy consumption, the calculation of embodied impacts is still not properly regulated. Being the current standard non-prescriptive, many key aspects are left to the practitioner discretion. As a results, there several sources of ECFs available which were populated based on different assumptions and boundary conditions (cradle-to-gate, cradle-to-grave etc.) that make difficult (or even useless) the comparison of results between projects. For instance, even considering the most reliable source of ECFs, the same product can have different embodied impacts based on the country where it is produced, or on the technology used during the industrial production, or on the location of the site where it must be delivered. In other words, embedded emission cannot be easily extended outside the context where they were derived. Among the main sources of ECFs there are industry and government data, environmental product declarations (EPD), commercial LCA databases (e.g., ICE database [Hammond and Jones, 2008]) or scientific literature.

From the structural engineering viewpoint, embodied emissions can be minimized by the selection of materials and structural system solutions for new constructions or for refurbishment of existing buildings under the light of LCT. Within the context of the present thesis, with the aim of measuring the environmental benefits of the re-engineered timber retrofit system, the materials embodied impacts of the two solutions were computed and compared. As introduced, the structural retrofit intervention on a building belongs to the recurring embodied impact, which can be quantified using an ECF database. For comparison purposes, only the quantity of timber and steel required to retrofit the case-study building is compared. The ICE database is employed to measure embodied carbon quantities in terms of CO_2e. The database was developed by Hammond and Jones, [2008] for the construction materials in the UK, it collects ECF considering the system boundaries cradle-to-gate. It is here used being one of the most updated since its creation, allowed by the relative nature of the comparison carried out. The analysis was performed considering the most comprehensive retrofit scheme applied to the Dutch terraced house case-study building (par. 4.5), that is including OSB also on transversal sides and the roof diaphragm strengthened as for the second-floor one. The final outcomes of the study are the percentages of economical and embodied emission savings due to the improvement of the connection timber-to-masonry.

Results in terms of environmental impacts of the different retrofit components of the two retrofit schemes are collected in Figure 5.5, Table 5.1 summarises selected carbon factors,

total weights, costs, and embodied impacts for each retrofit component. The results of the calculations shows that the substitution of the non-dry connection with the new Python screws, beyond making the retrofit system entirely reversible and easier to be installed, reduces the number of employed steel angles and steel connectors of 40% and 5% respectively. However, it increases the costs related to screw connectors of 23 %. Overall, it allows to save around 15% of the steel employed with the original retrofit scheme. As final result of the study, the improvement of the connection can potentially allows to save 7.6% of the investment computed for the original scheme and to reduce the embodied emission by 4.1%.

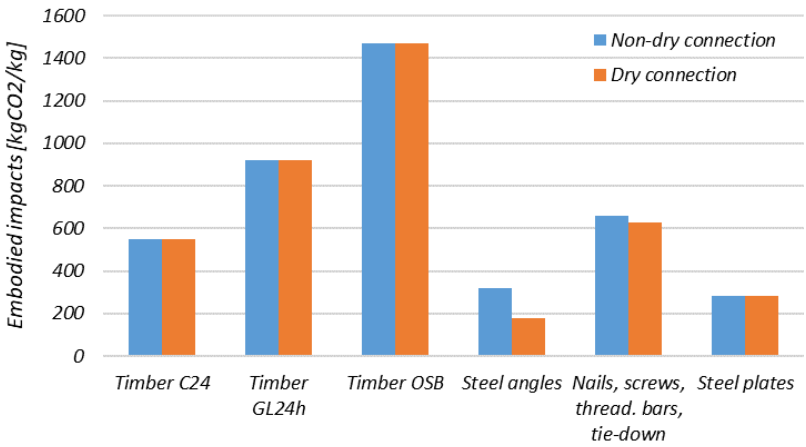

Figure 5.5 environmental impacts of the different retrofit components with original and improved connection timber-to-masonry

Table 5.1 Partial weights, costs, and embodied carbon for the original and the improved retrofit system

Retrofit component	*Original retrofit*				*Improved retrofit*		
	ECF	*Weight*	*Cost*	*Embodied impact*	*Weight*	*Cost*	*Embodied impact*
	[kgCO₂e/kg]	*[kg]*	*[€]*	*[kgCO₂e]*	*[kg]*	*[€]*	*[kgCO₂e]*
Timber C24	1.29	552	343	552	552	343	552
Timber GL24h	0.9	1021	1425	919	1021	1425	919
Timber OSB	1.05	1400	1427	1470	1400	1427	1470
Steel angles	2.28	139	1566	318	77	443	176
Nails, screws, threaded bars, tie-down	2.76	240	4437	661	228	5412	630
Steel plates	2.46	116	58	285	116	58	285
		TOT 3468	***TOT*** 9256	***TOT*** 4205	***TOT*** 3395	***TOT*** 9108	***TOT*** 4032

The present study is not intended to give quantitative information on the sustainability of the proposed retrofit system compared to other solutions, but it is intended to show the influence that small structural details can have on the environmental impacts. Even if the revision of the system was carried out *a-posteriori*, if possible, it is the author opinion that it is very important to perform such kind of assessments for new retrofit systems before their approach to the market. Indeed, the two solutions are only differentiated by a connection detail, which use the same materials of the original system but allows to reduce costs and emissions, and makes the retrofit system easier to be installed and entirely reversible. This translates also in energy, emission, working-time, and cost savings during the retrofit construction that could not be quantified in the present study. However, it is worth to note that environmental impacts related to the transportation of materials to the site were not considered, while a comprehensive evaluation of improvements in terms of sustainability should consider it for the two alternatives. The presented results are also not intended to give a precise estimation of the embodied impacts or to offer benchmark values, a thorough selection of ECF requires the knowledge of the industrial processes behind each retrofit element, which is not the case of the present study. However, the relative nature of the assessment carried out allowed to compare the two configurations in terms of emissions, through the consistent choice of ECF, and to estimate economic and carbon emission saving percentages.

5.4 CONCLUSIONS

The newly proposed timber retrofit system is analysed under the principles of sustainability to meet higher objectives in terms of environmental impact. The focus was placed on the use of materials and the technologies employed to connect the different retrofit components, among each other and with the existing structure.

The availability in the market of new screw connectors specifically designed to connect timber elements to masonry walls allows to investigate the effects of substituting the non-dry connection with a dry one in terms of sustainability. The new solution avoids the use of non-recyclable materials (epoxy glue), makes the retrofit system easier to be installed and repaired, and entirely reversible. Experimental withdrawal tests were performed to preliminary assess the compatibility of the new screws with calcium silicate bricks and the pull-out strength of the connection. The test results appeared promising for the utilization of the solution, nevertheless, the characterisation of the shear capacity is required to fully characterise the connection.

The environmental impacts of the original timber retrofit system and the improved one are compared through the computation of embodied impacts associated with the amount of materials needed to retrofit a typical Dutch terraced house unit. Beyond the non-quantifiable benefits of using a dry connection, overall, the upgrade would allow to save around 15% of steel, around 8% of the investment and reduced the embodied emissions of the intervention of around 4%. The presented results, in absolute terms, are strongly

affected by the assumption required to perform the assessment and the considered boundaries, and should not be used for comparison to other interventions. However, they are meaningful within the investigation performed due to the relative nature of the methodology used and the consistency of assumptions between the two cases.

The present considerations are intended to provide an estimation of the influence that small structural details can have on the environmental impacts of entire structural retrofit projects. It is in the author opinion that the review of newly proposed technologies or systems under the light of life cycle thinking is fundamental to face the climate change effects.

5.5 REFERENCES

ACI Committee 549 [2013] *Guide to design and construction of externally bonded FRCM systems for repair and strengthening concrete and masonry structures.* ACI, vol. 459. Farmington Hills, MI: American Concrete Institute. 4 R-13.

Al-Jaberi, Z., Myers, J.J., ElGawady, M. A. [2018] "Out-of-Plane Flexural Behavior of Reinforced Masonry Walls Strengthened with Near-Surface-Mounted Fiber-Reinforced Polymer". *ACI Structural Journal*, 115(4).

Ascione, L., Carozzi, F. G., D'Antino, T., Poggi, C. [2018] "New Italian guidelines for design of externally bonded Fabric-Reinforced Cementitious Matrix (FRCM) systems for repair and strengthening of masonry and concrete structures". *Procedia Structural Integrity*, 11, 202-209.

Arboleda, D., Babaeidarabad, S., Hays, C., Nanni, A. [2014] "Durability of fabric reinforced cementitious matrix (FRCM) composites". *In Proceedings 7th international conference on FRP composites in civil engineering*, CICE

Baek, C. H., Park, S. H. [2012] "Changes in renovation policies in the era of sustainability". *Energy and Buildings*, 47, 485–496.

Belleri, A., Marini, A. [2016] "Does seismic risk affect the environmental impact of existing buildings?". *Energy and Buildings*, 110, 149-158.

Banijamali, S.M., Esfahani, M.R., Nosratollahi, S., Sohrabi, M.R., Mousavi, S.R. [2015] "Reviewing the FRP strengthening systems". *American Journal of Civil Engineering*, 3(2–2):38–43

Bertoldi, P., Economidou, M., Palermo, V., Boza - Kiss, B., Todeschi, V. [2021] "How to finance energy renovation of residential buildings: Review of current and emerging financing instruments in the EU". *Wiley Interdisciplinary Reviews: Energy and Environment*, 10(1), e384.

British Standards Institution [2006] *BS EN ISO 14040: Environmental Management – Life Cycle Assessment Principles and Framework*. BSI.

British Standards Institution [2008a] *BS EN ISO 14044:2006+A1:2018 Environmental management - Life Cycle assessment - Requirements and guidelines*. BSI.

British Standards Institution [2008b] *BS EN ISO 15392:2008 Sustainability in building construction — General principles*. BSI.

Building Performance Institute Europe [2011] *Europe's buildings under the microscope: A country-by-country review of the energy performance of the buildings*, BPIE, Brussel, October 2011. Available at: http://www.bpie.eu.

Carozzi, F. G., Bellini, A., D'Antino, T., de Felice, G., Focacci, F., Hojdys, Poggi, C. [2017] "Experimental investigation of tensile and bond properties of Carbon-FRCM composites for strengthening masonry elements". *Composites Part B: Engineering*, 128, 100-119

Caruso, M., Pinho, R., Bianchi, F., Cavalieri, F., Lemmo, M. T. [2020] "A Life Cycle Framework for the Identification of Optimal Building Renovation Strategies Considering Economic and Environmental Impacts". *Sustainability*, 12(23), 10221.

Caverzan, A., Lamperti Tornaghi, M., Negro, P. [2016] *Proceedings of SAFESUST Workshop: A roadmap for the improvement of earthquake resistance and eco-efficiency of existing buildings and cities*. Publications Office of the European Union. https://doi. org/10.2788/499080. ISBN: 978-92-79-62618-0.

Circolare 21/01/2019 n. 7. [2019] *In: Ministero delle Infrastrutture e dei Trasporti – istruzioni per l'applicazione dell'Aggiornamento delle Norme tecniche per le costruzioni di cui al decreto ministeriale 17 gennaio 2018 (Suppl. Ordinario n.35)*. Gazzetta Ufficiale 11/02/2019 n. 35, Rome, Italy; 2019.

Clemett, N., Gallo, W. W. C., O'Reilly, G. J., Gabbianelli, G., Monteiro, R. [2022] "Optimal seismic retrofitting of existing buildings considering environmental impact". *Engineering Structures*, 250, 113391.

Colombi, P., D'Antino, T. [2019] "Analytical assessment of the stress-transfer mechanism in FRCM composites". *Composite Structures*, 220, 961-970.

D'Ambra, C., Lignola, G. P., Prota, A., Sacco, E., Fabbrocino, F. [2018] "Experimental performance of FRCM retrofit on out-of-plane behaviour of clay brick walls". *Composites Part B: Engineering*, 148, 198-206.

Del Zoppo, M., Di Ludovico, M., Prota, A. [2019] "Analysis of FRCM and CRM parameters for the in-plane shear strengthening of different URM types". *Composites Part B: Engineering*, 171, 20-33.

Directive (EU) [2018a] Directive 2018/2002 of the European Parliament and of the Council of December 11, 2018 amending Directive 2012/27/EU on energy efficiency.

Directive (EU) [2018b] Directive 2018/844 of the European Parliament and of the Council of May 30, 2018 amending Directive 2010/31/EU on the energy performance of buildings and Directive 2012/27/EU on energy efficiency.

Dizhur, D., Griffith, M., Ingham, J. [2013] "In-Plane Shear Improvement of Unreinforced Masonry Wall Panels Using NSM CFRP Strips". *Journal of Composites for Construction*, 17(6), 04013010-1-04013010-12. doi:10.1061/(ASCE)CC.1943-5614.0000400

Dizhur, D., Griffith, M., Ingham, J. [2014] "Out-of-plane strengthening of unreinforced masonry walls using near surface mounted fibre reinforced polymer strips". *Engineering structures*, 59, 330-343.

European Union [2018/1999]. *Regulation (EU) 2018/1999 of the European Parliament and of the Council of December 11, 2018 on the Governance of the Energy Union and Climate Action*. OJ L 328, December 21, 2018, p. 1–77

EU COM [2018] *Communication from the Commission to the European Parliament, the European Council, the Council, the European Economic and Social Committee, the Committee of the Regions and the European Investment Bank: A Clean Planet for all—A European strategic long-term vision for a prosperous, modern, competitive and climate neutral economy*. COM/2018/773 final.

European Building Observatory [2022] https://ec.europa.eu/energy/eu-buildings-factsheets_en

Giesekam, J., Pomponi, F. [2017] "Briefing: Embodied carbon dioxide assessment in buildings: guidance and gaps". *In Proceedings of the Institution of Civil Engineers-Engineering Sustainability* (Vol. 171, No. 7, pp. 334-341). Thomas Telford Ltd.

Graziotti, F., Penna, A., Magenes, G. [2019] "A comprehensive in situ and laboratory testing programme supporting seismic risk analysis of URM buildings subjected to induced earthquakes". *Bulletin of Earthquake Engineering*, 17(8), 4575-4599.

Guerrini, G., Damiani, N., Miglietta, M., Graziotti, F. [2021]. "Cyclic response of masonry piers retrofitted with timber frames and boards". *Structures and Buildings*, 174(5), 372-388.

Hammond, G. P., Jones, C. I. [2008] "Embodied energy and carbon in construction materials". *Proceedings of the Institution of Civil Engineers-Energy*, 161(2), 87-98.

IPCC [2018] *Summary for policymakers*. In V. Masson-Delmotte, P. Zhai, H. O. Pörtner, D. Roberts, J. Skea, P. R. Shukla, et al. (Eds.), Global warming of 1.5°C. an IPCC special report (p. 32). Geneva, Switzerland: World Meteorological Organization.

Junnila, S. I. [2006] "Empirical comparison of process and economic input-output life cycle assessment in service industries". *Environmental science & technology*, 40(22), 7070-7076.

La Greca, P., Margani, G. [2018] "Seismic and energy renovation measures for sustainable cities: A critical analysis of the Italian scenario". *Sustainability*, 10(1), 254. https://doi.org/10.3390/su10010254

Lenzen, M. [2000] "Errors in conventional and Input - Output–based Life–Cycle inventories". *Journal of industrial ecology*, 4(4), 127-148.

Magenes, G., Penna, A., Senaldi, I. E., Rota, M., Galasco, A. [2014] "Shaking table test of a strengthened full-scale stone masonry building with flexible diaphragms". *International Journal of Architectural Heritage*, 8(3), 349-375.

Mahmood, H., Ingham, J. M. [2011] "Diagonal compression testing of FRP-retrofitted unreinforced clay brick masonry wallettes". *Journal of Composites for Construction*, 15(5), 810-820.

Majeau-Bettez G, Strømman AH, Hertwich EG. [2011] "Evaluation of Process- and Input–Output-based Life Cycle Inventory Data with Regard to Truncation and Aggregation Issues". *Environmental Science Technology*; 45:10170–7. https://doi.org/10.1021/es201308x.

Menna, C., Vitiello, U., Mauro, G. M., Asprone, D., Bianco, N., Prota, A. [2019] "Integration of Seismic Risk into Energy Retrofit Optimization Procedures: A Possible Approach Based on Life Cycle Evaluation". *In IOP Conference Series: Earth and Environmental Science*, Vol. 290, No. 1, p. 012022. IOP Publishing.

Miglietta, M., Damiani, N., Guerrini, G., Graziotti, F. [2021] "Full-scale shake-table tests on two unreinforced masonry cavity-wall buildings: effect of an innovative timber retrofit". *Bulletin of Earthquake Engineering*, 19(6), 2561-2596.

Moncaster, A., Symons, K. [2013] "A method and tool for 'cradle to grave' embodied carbon and energy impacts of UK buildings in compliance with the new TC350 standards". *Energy & Buildings*, 66(C), pp.514-23. https://doi.org/10.1016/j.enbuild.2013.07.046

Nanni, A. [2012] "A new tool for concrete and masonry repair". *Concrete International*, 34(4):1–7.

Norton, B., Gillett, W. B., Koninx, F. [2021] "Briefing: Decarbonising buildings in Europe: a briefing paper". *Proceedings of the Institution of Civil Engineers-Energy*, 174(4), 147-155.

Papanicolaou, C.G., Triantafillou, T.C., Papathanasiou, M., Karlos, K. [2008] "Textile reinforced mortar (TRM) versus FRP as strengthening material of URM walls: out-of-plane cyclic loading". *Materials and Structures*, 41(1):143–157.

Passoni, C., Marini, A., Belleri, A., Menna, C. [2020] "Redefining the concept of sustainable renovation of buildings: State of the art and an LCT-based design framework". *Sustainable Cities and Society*, 64, 102519.

Petersen, R.B. [2009] "In-plane shear behaviour of unreinforced masonry panels strengthened with fibre reinforced polymer strips". *Doctoral dissertation*. University of Newcastle, United Kingdom.

Petersen, R. B., Masia, M. J., Seracino, R. [2010] "In-plane shear behavior of masonry panels strengthened with NSM CFRP strips. I: experimental investigation". *Journal of Composites for Construction*, 14(6), 754-763.

Preservation Green Lab. [2012]. *The greenest building: Quantifying the environmental value of building reuse*. Available at: http://www.preservationnation.org.

Riccadonna, D., Giongo, I., Schiro, G., Rizzi, E., & Parisi, M. A. [2019] "Experimental shear testing of timber-masonry dry connections for the seismic retrofit of unreinforced masonry shear walls". *Construction and Building Materials*, 211, 52-72.

Säynäjoki, A., Heinonen, J., Junnonen, J. M., Junnila, S. [2017] "Input–output and process LCAs in the building sector: are the results compatible with each other?". *Carbon Management*, 8(2), 155-166.

Sharma, S., Tomassetti, U., Grottoli, L., Graziotti, F. [2020] "Two-way bending experimental response of URM walls subjected to combined horizontal and vertical seismic excitation". *Engineering Structures*, 219, 110537.

Soti, R., Barbosa, A. R. [2019] "Experimental and applied element modeling of masonry walls retrofitted with near surface mounted (NSM) reinforcing steel bars". *Bulletin of Earthquake Engineering*, 17(7), 4081-4114.

Tomassetti, U., Correia, A. A., Candeias, P. X., Graziotti, F., Costa, A. C. [2019] "Two-way bending out-of-plane collapse of a full-scale URM building tested on a shake table". *Bulletin of Earthquake Engineering*, 17(4), 2165-2198.

Tsemekidi Tzeiranaki, S., Bertoldi, P., Diluiso, F., Castellazzi, L., Economidou, M., Labanca, N., Zangheri, P. [2019] "Analysis of the EU residential energy consumption: Trends and determinants". *Energies*, 12, 1065. https://doi.org/10.3390/en12061065

Türkmen, Ö. S., De Vries, B. T., Wijte, S. N. M., Vermeltfoort, A. T. [2020] "In-plane behaviour of clay brick masonry wallettes retrofitted with single-sided fabric-reinforced cementitious matrix and deep mounted carbon fibre strips". *Bulletin of Earthquake Engineering*, 18(2), 725-765.

UCL Urban Lab. [2014] *Demolition or refurbishment of social housing? – A review of the evidence*. In K. Crawford, C. Johnson, F. Davies, S. Joo, & S. Bell (Eds.). Available at: http://www.engineering.ucl.ac.uk.

United Nations. [1997] *Agenda for development*. New York, NY, USA.

Ürge-Vorsatz, D., Kelemen, A., Tirado-Herrero, S., Thomas, S., Thema, N., Mzavanadze, J., Chatterjee, S. [2016] "Measuring multiple impacts of low-carbon energy options in a green economy context". *Applied Energy*, 179, 179–1426. https://doi.org/10.1016/j.apenergy.2016.07.027

Valluzzi, M. R., Modena, C., de Felice, G. [2014] "Current practice and open issues in strengthening historical buildings with composites". *Materials and structures*, 47(12), 1971-1985.

Vaculik, J., Visintin, P., Lucas, W., Griffith, M. C. [2020] "Durability of near-surface-mounted FRP-to-clay brick masonry retrofits under environmental exposure". *Journal of Composites for Construction*, 24(1), 04019058.

Ward, H., Wenz, L., Steckel, J. C., Minx, J. C. [2018] "Truncation error estimates in process life cycle assessment using input‐output analysis". *Journal of Industrial Ecology*, 22(5), 1080-1091.

Wei, H. H., Skibniewski, M. J., Shohet, I. M., Yao, X. [2016] "Lifecycle environmental performance of natural-hazard mitigation for buildings". *Journal of Performance of Constructed Facilities*, 30(3), 04015042.

World Commission on Environment and Development [1987] *Our common future*. WCED, Oxford University Press, New York, p. 8

6. SUMMARY AND CONCLUSIONS

6.1 EXPERIMENTAL CAMPAIGN

A large testing campaign was carried out at the EUCENTRE laboratories in Pavia (Italy) aiming to design a new retrofit system for light unreinforced masonry (URM) cavity-wall buildings typical of The Netherlands (Groningen region). Quasi-static cyclic shear-compression tests were performed on full-scale masonry piers, while incremental shake-table tests were performed on full-scale building specimens up to near collapse conditions, in bare and retrofitted configurations.

The proposed retrofit solution was conceived to increase the in-plane and out-of-plane capacities of masonry piers and to favour buildings box-type lateral responses by improving masonry-to-diaphragms connections. It consisted of a timber frame connected to the masonry, on which oriented strand boards (OSB) are nailed. The frame included vertical timber posts and horizontal blocking (or nogging) elements. Timber sill plates allow to connect the frame to diaphragms and to footings. Member sizes were chosen to combine structural efficiency of the retrofit system with low invasiveness within real buildings. The effectiveness of the proposed solution depends on the connections between timber elements, masonry piers, and diaphragms and foundations. With regards to the considered building prototype, the retrofit intervention was completed by the improvement of inner- to outer-leaf connections and the strengthening/stiffening of flexible diaphragms.

The interested URM structural system was selected among the existing buildings of the Groningen region as the most vulnerable to seismic actions and is representative of typical Dutch URM cavity-wall terraced houses of late '70s-early '80s. The full-scale building prototype was a two-storey end-unit with cavity-wall structural system characterized by an internal loadbearing calcium-silicate leaf and an external clay-leaf with no structural function, by a reinforced concrete slab at the first floor, and by flexible timber diaphragms at the second floor and roof. The specimen presented significantly different lateral capacities along the two main directions and an irregular distribution of openings in front and back façades. Geometrical properties and diaphragm typologies were selected to present one of the most unfavourable conditions that can be found in-situ. The dimensions of the full-scale piers cyclically tested reproduced the longest resisting element of the tested buildings in the direction of motion at the ground floor level.

The common testing approach was to investigate first the performance of specimens in bare conditions, and then to repeat the experimental test with a retrofitted replica, using the same testing protocol. Two calcium-silicate piers were quasi-statically tested aiming to

explore the mechanical interaction between the retrofit system and the masonry, as well as to investigate the impact of the intervention on the lateral force and displacement capacity of structural elements, and to derive related analytical prediction equations. Subsequently, two full-scale cavity-wall buildings were incrementally tested on the shake-table along their weak direction up to the reaching of near collapse conditions. The aim was to investigate the impact of the retrofit system on a real building through the definition of damage states and limits as function of an engineering demand parameter. Several test runs were performed by scaling the same input ground motion, which was consistent with the seismic hazard of the considered area, presenting typical characteristics of induced earthquakes (i.e., low acceleration amplitude and short significant duration).

With regards to the performed in-plane cyclic shear-compression tests, the unretrofitted pier (named as EUC-COMP-1) exhibited a hybrid behaviour, characterized by low strength and displacement capacities, while the one retrofitted with the new timber system (named EUC-COMP-2) was forced to fail in diagonal stepped crack mode, caused by displacement compatibility between the strengthening system and the masonry. To summarize the experimental behaviours:

- EUC-COMP-1 developed first a flexural-rocking mechanism which then evolved in a sliding-shear mode. The first cracks appeared at a drift ratio of 0.075%, while ultimate conditions were reached at a drift ratio of 0.75% with out-of-plane distortion of the severely damaged specimen. The maximum recorded lateral strength was approximately 78 kN.

- EUC-COMP-2 maintained a flexural behaviour up to 1.50% drift ratio, because the timber frame inhibited shear-sliding and allowed some flexural overstrength to develop. The first cracks appeared at a drift ratio of 0.075%, while an ultimate drift ratio of 2.00% was reached when diagonal shear cracks formed within the masonry. Extensive toe crushing affected the base corners of the retrofitted masonry pier, with almost all vertical load carried by the timber frame at ultimate conditions. The only damage to the retrofit system was localised within the tie-down connection steel angles, which yielded and buckled. The maximum shear attained was about 105 kN.

Significant improvements of the seismic performance were achieved. Even though the timber retrofit did not delay first cracking, due to its high flexibility compared with the masonry pier, it allowed an increase in the specimen's ultimate displacement (by 167%) and its lateral strength (by 35%). The effectiveness of the proposed retrofit system depended on the good connection quality and on the top beam and foundation resistance to the transferred stresses. Analytical predictions of the in-plane stiffness and strength of the two specimens resulted in good agreement with the experimental values, with errors always within 5%.

The two full-scale building specimens, named as EUC-BUILD-6 and EUC-BUILD-7 for bare and retrofitted configurations respectively, showed two fundamentally different lateral responses, the former governed by a local failure mechanism while the latter by a global box-type response with torsional effects. Briefly:

- EUC-BUILD-6 exhibited a seismic response governed by the sliding of the second-floor timber diaphragm upon the supporting masonry piers, which fully activated with the input motion scaled at 66% (*PGA* = 0.25g). Displacement demand and structural damage concentrated at the second storey, preventing the development of a global building response. With the input motion scaled at 100% (*PGA* = 0.3g) the building reached an advanced state of damage, with significant residual displacements accumulated, hence, the last two runs were performed with inverted polarity. The near collapse conditions were reached by scaling the ground motion at 133%, with peak ground acceleration of 0.39 g. Loss of static equilibrium was observed on the hysteretic response during the last test runs, but collapse was inhibited by the dynamic nature of the base excitation.

- EUC-BUILD-7 exhibited a global box-type response throughout the whole incremental dynamic test. Damage recorded on the perpendicular walls with the input motion scaled at 133% (*PGA* = 0.41g) proved the triggering of a torsional response. The building reached its near-collapse condition after sustaining a peak ground acceleration of 0.78g. At the end of the incremental dynamic test, damage was fairly distributed throughout the building, even though it was more pronounced at the first storey. The roof diaphragm needed to be stiffened only after reaching a peak attic floor acceleration of 0.53g when applying the input motion with a 133% scale factor.

Overall, the intervention granted a global response of the building by preventing the onset of local failure mechanisms and allowed to fully exploit the improved in-plane resistance of masonry piers, which translated in doubled building shear and displacement capacities. The retrofitted specimens sustained twice the scaling of ground motion corresponding to the bare prototype near-collapse conditions. The concentration of damage at the second storey in unstrengthen configuration is opposed to a fairly distributed one throughout the height in retrofitted conditions.

The incremental dynamic tests also served to define damage states and limits from the onset of damage to near collapse conditions as function of an engineering demand parameter (i.e., second floor average drift ratio). They were carefully evaluated at the end of each test run based on agreed criteria, such as the extent, width, and nature of cracks, as well as the overall spreading of damage throughout the building. The near-collapse thresholds were found to be greater than expected for bare conditions, indeed, the two configurations of the building were able to sustain similar lateral displacements. However, the retrofitted prototype developed a global response, as opposed to the bare one, of which

second floor displacements were severely biased by the local sliding mechanism. Moreover, the retrofit system allowed the building to resist twice the input intensity when undergoing the same displacement demand of the bare conditions, and granted static stability throughout the whole incremental test. On average, the application of the retrofit system was not able to delay the occurrence of light damage at specific drift ratios, however, it allowed increasing the PGA associated to each DL by factors of the order of 120–260%, with larger factors for higher DLs.

In light of the performed experimental tests, the proposed retrofit solution effectively addresses and mitigates the main seismic deficiencies of unreinforced cavity-wall masonry buildings typical of the Groningen region. Moreover, given the limited cost of the proposed interventions, it appears promising for a large-scale territorial application. The result of this experimental campaign gives the basis for future numerical studies, to generate large-scale vulnerability models, to extend the proposed retrofit technique to other URM building typologies, and to perform cost/benefit and sustainability analyses of possible applications.

6.2 NUMERICAL STUDY

Numerical studies were performed to assess the impact of the proposed intervention on the seismic vulnerability of a case-study irregular Dutch terraced house building end-unit exposed to induced seismicity, considering simultaneously global and local failure mechanisms. The structure under scrutiny was derived by considering a building with the same features of the tested building prototypes, but with typical transversal dimensions and material properties that can be found in situ. Multiple-degrees-of-freedom (MDOF) systems were calibrated on the full-scale building dynamic tests and reduced to single-degree-of-freedom (SDOF) ones to perform non-linear time-history analysis (NLTHA) using a ground motion database representative of the study area. The outcomes of the procedure are presented in terms of global damage fragility functions conditioned to the PGA seismic intensity. Local OOP failure verifications were carried out to produce collapse fragility functions for each considered masonry pier using the same ground motion database for elements at the ground floor level, while filtered accelerations from global analysis were used to verify structural elements at the first-floor level. Finally, numerical results from global and local assessments were unified into single damage states fragility functions conditioned to the PGA seismic intensity.

The study demonstrated that the global NLTHA along the "strong" direction of the case-study building could have been neglected for both building configurations, since the exceedance of damage limit thresholds is entirely governed by the vulnerability along the weak direction. Instead, it suggested that is important to assess the local OOP vulnerability of masonry elements along both main directions and to combine them with global results of the weak direction in order to obtain more robust vulnerability results. It also suggested that local OOP behaviours have small influence on the building vulnerability associated to

low level of damage (DL1 and DL2), while they can have non-negligible effects on high levels (DL3 and DL4). Overall, it appeared fundamental to consider local OOP failure mechanisms for the exhaustive vulnerability assessment of irregular Dutch URM cavity-wall terraced houses of late '70s – early '80s, especially in bare conditions. Moreover, it is estimated that the application of the newly proposed retrofit system has significant positive effects on their seismic vulnerability to high level of damage and collapse, while it does not affect the occurrence of light damage.

The results of the study could not cover the wide range of uncertainties involved in these types of investigations. Dutch URM terraced houses can be characterized by a variety of materials and material properties, especially depending on their construction period. Nonetheless, the provided damage states fragility functions represent a reliable overall view of the vulnerability of typical irregular Dutch URM terraced houses in bare and retrofitted configurations which is in line with the previous studies carried out on regular prototypes and with post-earthquake observations from the Groningen area. With the view of future seismic risk assessment studies of the local building stock, since the parameters of the obtained fragility curves were derived from experimental tests, they could be taken as reference values to describe the record-to-record variability of irregular buildings belonging to the same typology. Nevertheless, the results of the numerical study are not intended to be representative of the entire URM building stock of the considered area.

6.2.1 Multiple-degrees-of-freedom models

Multiple-degrees-of-freedom (MDOF) numerical systems to simulate EUC-BUILD-6 and EUC-BUILD-7 experimental tests were generated using macroelements with the software TREMURI, which is based on the equivalent frame modelling method.

The MDOF model of the building prototype in bare conditions was stable in simulating base shears and accelerations at the first-floor level time-histories. The highest errors were lumped in the simulation of negative displacements and second-floor accelerations for the last 3 runs. Indeed, these were the parameters mostly emphasized by the local mechanism, which was fully developed during the last runs of the incremental dynamic test. Neglecting such effect on the building global lateral response allowed to consider the numerical model as able to reproduce the experimental global response of the building with a sufficient degree of accuracy up to the attainment of DL3. When the building responded in DS4, experimental displacements were severely underestimated.

The MDOF model of the retrofitted building was able to reproduce the experimental responses with a very high level of accuracy up to the reaching of DL3, then, the experimental variation of dynamic properties required the generation of a new MDOF model. The significant damage accumulated by the masonry made the global behaviour of the building prominently governed by the timber retrofit system, which gave to the

structure higher flexibility and displacement capacity. Therefore, a single numerical model was not sufficient to simulate the responses throughout the whole incremental dynamic test and another model with reduced masonry shear stiffness was generated.

The calibrated MDOF numerical models served not only to generate the case-study building MDOF systems, but also to define numerical damage limit thresholds for the post-processing of global NLTHA results in terms of displacements. Interstorey drift ratios associated to DLs for bare and retrofitted configurations were derived considering the ones previously proposed in literature for regular buildings belonging to the interested structural typology, the outcomes of the latest experimental shake-table tests, and the limitation of the selected numerical modelling approach.

6.2.2 Single-degree-of-freedom models

The case-study building MDOF numerical models were reduced to single-degree-of-freedom (SDOF) oscillators to perform the global seismic assessment with an affordable computational load. Other SDOF systems were used to simulate the out-of-plane (OOP) behaviour of masonry piers for local seismic assessment. Cloud NLTHAs were employed to evaluate the global response variability of the building, and the local OOP response variability of masonry piers.

Focusing on the case-study building global seismic assessment in bare conditions, a single oscillator could not reproduce the MDOF numerical responses in the weak direction throughout the whole damage states. Therefore, two SDOF oscillators were produced. Moving to the case-study building in retrofitted conditions excited in the weak direction, two SDOF systems were generated as well to simulate the lateral response of the MDOF equivalent-frame systems. Two additional SDOF oscillators were generated to simulate the MDOF numerical responses of the case-study building excited along its strong direction, one for bare and one for retrofitted conditions.

Cloud NLTHAs were performed using the latest ground motion database available for the interested area, a collection of 250 input signals highly representative of the site hazard. The resulting cloud data points were post-processed to derive damage state fragility functions conditioned to PGA. A first set of curves was derived through the global assessment of the case-study building in its two main directions, while a second set was derived through the OOP local assessment of masonry piers. All the outcomes were finally combined into a unique set of global damage state fragility functions which consider simultaneously the global and local mechanisms.

6.3 PRELIMINARY CONSIDERATIONS ON SUSTAINABILITY

The measuring of environmental impacts generated by buildings entire life cycles is a recent science that initially mainly focused on the reduction of operational energy consumptions. With the progressive decrease of potential green house gasses emissions related to the

operational phase, the relative importance of the ones associated to construction, repair, maintenance, or upgrade, and disposal (embodied emissions) increased. To address the issue, structural engineers should design under the life cycle thinking approach, aiming to minimize the embodied emissions of construction/interventions through the selection and correct management of materials and structural system solutions.

The newly proposed timber-based retrofit system has been reviewed to achieve higher objective in terms of sustainability reducing the embodied emissions of the intervention. Beyond the discussion of the non-quantifiable improvements obtained in terms of sustainability of the system, the environmental impacts of the two configurations are compared through the estimation of embodied impacts. Potential savings in terms of steel, which translated in savings of the economic investment and of emission were identified. The performed assessment was carried out to give an estimation of the influence that small structural details can have on entire intervention from the sustainability viewpoint. It is not intended to give quantitative information on the sustainability of the proposed retrofit system compared to other strengthening solutions.

6.4 TOPICS FOR FUTURE RESEARCH

The present study highlighted different topics that deserve further research attention:

- Incremental dynamic shake-table tests on full-scale building prototypes are not frequent in the engineering research field. The tested specimens were characterized by high plan and elevation irregularities, as well as by flexible timber diaphragms at the second floor and roof levels, therefore they exhibited very complex seismic responses. Considering that in the present study damage limit thresholds were defined as function of an engineering demand parameter based on observations, more similar experimental investigations should be carried out aiming at decreasing the uncertainty in the defined damage limit thresholds.

- The TREMURI software was used for the MDOF modelling of the incremental dynamic shake-table tests, a program that relies on the equivalent frame method using macroelements. Besides the neglecting of local OOP failure mechanisms, the limitations of the methodology required assumptions to be made for both configurations of the building specimens, in bare conditions due to the onset of a local mechanism, and in retrofitted ones due to the observed significant global stiffness decrease with the scaling of the external ground motion. Shared data from the discussed shake-table tests could be used to validate numerical models generated through a micro-modelling approach, which could capture more effectively the experimental response of the buildings, including OOP mechanisms, and allow further investigations considering other source of variability (e.g., inter- and intra-building mechanical properties variability).

- The nonlinear SDOF oscillators employed herein were originally derived to simulate the lateral response of regular low-rise masonry buildings. In the present study they were used to simulate the response of a highly irregular building, characterized by a cavity-wall system. Addressing more studies on the SDOF or on the simplified systems modelling of complex lateral responses of irregular masonry buildings would supply additional insight on the topic, and would allow to better evaluate the limitation of the presented study.

- The SDOF systems used to perform OOP NLTHA of masonry pier was developed to simulate the behaviour of single leaf and cavity-walls in bare conditions. To perform the local assessment of piers in retrofitted condition, the model proposed by Tomassetti *et al.*, [2018] required to be updated to consider the contribution of the timber system. To this end, a new force-displacement relationship was derived for positive and negative verse based on quasi-static tests (Cassol *et al.*, [2021]). While the procedure is reliable in the definition of backbones for static analysis in the two verses, it is not covering the dynamic aspects of the lateral behaviour (i.e., damping). Further OOP dynamic tests on retrofitted piers would allow to explore the energy dissipations mechanisms of the composite system, while the numerical simulation of them would be fundamental to calibrate a reliable hysteretic damping model.

- The proposed timber retrofit system is modular, and there are not industrial limitations on the choice of geometrical and mechanical properties of components, therefore, both timber and steel elements sizes could be adapted to different needs. Further experimental and numerical studies would supply insights on possible variations of the proposal and would allow to optimize features. Considering the lightness of the masonry structure to which the retrofit system was applied, further investigations are also needed to evaluate the effectiveness of the timber system in improving the lateral performance of different masonry system typologies (e.g., characterized by heavier masonry structural components). Moreover, parametric studies on the effectiveness of the retrofit system as function of member sizes and masonry wall thicknesses could provide useful information on the limitations of the intervention in terms of building internal invasiveness and structural convenience.

- A new connection between masonry and timber was characterised within the discussion on the sustainability of the proposed timber system. It relied on new timber screws specifically conceived to connect the two materials. Experimental tests on masonry components retrofitted with such technology should be performed to confirm the possible substitution of the tested connection with the new one, granting the same structural performance improvement.

- The final chapter contains a qualitative discussion on the sustainability aspects that should be considered within the proposal of a new structural retrofit system. The intervention was conceived to be potentially integrated with energetic refurbishments, aware that the energetic consumption of existing buildings is one of the main responsible of global pollution, and that the considered structural typology has an exhausted service life. The energetic assessment of an existing building requires engineering expertise that goes beyond the seismic field, and as such was not carried out. The presented seismic assessment could be combined with different energetic ones and new indexes that consider simultaneously energetic and structural improvements of an integrated intervention could be used to evaluate the environmental and economical advantages of the different combinations and the optimization of the intervention.

APPENDIX A. DATASETS FROM FULL-SCALE SHAKE TABLE TESTS ON TWO UNREINFORCED MASONRY CAVITY-WALL BUILDINGS TO EVALUATE AN INNOVATIVE TIMBER RETROFIT

INTRODUCTION

This section provides insights on the sensors measurements and on the data organization of two uniaxial incremental shake-table tests performed at the EUCENTRE laboratories in Pavia, Italy, on two full-scale replicas of a typical Dutch unreinforced masonry (URM) cavity-wall building, one tested in bare conditions and one in retrofitted configuration. Acceleration and displacement time histories of masonry elements, of floor and roof diaphragms, and of the shake table were acquired at full-scale. Two unique datasets were produced to allow the comparison between the two specimen experimental seismic performances. The presented data are freely available for the development of both analytical and numerical models for the seismic assessment and retrofit of masonry buildings. Test videos and all the recorded time histories (i.e. acceleration, displacements and forces) are downloadable upon request on the EUCENTRE repository at the URL: https://www.eucentre.it/project-nam/, referring to EUC-BUILD-6 and to EUC-BUILD-7 for the bare and retrofitted specimen configuration, respectively. A detailed discussion on the performed dynamic tests, with further interpretation of the recorded data, can be found in the article entitled: "Shake-table tests on two full-scale unreinforced masonry cavity-wall buildings: effect of an innovative timber retrofit system" [Miglietta *et al.*, 2020]

VALUE OF DATA

The presented data provide detailed information on the experimental responses of two full-scale buildings that could serve as a benchmark for laboratory testing of structures. The recorded time histories could be employed by researchers for the calibration of analytical and numerical models. The test outcomes could be used to validate simplified models for the estimation of earthquake-induced deformation demands with focus on unreinforced masonry buildings with and without retrofit. The experimental data can be used to analyse and evaluate the effects of the innovative timber system proposed for the seismic retrofit of URM buildings [Miglietta *et al.*, 2019, 2021, Guerrini *et al.*, 2021, Damiani *et al.*, 2019]. Moreover, the recorded data can be employed to conceive and validate analytical

formulations for the retrofit system response prediction. The measurements could be further analysed to evaluate the effects of flexible diaphragms in the dynamic response of masonry buildings. The recordings of the optical acquisition system could be used to reconstruct the building deformed shapes as well as to establish relationships with the global damage indicators suggested for URM buildings.

A.1 DATA DESCRIPTION

Datasets corresponding to uniaxial incremental shake-table tests performed on two full-scale URM cavity-wall buildings are provided. The specimens were two replicas of a typical Dutch terraced house, and were tested one in bare conditions and one retrofitted with an innovative timber system [Miglietta *et al.*, 2021, Guerrini *et al.*, 2021]. To monitor their structural responses, several sensors were placed inside and outside the buildings. The distributed instruments consisted of accelerometers, wire and linear potentiometers. Moreover, a three-dimensional optical-motion acquisition system was employed: passive reflective markers were densely attached to the external surface of building façades, while high-definition cameras monitored their trajectories. The monitoring reference system is displayed in Figure A.1.

The experimental tests data are stored into two different folders, one pertaining to the bare building (named as EUC-BUILD-6) and one to the retrofitted specimen (named as EUC-BUILD-7). Therein, other two folders cluster respectively the data recorded by accelerometers and potentiometers ('*Traditional Data*') and the ones acquired by the three-dimensional optical system ('*Optical Data*'). Each data folder contains several *.txt* files, named as reported in Table A.1 and Table A.2 for the bare and retrofitted building tests, respectively. The adopted nomenclature includes a first number identifying the run within the incremental test, the applied ground motion (named as EQ-NPR, [Miglietta *et al.*, 2021]) and the corresponding scaling of accelerations in terms of percentages. Each *.txt* files contains a data matrix, sized as reported in Table . All the experimental data and videos of each performed test are freely available upon request on the EUCENTRE repository at the URL: https://www.eucentre.it/project-nam/ referring respectively to EUC-BUILD-6 and to EUC-BUILD-7 for the bare and retrofitted specimen test.

Table A.1 EUC-BUILD-6 bare building test: traditional and optical shared data file names.

Test #	Test Name	Data file name	*Traditional Data* matrix size (rows x columns)	*Optical Data* matrix size (rows x columns)
1	EQ-NPR- 20%	#2 - EQ-NPR 20%	7681 x 166	Not usable
2	EQ-NPR- 33%	#3 - EQ-NPR 33%	7681 x 166	Not usable
3	EQ-NPR- 50%	#8 - EQ-NPR 50%	7681 x 166	Not usable
4	EQ-NPR- 66%	#10 - EQ-NPR 66%	7681 x 166	Not usable

5	EQ-NPR- 85%	#15 - EQ-NPR 85%	7681 x 166	7681 x 235
6	EQ-NPR- 100%	#21 - EQ-NPR 100%	7681 x 166	7681 x 235
7	EQ-NPR- 100%-rev*	#24 - EQ-NPR 100%-rev*	7681 x 166	7681 x 235
8	EQ-NPR- 133%-rev*	#25 - EQ-NPR 133%-rev*	7681 x 166	7681 x 235

* The ground motion was applied with a reversed sign

Table A.2 EUC-BUILD-7 retrofitted building test: traditional and optical shared data file names.

Test #	Test Name	Data file name	*Traditional data* matrix size (rows x columns)	*Optical data* matrix size (rows x columns)
1	EQ-NPR- 20%	#2 - EQ-NPR 20%	7681 x 201	Not usable
2	EQ-NPR- 33%	#5 - EQ-NPR 33%	7681 x 201	Not usable
3	EQ-NPR- 50%	#7 - EQ-NPR 50%	7681 x 201	Not usable
4	EQ-NPR- 66%	#10 - EQ-NPR 66%	7681 x 201	Not usable
5	EQ-NPR- 85%	#13 - EQ-NPR 85%	7681 x 201	Not usable
6	EQ-NPR- 100%	#15 - EQ-NPR 100%	7681 x 201	Not usable
7	EQ-NPR- 133%	#18 - EQ-NPR 133%	7681 x 201	7681 x 201
8	EQ-NPR- 133%-roof*	#21 - EQ-NPR 133%-roof *	7681 x 201	7681 x 201
9	EQ-NPR- 166%-roof*	#23 - EQ-NPR 166%-roof *	7681 x 201	7681 x 201
10	EQ-NPR- 200%-roof*	#25 - EQ-NPR 200%-roof *	7681 x 201	7681 x 201
11	EQ-NPR- 266%-roof*	#29 - EQ-NPR 266%-roof *	7681 x 201	7681 x 201

* The roof system was restrained to the second-floor diaphragm to limit displacements in the direction of motion

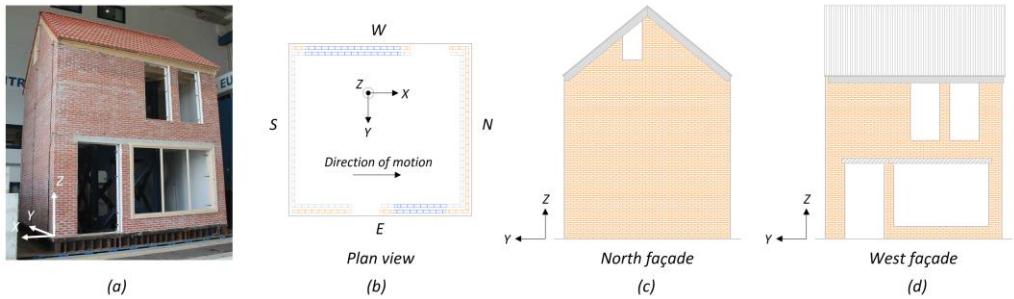

Figure A.1 Reference system for data acquisition: (a) full-scale building specimen; (b) ground-floor plan view; (c) North façade view; (d) West façade view.

A.1.1 Traditional data: accelerometers and potentiometer recordings

The contents of each *.txt* file matrix are listed in Table A.3 and Table A.4 for the bare specimen test, while in Table A.5 and Table A.6 for the retrofitted building test. Each row of the matrices corresponds to an individual instant of time. The provided acceleration and displacement time histories are filtered using a quadratic low-pass rule set at a frequency of 50Hz, and are organized as follows:

i. Column 1 is the time at a sampling rate of 256Hz (Table A.3 and Table A.5);

ii. Columns 2 to 68 provide the acceleration time histories in units of g corresponding to 67 degrees-of-freedom of the buildings (Table A.3 and Table A.5);

iii. Columns 73 to 137 of the bare building files provide the displacement time histories of all potentiometers installed on the specimen in units of mm (Table A.3);

iv. Columns 138 to 166 of the bare building files provide the derived data time histories in units of g, mm and kN (Table A.4);

v. Columns 73 to 172 of the retrofitted building files provide the displacement time histories of all the potentiometer installed on the specimen in units of mm (Table A.5);

vi. Columns 173 to 201 of the retrofitted building files provide the derived data time histories in units of g, mm and kN (Table A.6).

A set of 46 accelerometers with a range of ± 2 g or ± 6 g, allowed measuring the total accelerations of the shake table, of walls (along their height and length), of first-floor, second-floor and roof diaphragms, and of the internal steel frame. Table 3 and Table 5 list for each accelerometer: number of matrix column, sensor label and identification number, recorded degree of freedom, associated mass, recorded quantity, location and height above the ground.

Aiming to allow the most effective comparison between the bare and retrofitted specimen experimental responses, the amount and the distribution of accelerometers throughout the buildings was keep unvaried. Moreover, the adopted distribution of masses was kept consistent between the two specimens (as shown in Figure A.2 and Figure A.3), taking care to add the retrofit system mass to the accelerometers installed on the internal-leaf of the retrofitted building. It is worth to notice that, differently from Table A.5, in Table A.3, an additional column contains the associated masses after the sixth test (i.e. EQ-NPR 100%, [Miglietta *et al.*, 2021]). Indeed, after this run some instruments were removed to preserve

them in case of partial collapses (labelled with an asterisk in the "Sensor ID No" column, Miglietta *et al.*, 2021). Accordingly, the corresponding matrix columns were filled with "Not a Number" (NaN) for the following runs and the masses initially associated with removed accelerometers were redistributed to nearby ones (Figure A.4).

Displacement transducers were installed to monitor the relative displacements of structural elements and their deformations. A set of wire potentiometers recorded the out-of-plane displacements of the North and South facades with respect to the rigid frame, and the in-plane deformations of the squat walls at the first storey of the East façade inner leaf (Figure A.5a and b). On the retrofitted building, also the deformations of the second-storey squat wall of the West façade were monitored. Linear potentiometers were used to record the X and Y floor-diaphragms displacements with respect to the rigid frame, to capture possible uplifts and relative sliding of structural elements (Figure A.5c, d and e).

Table A.3 and Table A.5 list all the potentiometers installed on the bare and retrofitted buildings respectively, providing for each of them: number of matrix column, sensor label and identification number, recorded degree of freedom, connected element points, location and height above the ground. They can be grouped into two typologies, (i) one clustering potentiometers connecting a point of the specimen to a fixed one (i.e. internal steel frame, foundations or shake table) while (ii) the other one clustering potentiometers connecting two points of to the building prototype.

Time histories recorded by transducers belonging to the first group (specimen-to-fixed point) are processed in order to have along the *X* direction positive displacements towards North and negative displacements towards South (Figure A.1).

Displacements recorded by horizontal potentiometers belonging to the second group (specimen-to-specimen) are positive when the Northern structural element to which is attached moves towards the positive *X* direction. Displacements recorded by vertical potentiometers belonging to the second group (specimen-to-specimen) are positive when the upper element moves upwards. If the two points belong to the same structural element (i.e. #124, 126 and 172), positive displacements are recorded when the two points moved away from each other.

As per the accelerometers, to facilitate the comparison between the experimental structural responses, the displacement transducers of the second specimen were distributed consistently with numeration of the first one. However, the presence of the retrofit system prevented the installation of all the sensors previously employed, as well as, it required several new ones to monitor its relative displacements (Figure A.5d and e). Accordingly, the potentiometer locations in Table A.3 and Table A.5 are unvaried up to the Column No 137, and, if the position could not be maintained in the retrofitted specimen, the related

matrix column is filled with "Not a Number" (NaN). All the potentiometers added to the retrofitted building are appended to the list of instruments already installed in the bare specimen, starting from wire potentiometers and followed by the linear ones (columns 138 to 172 of Table 5).

The time histories derived by post-processing data are listed in Table 4 and Table 6 for the bare and retrofitted specimens, respectively. They are appended to the displacement transducer record columns and include average floors and roof acceleration and displacement time histories (in units of g and mm respectively), interstorey drift ratio and base-shear time histories (in percentages and in units of kN respectively), as well as, in-plan displacement time histories of floor diaphragms (in units of mm). To obtain the latter, couples of potentiometers were connected to the same points of the floor diaphragms (Figure A.5c), and their time histories were obtained through intersecting the circumferences described by the potentiometers with center at the single potentiometer origin (on the rigid frame). For further details on the instrumentation, the reader is referred to Miglietta *et al.*, [2019] and Damiani *et al.*, [2019].

A.1.2 Optical data: three-dimensional optical motion-capture system recordings

A three-dimensional motion-acquisition system was used to monitor displacements of the North, South and West external façades Vicon [2016]. It consisted of high-definition cameras that recorded throughout the tests the trajectories of passive reflective markers glued to several points of the building prototypes.

Optical acquisition data are provided for each specimen in separate folders, named '*Optical data*', containing *.txt* files named and sized as reported in Table A.1 and Table A.2. The provided time histories correspond to the changes in *X* coordinates of every usable marker. The coordinates at rest of each of them are provided in three *.txt* files named '*X*, *Y* or *Z coordinates at rest*', values are approximated to 5 cm. The column numbering uses the marker numerations reported in Figure A.6 and Figure A.7. Three markers outside the building at the South-West corner of the shake-table were used to define the origin of the optical capture system. Their time histories were appended at the end of the shared data matrices, which for this reason present three columns more than the last numbered marker of each specimen (see Table A.1 and Figure A.6 for the bare building, while Table A.2 and Figure A.7 for the retrofitted one).

Unfortunately, the first runs recorded by the system were found not usable since the signal noises were too similar to the building displacements and to the three-dimensional optical system tolerances (Table A.1 and Table A.2). Also within the shared data of each run, several marker signals appeared unusable. It happened due to the high sensitivity of the system to light condition, to the distance between markers and cameras, and to the relevant

dimensions of the building prototypes. In these cases, the corresponding columns were filled with the terminology "Not a Number" (NaN).

A.2 EXPERIMENTAL DESIGN, MATERIALS AND METHODS

Two full-scale replicas of an URM building, one in bare conditions and one retrofitted with a timber system, were subjected to incremental dynamic shake-table tests. The prototypes were representative of the end unit of a two-storey URM cavity-wall terraced house of late 1970s typical of the Groningen region, in the North-East part of the Netherlands (Figure A.8). The specimens presented cavity walls, made of a single-wythe load-bearing calcium silicate (CS) inner leaf and a single-wythe external clay veneer with no intended structural function, connected through steel ties. The building prototype was selected based on the visual assessment of structural deficiencies of the investigated building typology, which were deemed the most critical for the vulnerability to seismic excitation. The specimens were characterized by a significant amount of openings asymmetrically distributed at both the storeys, by a rigid reinforced concrete slab at the first floor and a flexible timber diaphragm at the second floor, both of them with a staircase hole in proximity of the North wall. The flexible diaphragm consisted of timber joists on which tongue-and-groove planks were nailed. Two gable walls atop the transverse facades (North and South) supported a 39° pitched flexible roof made of timber purlins on which tongue-and-groove planks were nailed at each intersection. Counter and tile battens were placed above the planks, while tiles completed the roof.

The prototypes were subjected to an input motion increasingly scaled in acceleration amplitude to reach the desired demand intensities up to near-collapse conditions. The applied input signal was representative of the induced seismicity of the Groningen region, with low significant duration and low magnitude and PGA. The main shocks were alternated with compensated of the ground motion for shake-table calibration purposes, and with random noise motions to track the evolution of the buildings dynamic properties with the accumulation of damage.

A detailed comparison of the experimental results, a full description of geometrical features, construction details, material properties, retrofit intervention, and major observations about the performed tests can be found in Miglietta *et al.*, [2019]. In that study, the recorded time histories were used to analyse the seismic responses of the buildings and to allow the correlation between a series of engineering demand parameters and the attainment of significant performance limits states throughout the tests. For further insight on the effects of the timber retrofit system on masonry piers lateral capacity, the reader is addressed to Guerrini *et al.*, [2021] where are presented the results obtained from two in-plane quasi-static cyclic tests performed on full-scale CS piers, one tested in bare and one in retrofitted configuration.

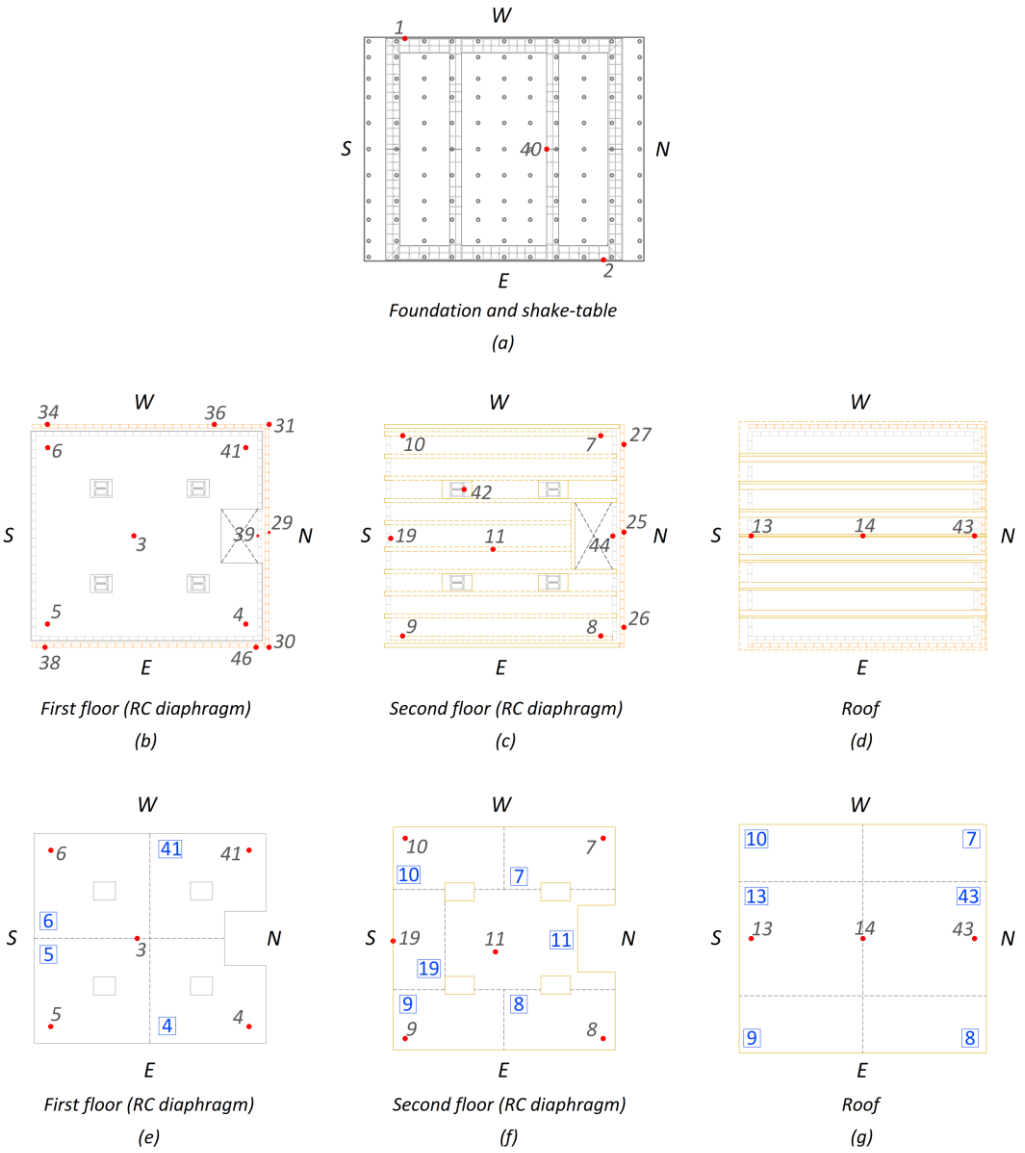

Figure A.2 EUC-BUILD-6 and EUC-BUILD7 in-plan accelerometer and mass distributions: a) to d) location of the accelerometers; e) to g) diaphragms mass distributions. Red points represent the accelerometers, black numbers are the corresponding Sensor ID numbers, and blue numbers in squares correspond to the accelerometer to which each area is assigned.

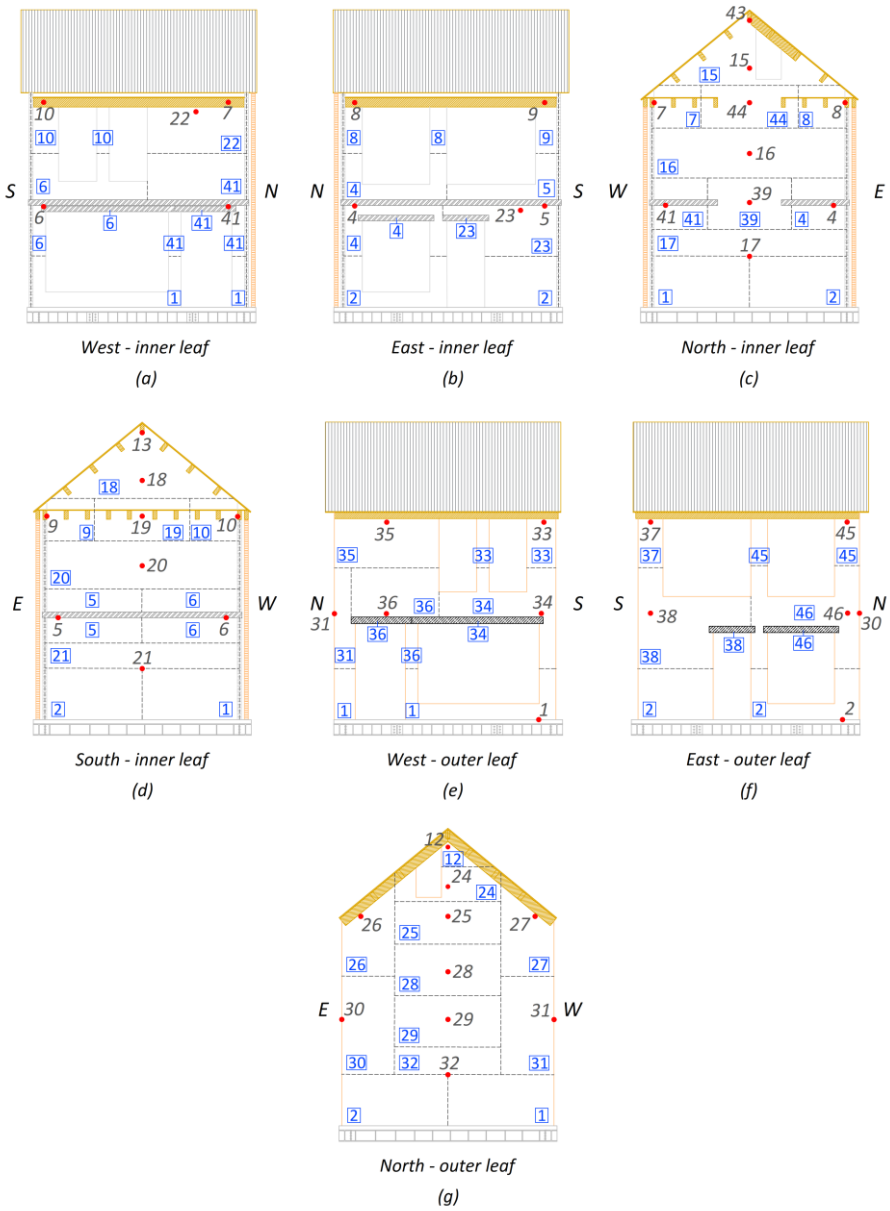

Figure A.3 EUC-BUILD-6 and EUC-BUILD-7 accelerometer and mass distributions: a) to d) mass distributions in height of specimen inner leaves (views from inside); e) to f) mass distributions in height of specimen outer leaves (views from outside). Red points represent the accelerometer locations, black numbers are the corresponding Sensor ID numbers, and blue numbers in squares correspond to the accelerometer to which the mass is assigned.

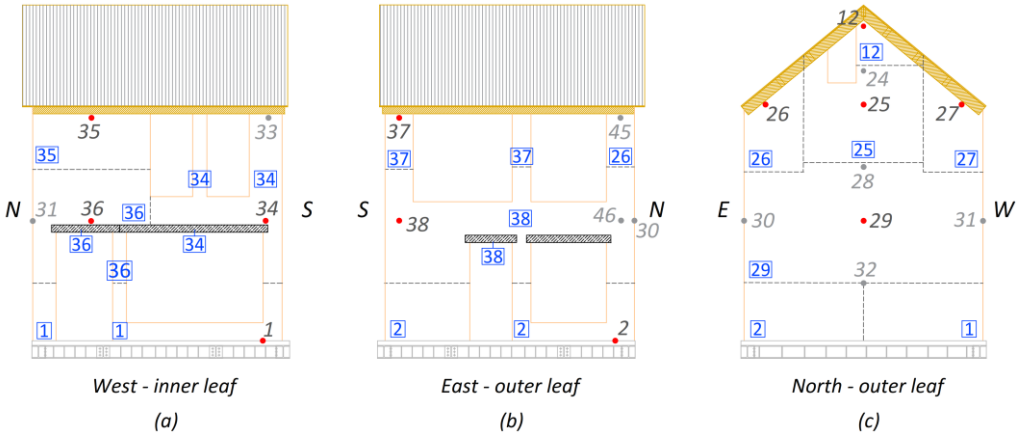

Figure A.4 EUC-BUILD-6 (bare building) outer-leaf mass distribution after the sixth test (#21 - EQ-NPR 100%, Table 1). Red points represent the accelerometer locations, black numbers are the corresponding Sensor ID numbers, and blue numbers in squares correspond to the accelerometer to which the mass is assigned. Removed instruments are displayed in grey.

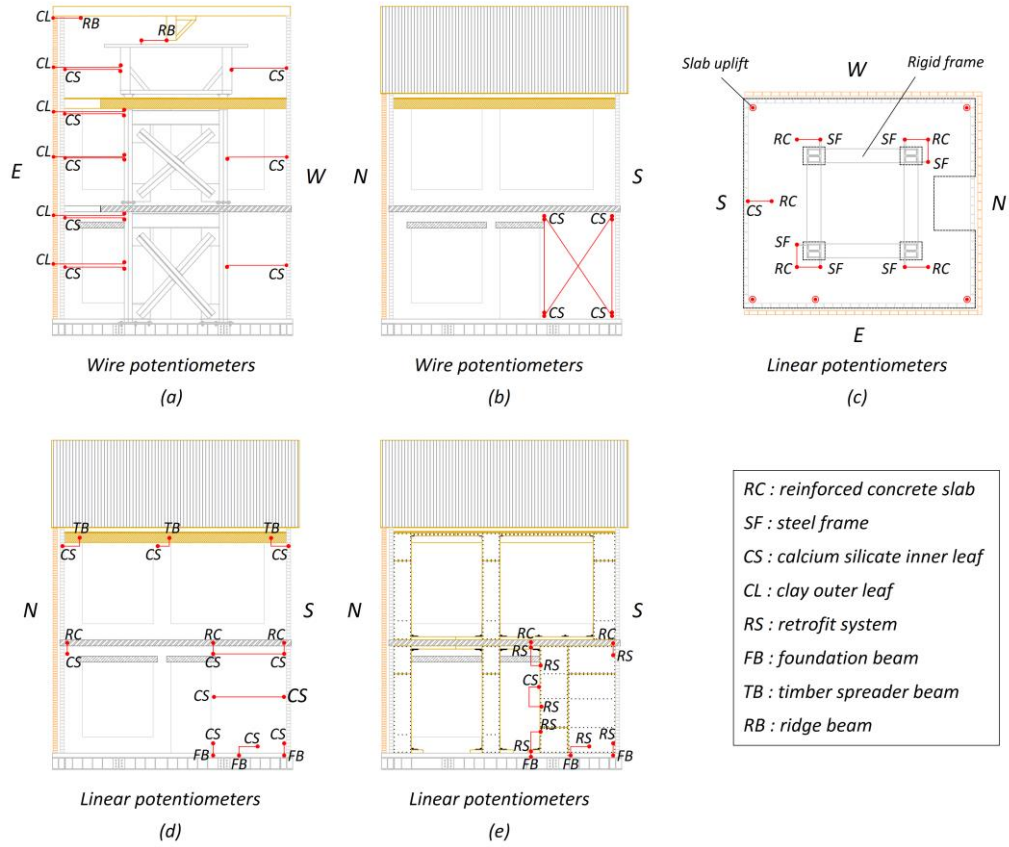

Figure A.5 EUC-BUILD-6 and EUC-BUILD-7 potentiometer qualitative distribution: a) out-of-plane displacements of North and South façades; b) in-plane deformations of squat walls; c) in-plane and relative displacements of floor diaphragms; d) relative displacements of masonry piers with respect to floor diaphragms and foundations; e) additional linear potentiometers for retrofit elements relative displacements.

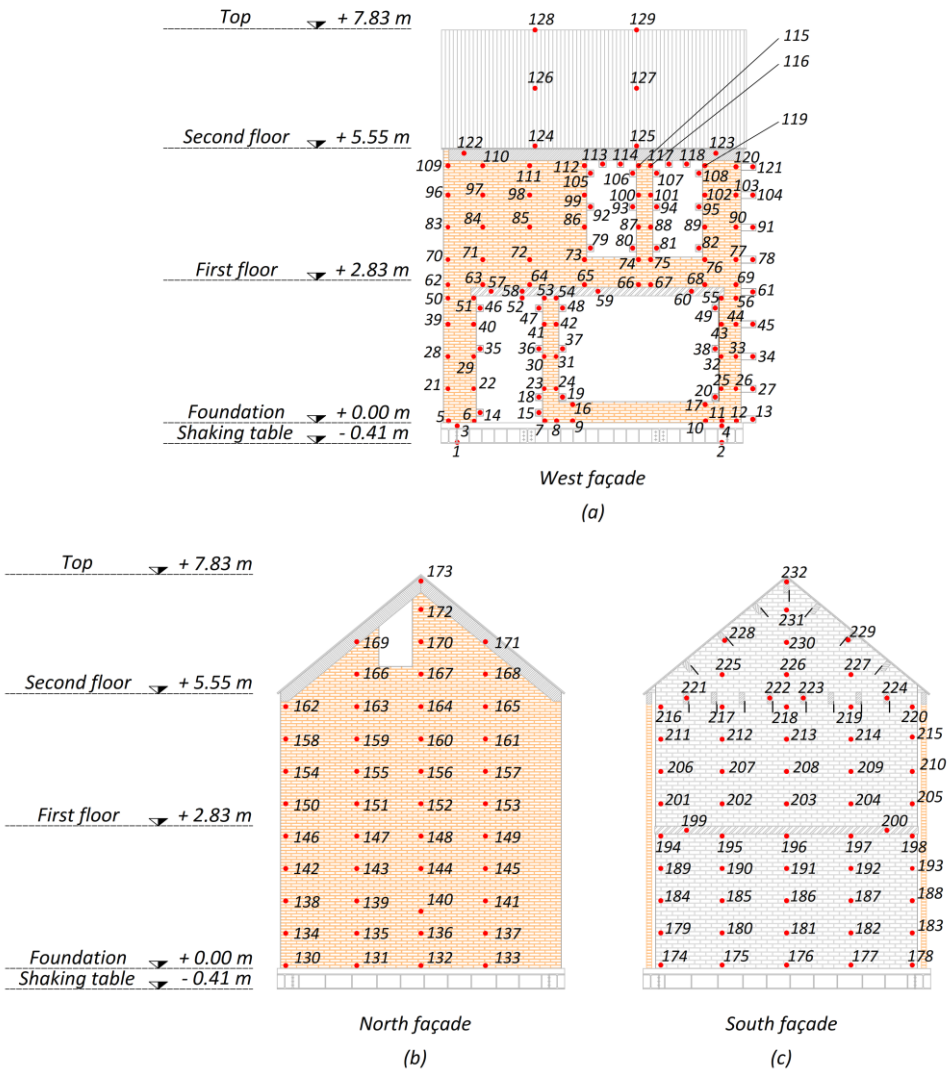

Figure A.6 EUC-BUILD-6 (bare building) markers distribution and enumeration: a) West façade distribution; b) North façade distribution; c). South façade distribution. Numbers are the column numbers of the optical data matrix file corresponding to each marker.

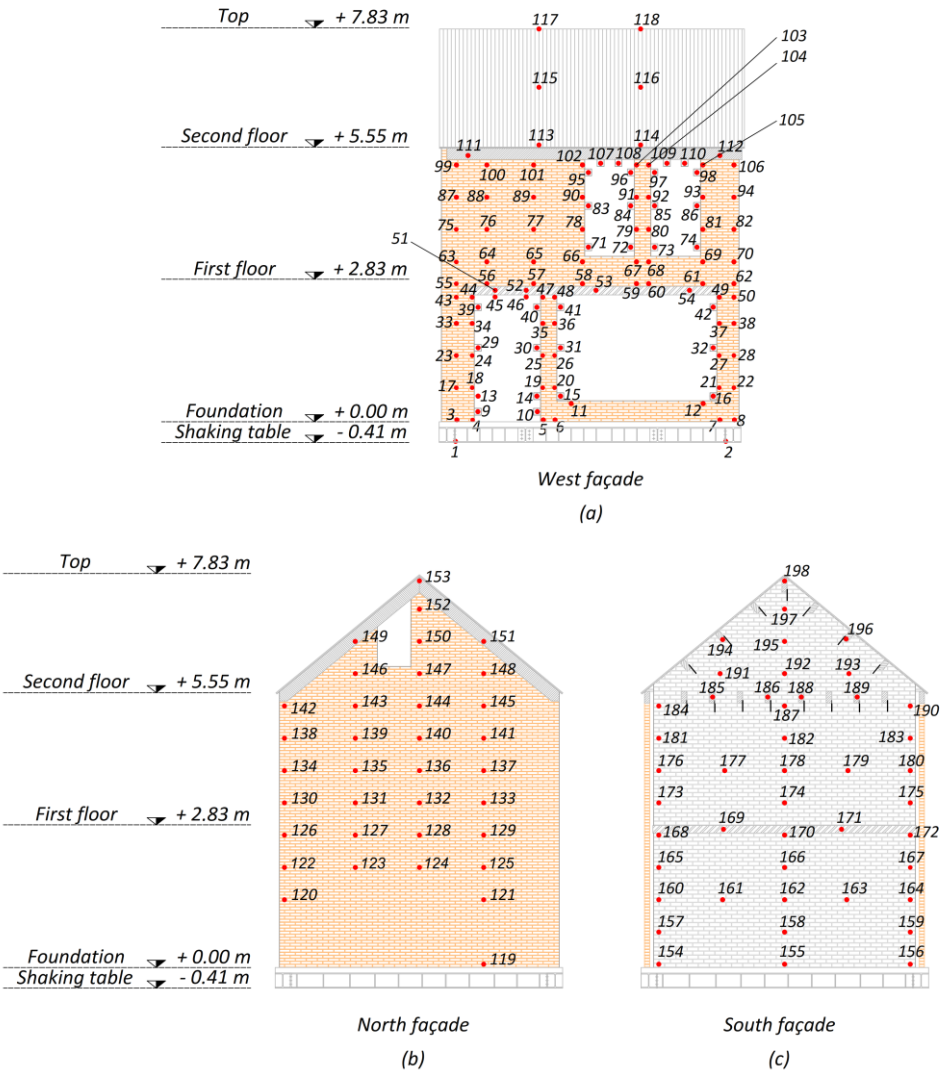

Figure A.7 EUC-BUILD-7 (retrofitted building) markers distribution and enumeration: a) West façade distribution; b) North façade distribution; c). South façade distribution. Numbers are the column numbers of the optical data matrix file corresponding to each marker.

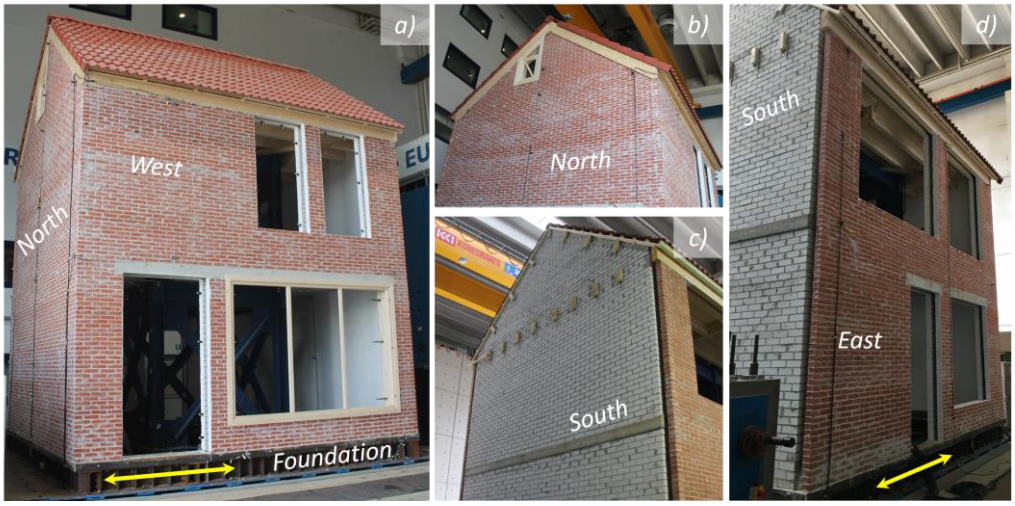

Figure A.8 Overall views of the bare specimens: a) North and West façades; b) North façade; c) South façade; d) South and East façades; yellow arrows indicate the shaking direction.

Table A.3 EUC-BUILD-6 (bare building) data matrix structure: accelerometers and potentiometers recordings, columns 1 to 137. Sensor ID: A, accelerometer; WP, wire potentiometer; P, linear potentiometer.

Column No.	Sensor ID No.	Rec. DOF	Units	Mass (X dir.) [kg]	Mass after test 6 (X dir.) [kg]	Measured quantity - Instrument location
1		-	[s]	-	-	Time
2	A 1	x	[g]	3167	3167	Foundation beam acceleration (West side, +0 mm)
3	A 2	x	[g]	3854	3854	Foundation beam accel. (East side, +0 mm)
4	A 3	z	[g]	-	-	R.C. diaphragm accel. (center, +2680 mm)
5	A 4	x	[g]	3705	3705	R.C. diaphragm (N-E corner, +2680 mm)
6		y	[g]	-	-	
7		z	[g]	-	-	
8	A 5	x	[g]	3854	3854	R.C. diaphragm accel. (S-E corner, +2680 mm)
9		y	[g]	-	-	
10		z	[g]	-	-	
11	A 6	x	[g]	4140	4140	R.C. diaphragm accel. (S-W corner, +2680 mm)

12		y	[g]	-	-	
13		z	[g]	-	-	
14	A 7	x	[g]	901	901	Timber diaphragm accel. (N-W corner, +5520 mm)
15		y	[g]	-	-	
16		z	[g]	-	-	
17	A 8	x	[g]	1117	1117	Timber diaphragm accel. (N-E corner, +5520 mm)
18		y	[g]	-	-	
19		z	[g]	-	-	
20	A 9	x	[g]	1039	1039	Timber diaphragm accel. (S-E corner, +5520 mm)
21		y	[g]	-	-	
22		z	[g]	-	-	
23	A 10	x	[g]	1144	1144	Timber diaphragm accel. (S-W corner, +5520 mm)
24		y	[g]	-	-	
25		z	[g]	-	-	
26	A 11	x	[g]	502	502	Timber diaphragm accel. (center, +5520 mm)
27		z	[g]	-	-	
28	A 12	x	[g]	137	295	North outer leaf accel. (top of gable, +7350 mm)
29	A 13	x	[g]	692	692	Ridge beam accel. (South end, +7550 mm)
30		y	[g]	-	-	
31		z	[g]	-	-	
32	A 14	x	[g]	-	-	Ridge beam accel. (mid-span, +7550 mm)
33	A 15	x	[g]	639	639	North inner leaf accel. (center of gable, +6300 mm)
34	A 16	x	[g]	1250	1250	North inner leaf accel. (second storey mid-height, +4050 mm)
35	A 17	x	[g]	672	672	North inner leaf accel. (first storey mid-height, +1350 mm)
36	A 18	x	[g]	851	851	South inner leaf accel. (center of gable, +6300 mm)
37	A 19	x	[g]	680	680	South inner leaf accel. (second-floor level, +5350 mm)
38	A 20	x	[g]	1204	1204	South inner leaf accel. (second storey mid-height, +4050 mm)
39	A 21	x	[g]	639	639	South inner leaf accel. (first storey mid-height, +1350 mm)
40	A 22	x	[g]	588	588	West inner leaf accel. (top of second-storey squat pier, +5130 mm)

41	A 23	x	[g]	582	582	East inner leaf accel. (top of first-storey squat pier, +2550 mm)
42	A 24*	x	[g]	390	-	North outer leaf accel. (center of gable, +6300 mm)
43	A 25	x	[g]	609	1220	North outer leaf accel. (second-floor level, +5550 mm)
44	A 26	x	[g]	580	739	North outer leaf corner accel. (second-floor level, East side, +5550 mm)
45	A 27	x	[g]	581	581	North outer leaf corner accel. (second-floor level, West side, +5550 mm)
46	A 28*	x	[g]	744	-	North outer leaf accel. (second storey mid-height, +4050 mm)
47	A 29	x	[g]	746	2951	North outer leaf accel. (first-floor level, +2800 mm)
48	A 30*	x	[g]	703	-	North outer leaf accel. (first-floor level, East side, +2800 mm)
49	A 31*	x	[g]	959	-	North outer leaf corner accel. (first-floor level, West side, +2800 mm)
50	A 32*	x	[g]	399	-	North outer leaf accel. (first storey mid-height, +1350 mm)
51	A 33*	x	[g]	279	-	West outer leaf accel. (second-floor level, South side, +5200 mm)
52	A 34	x	[g]	790	1073	West outer leaf accel. (first-floor level, South side, +2800 mm)
53	A 35	x	[g]	689	689	West outer leaf accel. (top of second-storey squat pier, +5200 mm)
54	A 36	x	[g]	728	972	West outer leaf accel. (bottom of second-storey squat pier, +2800 mm)
55	A 37	x	[g]	167	268	East outer leaf corner accel. (second-floor level, South side, +5200 mm)
56	A 38	x	[g]	1026	1924	East outer leaf corner accel. (first-floor level, South side, +2800 mm)
57	A 39	x	[g]	545	545	North inner leaf accel. (first-floor level, +2750 mm)
58	A 40	x	[g]	0	-	Shaking table accel. (-410 mm)
59	A 41	x	[g]	3845	3845	R.C. diaphragm accel. (North-West corner, +2680 mm)
60		y	[g]	-	-	
61		z	[g]	-	-	
62	A 42	x	[g]	-	-	Rigid frame accel. (second-floor level, +5350 mm)
63	A 43	x	[g]	692	692	Ridge beam accel. (North end, +7550 mm)
64		y	[g]	-	-	
65		z	[g]	-	-	
66	A 44	x	[g]	526	526	North inner leaf accel. (second-floor level, +5350 mm)
67	A 45*	x	[g]	266	-	East outer leaf corner accel. (second-floor level, North side, +5200 mm)

68	A 46*	x	[g]	919	-	East outer leaf corner accel. (first-floor level, North side, +2800 mm)
69	Offline	-	-	-	-	-
70	Offline	-	-	-	-	-
71	Offline	-	-	-	-	-
72	Offline	-	-	-	-	-
73	WP 1*	x	[mm]	-	-	Ridge beam - North outer leaf (top of gable, +7550 mm)
74	WP 2	x	[mm]	-	-	Ridge beam - Rigid frame (+7550 mm
75	WP 3	x	[mm]	-	-	North inner-leaf mid-height gable deflections (w.r.t. rigid frame, +6300 mm)
76	WP 4*	x	[mm]	-	-	North outer-leaf mid-height gable defl. (w.r.t. rigid frame, +6300 mm)
77	WP 5	x	[mm]	-	-	South inner-leaf mid-height gable defl. (w.r.t. rigid frame, +6300 mm)
78	WP 6*	x	[mm]	-	-	North outer-leaf defl. at second-floor level (w.r.t. rigid frame, +5150 mm)
79	WP 7	x	[mm]	-	-	North inner-leaf defl. at second-floor level (w.r.t. rigid frame, +5150 mm)
80	WP 8	x	[mm]	-	-	North inner-leaf defl. at second storey mid-height (w.r.t. rigid frame, +4050 mm)
81	WP 9*	x	[mm]	-	-	North outer-leaf defl. at second storey mid-height (w.r.t. rigid frame, +4050 mm)
82	WP 10	x	[mm]	-	-	South inner-leaf defl. at second storey mid-height (w.r.t. rigid frame, +4050 mm)
83	WP 11	x	[mm]	-	-	North inner-leaf defl. at first-floor level (w.r.t. rigid frame, +2550 mm)
84	WP 12*	x	[mm]	-	-	North outer-leaf defl. at first-floor level (w.r.t. rigid frame, +2550 mm)
85	WP 13	x	[mm]			North inner-leaf defl. at first storey mid-height (w.r.t. rigid frame, +1350 mm)
86	WP 14*	x	[mm]	-	-	North outer-leaf defl. at first storey mid-height (w.r.t. rigid frame, +1350 mm)
87	WP 15	x	[mm]	-	-	South inner-leaf defl. at first storey mid-height (w.r.t. rigid frame, +1350 mm)
88	WP 16	z	[mm]	-	-	East inner-leaf first-storey squat pier deformation (along vertical Northern edge)
89	WP 17	z	[mm]	-	-	East inner-leaf first-storey squat pier def. (along vertical Southern edge)
90	WP 18	diag onal	[mm]	-	-	East inner-leaf first-storey squat pier def. (along bottom/left to top/right diagonal)
91	WP 19	diag onal	[mm]	-	-	East inner-leaf first-storey squat pier def. (along bottom/right to top/left diagonal)
92	P 1	x	[mm]	-	-	Ridge beam - North inner-leaf top of gable (+7550 mm)
93	P 2	x	[mm]	-	-	Ridge beam - South inner-leaf top of gable (+7550 mm)
94	P 3	x	[mm]	-	-	Timber diaphragm displacement, N-W corner (w.r.t rigid frame, +5260 mm)

95	P 4	y	[mm]	-	-	Timber diaphragm displacement, N-W corner (w.r.t rigid frame, +5260 mm)
96	P 5	x	[mm]	-	-	Timber diaphragm displacement, N-E corner (w.r.t rigid frame, +5260 mm)
97	P 6	y	[mm]	-	-	Timber diaphragm displacement, N-E corner (w.r.t rigid frame, +5260 mm)
98	P 7	x	[mm]	-	-	Timber diaphragm displacement, S-E corner (w.r.t rigid frame, +5260 mm)
99	P 8	y	[mm]	-	-	Timber diaphragm displacement, S-E corner (w.r.t rigid frame, +5260 mm)
100	P 9	x	[mm]	-	-	Timber diaphragm displacement, S-W corner (w.r.t rigid frame, +5260 mm)
101	P 10	y	[mm]	-	-	Timber diaphragm displacement, S-W corner (w.r.t rigid frame, +5260 mm)
102	P 11	x	[mm]	-	-	Timber diaphragm displacement, South mid-span (w.r.t rigid frame, +5260 mm)
103	P 12	x	[mm]	-	-	Timber diaphragm, South mid-span - South inner leaf (+5260 mm)
104	Offline	-	-	-	-	-
105	P 13	x	[mm]	-	-	East outer-leaf - East outer-spreader beam (+5260 mm)
106	P 14	x	[mm]	-	-	West inner-leaf second storey squat pier - West inner-leaf spreader beam (+5260 mm)
107	P 15	x	[mm]	-	-	West outer-leaf second storey squat pier - West outer-leaf spreader beam (+5260 mm)
108	P 16*	x	[mm]	-	-	North inner-leaf top second storey - West inner-leaf spreader beam (+5260 mm)
109	P 17	x	[mm]	-	-	South inner-leaf top second storey - West inner-leaf spreader beam (+5260 mm)
110	P 18	x	[mm]	-	-	South inner-leaf top second storey - East inner-leaf spreader beam (+5260 mm)
111	P 19	x	[mm]	-	-	East inner-leaf second storey central pier - East inner-leaf spreader beam (+5260 mm)
112	P 20*	x	[mm]	-	-	North inner-leaf top second storey - East inner-leaf spreader beam (+5260 mm)
113	P 21	x	[mm]	-	-	R.C. diaphragm displ. North-West corner - (w.r.t rigid frame, +2680 mm)
114	P 22	y	[mm]	-	-	R.C. diaphragm displ. North-West corner - (w.r.t rigid frame, +2680 mm)
115	P 23	x	[mm]	-	-	R.C. diaphragm displ. North-East corner - (w.r.t rigid frame, +2680 mm)
116	P 24	x	[mm]	-	-	R.C. diaphragm displ. South-East corner - (w.r.t rigid frame, +2680 mm)
117	P 25	y	[mm]	-	-	R.C. diaphragm displ. South-East corner - (w.r.t rigid frame, +2680 mm)
118	P 26	x	[mm]	-	-	R.C. diaphragm displ. South-West corner - (w.r.t rigid frame, +2680 mm)
119	P 27	x	[mm]	-	-	R.C. diaphragm South mid-span - South inner-leaf mid-span (+2680 mm)
120	P 28	z	[mm]	-	-	R.C. diaphragm North-West corner - first storey top Inner-leaf (+ 2680 mm)

121	P 29	z	[mm]	-	-	R.C. diaphragm North-East corner - first storey top Inner-leaf (+ 2680 mm)
122	P 30	z	[mm]	-	-	R.C. Diaphragm - East inner-leaf first-storey squat pier top (Northern corner, +2680 mm)
123	P 31	z	[mm]	-	-	R.C. diaphragm South-East corner - first storey top Inner-leaf (+ 2680 mm)
124	P 32	x	[mm]			East inner leaf (top of first-storey squat pier)
125	P 33	z	[mm]	-	-	R.C. diaphragm South-West corner - first storey top Inner-leaf (+ 2680 mm)
126	P 34	x	[mm]	-	-	East inner-leaf first-storey squat pier mid-height deformations (+ 1350 mm)
127	P 35	x	[mm]	-	-	West outer-leaf first-storey mid-span - Foundation beam (+ 0 mm)
128	P 36	x	[mm]	-	-	West inner-leaf first-storey mid-span - Foundation beam (+ 0 mm)
129	P 37	x	[mm]	-	-	West outer-leaf first-storey squat pier mid-span - Foundation beam (+ 0 mm)
130	P 38	x	[mm]	-	-	West inner-leaf first-storey squat pier mid-span - Foundation beam (+ 0 mm)
131	P 39	z	[mm]	-	-	East inner-leaf first-storey squat pier Northern bottom corner - Foundation beam (+ 0 mm)
132	P 40	z	[mm]	-	-	East inner-leaf first-storey squat pier Southern bottom corner - Foundation beam (+ 0 mm)
133	P 41	x	[mm]	-	-	Foundation beam S-W corner - Shaking table (- 410 mm)
134	P 42	x	[mm]	-	-	Foundation beam S-E corner - Shaking table (- 410 mm)
135	P 43	x	[mm]	-	-	Shaking table N-E corner - Laboratory strong floor (-410 mm)
136	Offline	_	-	-	-	-
137	P 44	x	[mm]	-	-	R.C. diaphragm S-E corner - East inner-leaf first-storey squat pier top mid-span (+2680 mm)

Table A.4 EUC-BUILD-6 (bare building) data matrix structure: derived time-histories, columns 138 to 166.

Column No.	Recorded / Computed quantity	Units	Description
138	Ground acceleration (x direction, +0 mm)	[g]	Average of col. 2, 3
139	1st floor accel. (x dir., +2680 mm)	[g]	Average of col. 5, 8, 11, 59
140	2nd floor accel. (x dir., +5520 mm)	[g]	Average of col. 145, 146, 26

141	Roof accel. (x dir., +7550 mm)	[g]	Average of col. 29, 63
142	1st floor accel. (y dir., +2680 mm)	[g]	Average of col. 6, 9, 12, 60
143	2nd floor accel. (y dir., +5520 mm)	[g]	Average of col. 15, 18, 21, 24
144	Roof accel. (y dir., +7550 mm)	[g]	Average of col. 30, 64
145	2nd Floor accel. East (x dir., +5520 mm)	[g]	Average of col. 17, 20
146	2nd Floor accel. West (x dir., +5520 mm)	[g]	Average of col. 14, 23
147	Average displacement 1st floor - RC slab (x dir., +2680 mm)	[mm]	Average of col. 155, 115, 157, 118
148	Average displ. 2nd floor - Timber diaphragm (x dir., +5520 mm)	[mm]	Average of col. 152, 153
149	Roof displ. (x dir., +7550 mm)	[mm]	Col. 74
150	Average displ. 1st floor West - RC slab (x dir., +2680 mm)	[mm]	Average of col. 155, 118
151	Average displ. 1st floor East - RC slab (x dir., +2680 mm)	[mm]	Average of col. 115, 157
152	Average displ. 2nd floor West - Timber diaph. (x dir., +5520 mm)	[mm]	Average of col. 159, 165
153	Average displ. 2nd floor East - Timber diaph. (x dir., +5520 mm)	[mm]	Average of col. 161, 163
154	Overall base shear (x dir., with non-oscillatory mass)	[kN]	Sum of the products of each accelerometer reading with the associated mass
155	1st floor displ. N-W corner - RC slab (x dir., +2680 mm)	[mm]	Circle intersection, col. 113 & 114
156	1st floor displ. N-W corner - RC slab (y dir., +2680 mm)	[mm]	Circle intersection, col. 113 & 114
157	1st floor displ. N-E corner - RC slab (x dir., +2680 mm)	[mm]	Circle intersection, col. 116 & 117
158	1st floor displ. N-E corner - RC slab (y dir., +2680 mm)	[mm]	Circle intersection, col. 116 & 117
159	2nd floor displ. N-W corner - Timber diaph. (x dir., +5520 mm)	[mm]	Circle intersection, col. 94 & 95
161	2nd floor displ. N-E corner - Timber diaph. (x dir., +5520 mm)	[mm]	Circle intersection, col. 96 & 97
162	2nd floor displ. N-E corner - Timber diaph. (y dir., +5520 mm)	[mm]	Circle intersection, col. 96 & 97
163	2nd floor displ. S-E corner - Timber diaph. (x dir., +5520 mm)	[mm]	Circle intersection, col. 98 & 99
164	2nd floor displ. S-E corner - Timber diaph. (y dir., +5520 mm)	[mm]	Circle intersection, col. 98 & 99
165	2nd floor displ. S-W corner - Timber diaph. (x dir., +5520 mm)	[mm]	Circle intersection, col. 100 & 101
166	2nd floor displ. S-W corner - Timber diaph. (y dir., +5520 mm)	[mm]	Circle intersection, col. 100 & 101

Table A.5 EUC-BUILD-7 (retrofitted building) data matrix structure: accelerometers and potentiometers recordings, columns 1 to 172. Sensor ID: A, accelerometer; WP, wire potentiometer; P, linear potentiometer.

Column No.	Sensor ID No.	Recorded DOF	Units	Mass (X dir.)	Measured quantity - Instrument location
1		-	[s]	-	Time
2	A 1	x	[g]	3430	Foundation beam acceleration (West side, +0 mm)
3	A 2	x	[g]	4172	Foundation beam accel. (East side, +0 mm)
4	A 3	z	[g]	-	R.C. diaphragm accel. (centre, +2680 mm)
5	A 4	x	[g]	3808	R.C. diaphragm accel. (N-E corner, +2680 mm)
6		y	[g]	-	
7		z	[g]	-	
8	A 5	x	[g]	3952	R.C. diaphragm accel. (S-E corner, +2680 mm)
9		y	[g]	-	
10		z	[g]	-	
11	A 6	x	[g]	4254	R.C. diaphragm accel. (S-W corner, +2680 mm)
12		y	[g]	-	
13		z	[g]	-	
14	A 7	x	[g]	928	Timber diaphragm accel. (N-W corner, +5520 mm)
15		y	[g]	-	
16		z	[g]	-	
17	A 8	x	[g]	1166	Timber diaphragm accel. (N-E corner, +5520 mm)
18		y	[g]	-	
19		z	[g]	-	
20	A 9	x	[g]	1080	Timber diaphragm accel. (S-E corner, +5520 mm)
21		y	[g]	-	
22		z	[g]	-	
23	A 10	x	[g]	1196	Timber diaphragm accel. (S-W corner, +5520 mm)
24		y	[g]	-	
25		z	[g]	-	

26	A 11	x	[g]	502	Timber diaphragm accel. (center, +5520 mm)
27		z	[g]	-	
28	A 12	x	[g]	144	North outer leaf accel. (top of gable, +7350 mm)
29	A 13	x	[g]	692	Ridge beam accel. (South end, +7550 mm)
30		y	[g]	-	
31		z	[g]	-	
32	A 14	x	[g]	-	Ridge beam accel. (midspan, +7550 mm)
33	A 15	x	[g]	707	North inner leaf accel. (center of gable, +6300 mm)
34	A 16	x	[g]	1382	North inner leaf accel. (second storey mid-height, +4050 mm)
35	A 17	x	[g]	743	North inner leaf accel. (first storey mid-height, +1350 mm)
36	A 18	x	[g]	940	South inner leaf accel. (center of gable, +6300 mm)
37	A 19	x	[g]	732	South inner leaf accel. (second-floor level, +5350 mm)
38	A 20	x	[g]	1330	South inner leaf accel. (second storey mid-height, +4050 mm)
39	A 21	x	[g]	706	South inner leaf accel. (first storey mid-height, +1350 mm)
40	A 22	x	[g]	650	West inner leaf accel. (top of second-storey squat pier, +5130 mm)
41	A 23	x	[g]	639	East inner leaf accel. (top of first-storey squat pier, +2550 mm)
42	A 24	x	[g]	411	North outer leaf accel. (center of gable, +6300 mm)
43	A 25	x	[g]	642	North outer leaf accel. (second-floor level, +5550 mm)
44	A 26	x	[g]	611	N-E outer leaf corner accel. (second-floor level, North side, +5550 mm)
45	A 27	x	[g]	612	N-W outer leaf corner accel. (second-floor level, +5550 mm)
46	A 28	x	[g]	783	North outer leaf accel. (second storey mid-height, +4050 mm)
47	A 29	x	[g]	786	North outer leaf accel. (first-floor level, +2800 mm)
48	A 30	x	[g]	740	N-E outer leaf corner accel. (first-floor level, North side, +2800 mm)
49	A 31	x	[g]	1010	N-W outer leaf corner accel. (first-floor level, +2800 mm)
50	A 32	x	[g]	420	North outer leaf accel. (first storey mid-height, +1350 mm)

51	A 33	x	[g]	294	S-W outer leaf corner accel. (second-floor level, +5200 mm)
52	A 34	x	[g]	825	S-W outer leaf corner accel. (first-floor level, +2800 mm)
53	A 35	x	[g]	726	West outer leaf accel. (top of second-storey squat pier, +5200 mm)
54	A 36	x	[g]	763	West outer leaf accel. (bottom of second-storey squat pier, +2800 mm)
55	A 37	x	[g]	175	S-E outer leaf corner accel. (second-floor level, +5200 mm)
56	A 38	x	[g]	1079	S-E outer leaf corner accel. (East first-floor level, +2800 mm)
57	A 39	x	[g]	602	North inner leaf accel. (first-floor level, +2750 mm)
58	A 40	x	[g]	-	Shaking table accel. (-410 mm)
59	A 41	x	[g]	3964	R.C. diaphragm accel. (North-West corner, +2680 mm)
60		y	[g]	-	
61		z	[g]	-	
62	A 42	x	[g]	-	Rigid frame accel. (second-floor level, +5350 mm)
63	A 43	x	[g]	692	Ridge beam accel. (North end, +7550 mm)
64		y	[g]	-	Ridge beam accel. (North end, +7550 mm)
65		z	[g]	-	Ridge beam accel. (North end, +7550 mm)
66	A 44	x	[g]	582	North inner leaf accel. (second-floor level, +5350 mm)
67	A 45	x	[g]	280	N-E outer leaf corner accel. (second-floor level, East side, +5200 mm)
68	A 46	x	[g]	963	N-E outer leaf corner accel. (first-floor level, East side, +2800 mm)
69	Offline	-	-	-	-
70	Offline	-	-	-	-
71	Offline	-	-	-	-
72	Offline	-	-	-	-
73	WP 1	x	[mm]	-	Ridge beam - North outer leaf (top of gable, +7550 mm)
74	WP 2	x	[mm]	-	Ridge beam - Rigid frame (+7550 mm)
75	WP 3	x	[mm]	-	North inner-leaf mid-height gable deflections (w.r.t. rigid frame, +6300 mm)
76	WP 4	x	[mm]	-	North outer-leaf mid-height gable defl. (w.r.t. rigid frame, +6300 mm)

77	WP 5	x	[mm]	-	South inner-leaf mid-height gable deflections (w.r.t. rigid frame, +6300 mm)
78	WP 6	x	[mm]	-	North outer-leaf defl. at second-floor level (w.r.t. rigid frame, +5150 mm)
79	WP 7	x	[mm]	-	North inner-leaf defl. at second-floor level (w.r.t. rigid frame, +5150 mm)
80	WP 8	x	[mm]	-	North inner-leaf defl. at second storey mid-height (w.r.t. rigid frame, +4050 mm)
81	WP 9	x	[mm]	-	North outer-leaf defl. at second storey mid-height (w.r.t. rigid frame, +4050 mm)
82	WP 10	x	[mm]	-	South inner-leaf defl. at second storey mid-height (w.r.t. rigid frame, +4050 mm)
83	WP 11	x	[mm]	-	North inner-leaf defl. at first-floor level (w.r.t. rigid frame, +2550 mm)
84	WP 12	x	[mm]	-	North outer-leaf defl. at first-floor level (w.r.t. rigid frame, +2550 mm)
85	WP 13	x	[mm]	-	North inner-leaf defl. at first storey mid-height (w.r.t. rigid frame, +1350 mm)
86	WP 14	x	[mm]	-	North outer-leaf defl. at first storey mid-height (w.r.t. rigid frame, +1350 mm)
87	WP 15	x	[mm]	-	South inner-leaf defl. at first storey mid-height (w.r.t. rigid frame, +1350 mm)
88	WP 16	z	[mm]	-	East inner-leaf first-storey squat pier def. (along vertical Northern edge)
89	WP 17	z	[mm]	-	East inner-leaf first-storey squat pier def. (along vertical Southern edge)
90	WP 18	diagonal	[mm]	-	East inner-leaf first-storey squat pier def. (along bottom/left to top/right diagonal)
91	WP 19	diagonal	[mm]	-	East inner-leaf first-storey squat pier def. (along bottom/right to top/left diagonal)
92	P 1	x	[mm]	-	Ridge beam - North inner-leaf top of gable (+7550 mm)
93	P 2	x	[mm]	-	Ridge beam - South inner-leaf top of gable (+7550 mm)
94	P 3	x	[mm]	-	Timber diaphragm displacement, North-West corner (w.r.t rigid frame, +5260 mm)
95	P 4	y	[mm]	-	
96	P 5	x	[mm]	-	Timber diaphragm displacement, North-East corner (w.r.t rigid frame, +5260 mm)
97	P 6	y	[mm]	-	

98	P 7	x	[mm]	-	Timber diaphragm displacement, South-East corner (w.r.t rigid frame, +5260 mm)
99	P 8	y	[mm]	-	
100	P 9	x	[mm]	-	Timber diaphragm displacement, South-West corner (w.r.t rigid frame, +5260 mm)
101	P 10	y	[mm]	-	
102	P 11	x	[mm]	-	Timber diaphragm displacement, South mid-span (w.r.t rigid frame, +5260 mm)
103	P 12	x	[mm]	-	Timber diaphragm, South midspan - South inner leaf (+5260 mm)
104	Offline	-	-	-	-
105	P 13	x	[mm]	-	East outer-leaf - East outer-spreader beam (+5260 mm)
106	P 14	x	[mm]	-	REMOVED
107	P 15	x	[mm]	-	West outer-leaf second storey squat pier - West outer-leaf spreader beam (+5260 mm)
108*	P 16	x	[mm]	-	North inner-leaf top second storey - West inner-leaf spreader beam (+5260 mm)
109	P 17	x	[mm]	-	South inner-leaf top second storey - West inner-leaf spreader beam (+5260 mm)
110	P 18	x	[mm]	-	South inner-leaf top second storey - East inner-leaf spreader beam (+5260 mm)
111	P 19	x	[mm]	-	East inner-leaf second storey central pier - East inner-leaf spreader beam (+5260 mm)
112*	P 20	x	[mm]	-	North inner-leaf top second storey - East inner-leaf spreader beam (+5260 mm)
113	P 21	x	[mm]	-	R.C. diaphragm displ. North-West corner - (w.r.t rigid frame, +2680 mm)
114	P 22	y	[mm]	-	
115	P 23	x	[mm]	-	R.C. diaphragm displ. North-East corner - (w.r.t rigid frame, +2680 mm)
116	P 24	x	[mm]	-	R.C. diaphragm displ. South-East corner - (w.r.t rigid frame, +2680 mm)
117	P 25	y	[mm]	-	
118	P 26	x	[mm]	-	R.C. diaphragm displ. S-W corner - (w.r.t rigid frame, +2680 mm)
119	P 27	x	[mm]	-	R.C. diaphragm South midspan - South inner-leaf mid-span (+2680 mm)
120	P 28	z	[mm]	-	R.C. diaphragm N-W corner - first storey top Inner-leaf (+ 2680 mm)

121	P 29	z	[mm]		R.C. diaphragm N-E corner - first storey top Inner-leaf (+ 2680 mm)
122	P 30	z	[mm]	-	R.C. Diaphragm - East inner-leaf first-storey squat pier top (Northern corner, +2680 mm)
123	P 31	z	[mm]	-	R.C. diaphragm S-E corner - first storey top Inner-leaf (+ 2680 mm)
124	P 32	x	[mm]	-	REMOVED
125	P 33	z	[mm]	-	R.C. diaphragm S-W corner - first storey top Inner-leaf (+ 2680 mm)
126	P 34	x	[mm]	-	REMOVED
127	P 35	x	[mm]	-	West outer-leaf first-storey midspan - Foundation beam (+ 0 mm)
128	P 36	x	[mm]	-	REMOVED
129	P 37	x	[mm]	-	West outer-leaf first-storey squat pier midspan - Foundation beam (+ 0 mm)
130	P 38	x	[mm]	-	West inner-leaf first-storey squat pier midspan - Foundation beam (+ 0 mm)
131	P 39	z	[mm]	-	East inner-leaf first-storey squat pier Northern bottom corner - Foundation beam (+ 0 mm)
132	P 40	z	[mm]	-	East inner-leaf first-storey squat pier Southern bottom corner - Foundation beam (+ 0 mm)
133	P 41	x	[mm]	-	Foundation beam S-W corner - Shaking table (- 410 mm)
134	P 42	x	[mm]	-	Foundation beam S-E corner - Shaking table (- 410 mm)
135	P 43	x	[mm]	-	Shaking table N-E corner - Laboratory strong floor (- 410 mm)
136	P 44	Offline	-	-	-
137	P 45	x	[mm]	-	R.C. diaphragm S-E corner - East inner-leaf first-storey squat pier top mid-span (+2680 mm)
138	WP 20	diagonal	[mm]	-	West inner-leaf 2nd storey squat pier def. (along bottom/left to top/right diagonal)
139	WP 21	diagonal	[mm]	-	West inner-leaf 2nd storey squat pier def. (along bottom/right to top/left diagonal)
140	WP 22	z	[mm]	-	West inner-leaf 2nd storey squat pier def. (along vertical Northern edge)
141	WP 23	z	[mm]	-	West inner-leaf 1st storey squat pier def. (along vertical Southern edge)

142	P 46	z	[mm]	-	West side retrofit – 1st storey central slender pier – foundation beam-to-bottom sill plate - Southern corner (+0 mm)
143	P 47	z	[mm]	-	West side retrofit – 1st storey central slender pier – foundation beam-to-bottom sill plate - Northern corner (+0 mm)
144	P 48	z	[mm]	-	West side retrofit – 1st storey central slender pier – bottom sill-to-vertical post - Southern corner (+80 mm)
145	P 49	z	[mm]	-	West side retrofit – 1st storey central slender pier – bottom sill-to-vertical post - Northern corner (+80 mm)
146	P 50	z	[mm]	-	West side retrofit – 1st storey central slender pier – vertical post -to-top sill plate - Southern corner (+2600 mm)
147	P 51	z	[mm]	-	West side retrofit – 1st storey central slender pier – vertical post -to-top sill plate - Northern corner (+2600 mm)
148	P 52	z	[mm]	-	West side retrofit – 2nd storey squat pier – RC slab-to-bottom sill plate Southern corner (+2840 mm)
149	P 53	z	[mm]	-	West side retrofit – 1st storey central slender pier – top sill plate-to-RC slab - Southern corner (+2680 mm)
150	P 54	z	[mm]	-	West side retrofit – 1st storey central slender pier – top sill plate-to-RC slab - Northern corner (+2680 mm)
151	P 55	z	[mm]	-	West side retrofit – 2nd storey squat pier – RC slab-to-bottom sill plate Northern corner (+2840 mm)
152	P 56	z	[mm]	-	West side retrofit – 2nd storey squat pier – bottom sill plate-to-vertical post - Northern corner (+2920 mm)
153	P 57	z	[mm]	-	West side retrofit – 2nd storey squat pier – bottom sill plate-to-vertical post - Southern corner (+2920 mm)
154	P 58	z	[mm]	-	West side retrofit – 2nd storey squat pier – CS inner-leaf-to-vertical post - Southern corner (+4050 mm)
155	P 59	z	[mm]	-	West side retrofit – 2nd storey squat pier – vertical post-to-top sill plate - Southern corner (+5270 mm)
156	P 60	z	[mm]	-	East side retrofit – 1st storey squat pier – bottom sill plate-to-vertical post - Northern corner (+80 mm)
157	P 61	z	[mm]	-	East side retrofit – 1st storey squat pier – bottom sill plate-to- vertical post - Southern corner (+80 mm)
158	P 62	z	[mm]	-	East side retrofit – 1st storey squat pier – CS inner-leaf-to- vertical post - Northern corner (+1340 mm)

159	P 63	z	[mm]	-	East side retrofit – 1st storey squat pier – vertical post-to-top sill plate - Northern corner (+2600 mm)
160	P 64	z	[mm]	-	East side retrofit – 1st storey squat pier – vertical post-to-top sill plate - Southern corner (+2600 mm)
161	P 65	z	[mm]	-	East side retrofit – 2nd storey central slender pier – RC slab-to-bottom sill plate - Northern corner (+2840 mm)
162	P 66	z	[mm]	-	East side retrofit – 2nd storey central slender pier – RC slab-to-bottom sill plate - Southern corner (+2840 mm)
163	P 67	z	[mm]	-	East side retrofit – 2nd storey central slender pier – bottom sill plate-to- vertical post - Northern corner (+2920 mm)
164	P 68	z	[mm]	-	East side retrofit – 2nd storey central slender pier – bottom sill plate-to- vertical post - Southern corner (+2920 mm)
165	P 69	z	[mm]	-	East side retrofit – 2nd storey central slender pier – vertical post-to-top sill plate - Southern corner (+5270 mm)
166	P 70	z	[mm]	-	North side retrofit – 1st storey pier – vertical post-to-CS inner-leaf (+400 mm)
167	P 71	z	[mm]	-	North side retrofit – 2nd storey pier – vertical post-to-CS inner-leaf (+3160 mm)
168	P 72	z	[mm]	-	South side retrofit – 1st storey pier – vertical post-to-CS inner-leaf (+400 mm)
169	P 73	z	[mm]	-	South side retrofit – 2nd storey pier – vertical post-to-CS inner-leaf (+3160 mm)
170	P 74	z	[mm]	-	East side retrofit – 1st storey squat pier – top sill plate-to-RC slab - Southern corner (+2680 mm)
171	P 75	z	[mm]	-	West side retrofit – 2nd storey central squat pier – vertical post-to-top sill plate - Northern corner (+5270 mm)
172*	P 76	x	[mm]	-	East side retrofit – 1st storey squat pier – mid-height longitudinal deformations (+1340 mm)

Table A.6 EUC-BUILD-7 (retrofitted building) data matrix structure: derived time-histories, columns 173 to 201.

Column No.	Recorded / Computed quantity	Units	Description

173	Ground acceleration (x direction, +0 mm)	[g]	Average of col. 2, 3
174	1st floor accel. (x dir., +2680 mm)	[g]	Average of col. 5, 8, 11, 59
175	2nd floor accel. (x dir., +5520 mm)	[g]	Average of col. 145, 146, 26
176	Roof accel. (x dir., +7550 mm)	[g]	Average of col. 29, 63
177	1st floor accel. (y dir., +2680 mm)	[g]	Average of col. 6, 9, 12, 60
178	2nd floor accel.(y dir., +5520 mm)	[g]	Average of col. 15, 18, 21, 24
179	Roof accel. (y dir., +7550 mm)	[g]	Average of col. 30, 64
180	2nd Floor accel. East (x dir., +5520 mm)	[g]	Average of col. 17, 20
181	2nd Floor accel. West (x dir., +5520 mm)	[g]	Average of col. 14, 23
182	Avg. displacement 1st floor - RC slab (x dir., +2680 mm)	[mm]	Average of col. 155, 115, 157, 118
183	Avg. displ. 2nd floor - Timber diaphragm (x dir., +5520 mm)	[mm]	Average of col. 152, 153
184	Roof displ. (x dir., +7550 mm)	[mm]	Col. 74
185	Average displ. 1st floor West - RC slab (x dir., +2680 mm)	[mm]	Average of col. 155, 118
186	Average displ. 1st floor East - RC slab (x dir., +2680 mm)	[mm]	Average of col. 115, 157
187	Average displ. 2nd floor West - Timber diaphr. (x dir., +5520 mm)	[mm]	Average of col. 159, 165
188	Average displ. 2nd floor East - Timber diaphr. (x dir., +5520 mm)	[mm]	Average of col. 161, 163
189	Overall base shear (x dir., with non-oscillatory mass)	[kN]	Sum of the products of each accelerometer reading with the associated mass
190	1st floor displ. N-W corner - RC slab (x dir., +2680 mm)	[mm]	Circle intersection, col. 113 & 114
191	1st floor displ. N-W corner - RC slab (y dir., +2680 mm)	[mm]	Circle intersection, col. 113 & 114
192	1st floor displ. N-E corner - RC slab (x dir., +2680 mm)	[mm]	Circle intersection, col. 116 & 117
193	1st floor displ. N-E corner - RC slab (y dir., +2680 mm)	[mm]	Circle intersection, col. 116 & 117
194	2nd floor displ. N-W corner - Timber diaph. (x dir., +5520 mm)	[mm]	Circle intersection, col. 94 & 95
195	2nd floor displ. N-W corner - Timber diaph. (y dir., +5520 mm)	[mm]	Circle intersection, col. 94 & 95
196	2nd floor displ. N-E corner - Timber diaph. (x dir., +5520 mm)	[mm]	Circle intersection, col. 96 & 97
198	2nd floor displ. S-E corner - Timber diaph. (x dir., +5520 mm)	[mm]	Circle intersection, col. 98 & 99
199	2nd floor displ. S-E corner - Timber diaph. (y dir., +5520 mm)	[mm]	Circle intersection, col. 98 & 99
200	2nd floor displ. S-W corner - Timber diaph. (x dir., +5520 mm)	[mm]	Circle intersection, col. 100 & 101

201	2nd floor displ. S-W corner - Timber diaph. (y dir., +5520 mm)	[mm]	Circle intersection, col. 100 & 101

A.3 REFERENCES

Damiani, N., Miglietta, M., Mazzella, L., Grottoli, L., Guerrini, G., Graziotti, F. [2019] "Full-scale shaking table test on a Dutch URM cavity-wall terraced-house end unit—a retrofit solution with strong-backs and OSB boards—EUC-BUILD-7". *Research report EUC052/2019U*, EUCENTRE foundation, Pavia, Italy. https://www.eucentre.it/nam-project.

Guerrini, G., Damiani, N., Miglietta, M., Graziotti, F. [2021] "Cyclic response of masonry piers retrofitted with timber frames and boards". *Structures and Buildings*. https://doi.org/10.1680/jstbu.19.00134

Miglietta, M., Mazzella, L., Grottoli, L., Guerrini, G., Graziotti, F. [2019] "Full-scale shaking table test on a Dutch URM cavity-wall terraced-house end unit—EUC-BUILD-6". *Research report EUC160/2018U*, EUCENTRE foundation, Pavia, Italy. www.eucentre.it/nam-project .

Miglietta, M., Damiani, N., Guerrini, G., Graziotti, F. [2021] "Full-scale shake-table tests on two unreinforced masonry cavity-wall buildings: effect of an innovative timber retrofit". Bulletin of Earthquake Engineering, 19(6), 2561-2596.

Vicon Motion Systems [2019]. *Vicon Nexus user guide*. Centennial, Colorado, United States. Available at: https://www.vicon.com.